FACSIMILE COVER THESIS

Università degli Studi di Padova
Centro Ricerche Fusione

Universidade de Lisboa
Instituto Superior Técnico **(IST)**

Università degli Studi di Napoli Federico II

Universidad Carlos III de Madrid

JOINT RESEARCH DOCTORATE IN FUSION SCIENCE AND ENGINEERING
Cycle XXXII
and
ERASMUS MUNDUS International Doctoral College in Fusion Science and Engineering

ELECTROMAGNETIC TURBULENCE IN THE EDGE OF FUSION PLASMAS: SPONTANEOUS AND ACTIVELY MODULATED FEATURES

Promotor at Università degli Studi di Padova (Home Institution): Prof. Paolo Bettini
Supervisor at Università degli Studi di Padova (Home Institution): Dr. Monica Spolaore

Promotor at Universidad Carlos III de Madrid (Host Institution): Prof. José Ramón Martín Solís
Supervisor at Universidad Carlos III de Madrid (Host Institution): Dr. Boudewijn Van Milligen

Ph.D. student: Gustavo Guedes Grenfell

Padova, September 2019

Electromagnetic turbulence in the edge of fusion plasmas: spontaneous and actively modulated features

by

Gustavo Guedes Grenfell

A dissertation submitted in partial fulfilment of the requirements for the degree of Doctor of Philosophy in Plasmas y Fusión Nuclear

Universidad Carlos III de Madrid

Promoters:

Prof. Paolo Bettini

Prof. José Ramón Martín Solís

Supervisors:

Dr. Monica Spolaore

Dr. Boudewijn Van Milligen

September 2019

Abstract

This thesis aims to study the properties of turbulent transport, exploiting the cross-comparison between different magnetic configurations, fusion devices, and plasma regimes. Understanding and controlling cross-field transport in magnetized plasmas devices is a requirement for achieving a commercial fusion reactor. Turbulent transport plays a crucial role in both tokamak and stellarator, while shear flows can impact its growth and development. Such an effect has a beneficial impact on the overall plasma confinement, but it is detrimental for the energy exhaustion since it ultimately decreases the power deposition area on the divertors. The latter phenomenon seems to be, to a large extent, determined by the turbulent coupling between the plasma edge and the scrape-off layer (SOL), governed by travelling turbulent filaments. These structures share some features with the edge-localized mode (ELM) filaments that, in turn, typically result in a large transient heat flux on plasma-facing components. The existence of ELMs in future fusion reactors is a concern since they might reduce the device life-time, while the proper understanding of their characteristics and dynamics can help to control them.

The local effective turbulence growth and spreading rate are computed in the TJ-II stellarator from the edge to the SOL with a set of electrostatic sensors. The results show that the local turbulence growth reduces once a shear layer is formed in the plasma edge induced by an external electrode biasing. Besides, the turbulence spreading rate is mainly activated in the SOL, decreasing when the $E \times B$ shearing rate becomes comparable to the inverse of the turbulence correlation time, leading to a decoupling of the edge-SOL turbulence. The role of radial electric fields in regulating turbulence propagation is further confirmed in TJ-II by spontaneous neoclassical electron-ion root transition experiments. During this process, the edge radial electric field flips sign continuously from positive to negative values. Through the measurements of two electrostatic probes remotely separated, the zonal flows be-

come amplified during the transition, while turbulence decreases in the ion root phase. Furthermore, the turbulence propagation computed using the transfer entropy technique shows that turbulence propagates radially outward at $\sim$ 1 km/s during the electron root, reducing substantially in the ion root phase.

The electromagnetic properties of turbulent filaments are investigated in RFX-mod operating as tokamak in the single-null configuration. In this experiment, the edge biasing technique was applied to induce an improved plasma confinement so that a comparison between the L and H-mode regimes is possible. On this purpose, the plasma boundary was monitored with a set of electrostatic and magnetic sensors. Through advanced statistical techniques, filaments are detected and tracked from the edge to the SOL in a two-dimension floating potential map together with their associated plasma density and current density parallel to the equilibrium magnetic field. While in L-mode they travel almost freely, during H-mode their motion becomes restricted to the near SOL. The higher ExB shear in the latter regime is pointed out to be the reason for this effect. Filament dynamics in the two scenarios is discussed in the framework of analytical models and velocity scaling. During L-mode, filaments are better described by the sheath connected regime and the parallel current density and potential structure are shown to be roughly synchronized. In H-mode, however, filaments near the last closed flux surface (LCFS) scale roughly as the inertial regime. In addition, ELM filaments appear spontaneously during the biasing H-mode in RFX-mod. The properties of these structures are compared with the type I ELMs observed in the COMPASS tokamak. In both devices, the ELM filaments carry a substantial current towards the SOL. Statistical analysis reveals a complex and rich fine structure within the ELM cycles. Besides, the ELM filaments are expelled towards the SOL when the background profiles become less steep and the level of perpendicular magnetic field more intense. Finally, ELM precursors and quasicoherent modes are observed in both devices.

Riassunto

Lo scopo di questa tesi lo studio delle propriet del trasporto turbolento nella regione di bordo di plasmi fusionistici, sfruttando il confronto incrociato tra diverse configurazioni magnetiche, diverse macchine di fusione e diversi regimi del plasma. La comprensione dei meccanismi che regolano il trasporto e il loro controllo costituiscono un tassello essenziale per il raggiungimento dellobiettivo di un reattore a fusione commerciale. Il trasporto turbolento svolge un ruolo cruciale sia nella configurazione tokamak sia nello stellarator, daltro canto lo sviluppo di gradienti di velocit nella regione esterna del plasma pu influenzarne e controllarne linsorgenza e la crescita. Un tal effetto ha un impatto benefico sul confinamento globale del plasma, tuttavia presenta delle controindicazioni per quanto riguarda lo smaltimento dellenergia proveniente dal plasma, in quanto questa si concentra in unarea ridotta delle piastre dei divertori. Quest'ultimo fenomeno sembra essere in larga misura determinato dall'accoppiamento turbolento tra il bordo del plasma e lo 'scrape-off layer' (SOL) (all'esterno dellultima superficie chiusa - LCFS acronimo in inglese), governato da filamenti turbolenti. Queste strutture condividono alcune caratteristiche con i filamenti che si manifestano durante ELM (edge-localized mode/modi localizzati nella regione di bordo) che, a loro volta, generano un grande flusso di calore transitorio sui componenti esposti al plasma. L'esistenza di ELM nei futuri reattori a fusione costituisce una notevole sfida tecnologica attualmente perch pu ridurre la durata del dispositivo mentre la corretta comprensione delle sue caratteristiche e dinamiche pu aiutare a controllarli.

In questo lavoro di tesi la crescita della turbolenza locale e il tasso della sua dispersione radiale sono calcolati nello stellarator TJ-II dal bordo allo SOL con un sistema di sensori elettrostatici. I risultati mostrano che la crescita della turbolenza locale si riduce quando si forma un forte gradiente di velocit nel bordo del plasma indotto da un elettrodo esterno polarizzato. I risultati dimostrano che il tasso della

dispersione della turbolenza agisce principalmente nel SOL, diminuendo quando gradiente di velocitá $E \times B$ diventa paragonabile all'inverso del tempo di correlazione della turbolenza, portando a un disaccoppiamento della turbolenza edge-SOL. Il ruolo dei campi elettrici radiali nella regolazione della propagazione della turbolenza ulteriormente confermato nellesperimento TJ-II, mediante esperimenti di transizione spontanea electron-ion root. Durante questo processo, il campo elettrico radiale indotto al bordo cambia da valori positivi a negativi. Attraverso le misurazioni di due sonde elettrostatiche posizionate in due regioni lontane tra loro, si osserva che le regioni caratterizzate da velocit omogenea (zonal flows) vengono amplificati durante la transizione, mentre la turbolenza diminuisce nella fase di campo elettrico negativo (ion root). Inoltre, la propagazione della turbolenza calcolata usando la tecnica di trasferimento dellentropia mostra che la turbolenza si propaga radialmente verso l'esterno a $\sim$ 1 km / s durante la fase di campo elettrico positivo (electron root), riducendosi sostanzialmente nella fase della ion root.

Altro importante argomento trattato in questo levoro di tesi riguarda le propriet elettromagnetiche dei filamenti turbolenti. Queste strutture sono state studiate in dettaglio nellesperimento RFX-mod operato in configurazione tokamak con un punto a X nella separatrice (single-null). Anche in questo esperimento, stata applicata la tecnica di polarizzazione del bordo per indurre un miglioramento del confinamento del plasma in modo che sia possibile un confronto tra i regimi L e H-mode. A tal fine, il bordo del plasma stato monitorato con una serie di sensori elettrostatici e magnetici. Utilizzando tecniche statistiche avanzate, i filamenti vengono rilevati e tracciati dal bordo verso il SOL in una mappa di potenziale flottante bidimensionale insieme alla densit del plasma e alla densit di corrente parallela al campo magnetico di equilibrio. Mentre nella modalit L-mode i filamenti viaggiano quasi liberamente, durante la modalit H-mode il loro movimento limitato al SOL nella regione prossima allultima superficie chiusa (near SOL). Il gradiente di velocit ExB pi elevato in quest'ultimo

regime sembra essere la ragione di questo effetto. Le dinamiche del filamento nei due scenari sono discusse nell'ambito di modelli analitici e di scale di velocit e dimensione dei filamenti stessi. Durante la modalit L-mode, i filamenti sono meglio descritti dal regime che prevede i filamenti connessi allo strato di Debye nelle superfici esposte al plasma, in questo caso si osservato che la densit di corrente parallela e la struttura potenziale viaggiano approssimativamente sincronizzati. In modo H, tuttavia, i filamenti vicino alla LCFS sono meglio descritti dal regime inerziale. I filamenti ELM compaiono spontaneamente durante la polarizzazione del modo H in RFX-mod. Parte dello studio stato quindi dedicato alla loro caratterizzazione. Queste strutture sono state confrontate con gli ELM di tipo I osservati nel tokamak COMPASS. In entrambi i dispositivi, i filamenti ELM trasportano una sostanziale corrente verso il SOL. L'analisi statistica rivela una struttura fine complessa e ricca all'interno dei cicli ELM. I filamenti ELM sono espulsi nel SOL verso la parete in corrispondenza di una riduzione dei gradienti radiali medi e di una pi intensa fluttuazione del campo magnetico perpendicolare. Infine lesistenza di una fase di modi quasi coerenti prima del verificarsi degli eventi di ELM stata caratteristica comune in entrambi i dispositivi.

Acknowledgements

I would like to deeply thank all the people who help me over these last three years. First of all, I would like to thank my supervisors, Monica Spolaore and Boudewijn van Milligen, for their guidance and support. I also acknowledge Paolo Bettini and José Ramón Martín Solís for their support as promoters of this joint doctorate, representing, respectively, Universitá degli Studi di Padova and Universidad Carlos III.

During my research activities carried out in Padova, I had the support of many people. I acknowledge Emilio Martines, Nicola Vianello, Marco Veranda, Domenico Abate, Italo Predebon, Piero Agostinetti, Lionello Marrelli, Lorella Carraro, and all the RFX-team for the cooperation. I would like to thank Carlos Hidalgo for the great support he gave me during my stay in Madrid working in CIEMAT. I acknowledge also Ulises Losada for helping me during the experimental campaign in TJ-II. Furthermore, I would like to thank Teresa Estrada, Alexander Melnikov, Enrique Ascasibar, and all the TJ-II team for their assistance. I would like to thank Jan Stöckel and Karel Kovařík for their support during my stay in Prague working with the COMPASS tokamak. I acknowledge also Carsten Killer for his collaboration in the High-Resolution Probe Head project for W7-X.

I would like to acknowledge that this work was supported by the European Commission in the framework of the Erasmus Mundus International Doctoral College in Fusion Science and Engineering (FUSION-DC). Lastly, I wish to thank my parents for their support and encouragement, and my beloved Pamela Kakimoto for standing with me throughout this period, encouraging me all the time, and for her careful proofreading of this thesis.

Published and Submitted Content

Articles (co)-authored by the Doctoral candidate that are included as part of the thesis and that have been published:

- Grenfell, G., Spolaore, M., Abate, D., Carraro., L., Marrelli, L., Predebon, I., Spagnolo, S., Veranda M., and the RFX-mod Team (2019). Turbulent filament properties in L and H-mode regime in the RFX-mod operating as a tokamak. *Nuclear fusion* (Submitted).

  This item is partially included in Chapter 7;

- Grenfell, G., van Milligen, B. P., Losada, U., Estrada, T., Liu, B., Silva, C., Spolaore, M, Hidalgo, C. and TJ-II Team (2019). The impact of edge radial electric fields on edge-SOL coupling in the TJ-II stellarator. *Nuclear Fusion*, 60(1), 014001 (https://doi.org/10.1088/1741-4326/ab538c).

  This item is wholly included in Chapter 6. Whenever material from this source is included in this thesis, it is singled out with typographic means and an explicit reference. Reproduced here with permission of the copyright owner, Institute of Physics (IOP) Publishing Ltd;

- Spolaore, M., Agostinetti, P., Killer, C., Moresco, M., Brombin, M., Cavazzana, R., et al. (2019). High Resolution Probe for filament transport and current density study at the edge region of W7-X. *Journal of Instrumentation*, 14(09), C09035 (https://doi.org/10.1088/1748-0221/14/09/C09035);

- Ascasibar, E., Alba, D., Alegre, D., Alonso, J. A., Alonso, J., de Aragn, F., et al. (2019). Overview of recent TJ-II stellarator results. *Nuclear Fusion*, 59(11) (https://doi.org/10.1088/1741-4326/ab205e);

- Grenfell, G., van Milligen, B. P., Losada, U., Ting, W., Liu, B., Silva, C., Spolaore, M, Hidalgo, C. and TJ-II Team (2018). Measurement and control of turbulence spreading in the scrape-off layer of TJ-II stellarator. *Nuclear Fusion*,

59(1), 016018 (https://doi.org/10.1088/1741-4326/aaf034).

This item is partially included in Chapter 5. Whenever material from this source is included in this thesis, it is singled out with typographic means and an explicit reference. Reproduced here with permission of the copyright owner, Institute of Physics (IOP) Publishing Ltd;

- Spolaore, M. , Cavazzana, R., Marrelli, L., Carraro, L., Franz, P., Spagnolo, S., Zaniol, B., Zuin, M., Cordaro, L., Dal Bello, S., De Masi, G., Ferro, A., Finotti, C., Grando, L., Grenfell, G., Innocente, P., Kudlacek, O., Marchiori, G., Martines, E., Momo, B., Paccagnella, R., Piovesan, P., Piron, C., Puiatti, M.E., Recchia, M., Scarin, P., Taliercio, C., Vianello, N., Zanotto, L. (2017). H-mode achievement and edge features in RFX-mod tokamak operation. *Nuclear Fusion*, 57(11), 116039 (https://doi.org/10.1088/1741-4326/aa7f1e).

Conferences and Seminars as principal author and schools by the Doctoral candidate that are included as part of the thesis and that have been published:

- Workshop on Electric Fields, Turbulence and Self-Organization in Magnetized Plasmas (EFTSOMP), '3D filamentary transport and the role of edge sheared radial electric fields in the RFX-mod tokamak operation', Oral presentation and member of the LOC committee, Padova, July 14th -16th, 2019;

- 46th European Physical Society Conference on Plasma Physics, 'The influence of edge sheared radial electric fields on edge-SOL coupling in the TJ-II stellarator', Poster, Milan, July 8th - 12th 2019;

- 19th Coordinated Working Group Meeting (CWGM), 'On the role of sheared radial electric fields on turbulence spreading in the plasma boundary of fusion devices', Oral presentation (remotely), Berlin, Germany, March 12nd 14th 2019;

- 27th IAEA Fusion Energy Conference (FEC 2018), 'The impact of the radial electric fields on turbulence spreading in the edge and Scrape-Off Layer of TJ-II', Poster, Gandhinagar (India), October 22nd - 27th 2018;
- PhD Event 2018 ITER. Cadarache, France. November 6th to 9th;
- SUMTRAIC summer school in Prague, from August 27th to September 7th 2018, organized by the Institute for Plasma Physics Prague (supervisor);
- Workshop on Electric Fields, Turbulence and Self-Organization in Magnetized Plasmas (EFTSOMP), 'Measurement and control of turbulence spreading in the Scrape-Off Layer of TJ-II', Invited presentation, Prague, July 9th -10th;
- 45th European Physical Society Conference on Plasma Physics, '2-D filament dynamics in high and low shear flows in the edge of the RFX-mod tokamak', Poster, Prague, July 2nd - 6th 2018;
- SUMTRAIC summer school in Prague, from August 28th to September 9th 2017, organized by the Institute for Plasma Physics Prague;
- 44th European Physical Society Conference on Plasma Physics, 'Electromagnetic filaments and edge modifications induced by electrode biasing in the RFX-mod tokamak', Poster, Belfast, from June 26th to June 30th 2017).

Other Research Merits

- Vianello, N., Carralero, D., Tsui, C. K., Naulin, V., Agostini, M., Cziegler, I., et al. (2019). Scrape-off layer transport and filament characteristics in high-density tokamak regimes. *Nuclear Fusion*, 60(1), 016001 (https://doi.org/10.1088/1741-4326/ab423e);

- Hernandez, W. A., Guimares-Filho, Z. O., Grenfell, G. G., and Nascimento, I. C. (2019). Spatial inhomogeneity effects on burst temperature estimation using a triple probe configuration in Tokamak Chauffage Alfvn Brésilien tokamak. *Journal of Plasma Physics*, 85(4) (https://doi.org/10.1017/S0022377819000503);

- Van Milligen, B. P., Nicolau, J. H., Liu, B., Grenfell, G., Losada, U., Carreras, B. A., L. Garcia, Hidalgo, C and TJ-II Team. (2018). Filaments in the edge confinement region of TJ-II. *Nuclear Fusion*, 58(2), 026030 (https://doi.org/10.1088/1741-4326/aa9db6);

- Grenfell, G. G., Nascimento, I. C., Oliveira, D. S., Guimares-Filho, Z. O., Elizondo, J. I., Reis, A. P., Galvo R. M. O., Baquero, W. A. H., Oliveira, A. M., Ronchi , G., de S , W. P., Severo , J. H. F., and TCABR Team. (2018). H-mode access and the role of spectral shift with electrode biasing in the TCABR tokamak. *Physics of Plasmas*, 25(7), 072301 (https://doi.org/10.1063/1.5029561).

Contents

Abstract ii

Acknowledgements vii

1 Introduction **1**

1.1 Motivation and thesis outline 2

2 The route to a thermonuclear fusion device **6**

2.1 Kinetic description 9

2.1.1 Fluid description 10

2.2 Magnetically Confined Plasmas 11

2.2.1 Tokamak 12

2.2.2 Stellarator 13

2.2.3 Neoclassical transport in tokamaks and stellarators 14

2.2.4 Reversed Field Pinch (RFP) 16

2.2.5 Scrape-off layer (SOL) 17

2.2.6 High confinement mode (H-mode) 20

2.2.7 Electrode biasing technique 23

3 Plasma turbulence **26**

3.1 Drift wave 28

3.2 Interchange instability 31

3.3 Kolmogorov turbulence description 32

3.4 Turbulence saturation mechanisms 34
3.4.1 $E \times B$ shear flow and eddy decorrelation paradigm 34
3.4.2 Zonal flows (ZFs) 37
3.5 Turbulent filaments 39
3.5.1 Experimental evidences of filaments 42
3.5.2 Blobs simple model 44
3.5.3 Electromagnetic filaments 49
3.5.4 Blob suppression criterion 49

4 Experimental systems, plasma diagnostics, and experimental tools 51
4.1 Experimental systems 51
4.1.1 COMPASS 51
4.1.2 RFX-mod 53
4.1.3 TJ-II 54
4.1.4 Wendelstein 7-X 57
4.2 Some turbulence diagnostics 58
4.2.1 Electrostatic probe 58
4.2.2 Magnetic sensors 63
4.2.3 Filamentary probe 65
4.2.4 ISIS 69
4.3 Useful statistical tools for turbulence investigation 70
4.3.1 Probability distribution function 70
4.3.2 Correlation function 71
4.3.3 Cross power spectrum and coherence 72
4.3.4 Wavenumber frequency spectrum - S(k,f) 76
4.3.5 Wavelet and local intermittency measurement (LIM) 77
4.3.6 Conditional average 80

5 Turbulence Spreading in the TJ-II stellarator **81**

5.1 Local mixing paradigm 81

5.2 Turbulence Spreading 84

5.3 Experimental observations of turbulence spreading 92

5.4 Edge-SOL model for Turbulence Spreading 95

5.5 Turbulence Spreading in the TJ-II 99

5.5.1 Electron to the ion root transition 102

5.5.2 NBI + biasing 107

5.6 Conclusion 112

6 Edge-SOL turbulence coupling **114**

6.1 Statistical tools 115

6.1.1 Mutual information 115

6.1.2 Transfer Entropy 116

6.1.3 TE and blob 'toy model' 117

6.1.4 Biorthogonal decomposition 121

6.2 Divertor heat flux width (λ_q) in fusion devices 124

6.3 Slow electron-ion-electron root transition in TJ-II 130

6.4 Conclusion 149

7 Cross Field Transport in the RFX-mod tokamak **151**

7.1 L-H transition in the RFX-mod tokamak 154

7.1.1 Plasma-wall interaction 168

7.2 Blobs detection and characterization 171

7.2.1 Threshold criterion 171

7.2.2 2D cross correlation technique for cross-field filament detection 176

7.2.3 Eigendecomposition of a covariance matrix 179

7.3 L-mode filaments 183

7.4 H-mode filaments . . . 186
7.5 L-H mode filament comparison . . . 192
7.5.1 Magnetic fluctuations and parallel current density . . . 193
7.5.2 Blob suppression . . . 197
7.5.3 Filament velocity scaling . . . 200
7.6 Conclusion . . . 202

8 ELMs filaments 206
8.1 Edge-Localized Modes (ELM) . . . 207
8.2 Electromagnetic filaments . . . 211
8.3 ELMs in RFX-mod tokamak . . . 214
8.3.1 Experimental evidences of ELMs in RFX-mod . . . 216
8.3.2 The ELM cycle . . . 226
8.3.3 Filamentary transport during ELM cycle . . . 232
8.3.4 Scale dependence through the ELM cycle . . . 241
8.4 ELMs in the COMPASS tokamak . . . 247
8.4.1 Quasicoherent mode . . . 254
8.5 Conclusion . . . 257

9 Final conclusion 260

A List of Symbols and Abbreviations 267
A.1 List of Symbols . . . 268
A.2 List Abbreviations . . . 270

Bibliography 272

Chapter 1

Introduction

Nuclear fusion is one of the most energetic processes known in the universe. It is the means whereby stars, e.g., the sun, generate their energy: light atoms are fused in their core pulled by the enormous gravitational forces. The simplest fusion reactions in terms of the high cross-section for low energy are:

$$\begin{aligned} D^2 + D^2 &\rightarrow He^1 + T^3 + 4.03 \text{ MeV} \\ D^2 + D^2 &\rightarrow n^1 + He^3 + 3.27 \text{ MeV} \\ D^2 + T^3 &\rightarrow He^4 + n^1 + 17.6 \text{ MeV} \\ D^2 + He^3 &\rightarrow He^4 + He^1 + 18.4 \text{ MeV} \end{aligned} \tag{1.1}$$

The last reaction (between deuterium and helium-3) is considered the ideal for a fusion reactor since it does not produce neutrons. However, helium-3 is extremely rare on earth. The most promising reaction (as can be seen in Fig. 1.1) is between deuterium and tritium since it presents the highest cross-section for relatively low temperature. Due to the tunnelling effect of the energetic particles, the required temperature is even lower, around l0 keV [287]. The reaction yields an alpha particle of high energy up to 3.5 MeV and a neutron with energy 14.1 MeV. However, particles must be confined for long enough time in a given volume to sustain the reactions since the

cross-section for elastic scattering is much larger than for fusion, i.e., many elastic collisions occur before a fusion reaction is achieved. With this in mind, there are two leading approach to confine particles on the purpose to achieve the suitable conditions for nuclear reaction: *inertial confinement* and *magnetic confinement*. This thesis is focus on the latter one.

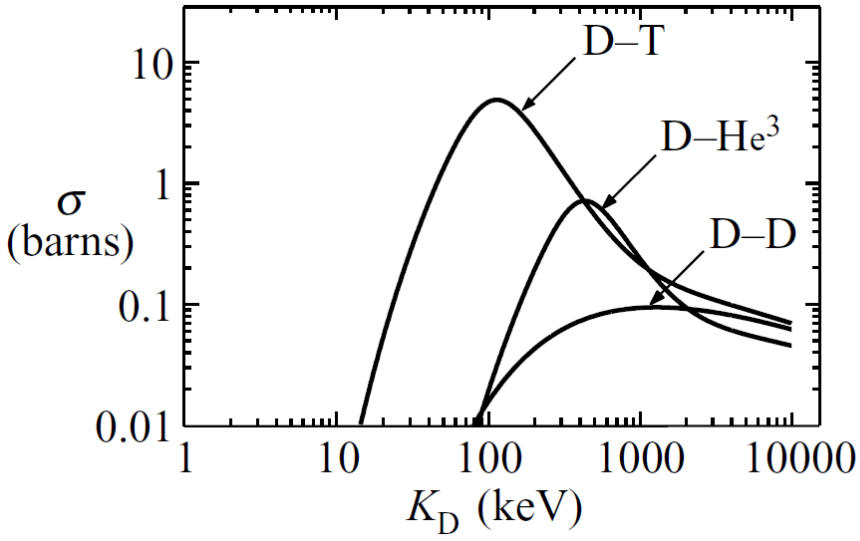

Figure 1.1: Fusion cross-section as function of particles energy.

1.1 Motivation and thesis outline

The feasibility of the future fusion reactors will depend on the quality of plasma confinement and the efficiency of the energy exhaustion. These two requirements are ultimately associated with plasma cross-field transport, with an important role played by filamentary transport, i.e., field-aligned turbulent structure ejected from a hotter and denser region towards the plasma-facing components. While in the low confinement regime (L-mode) the cross-field transport is dominated by turbulence, yielding an energy and particle flux much larger than what is expected from Coulomb collisions in toroidal geometry (i.e., neoclassical transport). In H-mode, a large poloidal flow shear leads to massive turbulence suppression in the plasma edge that allows the

pressure gradient and the plasma stored energy to growth. While this effect has a beneficial impact on the confinement, the reduced cross-field transport in the scrape-off layer (SOL) results in a narrow energy deposition area on the divertor plates, with possible detrimental effects on the involved material surfaces. Predictions for ITER (the largest tokamak in the world that is being constructed in Cadarache, France) based on the regression of data collected from some of the present tokamaks [67] suggest that the heat flux width will be even smaller than of the present-day machines due to a strong inverse dependence with the plasma current. This perspective would limit the margins of operation of ITER and beyond. On the other hand, recent simulations [42, 292] have pointed out to the leading role of turbulence in ITER. In particular, the propagation of turbulence from the pedestal towards the scrape-Off Layer (SOL) is believed to enhance the cross-field transport throughout this range, coupling these two regions. The 'agent' of this propagation is possibly turbulent filaments. These structures have been observed in the plasma periphery of tokamaks, stellarators, reversed field pinches, and simple toroidal and linear devices. The universal behaviour of filaments and turbulence, in general, makes the device comparison an interesting and important approach. It has become clear that to make safer predictions for future fusion devices, deeply understanding of the mechanisms regulating the turbulent plasma behaviour in the edge and SOL is essential.

Within this framework, this thesis aims to investigate the mechanisms that set turbulent transport in magnetized plasmas, exploiting the comparison of different devices and magnetic configuration. The focus is the plasma edge and SOL, while the main diagnostic used is probes: electrostatic and magnetic, but with some inputs from other diagnostics. In particular, a detailed investigation of turbulent features and filamentary transport was performed in the edge and SOL region of different devices: TJ-II stellarator, COMPASS tokamak, and RFX-mod operated as tokamak. Different plasma regimes were obtained in both TJ-II and RFX-mod through the

active modulation of the plasma edge via electrode biasing technique. In addition, in the tokamak configurations, a comparison between the improved confinement regime (H-mode) obtained in COMPASS and RFX-mod was provided. The detailed thesis outline is described in the following:

- **Chapter 2** presents some of the basic equations that describe a magnetized plasma in the framework of the kinetic and fluid description. In addition, the concept of tokamak, stellarator, and reversed field pinch (RFP) is introduced together with the scrape-off layer (SOL). Lastly, the high confinament mode (H-mode) in tokamak and stellarator is discussed and the biasing technique (widely used through the thesis);
- **Chapter 3** gives a general view on turbulence in magnetized plasmas, discussing also the mechanism for its saturation. Besides, this chapter introduces the concept of turbulent filaments and their common description;
- **Chapter 4** introduces the experimental systems where the experimental activities were carried out. In additional, the main diagnostics used and the statistical tools considered to interpreter the data are also introduced;
- **Chapter 5** discusses the turbulence spreading phenomenon and presents some experimental result obtained in the TJ-II where turbulence spreading was studied systematically;
- In **Chapter 6** the topic propagation of turbulence is further investigated but with a different approach. Particularly, the transfer entropy technique is used to measure the propagation of turbulence during the spontaneously electron-ion-electron root transitions in TJ-II;
- **Chapter 7** discusses the L-H transition obtained with external electrode biasing in RFX-mod running as tokamak in single-null configuration. In addition, the properties of turbulent filaments in L and biasing H-mode is discussed in detail.

- In **Chapter 8** is discussed the properties of edge-localized mode (ELM) filaments. These structures are observed in RFX-mod in biasing experiments. With similar experimental and analysis tools, ELM filaments observed in RFX-mod and in the COMPASS tokamak are compared. In addition ELM precursors and quasicoherent modes, common for both devices, are also discussed;
- **Chapter 9** presents the final conclusions.

Chapter 2

The route to a thermonuclear fusion device

As discussed in the previous chapter, the easiest way to produce fusion reaction on earth is by the deuterium-tritium reaction. The fusion reaction starts to occur when both gases reach temperatures around l0 keV, which corresponds to approximately 100 million degrees centigrade. At such high temperature, the gas becomes almost fully ionized, turning into a *plasma* [82].

Fusion reactions in a plasma occurs, according to the triple product or Lawson criterion [287], when $nT\tau_E > 5 \times 10^{21}$ m^{-3}keV, where n and T are the plasma density and temperature, respectively, and τ_E is the energy confinement time defined as $\tau_E = W/P_L$, where W is the total plasma energy and P_L is the power losses. Therefore, the confinement time must be long enough to guarantee that the power losses (radiation, conduction, and convective) will be lower than the fusion energy released in the plasma (through the alpha particles). If, e.g., the temperature is about 10 keV and the density 2×10^{20} m^{-3}, the confinement time is in the order of seconds.

A convenient way to confine charge particles is through magnetic fields. The particles travel freely along the magnetic field line, but they are confined in the cross-field plane in circular orbits with Larmor (or gyro) radius of $mv_\perp/|q|B$, where m and q are the particle mass and charge, $v_\perp$ is its perpendicular velocity, and B is the magnetic field. The equation of motion of a charge particle embedded by a magnetic field is given by:

$$m\frac{d\mathbf{v}}{dt} = \mathbf{F} + q(\mathbf{v} \times \mathbf{B}) \tag{2.1}$$

Where m is the mass, q is the charge, and $\mathbf{F}$ is an external force. When this force is negligible and the magnetic field is homogeneous and stationary, the solution of the previous equation describes a particle moving circularly around the magnetic field with frequency given by the cyclotron or Larmor frequency $\omega_c = q|B|/m$, and gyroradius or Larmor radius r_L. Neglecting the particle acceleration, which means ignoring the gyration of the particle, the equation becomes:

$$\mathbf{F} + q(\mathbf{v} \times \mathbf{B}) = 0$$

where is easy to demonstrate that:

$$\mathbf{v}^F = \frac{\mathbf{F} \times \mathbf{B}}{qB^2} \tag{2.2}$$

The previous equation shows that any force acting on a charged particle embedded in a homogeneous and stationary magnetic field will result in a drift velocity $\mathbf{v^F}$ perpendicular to both $\mathbf{B}$ and $\mathbf{F}$. If this is force is given by a constant electric field $\mathbf{F}^E = q\mathbf{E}$, the drift becomes:

$$\mathbf{v}^{E\times B} = \frac{\mathbf{E} \times \mathbf{B}}{B^2} \tag{2.3}$$

Note that $\mathbf{v}^{E\times B}$ does not depend on the charge or mass of the particle, meaning that electrons and ions move in the same direction. This drift is fundamental in the study of turbulent transport as will be discussed throughout this thesis.

In the case where the magnetic field is not homogeneous, an effective force arises given by $\mathbf{F}^{\nabla B} = -\mu\nabla B$, where $\mu = mv_\perp^2/2B$ is magnetic moment. Charged particles are reflected in regions where ∇B is large, i.e., the parallel velocity flip sign while the perpendicular one increases due to the conservation of energy and magnetic moment. This concept was employed to confine plasmas magnetically through mirror machines [82]. However, the existence of a cone loss together with the presence of drifts and MHD instabilities make this kind of configuration infeasible [62]. Toroidal configurations are more promising since the parallel losses are naturally reduced. In this case, the magnetic field lines are bent, so particles moving along the magnetic field with velocity $v_\parallel$ will feel a centrifugal force $\mathbf{F}^C = mv_\parallel^2/R_c$ perpendicular to the field direction, where R_c is the curvature radius. The ∇B and the centrifugal force acting together can yield an unified drift [287] given by:

$$\mathbf{v}^{\nabla B} = \frac{m}{q}\left(v_\parallel^2 + \frac{v_\perp^2}{2}\right)\frac{\mathbf{B}\times\nabla_\perp B}{B^2} \tag{2.4}$$

Since electrons and ions experience this drift differently, with electrons moving in the opposite direction of ions, a charge-polarizing current can be created. However, to assure the plasma quasineutrality, a perpendicular electric field arises, which results in an $E \times B$ drift that moves electrons and ions together towards the wall. The presence of this drift motivated magnetic configurations with the helical field since this effect is canceled on average with the action of the Pfirsch-Schlüter current [287]. Among the configurations aimed to do that, tokamak, stellarator, and reversed field pinch (RFP) are the most successful. Each of them will be discussed in section 2.2.

The basic forces acting on a magnetically confined plasma in toroidal geometry are ∇p and $\mathbf{j} \times \mathbf{B}$, where p and $\mathbf{j}$ are, respectively, the plasma pressure and the current density. Equilibrium is achieved when:

$$\nabla p = \mathbf{j} \times \mathbf{B} \tag{2.5}$$

Since $\mathbf{B}.\nabla p = 0$ and $\mathbf{j}.\nabla p = 0$, one can deduce that magnetic field and current lines define an isobar surface. Besides, since $(\nabla \times B).\mathbf{B}. = \mu_0 \mathbf{j}.\mathbf{B} = 0$, they are also perpendicular to each other. These simple requirements define toroidally nested magnetic surfaces where the pressure is constant. The balance between the magnetic and the plasma kinetic pressure is described by the beta parameter:

$$\beta = \frac{p}{B^2/(2\mu_0)} \tag{2.6}$$

2.1 Kinetic description

To describe the plasma behaviour properly is necessary to take into account the different kind of interaction between the particles that compose it. However, describing the motion of each particle in the plasma and how they interact with the others is humanly impossible. A better approach comes for statistical mechanics, where the relevant parameter is the distribution function of a given spices α defined in a six dimensional phase space $f_\alpha(\mathbf{x}, \mathbf{v}, t)$. The *Vlasov equation* describes the time evolution of $f_\alpha(\mathbf{x}, \mathbf{v}, t)$ governed by the interaction forces that arise due to the motion of the charge particles that compose the plasma [25, 62]:

$$\frac{\partial f_\alpha}{\partial t} + \mathbf{v}.\nabla f_\alpha + \frac{q}{m}\left(\mathbf{E} + \mathbf{v} \times \mathbf{B}\right).\nabla_v f_\alpha = 0 \tag{2.7}$$

Where **B** and **E** are the magnetic and electric field, respectively, obtained from charge and current distribution through Maxwell's equations. This equation implicitly assumes that the collision between particles is negligible. This approximation is fairly good for hot or low-density plasmas, where the collision frequency is expected to be low, the particles mean free path is in the order of the machine size. If this is not the case, one has to add a collision term $(\partial f_\alpha/\partial t)_{coll}$ on the right-hand side of eq. 2.7. In practice, the proper collision term for a give problem is not so easy to define. When, e.g., the collisions are considered Coulomb type, the resulting equation becomes the *Fokker-Planck* equation [287].

2.1.1 Fluid description

When employing the kinetic approach in the study of instabilities in the plasma, it is useful to separate the background distribution function (typically Maxwellian) from the perturbed part. Considering that $(\partial f_\alpha/\partial t)_{coll}$ can be described by a Maxwellian, macroscopic variables such as density, velocity, kinetic pressure, and thermal energy can be defined from the moments of the distribution function [62]:

$$\int \mathbf{v}^k f_\alpha(\mathbf{v}) d^3v \tag{2.8}$$

where $k = 0, 1, 2, 3, ...$ are the order of the moments. The zero order ($k = 0$) yields the continuity equation for species α:

$$\frac{\partial n_\alpha}{\partial t} + \nabla(n_\alpha \mathbf{v}_\alpha) = 0 \tag{2.9}$$

While the first order integrating $m_\alpha \mathbf{v}$ on Eq. 2.8 produces the force balance equation:

$$\left[\frac{\partial \mathbf{v}_\alpha}{\partial t} + (\mathbf{v}_\alpha.\nabla)\mathbf{v}_\alpha\right] - q_\alpha n_\alpha(\mathbf{E} + \mathbf{v}_\alpha \times \mathbf{V}) + \nabla p_\alpha = \mathbf{R}_{\alpha\beta} \tag{2.10}$$

Where $\mathbf{R}_{\alpha\beta}$ is the friction force obtained from the collision term. One of the limitations of this approach is that the equation for moment k will always have a term $k+1$. This naturally makes the system insoluble. Hence, it is necessary a closure or a bond that reduces the number of variables. Eq. 2.10 can be closed, e.g., assuming that the system is adiabatic. Besides, it is common to reduce a plasma composed of two fluids (e.g. electrons and ions) in a single fluid by making some assumptions on the density, velocity, and current density [25]. In this case, one can define the Magnetohydrodynamics (MHD) equations [62].

2.2 Magnetically Confined Plasmas

It was discussed that the essential ingredient to confine plasmas with magnetic fields in a toroidal geometry is to make the field helical. This can be translated into the rotational transform (ν) defined from the average number of poloidal by toroidal turns around the magnetic axis [112]. To achieve a non-zero ν is necessary: 1) induce a toroidal current; 2) elongate the flux surface while rotates it poloidally along the toroidal direction; 3) a non-planar magnetic axis. The first concept is adopted by tokamaks and reversed field pinches (RFPs), making them axisymmetric, while requires a non-steady-state operation. Most of the stellarators rely on the second and third concepts that allow these devices operating in steady-state, but make them non-axisymmetric.

2.2.1 Tokamak

The tokamak concept was first proposed by Tamm and Sacharov in 1952 [175]. Helical field in this configuration is obtained by a combination of toroidal magnetic field induced by external coils and poloidal magnetic field created by a flowing plasma current induced by a central solenoid, i.e. the plasma is the secondary of a transformer. In addition, vertical field coils are usually needed to control the plasma position and shape. Tokamaks are axisymmetric, exhibiting toroidal symmetry, and they are characterized by the major radius (R, torus axis) and the minor radius (a), where the relation of these two parameters defines the aspect ratio: $A = R/a$. The tokamak cross-section can be very different, from circular as the first limiter configurations to more complex shapes that is typically motivated by stability and equilibrium properties [287].

A relevant parameter for plasma stability in tokamaks is the so-called safety factor:

$$q = \frac{r}{R}\frac{B_\phi}{B_\theta} \tag{2.11}$$

Such a parameter is also relevant for RFP configuration. In stellarators, for historical reasons, the rotational transform $\imath = 1/q$ has been used. Fig. 2.2 b) shows a comparison of typical q profiles found in these devices.

The heating power in a tokamak is primarily provided by ohmic heating ($P_{OH} = R_p I_p^2$, where R_p is the plasma electrical resistance and I_p is the plasma current). However, $R_P \propto T^{-3/2}$ [198], where T is the plasma temperature. It follows that ohmic heating becomes inefficient for high-temperature. Therefore, to achieve the high temperatures requirements for sustaining fusion reactions, auxiliary power sources are needed. Among those typically used on this purpose are the Neutral beam injection (NBI), Electron Cyclotron Resonance Heating (ECRH), and Ion Cyclotron Resonance

Heating (ICRH) [287]. The total heating power becomes $P_{tot} = P_{OH} + P_{aux}$ and so energy growth rate is $dW/dt = P_{tot} - W/\tau_E$, where W is the total plasma energy and τ_E the energy confinement time that, as the name suggests, is related to the quality of the plasma confinement, appearing in the Lawson or triple product criterion. In a typical tokamak regime (L-mode), the confinement time decreases with the total power $\tau_E \propto 1/\sqrt{P_{tot}}$ due to the dominance of turbulent transport [198]. This unfavourable scaling, however, is modified when the plasma transits to the high-confinement regime (H-mode), as will be discussed in section 2.2.6. In a fusion reactor, most of the heating power will be provided by the alpha particles from the nuclear reactions (through a process similar to NBI heating [287]). The Q-factor, $Q = P_{fusion}/P_{tot}$, quantifies how large the fusion power is compared to the external heating power. When they become comparable, the break-even is achieved, i.e., $Q = 1$, while if the fusion power is enough to sustain the plasma and the fusion reactions, $Q \to \infty$, i.e., the ignition is achieved. A large tokamak (that will be the largest one in the coming years) called ITER [287] is currently being built in Cadarache, France, under a partnership that involves several countries worldwide: United States of America, India, China, Japan, Russia, South Korea, and the European Union. ITER is aimed to operate with $Q = 10$ to show the viability of tokamaks as fusion reactors.

2.2.2 Stellarator

While in tokamak the rotational transform is obtained through a combination of toroidal magnetic field, that is externally generated by a set of coils, and poloidal magnetic field induced by a toroidal plasma current. In stellarators, field line helecity is fully obtained by external coils, i.e., without relying on plasma properties. This allows stellarators to operate in steady-state condition, which implies that these devices are more stable to magnetohydrodynamic (MHD) instabilities [112]. Although transient currents, like the bootstrap current, can arise and lead to undesirable ef-

fects (e.g. tearing modes) [112]. Besides, the Pfirsch-Schlüter current is naturally present to guarantee that $\nabla.\mathbf{j} = 0$, i.e., to assure the plasma quasineutrality. However, to accomplish that is necessary three-dimensionally shaped magnetic field coils with typically complex geometry. This one of the drawbacks of this configuration, especially from the engineering point of view. Besides, the complex arrange of coils makes stellarators non-axisymmetric.

2.2.3 Neoclassical transport in tokamaks and stellarators

Neoclassical transport refers to collisional transport in toroidal geometry. The collision frequency in a magnetized plasma determines the type of transport regime. When plasma becomes hotter in tokamaks and stellarators, the mean free path becomes larger and so the collision frequency drops. In this regime, charged particles can move along the field lines almost freely without undergoing collisions with the other particles. In tokamaks, due to the mirror effect, some particles will be reflected in the high field side, where the magnetic field is more intense, while some will simply circulate the torus depending on the relationship between parallel and perpendicular velocity. The trapped particles will exhibit 'banana' orbits, referring to how their trajectory looks like in a cross-field plane. The ∇B and curvature drift, however, produce an unbalance in the particle trajectory that leads to a radial displacement and ultimately to plasma diffusion. In a stellarator, however, this banana regime is quite different. The three-dimension field imposes a complicated path for the particles, with trapping and passing zones. Besides, different from tokamak where the ambipolarity condition $\Gamma_e = Z\Gamma_i$ is satisfied independently of the local radial electric field (E_r) [287], in stellarators this condition is only consistent with a particular set of E_r solutions [112]. The 'ion root' solution is for $E_r < 0$, where typically $T_e \sim T_i$, while the 'electron root' is the stable solution for $E_r > 0$ where $T_e \gg T_i$. The ion root regime expected to be the dominant one in deuterium-tritium fusion

scenario [61]. When the radial electric field is small, the diffusion coefficient scales

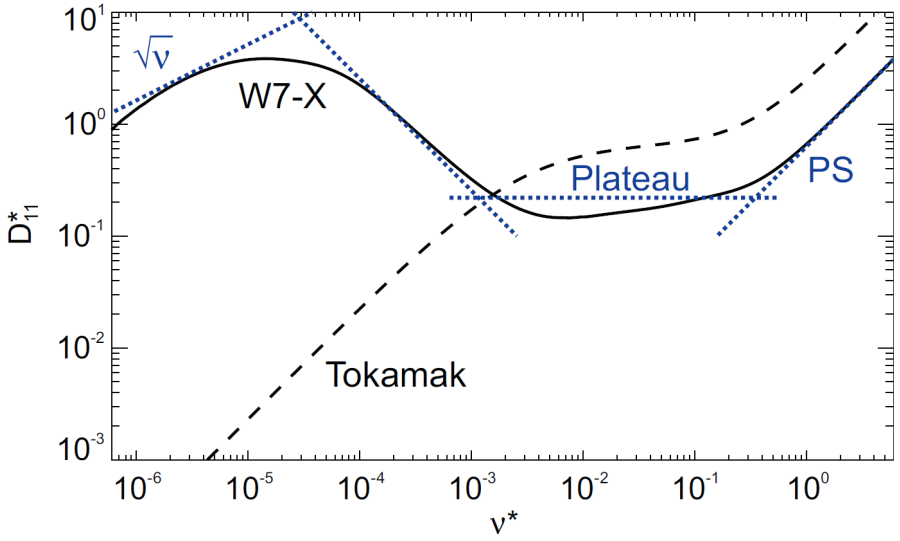

Figure 2.1: Mono-energetic diffusion coefficient as function of the collisionality ($\nu^* = \nu R/\iota v$, where v is the particles velocity, R is the major radius, ι is the rotational transform, and ν the mono-energetic pitch-angle-scattering frequency) for typical tokamak parameter (dashed line) and for W7-X (bold line) [112].

as $D^{1/\nu} \propto \epsilon_{eff}^{3/2} T^{7/2}$ [112], yielding a strong dependency with the temperature, where ν refers to the collision frequency and ϵ_{eff} is a geometric parameter related to the trapped orbits. The radial electric field has a beneficial effect on trapped particles, which results in a modified scale $D^{\sqrt{\nu}} \propto T^{5/4} E_r^{-3/2}$ [61]. Fig. 2.1 shows the diffusion coefficient as a function of the collisionality for a tokamak and a stellarator (in this case Wendestein-7X) [112]. Note the large discrepancy in the low collisionality branch between tokamak and stellarator. This difference becomes smaller for a higher radial electric field absolute value. For collisionality higher than $\nu^* > 10^{-3}$, both devices exhibit a comparable diffusion coefficient in the plateau and Pfirsch-Schlüter regimes. High collisionality at such level is likely observed in the plasma edge. Nevertheless, turbulent transport is typically dominant in this region in both devices [252].

2.2.4 Reversed Field Pinch (RFP)

The Reversed Field Pinch (RFP) is a type of device that confines plasmas in a toroidal geometry through the combination of poloidal (B_θ) and toroidal (B_ϕ) magnetic fields. The configuration is similar to the tokamak, both are axisymmetric, but the poloidal and toroidal magnetic fields are comparable in absolute value in RFP. B_ϕ is created by external coils (its strength is typical 10× weaker than in tokamaks) and B_θ induced by a toroidal plasma current. The good confinement in this device relies on the dynamo effect that, owing to the plasma self-organization, reversed the toroidal magnetic field in the plasma edge (Fig. 2.2 a). As result, the safety factor profile drops with the radius and so the magnetic shear ($s = r/qdq/dr$) becomes negative over the entire plasma column which has a stabilizing effect on pressure-driven instabilities.

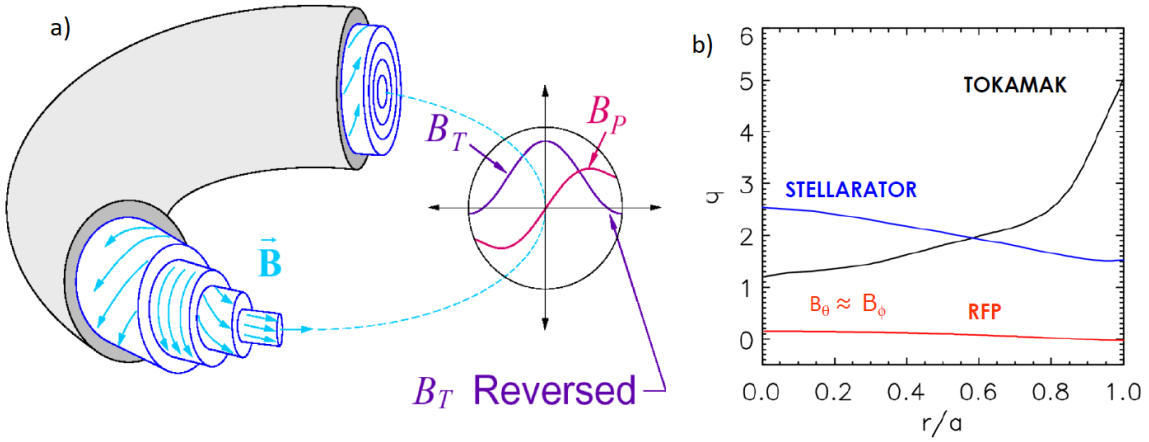

Figure 2.2: a) schematic figure showing the nested magnetic surfaces in a reversed field pinch (RFP) and the poloidal (B_P) and toroidal (B_T) magnetic field profiles, the latter reversed in the plasma edge [149]; b) shows a comparison between the typical safety factor profiles found in tokamkas, stellarators, and RFPs [171].

In addition, the conducting shell is an important piece of a RFP since it is related to the dynamo effect. Besides, the thickness of the shell together if the conducting material determines the magnetic field penetration time. This quantity is important for the stability since resistive wall modes (RWMs) tends to growth at this characteristic time. However, this represents a natural constraint since 'thick' shells are

challenging from the engineering point of view. A great breakthrough was the developed of 'smart' shells [299], which is realized by MHD active control thanks to a set of saddle coils installed on the wall. This configuration permits to operate with thinner shells since the effective control reduces the magnetic field penetration.

The presence of tearing modes (TE) has an ambiguous effect on RFP. While its existence is important for inducing the dynamo effect [33], the unimpeded growth of magnetic islands can lead to field line stochastization and thus to the fast degradation of the plasma confinement. Therefore, it is necessary to control them properly in RFP. Typical RFP operation with relatively low currents tends to induce multiple helicities (MH), with enhanced tearing modes over the whole plasma column due to the infinite number of resonant surfaces. For large plasma current, however, the $m = 1$ island dominates over the others (satellites). A substantial improvement of the plasma confinement is achieved in this case, called quasi single helicity (QSH) [170]. In this situation, the inner part of the plasma loses the axisymmetry, becoming similar to a stellarator, while the outer part remains axisymmetric. This regime was predicted theoretically [70] and achieved for the first time in RFX-mod [161].

2.2.5 Scrape-off layer (SOL)

The scrape-off layer (SOL) is the region where the magnetic field lines are open, i.e., they intercept a material surface. In this region, one has, naturally, a channel of particles and energy dissipation since the solid surface behaves as a sink. The interface that separates these two regions is called the last closed flux surface (LCFS). In the process of exhaustion of ionized particles along field lines, they might eventually recombine on the material surface, releasing neutral particles back to the confinement region: a phenomenon known as *recycling*. The transition for 'closed' to 'open' field lines is realized through two designs: limiter and divertor (see Fig. 2.3). Limiter is the historically way employed to restrict the plasma volume and promotes the exhaustion

of particles and energy. It relies on the presence of a material surface touching the plasma and thus defines the LCFS. The rapid loss of particles and energy towards the limiter competes against the cross-field transport that, in first an approximation, defines the SOL width. However, the proximity of limiter with the plasma bulk can enhance the impurity contamination and ultimately the plasma performance. A competing and more promising design, the divertor configuration reduces significantly the impurity influx since the material surface is placed relatively far from the plasma bulk. This is done by a field line configuration tailored to 'carry' the plasma that crosses the LCFS up to divertor plates where the exhaust occurs.

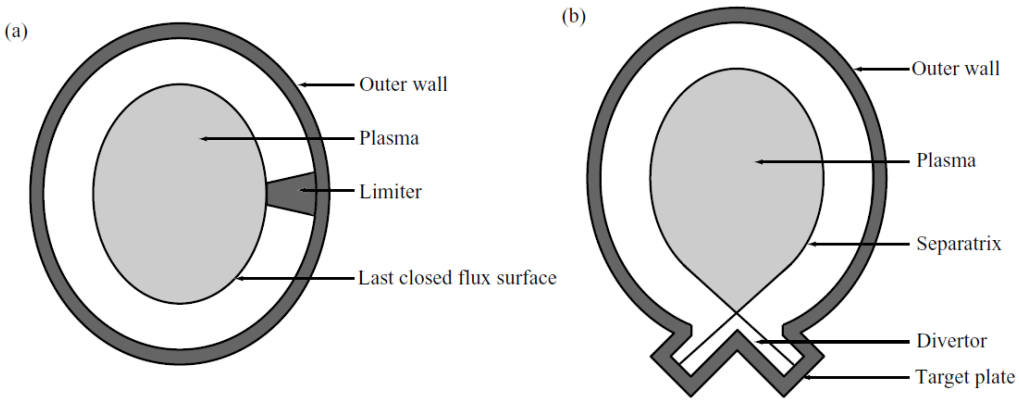

Figure 2.3: a) Limiter and b) divertor configuration [82].

Stellarators typically operate with a limiter. However, a new divertor design based on the presence of external generated magnetic islands in the plasma periphery has been recently tested in W7-X [300]. Most of the present tokamaks operate with divertor in single-null configuration (as shown in Fig. 2.3). Besides, the ITER baseline scenario is foreseen to operate in this configuration. However, the power exhaustion, as will be discussed in chapter 6, is one of challenging for the feasibility of ITER and the future fusion reactors.

Supposing that the cross-field transport in the SOL is dominated by diffusion given by Ficks law [250]:

$$\Gamma_\perp = -D_\perp \nabla_\perp n \tag{2.12}$$

Where $D_\perp$ is the diffusion coefficient and n is the plasma density. On the other hand, assuming that the parallel dissipation occurs typically at sound speed $c_s \approx \sqrt{kT/m_i}$, where k is the Boltzmann constant, m_i is the ion mass, and T is the plasma temperature. It follows that the dissipation characteristic time is:

$$\tau_\parallel = L_\parallel / c_s \tag{2.13}$$

Where $L_\parallel$ is the parallel connection length, i.e. the distance along the field line that connects a material surface to a point in the SOL. For limiter plasmas with circular shape, the connection length can be defined as $L = 2\pi r/\sin(\alpha)$, where $\alpha = \tan^{-1}(B_\theta/B_\phi)$ is the pinch angle. In a tokamak where typically $B_\phi \gg B_\theta$, so $\sin(\alpha) \cong \tan(\alpha)$. It follows that:

$$L_\parallel = 2\pi r \frac{B_\phi}{B_\theta} = 2\pi R q \tag{2.14}$$

where q is the safety factor and R is the major radius.

Defining $\Gamma_\perp \equiv n v_\perp = -D_\perp \nabla_\perp n \approx -D_\perp n/\lambda_n$ [250], where λ_n is the SOL density width. The SOL cross-field characteristic time is $\tau_\perp = \lambda_n / v_\perp$. By balancing in the SOL the cross and the parallel field transport and considering $\tau_\parallel = \tau_\perp$, the SOL density width becomes:

$$\lambda_n = \sqrt{D_\perp L_\parallel / c_s} \tag{2.15}$$

The previous formula permits to gain some intuition about the mechanism that set the SOL. The diffusion coefficient $D_\perp$ is typically turbulent and depends on the nature

of the instability [186]. A large $D_\perp$ coefficient can enhance λ_n or make it small when $D_\perp$ becomes reduced (e.g. H-mode), while long parallel connection length tends to enlarge λ_n since the dissipation happens in a longer time. In the real situation, however, pure diffusive transport does not explain the cross-field transport observed experimentally in the SOL. The reason is that cross-field transport in the SOL is dominated by convective transport [146]. The responsible for that are filaments or blobs (see chapter 3) that typically dominate the transport in the far SOL, while diffusion is thought to play a role in the near SOL [181]. A similar argument can be employed for energy transport to obtain λ_T, i.e., the SOL temperature width.

The energy exhaustion on a divertor in attached condition is dominated by parallel transport ($q_\parallel$). The power crossing the LCFS (P_{SOL}) is exhausted with parallel energy transport that typical exhibits an exponential decay $q(r) = q_\parallel e^{-r/\lambda_q}$, where $r = R - R_{sep}$, with R_{sep} is the separatrix position at the outboard midplane. The power fall-off length (λ_q) as mapped from the outboard midplane to the divertor gives the heat flux width [67]. In the sheath-limited regime $\nabla_\parallel T \approx 0$, convective parallel transport dominates over the conductive one ($q_\parallel^{conv} > q_\parallel^{cond}$), and so one can demonstrate [249] $\lambda_q = [\lambda_n^{-1} + \frac{3}{2}\lambda_T^{-1}]^{-1}$; while in the conductive-limited ($\nabla_\parallel T \neq 0$), $q_\parallel^{conv} < q_\parallel^{cond}$ and $\lambda_q = \frac{2}{7}\lambda_T$. The parameter that defines the different regimes is the SOL electron collisionality: $\nu^* = L_\parallel/\lambda_e$, where λ_e is the electron mean path. The sheath limited is characterized by $\nu^* < 10$, while in the conductive regime $10 < \nu^* < 85$. By increasing further the collisionality, the SOL might become detached, i.e. the pressure along the field lines drops substantially [249].

2.2.6 High confinement mode (H-mode)

The high confinement mode (H-mode) is presently the most reliable regime of operation for future fusion reactors, being the adopted scenario for ITER baseline [159]. First observed in ASDEX in 1982 [280], the regime is characterized by a substantial

improvement of the overall plasma confinement and the rise of a density and temperature pedestal, with stepper pressure gradients compared to L-mode (Fig. 2.4). When the transition happens, the central line averaged density typically increases, while the divertor (or limiter) $D_\alpha(H_\alpha)$ emission line decreases, suggesting a reduction of the outward particle flux. The confinement time in H-mode is typically twice higher than in L-mode, which has allowed reducing the machine size (and consequently its cost) to achieve the same plasma condition (density, temperature, and confinement time) as in L-mode. This finding made possible the ITER project. The transition happens when the external power heating exceeds a threshold that, in turns, might depend on several parameters such as the plasma shape, whether it is divertor or limiter, wall conditioning (e.g. boronization), the $\nabla B \times B$ drift direction, and so on [279]. In addition, isotopic effects play a key role, where lower power threshold P_{th} is obtained for deuterium as working gas compared to hydrogen [19]. H-mode has also been observed in stellrators [69, 71] and mirror machines [218] with similar features observed in tokamaks: steeper density and temperature profiles, reduced plasma recycling, rise of an edge transport barrier (ETB), and improved confinement time of particles and energy. Fig. 2.4 shows a schematic drawing with a tokamak toroidal cross-section in single-null configuration (on the left) and the outer midplane pressure profile in L and H-mode. Note that in H-mode a pedestal arises together with an edge transport barrier (ETB).

It well accepted that the massive turbulence reduction that leads to the L-H transition results from an enhanced $E_r \times B$ shear flow. The possible mechanism behind this process will be explained in chapter 3 and the direct consequence is a reduced turbulent transport. In addition, a minimum radial electric field (absolute value) has been observed experimentally regardless of the pedestal density [221] during the transition. All of these pieces of evidence point out for the key role of edge radial electric fields to induce the L-H transition.

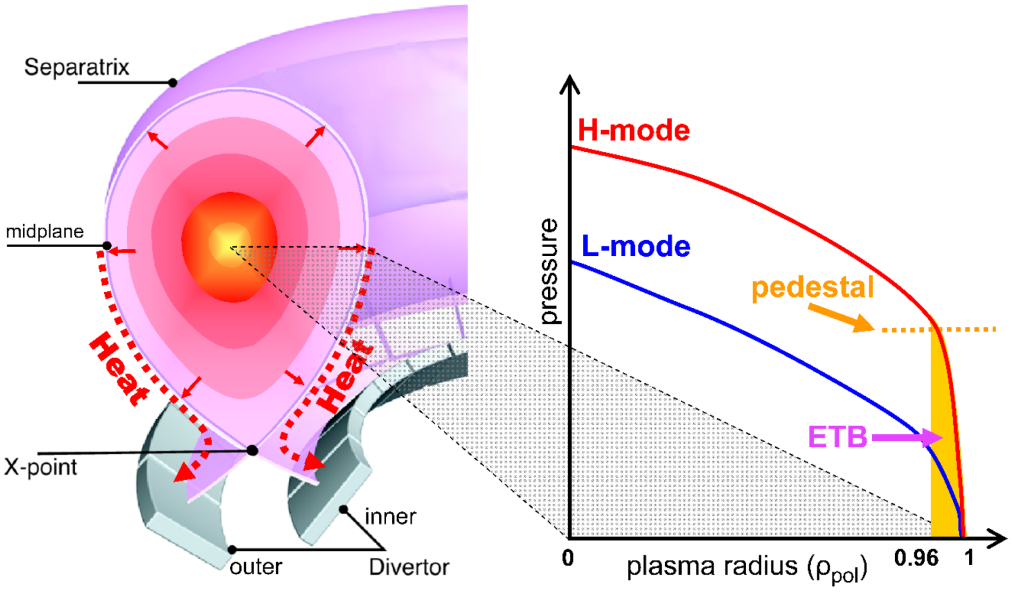

Figure 2.4: Comparison between the radial pressure profile at outboard midplane during L and H-mode for a divertor tokamak. Figure borrowed from Ref. [51]

In steady-state condition, the radial electric field can be obtained in first order from the radial force balance equation:

$$E_r = \frac{1}{n_i Z_i e}\nabla_r P_i - v_{\theta i} B_\phi + v_{\phi i} B_\theta \tag{2.16}$$

where P_i is the ion pressure, n_i is the ion density, with ion charge $Z_i e$, and v_θ and v_ϕ are, respectively, the poloidal and toroidal rotation. The first term RHS is the diamagnetic term, while the two last terms are obtained from $v \times B$ projected over the radial direction. The previous equation neglects the term $(m/Z)v.\nabla v$ and so it rules out fluctuating contribution, e.g. from the Reynolds stress. However, although this approximation seems to be fine for the core, in the plasma edge it might not so ease satisfied [29]. The role of this term and the presence of zonal flows will be discussed in chapter 3. The diamagnetic term develops from the power balance, where

heating and particle sources compete with sinks, yielding the final $\nabla_r P_i$ profile. The typical time scale of this parameter is slow, in opposition to the fast L-H transition observed in some experiments ($\leq 100\ \mu s$) [101]. For that reason this term, although important for sustaining H-mode [223], where in the shear layer $E_r \approx \frac{1}{n_i Z_i e}\nabla_r P_i$, it does not seem to be the trigger for the transition [29]. Toroidal rotation can be modified by external toroidal torque following NBI co or counter-beam injection then affecting the local radial electric field through the term $v_{\phi i} B_\theta$. Alternatively, ion orbit loss (e.g. banana orbits with a width beyond the confinement region) can produce a net radial current. However, the ambipolarity condition for the radial particle flux imposes a counter (neoclassical) current to assure $\langle j_r \rangle = 0$. This requirement will untimely impact on the radial electric field. This mechanism was proposed as a candidate for the L-H transition. The fast transition is compatible with a fast radial electric field variation as a result of an enhanced ion loss current [131].

2.2.7 Electrode biasing technique

The 'spontaneous' H-mode described in the previous section happens after the rise of a transport barrier, with an increased sheared flow, that leads to turbulence suppression and the stabilization of its driven instability [28]. The enhancement of the radial electric field occurs in this case because the edge pressure gradient becomes further steeper after the plasma being externally heated (e.g., NBI or ECRH), where from the radial force balance $E_r \approx \frac{1}{n_i Z_i e}\nabla_r P_i$. Intuitively, since the plasma wants to keep neutral, any charge building-up is promptly neutralized. In particular, as a response for the ion orbit loss, the edge electric field becomes further negative. More generally, any radial current in the plasma drives local polarization that is compensated by a local radial electric field that, in turns, generates poloidal rotation and return current [52]. In steady-state, no net current can flow ($\langle j_r \rangle = 0$) in the system assuring the ambipolarity of the radial particle flux. However, by inducing a transient current

one can modify the radial electric field. This can be achieved for relatively cold plasmas by inserting a bias electrode in the plasma edge. This technique has been shown to induce H-mode or biasing H-mode (to distinguish from the 'spontaneous' H-mode) in tokamaks [258, 288, 189, 243] and stellarators [116, 233].

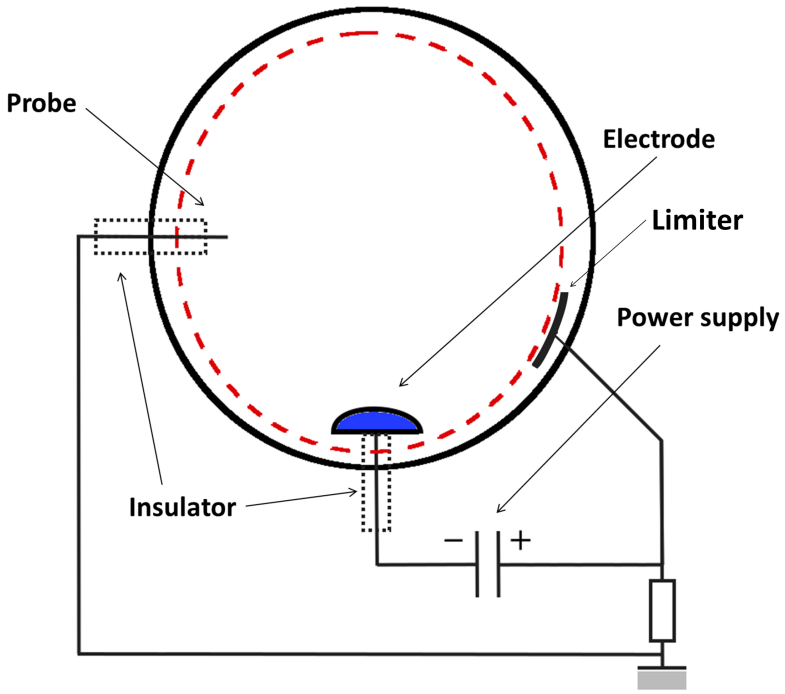

Figure 2.5: Electrode biasing technique typical configuration.

Fig. 2.5 shows a typical configuration find in several biasing experiments [258, 273, 101]. A similar configuration can also be found in TJ-II [116, 233, 103] and RFX-mod operating as tokamak [243], although with different plasma shape and without limiter in some cases. Biasing is induced with respect to the wall or limiter, both in ground connection, with positive or negative voltage. The sign of the biasing and its strength are control parameters together with the position of the electrode with respect to the LCFS. The latter restricts the operational range for this kind of experiment and, naturally, the type of machine. Although the electrode in Fig. 2.5 is out of scale, its presence at the plasma edge can sometimes act as a limiter, whose effect is more pronounced the bigger the electrode is. Since the biasing effect becomes more

effective when the electrode is placed in the plasma edge, through the spontaneous $E \times B$ shear layer, in big/hot machines this technique is not applicable since it can lead the damage of the electrode (the high heating power could destroy it), and the plasma contamination. The typical bias current path is: power supply, electrode, plasma, limiter (and/or wall), and power supply again. Empirical observations of biasing H-mode shows an abrupt change of the biasing current once the electrode polarization increases (or decreases for negative biasing) beyond a certain limit [26]. This phenomenon is also known as the radial electric field bifurcation, a signature of the L-H transition [52].

Chapter 3

Plasma turbulence

From early on, it has become clear for the plasma community that the collision transport in toroidal geometry, i.e., the neoclassical transport, could not account for the actual transport observed experimentally. Such *anomalous* transport must have originated from a different mechanism. Indeed, turbulence was pointed out as the leading transport mechanism in magnetized plasmas [134]. Turbulent process is responsible for a massive outward flux of particles and energy in tokamaks and stellarators. The typical gyro-Bohm scale yields a dependence of the form $\chi \sim T^{3/2}$ on the thermal diffusive coefficient [62], leading to stiff temperature profiles. This dependency is related to the presence of instabilities at the Larmor radius scale, called microinstabilities. They typically have an electrostatic nature, but in some regimes (e.g., H-mode) electromagnetic effects might become important. The non-linear interaction of different modes turns the system turbulent. The spectrum of the plasma density and potential manifest as *broadband* turbulence. This spectrum can also exhibit: *monochromatic* oscillations, with narrow frequency width Δf compared to the background frequency, and *quasicoherent* oscillations, with a broader frequency width compared to monochromatic oscillations but narrower than the broadband turbulence spectrum.

It is relevant in the study of turbulence to separate the fluctuating part (time-varying), of a given quantity (e.g. density, temperature or potential), from its mean or background value:

$$a(\mathbf{r},t) = a_0(\mathbf{r}) + \tilde{a}(\mathbf{r},t) \tag{3.1}$$

where $\tilde{(...)}$ represents the fluctuation. On the other hand, the fluctuating part can be decomposed in complex Fourier series:

$$\tilde{a}(r,t) = \sum_{k,\omega} \tilde{A}_{k,\omega} e^{i[\mathbf{kr}-\omega t]} \tag{3.2}$$

Where ω and k are the frequency and wavenumber, respectively. As an example, the plasma turbulent particle transport averaged over a flux surface is typically written as function of the density and radial velocity fluctuation:

$$\tilde{\Gamma}_r = \langle \tilde{n}\tilde{v}_r \rangle \tag{3.3}$$

with $\tilde{n} = |\tilde{n}|e^{i\alpha_n}$ and $\tilde{v}_r = |\tilde{v}_r|e^{i\alpha_v}$, where α_n and α_v are the density and velocity phases. It follows that the radial turbulent particles flux becomes:

$$\tilde{\Gamma}_r = 2|\tilde{n}||\tilde{v}_r|\sin\,\alpha_{nv} \tag{3.4}$$

where $\alpha_{nv} = \alpha_n - \alpha_\phi$ is the cross-phase between the density and the velocity field fluctuation. The previous equation shows that a high turbulent transport depends not only on the level of fluctuation but also on a favour phase relation between density (but also pressure or temperature) and the fluctuating velocity.

3.1 Drift wave

Drift waves is the most important mechanism whereby turbulent transport occurs in a magnetized plasma. Their existence has been reported in several devices [113, 122]. They are defined as a three-dimension electrostatic structure characterized by finite parallel wavelength, but larger than the perpendicular wavelength $k_{\parallel} \ll k_{\perp}$ (flute-like).

Although the drift wave theory can be very complex and general (see the review [122]), it worthwhile to describe some of its basic concepts. Considering a density wave perturbation along the poloidal direction $\tilde{n} = n_0 \exp\left[i(-\omega t + k_\theta \theta)\right]$ (as shown in Fig. 3.1) in a shearless plasma in slab geometry. As a response for this perturbation, electrons move along the field lines to neutralize the change build-up. In the adiabatic limit ($m_e \to 0$), the force balance equation along the field lines is:

$$n_e e E_{\parallel} + \nabla_{\parallel} p_e = 0 \tag{3.5}$$

Considering that $E_{\parallel} = -\nabla_{\parallel}\phi$ and isothermal pressure $\nabla_{\parallel} p_e = T_e \nabla_{\parallel} n_e$, one can demonstrate [122] that in first order:

$$\frac{\tilde{n}_e}{n_0} \approx \frac{e\tilde{\phi}}{T_e} \tag{3.6}$$

where $e\tilde{\phi}/T_e \ll 1$. Note from Fig. 3.1 that the charge accumulation along the y direction results in an electric field (E_θ) to neutralize it. An $E \times B$ drift arises as a response to that, acting to reduce the density in denser regions and enhance in less dense spots. This situation can be simply described by considering the density continuity equation neglecting sources and sinks and for incompressible flows ($\nabla . v = 0$):

$$\left[\frac{\partial}{\partial t} + \mathbf{v}^{\mathbf{E}\times\mathbf{B}}.\nabla\right] n_e = 0 \tag{3.7}$$

where $\mathbf{v}^{E\times B} = -\nabla\phi \times \mathbf{B}/B^2 \approx -B^{-1}k_\theta\tilde{\phi}$. Using Eq. 3.7, the drift wave frequency in first order is:

$$\omega = \frac{T_e \nabla n_0}{eBn_0} k_\theta = v^{de} k_\theta \tag{3.8}$$

where one can recognize the electron diamagnetic drift. The perturbation along the θ-direction travels with the electron diamagnetic velocity. However, at small wavelength perturbation, compressibility becomes relevant. In this case, the $\nabla.v$ term can be approximated using the polarization drift. Density continuity equation then becomes:

$$\left[\frac{\partial}{\partial t} + \mathbf{v}^{\mathbf{E}\times\mathbf{B}}.\nabla\right] n_e + \nabla.\left(\frac{m_i}{eB^2}\frac{\partial E_\perp}{\partial t}\right) = 0 \tag{3.9}$$

where $\nabla.\left(\frac{m_i}{eB^2}\frac{\partial E_\perp}{\partial t}\right) = \frac{m_i T_e}{e^2 B^2}\frac{\partial}{\partial t}\left(\nabla_\perp^2 \frac{e\phi}{T_e}\right)$, and so the wave dispersion relation becomes:

$$\omega - v^{de}k_\theta + \omega(\rho_i k_\theta)^2 = 0. \tag{3.10}$$

where $\rho_i \approx \sqrt{m_i T_e}/B$. The previous equation although more complex than Eq. 3.8, it is still stable, i.e. the solution is real. However, if the response of the electrons is not adiabatic due, for example, high collisionality or trapping effects along the parallel direction, the equation Eq. 3.6 becomes:

$$\frac{\tilde{n}_e}{n_0} = \left[\left(\frac{e\tilde{\phi}}{T_e}\right) - i\delta^*\right] \tag{3.11}$$

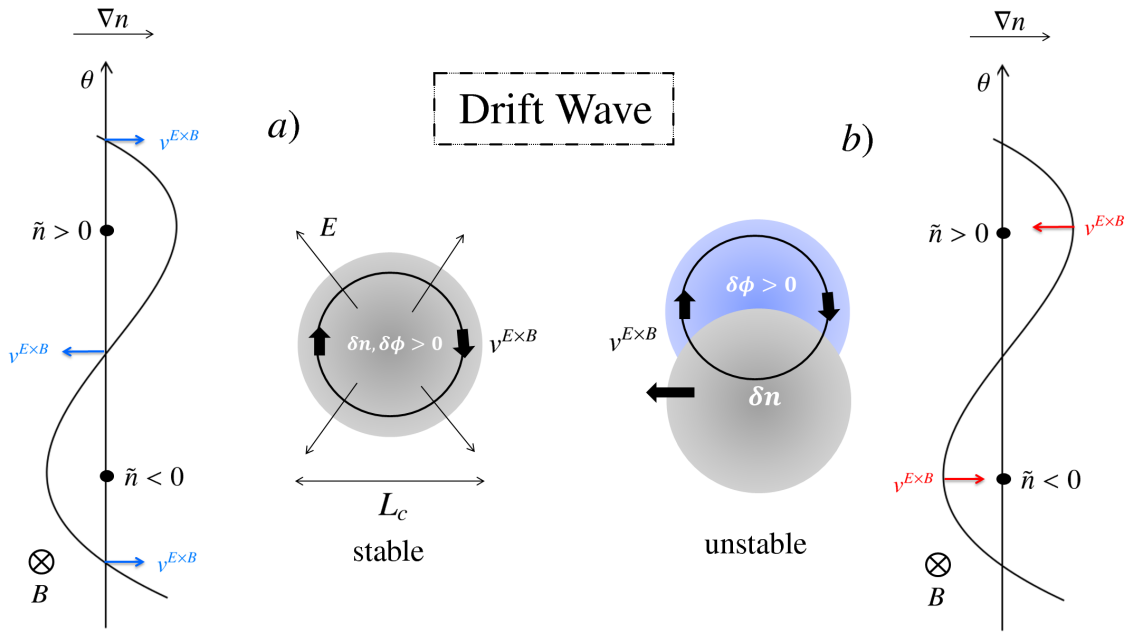

Figure 3.1: Drift wave: a) stable, the potential and density fluctuation are in phase, b) unstable, the potential and density fluctuation are out of phase and, therefore, a net radial flux arises.

where δ^* is a phase delay. In this situation, one can demonstrate [122] that the drift wave becomes unstable with a positive linear growth rate. Fig. 3.1 illustrates the two cases. While in the stable situation the potential and density perturbations are in phase and so the wave oscillates along the poloidal direction without resulting in a net radial flux. In the unstable case, the potential and density perturbation are out of phase and so the resulting $E \times B$ is in the radial direction producing a net transport $\Gamma_r = \left\langle v^{E\times B}\tilde{n}\right\rangle$.

The non-linear version of the drift wave equation is described by the Hasegawa-Mima equation [122]. From this model, turbulence saturation can occour by the energy forward cascade (see sectio 3.3) where inverse cascade with energy transfer from small to big scales has been observed in simulations [111]. Besides, if the magnetic field fluctuation is not negligible, electromagnetic effects might become important. The electromagnetic generalization includes Alfvén waves [122].

3.2 Interchange instability

It was discussed in the previous section that drift waves emerge in a plasma with an arbitrary magnetic field induced by the pressure gradient. The wave propagates perpendicularly to the equilibrium magnetic field typically in the electron diamagnetic direction. Besides, the high mobility of electrons along the magnetic field yields a long but finite parallel wavelength. While drift waves can arise in a region of constant magnetic fields, if the magnetic curvature is not negligible, e.g. in tokamak or stellarator, interchange instability might be important. The key ingredient behind this instability is that the ∇B and the curvature drifts separate electrons from ions, creating a charge accumulation and thus an electric field. However, while in the so-called good curvature (see Fig. 3.2) the resulting $E \times B$ drift acts to reduce the initial perturbation (temperature, density or pressure), in the bad curvature the drift enhances it. The good curvature in a tokamak is the high field side where $\nabla T(\nabla n).\nabla B < 0$, while the bad curvature is the low field side where $\nabla T(\nabla n).\nabla B > 0$. Therefore, interchange instability is expected to be larger in outboard midplane in tokamaks (ballooning type). This kind of instability is believed to be responsible for the generation of *streamers*, turbulent radial elongated structures, that ultimately create blobs once they cross the edge $E \times B$ shear layer [195]. A notable example of interchange instability the *ion temperature gradient* (ITG) mode arises for adiabatic electron response ($\tilde{n}/n_e \approx e\tilde{\phi}/T_e$). The $\nabla B \times B$ drifts depends on the particles thermal energy and so it is proportional to $-T/qBR$, where q is the particle charge and R is the major radius. Therefore, in hotter plasma regions the drift is faster than in the colder ones, causing a charge unbalanced and so an electric field. It follows that the situation is the same as described before, in the bad curvature region the hot and cold plasma tend to mix, releasing the energy content of the temperature gradient in fluctuation, while in the good curvature the perturbation is promptly restored by a favour $E \times B$ drift.

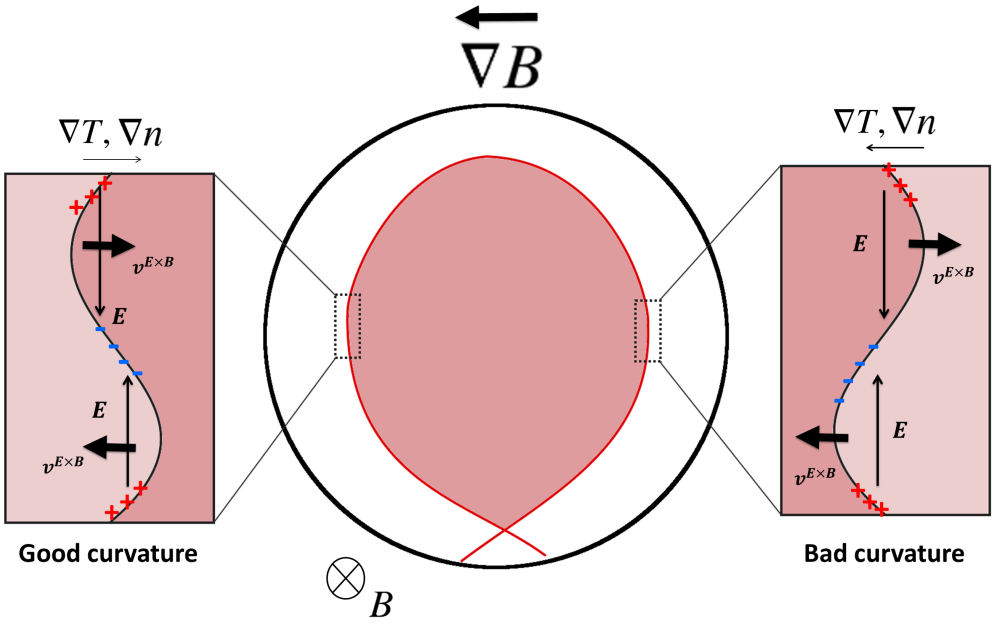

Figure 3.2: Interchange instability: while in the bad curvature an unfavoured $E \times B$ drift yields an unstable situation, in the good curvature region the $E \times B$ drift tends to counteract the perturbation leading to a stable state.

3.3 Kolmogorov turbulence description

To explain the Kolmogorov concept of self-similarity and forward cascade and their implications for fusion plasmas, it is useful starting from the well-known Navier-Stokes equation for incompressible flow ($\nabla.\mathbf{u} = 0$) [211]:

$$\left[\frac{\partial \mathbf{u}}{\partial t} + (\mathbf{u}.\nabla)\mathbf{u}\right] = -\frac{1}{\rho}\nabla P + \mu\nabla^2\mathbf{u} \tag{3.12}$$

where P is the pressure, ρ is the fluid density, and μ is the viscosity. This equation essentially describes the velocity of a fluid subjected to a pressure force and viscous damping. The *Reynolds number* is a dimensionless parameter define as: $Re = (\mathbf{u}.\nabla)\mathbf{u}/\mu\nabla^2\mathbf{u}$ and useful to decide whether the fluid is in a turbulent regime. The term $(\mathbf{u}.\nabla)\mathbf{u}$ is non-linear and yields a coupling between scales [211]. Fig. 3.3 shows a fluid with velocity U_0 in a region with obstacles of size L. By increasing

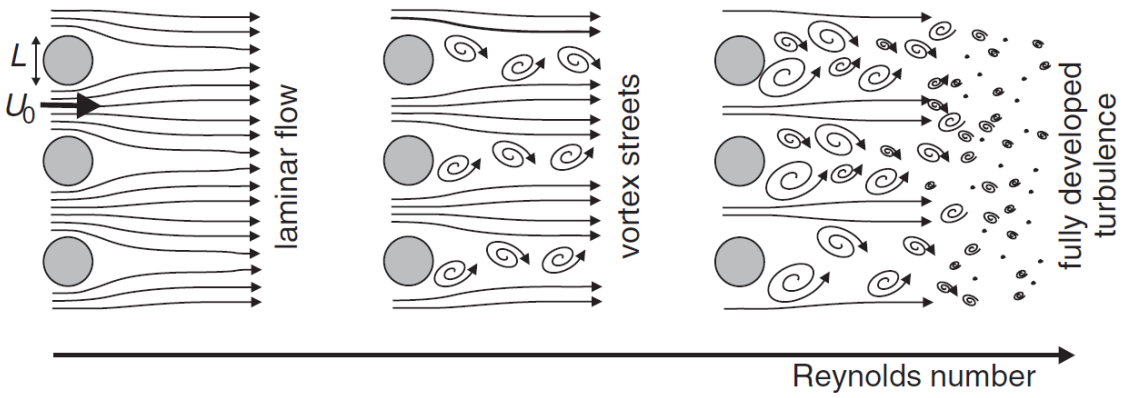

Figure 3.3: Comparison between a) mean flow and b) zonal flows radial profiles [62].

the Reynolds number $Re \approx U_0 L/\mu$, the fluid regime changes from laminar flow to the fully developed turbulent regime. Note that in this case vortexes with different sizes are presented. The smaller eddies eventually are damped (energy is converted in heat) in the dissipation range, setting thus a limit scale. The range from large scales (e.g. the obstacle size in the example of Fig. 3.3) to the limit scale or Kolmogorov microscale is called inertial. In this range, the energy spectrum is $E_k \sim k^{-5/3}$, $k \sim 1/l$ where l is the spatial scale, defining the energy forward cascade [211]. The energy flux between scales neglecting viscous dissipation is $\epsilon \sim u^3/l$, where u is the eddy flow velocity. The minimum scale is obtained by balancing the straining rate ($\epsilon^{1/3}/l^{2/3}$) with the viscous dissipation (ν/l^2):

$$l_d \sim \nu^{3/4}/\epsilon^{1/4} \tag{3.13}$$

The hypotheses behind the Kolmogorov theory are spatial homogeneity, isotropy, local interaction, and self-similarity [60]. The self-similar energy transfer happens at the eddy decay or turnover time $\sim l/u$. The Reynolds number equivalent in magnetized plasmas is called Lundquist number defined from the ratio of Alfvén to resistive timescales [62].

Fusion plasmas are thought to be at some extent self-similar [40], i.e. it exhibits power-law scaling. However, the rise of intermittency in a turbulent system is related to a deviation from self-similarity behaviour. While intermittency in the dissipation range is a common phenomenon and does not represent a violation of the Kolmogorov hypothesis (or K41) [83, 11], in the inertial range it might be. However, strong nonlinear coupling and dissipation in the plasma possibly reduce the extension of the inertial range [39]. Besides, in certain conditions (notable when the plasma system exhibits some degree of symmetry), inverse cascade processes can occur in the inertial range (see section 3.4). The emergence of coherent mesoscale structures with non-Gaussian probability distribution function (PDF) is a clear evidence of intermittency in fusion devices [63].

3.4 Turbulence saturation mechanisms

3.4.1 $E \times B$ shear flow and eddy decorrelation paradigm

The massive suppression of turbulence in the plasma edge followed by the rise of a transport barrier are the key factors that lead to the L-H transition in tokamaks and stellarators. The suppression or stabilization of turbulence is widely understood to be impacted by $E \times B$ shear flows [21, 230, 28, 259], resulting in a lower radial correlation length and decreased turbulent transport. The Biglari-Diamond-Terry (BDT) criterion states that turbulence is suppressed if the $E \times B$ shearing rate is fast enough to decorrelate eddies before they decay [21, 259]. Considering eddies with a radial extension L_r and characteristic poloidal wavenumber k_θ (Fig. 3.4), the anomalous diffusion coefficient resulted from the interaction between them is:

$$D \approx \omega_t L_r^2 \tag{3.14}$$

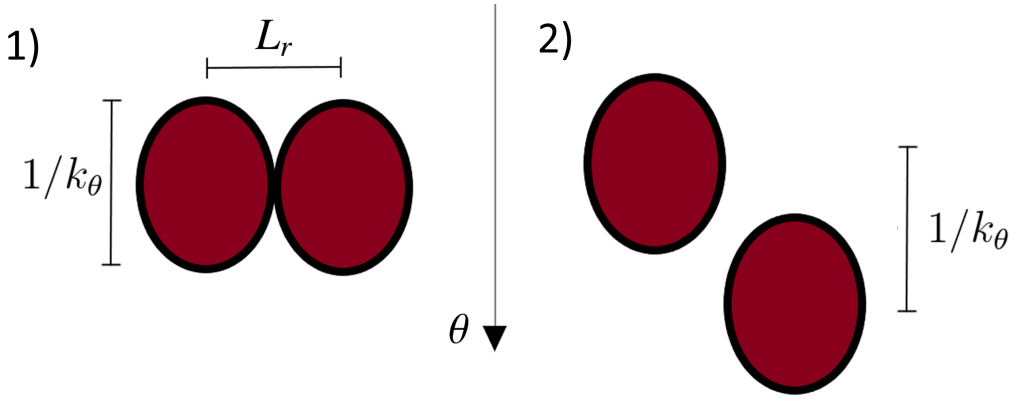

Figure 3.4: Cartoon showing 1) connected eddies without shear flows and 2) with a poloidal shear flow that leads to their displacement (or decorrelation).

where ω_t is the eddy life-time (or eddy turnover time). If these eddies exist in a region of poloidal shear $dv_\theta/dr \approx B^{-1}dE_r/dr$, the time that takes to separate them poloidally $1/k_\theta$ (i.e. decorrelate them) is $\delta t = \delta\theta/\delta v_\theta \approx (1/k_\theta)/(L_r dv_\theta/dr)$. Fig. 3.4 shows a cartoon illustrating the criterion.

It follows that according to the BDT criterion the suppression happens if this time is shorter than the eddy turnover time:

$$\left|\frac{\nabla E_r}{B}\right| > \frac{\Delta\omega_t}{k_\theta L_r} \tag{3.15}$$

Experimental evidence of the validity of this criterion came out in the same year the BDT paper was published [216]. Fig. 3.5 shows an original graph from the Ref. [216] where it is compared the turbulence correlation time τ_c^{lab} in the laboratory frame and the diffusive correlation time τ_D (that is expected to be $\tau_D \approx \tau_c$ in the plasma frame) with the shearing time τ_{sh} and the time at constant radial electric field (or poloidal rotation) τ_E that is also believed to decorrelate turbulence through non-rigid-body rotation. They have observed that the shearing time becomes comparable to the turbulence correlation time and the diffusive correlation time close to the shear layer, where, indeed, turbulence suppression is observed. As they pointed out, the

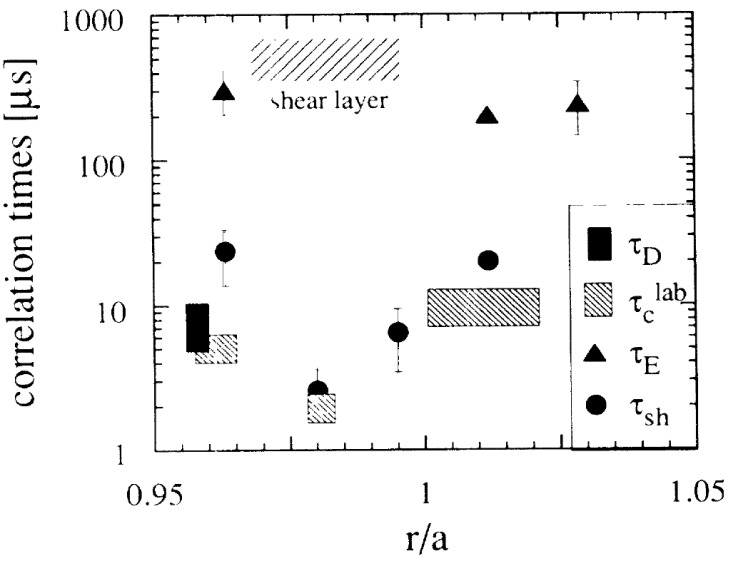

Figure 3.5: Comparison between the turbulence correlation time τ_c^{lab}, diffusive correlation time τ_D, shearing time τ_{sh}, and the time at constant radial electric field τ_E in TEXTOR tokamak during H-mode [216].

correlation time was measured in the laboratory frame, where eddies are seen rotating with the background flow. This means that if this velocity is high enough, the frozen turbulence hypothesis can be applied [155] and, therefore, $\tau_c^{lab} \approx (1/k_\theta)/v_\theta$. However, in the shear layer this hypothesis does not hold anymore [155], while in the particular case $v_\theta \approx 0$ [216], and so $\tau_c^{lab} \approx \tau_c$, whilst far from the shear layer $\tau_c^{lab} \leq \tau_c$. In short, this analysis shows that the turbulence correlation time as measured in the laboratory frame is a lower limit of τ_c measured in the plasma frame, therefore if τ_c^{lab} is larger than the shearing time the criterion is automatically satisfied. The opposite is not necessarily false.

In addition, the tilt of eddies can also yield a reduced turbulent transport either by changing the phase relationship between the fluctuating velocity and the density (or pressure) perturbation or by directly reducing their amplitude [28]. Magnetic shear can also induce eddy tilt and so contribute to this effect. In toroidal geometry, the shearing rate can be written as [107]:

$$\gamma_{E\times B} = \left| \frac{(RB_\theta)^2}{B} \frac{\partial}{\partial \psi} \frac{E_r}{RB_\theta} \right|. \tag{3.16}$$

In nonlinear turbulence simulation, the maximum linear growth rate of unstable modes (γ_{MAX}) has been shown to become stabilized by the $E \times B$ shearing rate when $\gamma_{E\times B} > \gamma_{MAX}$ [283].

3.4.2 Zonal flows (ZFs)

Turbulence arises and grow naturally in magnetized plasmas. In section 3.1, it was discussed that microinstabilities (drift wave type) benefit from the free energy in the plasma represented by gradients: pressure, density, and temperature, or currents to increase and then releasing energy in terms of fluctuating fields, e.g. δB and δE. However, the nonlinear coupling of the different unstable modes inhibits the further growth of turbulence leading to its saturation. One of the most important mechanisms for turbulence saturation comes from the turbulence self-regulation and its ability to generate flows. As observed by *P.H. Diamond and Y.-B. Kim* [60], turbulence can generate poloidal flow by means of the Reynolds stress. Zonal flow is defined as long and nearly constant toroidal and poloidal wavelength perturbation (m = n = 0) with typical radial length $\lambda_r = \sqrt{a\rho_i}$ [85]. Fig. 3.6 compares the radial profile of the mean poloidal flow (in the slab geometry approximation: x - radial and y - poloidal) with the zonal flow profile. Note that the radial characteristic scale is quite different, while the mean flow is a macroscale phenomena, i.e. the characteristic size is comparable to the machine size or the characteristic gradient length $\sim n/\nabla n$, zonal flow is a mesocale phenomenon: $\rho_i < l < a$, where ρ_i is ion Larmor radius and a is a machine characteristic size (e.g. minor radius), and exhibits a fast variation along the radial direction. The time evolution of poloidal zonal flows can be obtained by the momentum balance equation [85]:

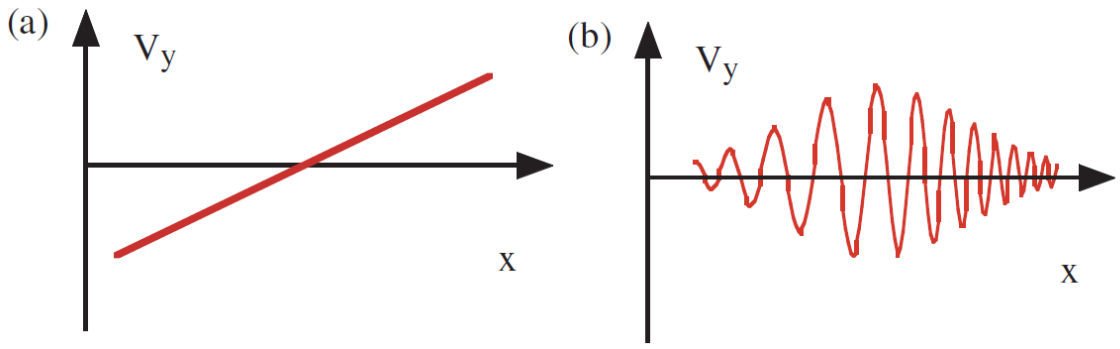

Figure 3.6: Comparison between a) mean flow and b) zonal flows radial profiles. Figure adapted from [59].

$$\frac{\partial}{\partial t}\left\langle V_{\theta,ZF}\right\rangle = -\frac{\partial}{\partial r}\left\langle \tilde{v}_\theta \tilde{v}_r \right\rangle + \frac{1}{\rho_m \mu_0}\frac{\partial}{\partial r}\left\langle \tilde{B}_r \tilde{B}_\theta \right\rangle - \gamma_{damp} V_{\theta,ZF} \tag{3.17}$$

Where $\langle ... \rangle$ is the flux surface or zonal average. The equation is composed of the Reynold stress ($\langle \tilde{v}_\theta \tilde{v}_r \rangle$), Maxwell stress ($\frac{1}{\rho_m \mu_0}\left\langle \tilde{B}_r \tilde{B}_\theta \right\rangle$), and a damping term represented by the damping rate (γ_{damp}). The competition of these terms determines whether zonal flows is high in a certain region, while it sets the ZF radial extension.

While stationary zonal flows exhibit a very slow time oscillation, the so-called Geodesic Acoustic Mode (GAM) is thought to be the ZF dynamical version with higher characteristic frequency [59]. The first evidence of zonal flows observed in simulations came up in 1987 where the Hasegawa-Mima equation applied for a plasma in a cylindrical geometry showed the emergence of long wavelength potential structures. These structures were identified as zonal flows generated by the potential self-organization [111]. The process happens by means of an inverse energy cascade.

Zonal flows can act on the turbulence through $E \times B$ shear or wave trapping (for drift waves) [85]. Its role in regulating the turbulence growth with implications for the L-H transition has been discussed in the last few years. The experimental evidences of a limit cycle oscillation (LCO), i.e. low-frequency oscillation of several quantities

before the L-H transition, has motivated a L-H transition model that puts zonal flows as the trigger. The *predator-pray* model [139] predicts that zonal flows will impact on the turbulence growth prior to the development of the massive mean flow that sustains H-mode. Since turbulence itself generates zonal flows, the relation between the two fields would be depicted as an oscillatory phase. Although some experimental evidences corroborate with this model, in some situations (e.g. fast transition) the effect seems to be absent [101].

3.5 Turbulent filaments

Filaments or blobs (due to their shape in the cross-field plane) are turbulent structures presented in the edge and SOL of tokamaks, stellarators, and Reversed field pinch, as well as in simple devices [146, 63]. They are mesoscale structure and contribute substantially to the cross-field transport in the edge and SOL. The basic blob or filament properties as observed by several experiments are: 1) monopole density (or pressure) in the cross-field plane with amplitude larger than the background; 2) magnetic field-aligned, yielding a long and stretched structure in the parallel direction with respect to the perpendicular one ($k_{\|} \ll k_{\perp}$); 3) cross-field motion propelled by $E \times B$ drift. Since they are more likely to be observed in the low than in the high field side, their drive instability is believed to be interchange-like.

The mechanism that drive filament motion was first proposed by *S. I. Krasheninnikov* [145]. According to this model, filaments are created as result of interchange instability around the LCFS due to ∇B drift. In the bad curvature region, this flow will detach hot plasma from the confinement region towards the SOL where the fast parallel transport along the field lines will act to dissipate it. In the far SOL, where the gradients are flatter, the intermittent behaviour of density fluctuation cannot be explained by pure anomalous Bohm diffusion, therefore, convective transport is

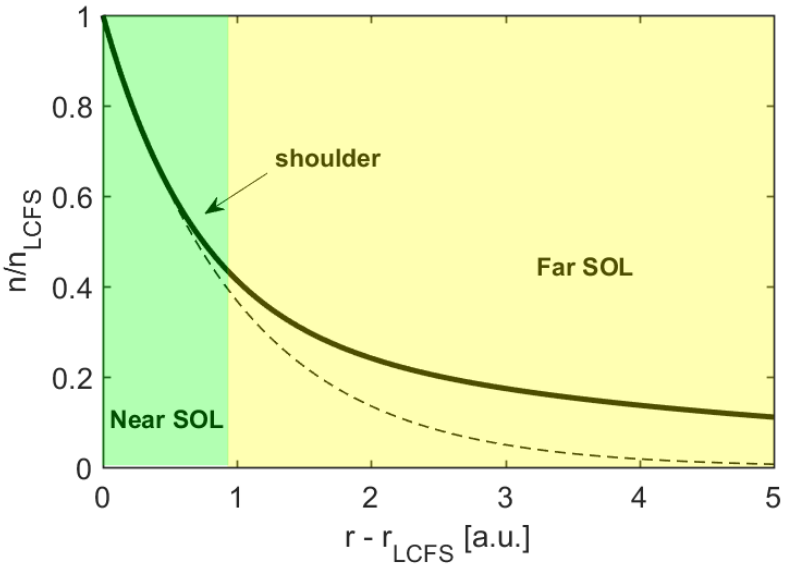

Figure 3.7: SOL density profile in tokamaks exhibiting a typical double exponential decay.

dominant in this region and blobs or filaments are believed to be responsible for that. Indeed, the SOL density profile is typically observed with two exponential decay [181]: faster in the near SOL and slower in the far SOL (see Fig. 3.7). This difference seems to be related to a dominant role of conductive transport in the near SOL (where gradients are still rather steep), while travelling blobs dominate the far SOL, flattening the profiles in this region. The boundary between these two region is called *shoulder* (see Fig. 3.7). This modern view of seeing the SOL profiles and the mechanism that set contrasts with the classic view where diffusive transport was thought to be the dominant mechanism in the SOL, leading to unrealistic diffusion coefficients to match the experimental results [267].

Blobs are thought to be created in the near edge where the pressure gradient is maximum [63], where microinstabilities are unstable. Measurements of density fluctuation in the edge and SOL show a significant variation of the sampling skewness and kurtosis over the radial profile. Skewness and kurtosis refer to the third and fourth moments, respectively, of a probability distribution function (PDF) (see chapter 4):

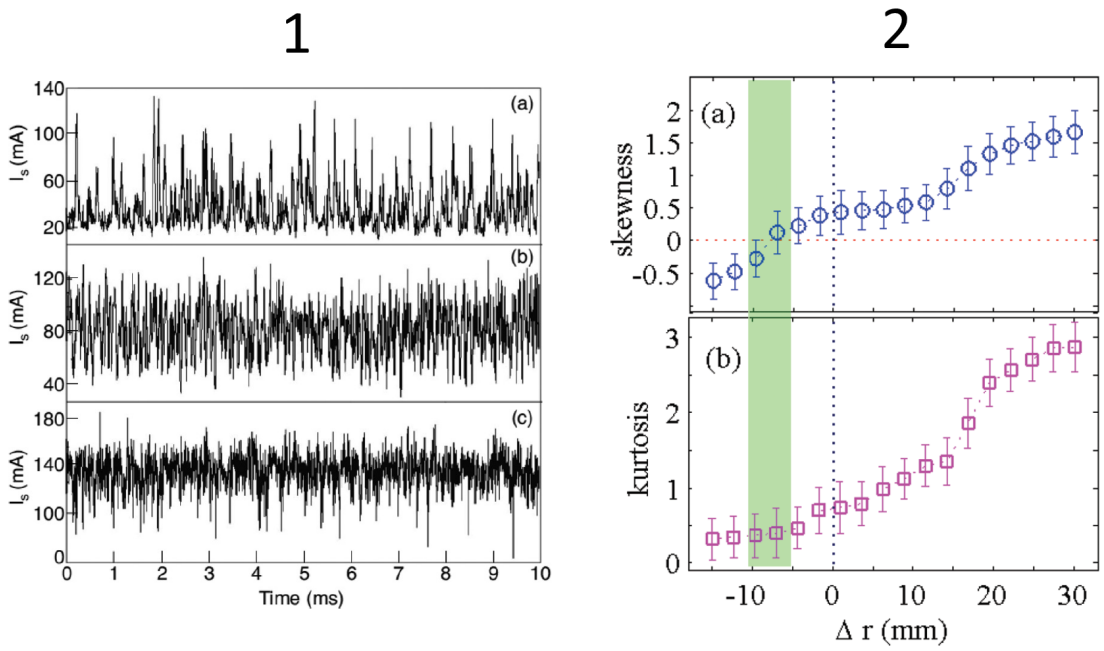

Figure 3.8: 1 - ion saturation current measurement at three distinct position in JET: a) far SOL, b) shear layer, and c) plasma edge [289]. 2 - radial profile of the skewness and kurtosis ($K-3$) of density fluctuation measure with probes in HL-2A tokamak [45].

$$S = \frac{1}{N}\sum_{i=1}^{N}\frac{(X_i - \bar{X})^3}{\sigma_X^3} \quad \text{(Skewness)} \tag{3.18}$$

$$K = \frac{1}{N}\sum_{i=1}^{N}\frac{(X_i - \bar{X})^4}{\sigma_X^4} \quad \text{(Kurtosis)} \tag{3.19}$$

Where σ_X is the standard deviation. The skewness measures the level of asymmetry of a PDF, where the kurtosis its flatness. A pure Gaussian distribution has $S = 0$ and $K = 3$. Deviations from Gaussian distribution has been observed in the edge and SOL of different devices and is likely related to avalanching and intermittency [108].

Figure 3.8 shows the time series of the ion saturation current measured in three different positions (a - far SOL; b - shear layer; c - plasma edge) in JET [289]. While in the SOL fluctuations are mainly positive (with respect to sampling mean) related to

the presence of denser coherent structures, in the edge negative fluctuation dominates the signal possibly associated to the presence of *holes*. In the shear layer, both positive and negative oscillation seems to be equally balanced. Indeed, blobs and consequently holes, travelling in the opposite direction, are believed to be created in this region [63]. Fig. 3.8 shows the skewness and kurtosis ($K-3$) profiles from ion saturation current measurements in HL-2A tokamak [45]. One can note that the SOL (especially the far SOL) exhibits higher skewness and kurtosis indicating that the corresponding PDF in this region is non-Gaussian, and it is dominated by positive fluctuations. Near the LCFS both skewness and kurtosis becomes lower, approaching to a Gaussian distribution. In the deeper edge, the skewness turns negative suggesting a dominance of negative fluctuation possibly related to the presence of holes. The role of the shear layer in creating blobs has also been verified in simulations [196, 166], resulting from the breaking of streamers [23, 196]. In a more general view, turbulence is created in an unstable region where microinstabilities are linear unstable, while blobs or turbulent filaments will result from the non-linear saturation of turbulence [63, 146].

3.5.1 Experimental evidences of filaments

The first unambiguous experimental observation of turbulent filaments was carried out by *D.H.J.Goodall* [98] using fast cameras and later on by *S. J. Zweben* using electrostatic probes [304]. Since then, filaments have been observed in several devices, in tokamaks [306, 289, 36, 201, 265, 276], stelarators [247, 10], Reversied field Pinch [245, 246], and linear and simple toroidal devices [41, 88, 261]. Today filaments are measured with a great level of detail which permits to improve the knowledge about them and to confront with predictions from theory and simulation. Among the diagnostics used to visualize filaments and characterize them, the spectroscopic ones have proved to be a great tool. They typically measure the emission from the plasma passively or actively, the latter, e.g., by ejecting neutrals into the plasma to

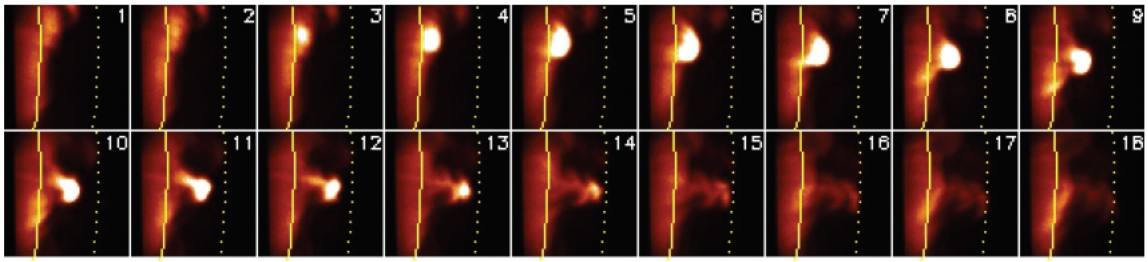

Figure 3.9: GPI measurements of blobs in the NSTX tokamak [167].

enhance the light emission. The light is then collected by fast detectors. The Gas Puffing Imaging (GPI) has been used in several devices [10, 245, 306] to characterize the edge and SOL turbulence with good spatial and temporal resolution. However, the signal is of difficult interpretation, having a complicate dependence on pressure. Fig. 3.9 shows the detachment of a blob from the bulk plasma towards the SOL as measured by GPI in NSTX [167].

Electrostatic probes are still an important tool to investigate blobs in the SOL. Typically one can measure the ion saturation current $I_s \propto n_e\sqrt{T_e}$ (commonly used as a proxy for the density fluctuation [196]), potential fluctuation (typically floating, but also plasma potential with ball pen probes or emissive probes [4]), and electron temperature. With the right arrangement of probes, one can also measure the turbulent particle flux. These quantities are studied with statistical tools presenting a common feature among different devices (including tokamaks, stellarators, and RFP) [63] suggesting that filamentary transport is a general phenomenon in magnetized plasmas. Filamentary probes (see chapter 4) have been used to measure the parallel current density fluctuation related to filaments [245, 248], which is a crucial parameter to validate models. Measurements of blobs inside the confinement region are usually scarce since probes can perturb the plasma as well as being damaged by the high heat flux that is presented in this region.

3.5.2 Blobs simple model

In the scrape-off layer region of fusion devices, the magnetic field lines intercept a material surface and so parallel transport becomes an important channel for dissipation. In a simple electrostatic filament model [146], deduced from charge conservation arguments, an effective gravity force $\mathbf{F}$ (e.g. curvature force for interchange instability) acts as a source of diamagnetic current perpendicular to the local magnetic field ($j_F = \mathbf{F} \times \mathbf{b}/B$), since electrons and ions are drifted in opposite direction. As a response to that, a parallel current density arises to dissipate it. Furthermore, the inertia of the ions results in the polarization drift perpendicular to the magnetic field. The combination of these terms is described by the vorticity equation obtained from charge conservation ($\nabla.\mathbf{j} = 0$):

$$\nabla j_{\parallel} + \nabla j_{\perp} = \nabla j_{\parallel} + \nabla.\left(\frac{\mathbf{F}\times\mathbf{b}}{B}\right) + \nabla.\frac{d}{dt}\left(\frac{nm_i}{B^2}\nabla_{\perp}\Phi\right) = 0 \tag{3.20}$$

where it was assumed that the ions temperature is negligible over the electron one. Besides, Φ is the electrostatic potential, n is the plasma density, B is the magnetic field, m_i is the ion mass, $\mathbf{b} = \mathbf{B}/B$ and $d/dt = \partial/\partial t + \mathbf{v}^{\mathbf{E}\times\mathbf{B}}.\nabla$, where $\mathbf{v}^{\mathbf{E}\times\mathbf{B}} = (\mathbf{b}\times\nabla\Phi)/B$. It is common to define $\mathbf{F} = nm_i\mathbf{g}$, where $\mathbf{g}$ is an effective gravitational acceleration. One can demonstrate [146] that in simple slab geometry, where x represents the radial coordinate and y the poloidal one, the vorticity equation becomes:

$$\nabla.\frac{d}{dt}\left(\frac{nm_i}{B^2}\nabla_{\perp}\Phi\right) = \nabla_{\parallel}J_{\parallel} + \frac{m_i}{B}g_{sp}.\frac{\partial n}{\partial n} \tag{3.21}$$

where the curvature force yields $g = 2c_s/R$, where c_s is the sound speed.

In addition, the blob density equation can be deduced from the continuity equation without sources and sinks [146]. In the lowest ordering, neglecting ionization sources, parallel dissipation, etc, the blob density equation is:

$$\left[\frac{\partial}{\partial t} + \mathbf{v}^{\mathbf{E}\times\mathbf{B}}.\nabla\right] n = 0 \tag{3.22}$$

The equations 3.21 provides a mechanism whereby filaments are propelled and dissipated. The density blob travels with $\mathbf{v}^{\mathbf{E}\times\mathbf{B}}$, that in turns is fed by the vorticity equation, thus making the two equations coupled. Fig. 3.9 a) shows how a blob according to this model looks like. The density positive perturbation is surrounded by a dipole potential that generates $\mathbf{v}^{\mathbf{E}\times\mathbf{B}}$ pattern flow. Note that the phase shift between the potential and the density perturbation yields an effective velocity towards increasing r. Once a blob crosses the SOL, the rapid parallel transport along the field lines acts to dissipate it in competition with the cross-field transport. Therefore, the parallel closure impacts on the blob cross-field motion and life-time. Fig. 3.9 b) shows a blob equivalent circuit [146]. The curvature generates a charge-polarizing current that creates a dipole in the cross-field plane. The charge build-up is balanced by parallel dissipation along the field lines up to the sheath of a material surface (e.g. limiter, divertor or wall). In addition, the ion polarization drift also acts to reduce the charge accumulation. In the limit where parallel resistivity is negligible, the parallel current density is only regulated by the sheath resistivity:

$$\nabla_{\parallel} j_{\parallel} \rightarrow \frac{2nec_s\left[1 - e^{-(\phi-\phi_f)/T_e}\right]}{L_{\parallel}} \approx \frac{2ne^2c_s(\phi-\phi_f)}{L_{\parallel}T_e} \tag{3.23}$$

where $L_{\parallel}$ is the parallel connection length and $\phi_f \approx 3T_e/e$ is the floating potential at the sheath. One can demonstrate that the blob velocity in this regime, neglecting the ion polarization drift and assuming Gaussian shape is [63]:

$$v_b = 2c_s\left(\frac{\rho_s}{\delta_b}\right)^2 \frac{L_{\parallel}}{R} \tag{3.24}$$

where δ_b is the blob size.

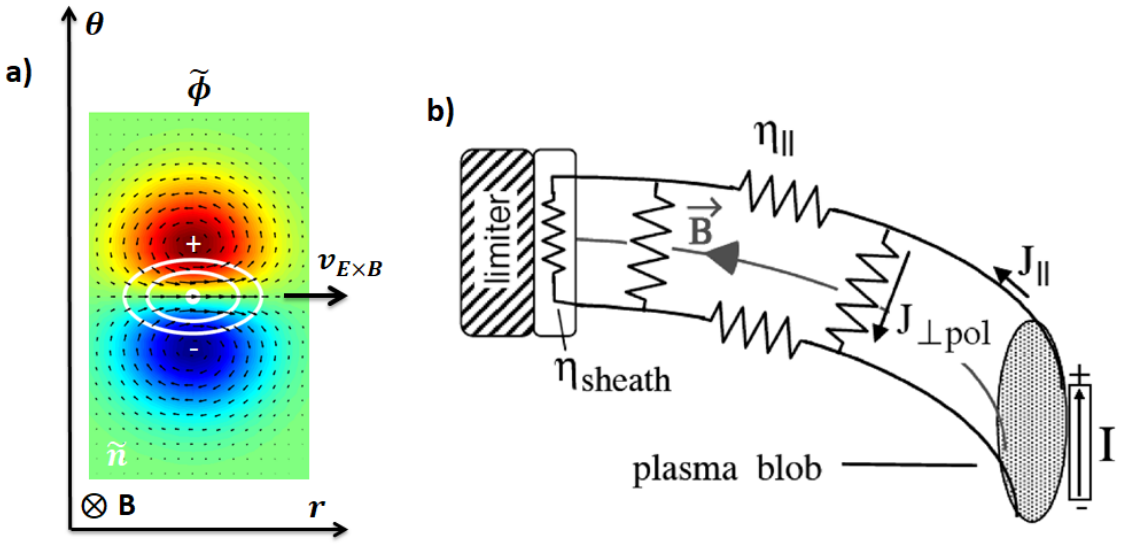

Figure 3.10: Filament simple representation: a) density blob (white contour) surrounded by a dipole potential that acts to propel it through $E \times B$ drift, b) blob equivalent circuit [146].

However, if the parallel current becomes negligible ($\nabla_{\|} j_{\|} \to 0$), e.g. when the parallel resistivity becomes too large, the closure is provided by the ion polarization drift. This regime called inertial presents blob with velocity given by [91]:

$$v_b = \sqrt{\frac{2\delta_b}{R}} c_s \tag{3.25}$$

Two-region model

J.R. Myra et al. [188] has proposed an electrostatic cold ions two-region model [188] that captures the fundamental properties of filaments in the midplane SOL and divertor region. The model predicts that connection or not between these two regions along the field line is expected to deeply impact the filament cross-field velocity and size. The density equation in these two regions is given by the lowest order continuity equation (Eq. 3.22), while the potential one captures the essential features of these two regions. At the midplane, the vorticity equation is similar to the one shown in

Eq. 3.21, with a drive (charge polarization) term and a parallel current term connecting the two regions. At divertor region, the drive term is neglected and the parallel one is connected with the sheath. The resistivity along the field lines is given by:

$$\Lambda = \frac{L_{\parallel}\nu_{ei}}{(\Omega_e \rho_s)} \tag{3.26}$$

where ν_{ei} is the electron-ion collision rate.

The solutions for this model is obtained by employing the blob correspondence principle, i.e., the blob size and velocity are related to the drive instability $\gamma \rightarrow v_b/\delta_b$, where γ linear growth rate of the dominant instability. When these two regions are electrically connected, one might find two regimes according to this model. The sheath-connected regime ($\mathbf{C_s}$): the parallel flow is predominately toward the sheath, which might be located at the divertor plates, but also any material surface intercepted by the field lines. For smaller blobs, distortions in the dipole potential close to the x-point (due to the magnetic 'fanning' effect) can produce a cross-field current, reducing charge polarization and acting as an alternative current closure path; such regime is called connected ideal-interchange ($\mathbf{C_i}$). If the collision disconnection factor (Λ), where ν_{ei} is the ion-electron collision rate) is high enough, above a limit ($\Lambda > 1$) [188], the just mentioned current closure at the x-point region can be dominant over the parallel current into the sheath. In that case, the two regions might become electrical disconnected; this regime is called resistive x-point (**RX**). The current path might be even shorter in high collisionality regimes when the parallel conductivity becomes so low that the ion polarization drift largely dominates. This regime is called resistive ballooning (**RB**), where the name refers to the the drive instability. Fig. 3.11 shows a diagram corresponding to the boundaries of the four solutions. The normalized velocity and size are:

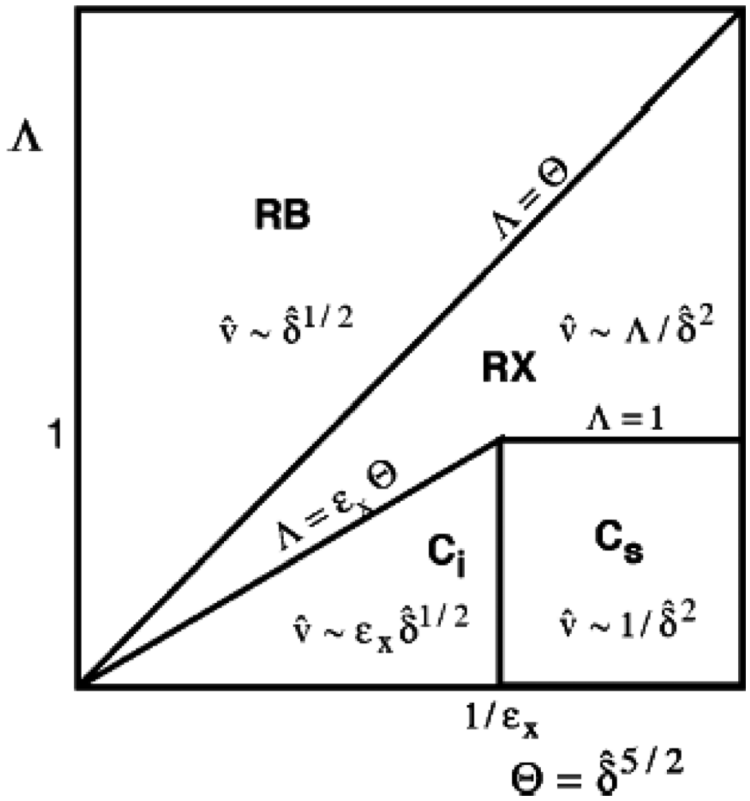

Figure 3.11: Diagram showing the different filament regimes according to the two-region model [188].

$$\hat{v} = \frac{v_r}{\left(\frac{2L_\parallel \rho_s^2}{R^3}\right)^{1/5} c_s} \quad ; \quad \hat{\delta} = \frac{\delta_b R^{1/5}}{L_\parallel^{2/5} \rho_s^{4/5}} \tag{3.27}$$

where where $L_\parallel$ is the parallel connection length and R is the major radius, and $\Theta = \hat{\delta}^{4/5}$.

Note that the two disconnected regimes are dominant for $\Lambda > 1$. The onset of detachment has been correlated with filament transition from connected regime to disconnected resistive ballooning regime [36].

3.5.3 Electromagnetic filaments

Electromagnetic effects become important typically when $\beta > (m_e/m_i)$, where $\beta = n_e T_e/(B^2/2\mu_0)$. Large beta can induce field line bending $\Delta \sim L_\parallel^2 \beta/R$, where $L_\parallel$ is the parallel connection length and R is the major radius. If large enough, the bent lines can, for example, short-circuit the near edge with the close wall, reducing the parallel connection length. Besides, such modification in the magnetic field is related to Alfvén waves emission along the field lines which can modify the parallel closure [146]. A drift-Alfvén model has been used [165] to describe the dynamics of high beta blobs in the SOL. In addition, the model includes the ion temperature fluctuation that is typically not negligible in this region [37]. The model predicts a velocity scaling with the square root of the blob size, as indeed has been observed for high beta ELM filaments [225].

3.5.4 Blob suppression criterion

Blobs can be torn apart by a shear layer when the shearing rate is equivalent to the inverse of the blob convective time. According to Ref. [23], radially elongated turbulent structures, known as streamers, or blobs can be torn apart by an external shear if:

$$\tau^{blob} = L_r/(|v_r|) > L_\theta/(L_r|\gamma^{E\times B}|) \tag{3.28}$$

where $\gamma_{E\times B} \cong B^{-1} dE_r/dr$ and L_r and L_θ are, respectively, the blob radial and poloidal size. This criterion is similar to the well-known eddy decorrelation [21]. Besides, while blobs generation by the break of streamers demands a high enough poloidal shear flow, blobs are also observed in simulations when the shear layer is

absent or very weak. In this regime if $dE_\theta/dr \gg dE_r/dr$, radial stretching can also lead to blob formation [22].

As first suggested by *J.R. Myra et al.* [185], and recently discussed *N.R Walkden et al* [281], hot blobs, i.e. hotter than the surrounding background, can produce an unbalanced potential dipole. Since the $E \times B$ is fundamental for the blob motion, this effect can make the blob to spin rather than radially propagates. This mechanism might lead to self 'trapping' of the blob and then its dissipation by means of parallel transport in the SOL. More generally, any perturbation in the potential dipole might yield a similar effect. Vortex selection is an effect commonly observed in fluids [168], where the mean shear (the background) with a given orientation (positive or negative) tends to amplify vortex with the same orientation and destroy those with opposite one. In the former, the vortexes (or eddy) are called 'prograde' (stable), while in the latter they are called 'adverse' (unstable). Therefore, the shear flow can change the population of eddies according to their relative vorticity signal ($\nabla \times \mathbf{v}$). In the plasma edge and SOL of fusion devices, an unbalance between the dipole and monopole potential population has been observed [241]. This effect can ultimately affect the turbulent transport properties [242]. The critical parameter is the strength of the background shear with respect to the eddy vorticity [75].

Chapter 4

Experimental systems, plasma diagnostics, and experimental tools

The purpose of this chapter is to introduce the experimental systems considered in this thesis. They are a tokamak, COMPASS (IPP, Prague), two stellarators, TJ-II (CIEMAT, Madrid) and Wendelstein-7X (IPP, Greifswald), and the RFX-mod (Consorzio RFX, Padova), a reversed field pinch (RFP) that can also operate as a low current tokamak. In addition, the principal experimental diagnostics considered will be discussed. Lastly, some statistical tools used to characterize the turbulence features in these devices will be presented.

4.1 Experimental systems

4.1.1 COMPASS

COMPASS is a tokamak that has been operating in Prague, Czech Republic, since 2012 [202]. Originally COMPASS-D [80], a compact tokamak that ran in UKAEA Culham (United Kingdom), from 1992 to 2002, the machine was later transferred to the Institute of Plasma Physics of the Academy of Sciences of Czech Republic (IPP

AS CR) in 2006 [203]. Since then, the device went through several updates, on its power suply [298], diagnostic and data acquisition systems [286, 123]. The device has major and minus radius, respectively, $R = 0.56$ m and $a = 0.2$ m. In the COMPASS

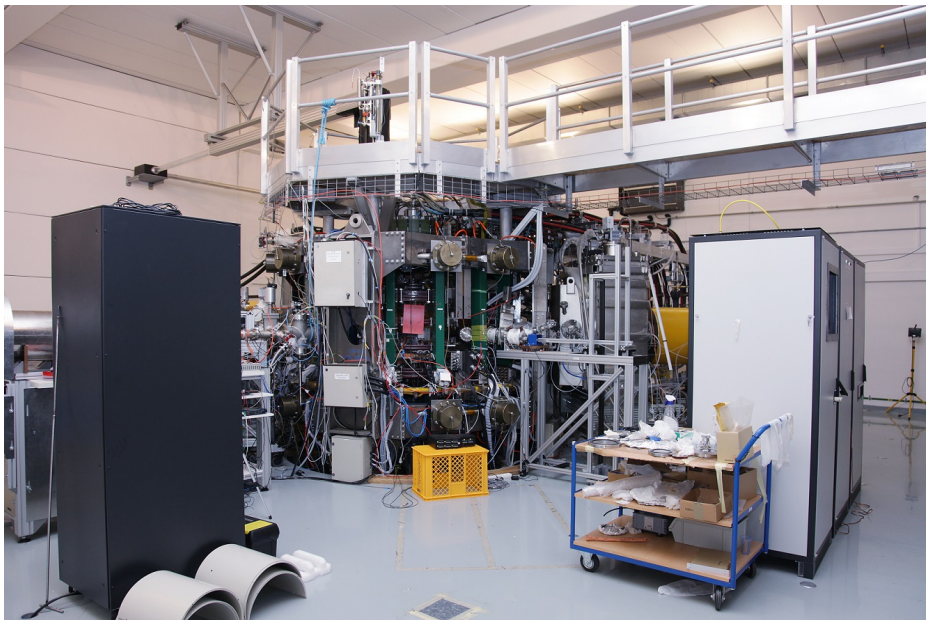

Figure 4.1: Image of the COMPASS tokamak.

standard operation, the magnetic cross-section is ITER-like (scaling 1:10) with single null X-point (SND). Besides, COMPASS divertor is composed of carbon tiles. Two Neutral Beam Injectors (NBIs), operating in co-, counter-, or balanced injection, with beams of deuterium or hydrogen, allow COMPASS to operate in H-mode. In the latter, Edge Localized Modes (ELMs), Type-III and Type-I, have been observed [202]. Ohmic H-mode has also been reported. The beam energy is $\sim$ 40 keV, with port-through power $P_{NBI} \leq 0.35$ MW, and diameter of 5 cm, with pulse duration up to 0.3 s [55]. The toroidal magnetic field can operate in the range 0.8-2.1 T, with elongation up to 1.8. The maximum plasma current achieved is $\sim$ 400 kA. Wall conditioning, including helium glow discharge (GDC) ever 10 minutes before shots, and periodic baking of the vacuum vessel and plasma-facing components (PFCs) together with boronization guarantee low impurity influx and better plasma performance.

Table 4.1: COMPASS parameters.

Parameters	**Values**
Major radius (R):	0.56 m
Minor radius (a):	0.23 m
Plasma current:	$\leq$400 kA
Toroidal magnetic field:	$\leq$2.1 T
Pulse length:	$\sim$1 s
External heating power (NBI):	2$\times$0.4 MW

4.1.2 RFX-mod

RFX-mod is the biggest RFP device in the world. The RFX (Reversed Field eXperiment) machine started operating in 1992. The upgrade of RFX, called RFX-mod, was designed to have an active control to avoid detrimental effects on confinement already observed in RFX, namely: the growth of restive wall mode (RWM) and other MHD instabilities [239]. The system is composed of 192 saddle coils covering the entire torus. In addition, the new system was equipped with a close-fitting 3 mm thick Inconel shell, in replace to the older 65 mm aluminum shell. The conducting shell is crucial in RFP since it sets the magnetic boundary for the tearing mode which in turns is important for the dynamo effect [33]. However, it has been observed that the RWM growth happens in a comparable time as the shell effective penetration time for a vertical field. Meaning that the wall-locked MHD modes happen on this time which might lead to plasma disruption. The shell time is proportional to its thickness and the conductivity of the material, the previous shell time was $\sim$ 400 ms, while the new one is $\sim$ 100 ms. This apparent drawback is compensated by the new MHD control system that mimics an ideal conducting wall ($B_r \approx 0$) but avoiding sideband harmonics [299], allowing much longer pulses [170]. In addition, the flexibility of RFX-mod permits to operate in tokamak configuration in both circular and single-null cross-section. However, since the toroidal magnetic field is relatively low (see table 4.1.2), the plasma current must also be low to avoid MHD instabilities [302].

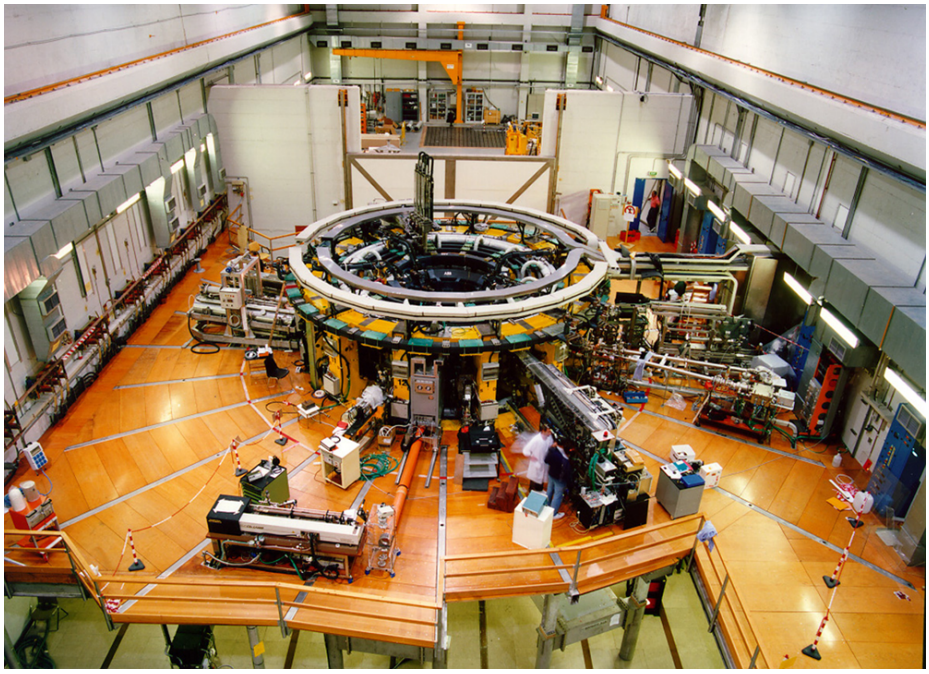

Figure 4.2: Picture of RFX-mod.

RFX-mod is currently under upgrade, the RFX-mod 2 is foreseen to start operating soon. Among the improvements of the new system with respect to the previous RFX-mod are [169]: a new copper shell nearer to the plasma aimed to reduce the effect of RWMs and a first wall covered by graphite tiles attached to the shell.

Table 4.2: RFX-mod parameters.

Parameters	**Values (RFP)**	**Values (tokamak)**
Major radius (R):	2.0 m	2.0 m
Minor radius (a):	0.5 m	0.5 m
Toroidal magnetic field:	$\leq$ 0.55 T	$\leq$ 0.55 T
Plasma current:	$\leq$ 2.0 MA	$\leq$ 0.3 MA
Pulse length:	$<$ 250 ms	$<$ 1100 ms

4.1.3 TJ-II

TJ-II is a heliac device currently operating in CIEMAT, Madrid (Spain). The machine started being designed in the late '80s, but the first plasma was only achieved in 1996 [8]. The toroidal magnetic field is generated by 32 coils covering the whole

torus, while the helicity is obtained with a combination of a central circular conductor and two wrapped helical coils around the conductor, allowing operation with a wide rotational transform range (from 1.0 to 2.2 at the edge). Besides, vertical field coils control the horizontal position of the plasma. The plasma is limited by toroidal symmetric stainless steel limiter, where movable carbon limiter can also be used. The principal TJ-II parameters are shown in table 4.1.3. The external power is provided by two-electron cyclotron resonance heating (ECRH) operating in X-mode with a frequency of 53.2 GHz and delivering power up to 0.3 MW. The power deposition can be externally controlled with a mirror inside the vacuum vessel and the same system can be used for inducing currents in the plasma, i.e. electron cyclotron current drive (ECCD) [79]. In addition, two neutral beam injectors (NBI), co- and/or counter-beam, of H or He (depending on the working gas) can deliver up to 2×0.7 MW port-through power.

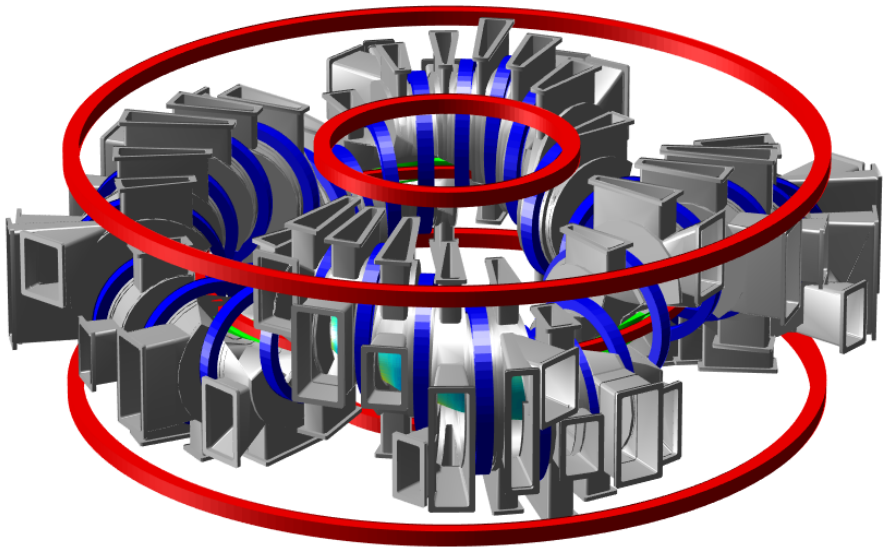

Figure 4.3: TJ-II perspective view.

The vacuum vessel is made of stainless steel. Wall conditioning is regularly performed with glow discharges and boronization to reduce the content of carbon and oxygen in the plasma [256]. TJ-II, as most of the stellarators, operates with a wide

negative magnetic shear range, which has a stabilizing effect on neoclassical tearing modes. Fig. 4.4 shows the rotational transform $\imath/2\pi$ profile of TJ-II in standard magnetic configuration (data presented in this thesis was for this configuration).

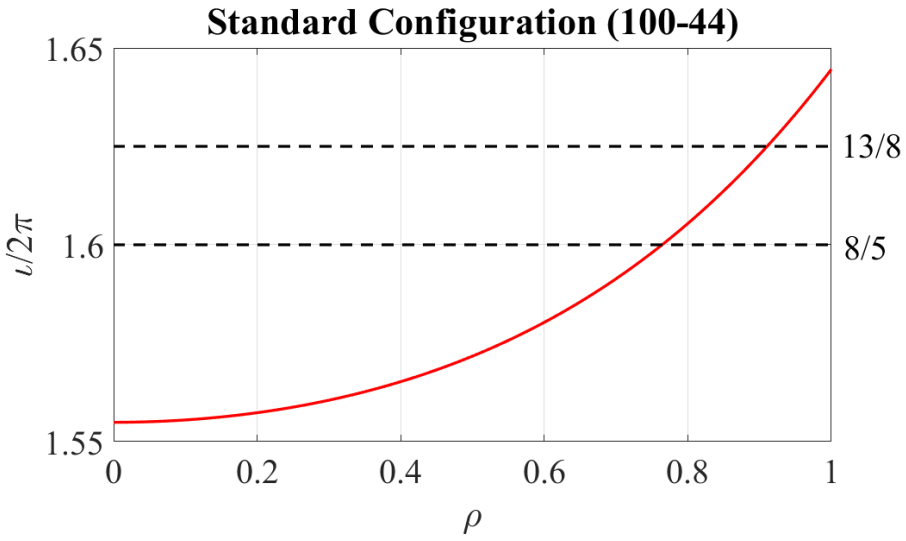

Figure 4.4: Iota profile of TJ-II standard configuration.

The main topics of research in TJ-II are [12]: turbulence, impurity accumulation and transport, the role of the magnetic configuration on transport, plasma core fuelling with pellet injection (PI), power exhaust physics and technology, fast particle driven modes, etc.

Table 4.3: TJ-II parameters.

Parameters	**Values**
Major radius (R):	1.5 m
Minor radius (a):	$\leq$ 0.22 m
Toroidal magnetic field:	$\leq$ 1.2 T
Pulse length:	$<$ 200 ms
ECRH power (X-mode, 53.2 GHz):	2×0.3 MW
NBI power (Co and Counter-beam):	2×0.7 MW

4.1.4 Wendelstein 7-X

Wendelstein 7-X (W7-X) was designed to reduce as much as possible the neoclassical loss typical common in stellarators. W7-X belongs to the helical-axis advanced stellarator (HELIAS) concept aimed to reduce the influence of self-generated plasmas currents that in turns can be a source of instabilities. The basic HELIAS requirements are:

- Reduced neoclassical losses;
- MHD stability and low Shafranov shift up to $\langle\beta\rangle \sim 5\%$;
- Magnetic island formation restricted to the plasma edge for divertor configuration;
- Small bootstrap current;
- Good confinement of fast particles;
- Sufficient space for blanket and shield.

The confinement magnetic field is composed of 50 modular and 20 planar coils, the latter used to modify the rotational transform ($\imath/2\pi$) as well as change the plasma radial position. The coils are superconducting putting W7-X as the first HELIAS device operating with superconducting coils. Besides, the bootstrap current is virtually absent in W7-X thanks to its quasi-isodynamic field configuration [61]. This configuration is also responsible for a much reduced neoclassical loss compared to other stellarators. Magnetic islands can be created in the plasma for $\imath/2\pi = 1$ to mimic a divertor configuration. Recent results show that feasibility of this configuration [206], proving its robustness in exhausting energy out the plasma. However, the complicated interaction between the plasma and the islands (with turbulence playing a role) must be better understood.

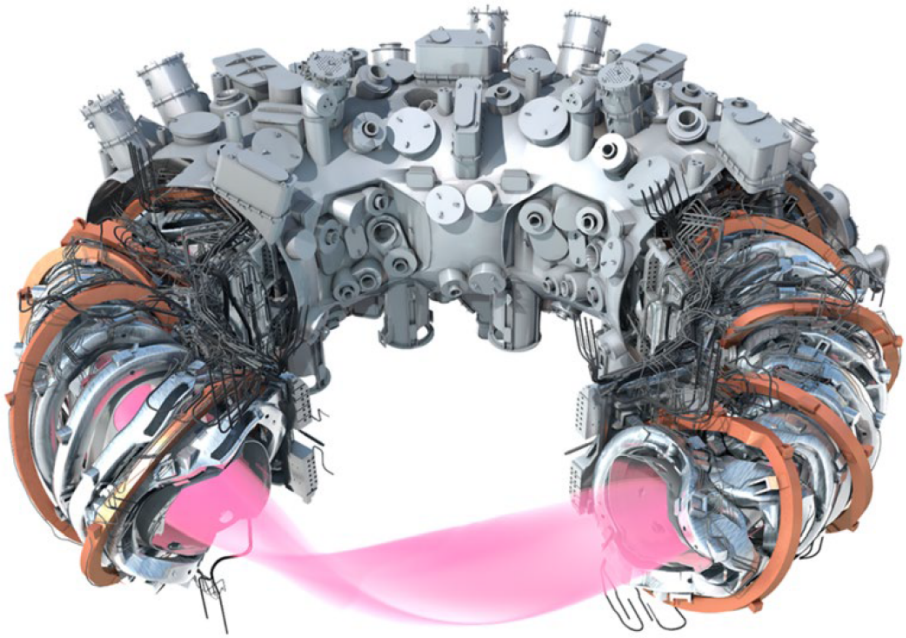

Figure 4.5: Schematic drawing of W7-X.

Table 4.4: W7-X parameters.

Parameters	**Values**
Major radius (R):	5.5 m
Minor radius (a):	$\leq$ 0.53 m
Toroidal magnetic field:	$\leq$ 3.0 T
Pulse length:	$\leq$ 30 min
Power heating:	10-30 MW

4.2 Some turbulence diagnostics

4.2.1 Electrostatic probe

Electrostatic probes were invented by the American physicist Irving Langmuir to measure the physical characteristics of a plasma. They consist of an electrode inserted into the plasma that might not be polarized with respect to the enclosing material surface. Through current and voltage measurements it is possible to estimate some plasma relevant parameters, such as temperature and electron density, as well as the local plasma potential. Because of its invasive characteristics, probes are restricted to

the edge or SOL range in a fusion device, as it can be damaged in more internal regions due to the higher temperature and density. The interpretation of data from probes is based on Debye sheath theory [126]. When a conductor material interacts with a plasma with temperature (T_e), density (n_e), and potential (ϕ_p), the charge particles in the plasma rearrange to equalize the flow of positive and negative particles towards the material surface. Because electrons have higher mobility than ions, they interact with the external material faster, thus, creating an electric field that accelerates ions and slows down electrons. As a result, the material will have a potential different from the local plasma potential in a short-range called Debye length λ_D. This collective displacement of plasma acts to shield external electrical perturbation.

By applying a negative voltage to the probe with respect to the limiter (or wall) more ions are collected than electrons. For an even more negative voltage, the current becomes approximately constant, called the *ion saturation current* (I_s). On the other hand, by increasing the voltage to positive values, the drain current becomes predominantly of electrons, saturating once the biasing voltage is equal to the plasma voltage. In the region between the two saturation points, the curve grows exponentially. The zero current point on the curve, where the ion flux is balanced with the electron one, is called the *floating potential* (ϕ_f). In magnetized plasmas, however, the ion saturation does not saturate because of the projected surface area of the probe changes with the biasing voltage (sheath expansion effect) [126].

Ion current density is determined by the Bohm criterion, which assumes that the flux of ions towards the sheath is constant with a velocity equal to the velocity of the sound (c_s) [249]:

$$j_i = \frac{1}{2} e n_0 c_s \tag{4.1}$$

where $c_s = \sqrt{(ZT_e + T_i)/m_i}$.

On the other hand, the electron current density in the sheath region is represented by a Maxwellian distribution, where the electron flow towards the probe is: $\frac{1}{4}n_e\bar{c}_e$, with the electron thermal speed given by $\bar{c}_e = (8T_e/\pi m_e)^{1/2}$. The electron current density, taking into account the effect of secondary electron emission (γ_e), is given by:

$$j_e = -\frac{1}{4}en_0\left(\frac{8T_e}{\pi m_e}\right)^{1/2}(1-\gamma_e)e^{\frac{e(\phi-\phi_p)}{T_e}} \tag{4.2}$$

where the plasma potential (ϕ_p) is taken as a reference.

When the potential applied to the probe is equal to the floating potential, the current collected by the probe is zero ($j_i = j_e(\phi_f)$), thus:

$$\phi_p = \phi_f + \frac{T_e}{2e}\ln\left[\frac{m_i(1-\gamma_e)^2}{2\pi m_e\alpha^2(1+T_i/T_e)}\right] \tag{4.3}$$

In addition,

$$j_i e^{-\frac{e(\phi_f-\phi_p)}{k_b T_e}} = \frac{1}{4}en_0c_e(1-\gamma_e)$$

so the electron current density can be written as:

$$j_e = -j_i e^{\frac{e(\phi-\phi_f)}{T_e}}.$$

It follows that the total current collected by the probe ($I = (j_i + j_e)A$) becomes:

$$I(\phi) = I_i\left[1 - e^{\frac{e(\phi-\phi_f)}{T_e}}\right] \tag{4.4}$$

The plasma sheath expansion described before can be taken into account by defining an effective area $I_s = A_{eff}(\phi) j_i$ [114].

The electron density can be obtained from the ion saturation current, considering the Bohm criterion (Eq. 4.1),

$$n_e \approx \frac{2I_s}{A}\sqrt{\frac{m_i}{T_e}} \tag{4.5}$$

Triple probe

The triple probe configuration is a technique to measure the electron temperature in the plasma. The method consists in to insert three tips into the plasma, one in floating potential configuration and the other two in a double probe configuration (see Fig. 4.6 a). This two tips are externally biased with expect to each other ($\Delta\phi = \phi_+ - \phi_-$), satisfying the current continuity of the double circuit that imposes: $I_+ + I_- = 0$, while the negative branch can be used to measure the ion saturation current. In addition, considering that at the floating potential the probe does not drain any current and using the equation 4.4, one can demonstrate that [114]:

$$T_e = \frac{(\phi_+ - \phi_f)}{\ln(2)} \tag{4.6}$$

where it was assumed that the collection area of the two tips in the double configuration is the same and that $\Delta\phi \gg T_e/e$, which is easily satisfied, with a proper power supply, in the edge and SOL of tokamaks and stellarators where the temperature is typical $T_e \ll 100$ eV.

The three probe configuration implicitly assumes that three tips are sufficiently close to each other, so eventual plasma inhomogeneity does not affect the measurement. However, the plasma edge and SOL is fully dominated by turbulence with the

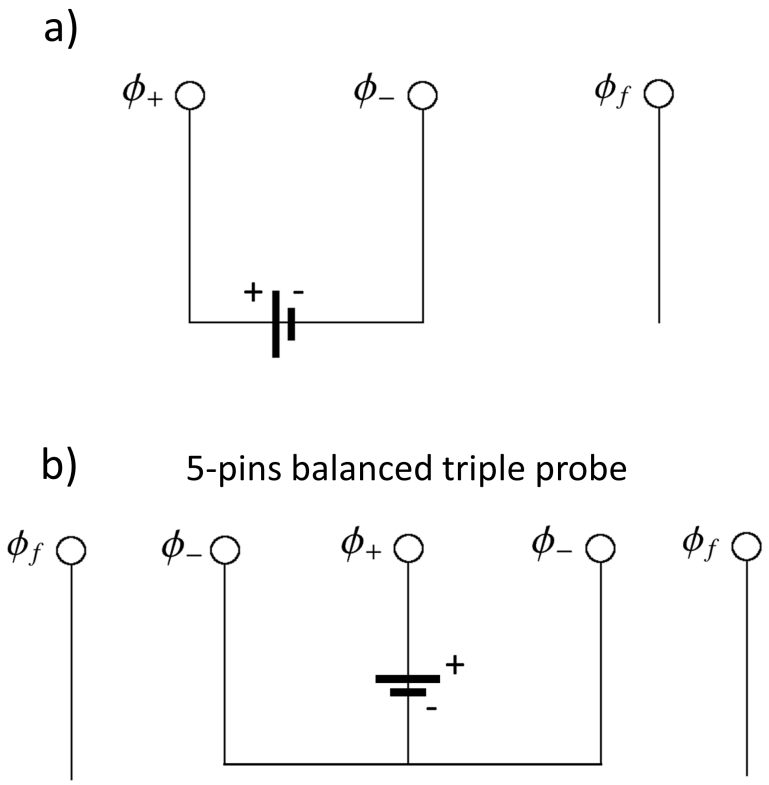

Figure 4.6: a) standard triple probe configuration, b) 5-pins balanced triple probe configuration.

presence of travelling mesoscale structures like blobs. Therefore, turbulent structures passing through the tips must be larger than the distance between tips to guarantee the validity of the hypothesis behind the triple probe method. As discussed by several authors [266, 114, 260], if this requirement is not satisfied, the T_e fluctuations measured with the triple probe configuration is not reliable, although the method still works well for measuring the background temperature [114].

5-pins balanced triple probe

Temperature fluctuation is one of the most difficult quantities to measure with probes. However, this quantity is crucial to determine the turbulent energy transport towards the SOL, which in turns is relevant for the power balance in this region. In the previous section, it was discussed that the standard triple probe configuration can

provide reliable measurements of the background temperature, but fluctuations can suffer phase delay errors because the tips do not measure at the same point. In theory, one can approach the tips so close to each other that this error would be minimized to nearly zero. However, in the practical situation, this is not simple to do since the tips themselves could cross-perturb. *H. Y. W. Tsui et al.* [266] have proposed a method to deal with this problem. The technique is based on a balanced three probe configuration realized with a minimum set of five tips (see Fig. 4.6 b). The additional tips make the system symmetric with respect to the central one, reducing the phase error to second order in kd, where k is the perturbation perpendicular wavenumber and d is the largest tip separation (between the two floating potential signals). The temperature in this configuration is given be [266]:

$$T_e = \frac{(\phi_+ - \phi_f)}{\ln(3)} \tag{4.7}$$

Although the method offers a practical solution for the phase delay error in the temperature fluctuation measurement, it still requires that the separation of the tips must be smaller than the turbulent correlation length. Although the error of the separation of the tip becomes a second-order effect, the price to pay is to insert two more tips that tend to increase d.

4.2.2 Magnetic sensors

Magnetic sensors are fundamental diagnostics in fusion devices. They are used for different purposes, from plasma shape control to the detection of MHD fluctuation. They are usually found outside the confinement to avoid plasma perturbation and the damage of the diagnostic. Magnetic measurements can provide the plasma current

and the stored plasma energy, which are two crucial quantities for tokamak operation. The focus of this section is, however, diagnostics used for detecting and characterizing turbulence. Therefore, they must be sufficiently fast, i.e. have a high temporal resolution to resolve the relevant oscillations coming from the plasma. The frequency range: 0-1000 kHz is usually a safe interval for measurements of this type. In addition, to study some specific plasma phenomenons, local measurements are required. In this case, small pick-up coils can be used (to reduce as much as possible the plasma perturbation) and preferentially with a cover to protect it from the hot plasma. As will be discussed next, the filamentary probe uses its own insulator body to protect the pick-up coils that are installed inside of it.

The measurement of magnetic field fluctuation from the plasma can be easily done using coils. If the magnetic field varies in time, the induced voltage is:

$$V = -\frac{d}{dt}\int\int \mathbf{B}.\mathbf{dS} \approx -A_{eff}\dot{B} \tag{4.8}$$

Where A_{eff} is an effective area that takes into account the number of turns in the coil. The magnetic field fluctuation can be obtained by numerically integrating the coils signals, $B_i = 1/A_i \int \dot{B}_i dt$, where A_i is the coil effective area orthogonal to the magnetic field component of index i. Alternatively, one can design an analogic integrating circuit to obtain B directly. Orthogonal coils can be used simultaneously to measure magnetic field fluctuations of all the three component. However, the misalignment of the coil with respect to magnetic field can lead to misinterpretation. It is possible to overcome this limitation by using statistical analysis to find the proper frame where the magnetic field is ortoghonal [277].

4.2.3 Filamentary probe

Probes that combine electrostatic and magnetic sensor have been used to characterize the plasma boundary turbulence fluctuation of several devices [234, 225, 246, 199, 88, 144] as well as being used to measure current carrying filaments related to ELM events [277, 244]. On the other hand, filamentary probes are equipped with a set of magnetic sensors suitable to provide direct information on the fluctuation of parallel current density associated with traveling filaments passing around it. This concept was first applied in atmospheric sciences, where it has been employed to study the properties of the magnetosphere [268]. The measurements of the magnetic field from four cluster spacecraft were used to compute the three components of the current density in the magnetosphere. Since three points are coplanar, to measure the three components of the parallel current density is necessary at least four coils, where the fourth one must be in a plane out of the plane defined by the other three coils. Such tetrahedron configuration is capable to measure the three components of $\nabla \times B$, necessary to obtain $[j_x, j_y, j_z]$ in Cartesian coordinate [268]. The method was first used in hotter plasmas in the RFX-mod [246]. A probe was designed to measure the parallel current density fluctuation in the plasma edge and SOL of the RFX-mod in RFP configuration. This quantity is relevant for the study of turbulent filaments in magnetized plasmas. The minimum set of coils and their arrangement to measure $j_\parallel$ in slab geometry approximation is shown in Fig. 4.7. From the cross-field magnetic field fluctuation, the parallel current is obtained with the Ampére's Law: $j_\parallel \approx \mu_0^{-1} \nabla_\perp \times \mathbf{B}$, where the derivative can be approximated by finite differences.

The U-probe is a type of filamentary probe designed to measure the parallel current density fluctuation of turbulent filaments without affecting much their trajectory. This probe is composed of two towers where a set of electrostatic and magnetic sensors are installed. The separation of the towers is aimed to allow filaments to propagate between them, where the current density measurement, following the minimum set

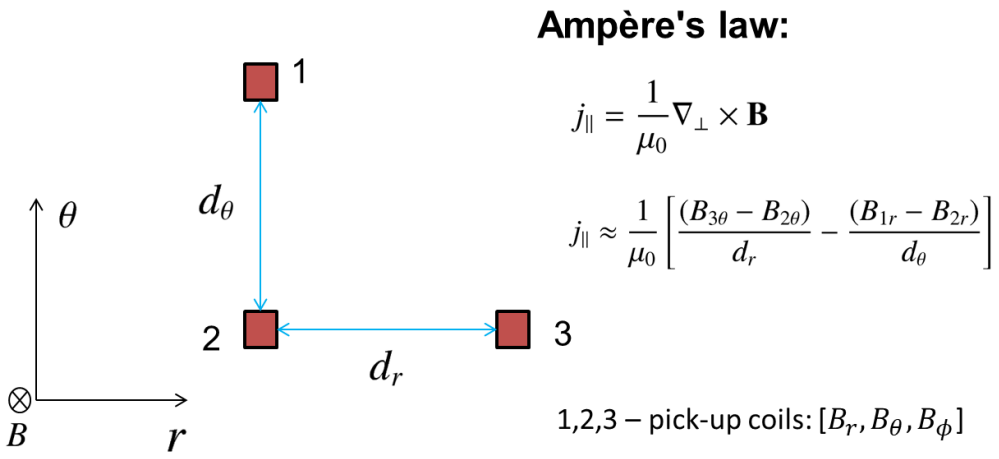

Figure 4.7: Minimum set for measuring the parallel current density with pick-up coils.

(Fig. 4.7), lies approximately on the barycentre formed by three coils. The probe body or head is made of boron nitrite (BN). The choice of BN relies on: 1) it is a low-Z insulator; 2) can withstand high heat flux. Besides, boron nitrite is virtually transparent to high magnetic field fluctuation, thus the 3-axial coils, installed in the probe head, are not shielded. An U-probe type has been used in RFX-mod to measure turbulent filaments in both RFP and tokamak configuration [246, 245, 247] (Fig. 4.8 a). Each tower is equipped with 40 tips of graphite in a 5x8 array and seven 3-axial pick-up coils (cubic shape with length 8 mm) displaced collinearly with mutual separation of 6 mm. The distance between the two towers is of 8.8 cm. A similar probe has been used in COMPASS tokamak [144, 244] (Fig. 4.8 b). This probe is more compacted than the one in RFX-mod aimed to reduce the plasma perturbation, but with a tower separation (4.4 cm) that allows the filament to pass through it without being significantly perturbed. In each tower of this probe were installed three 3-axial coils (similar to the ones used in RFX-mod). In addition, each tower works in a rake probe configuration with six electrostatic probes radially separated 4 mm and with a triplet of electrostatic probes in front of it, permitting to monitor the plasma at the same radial position but with a poloidal displacement.

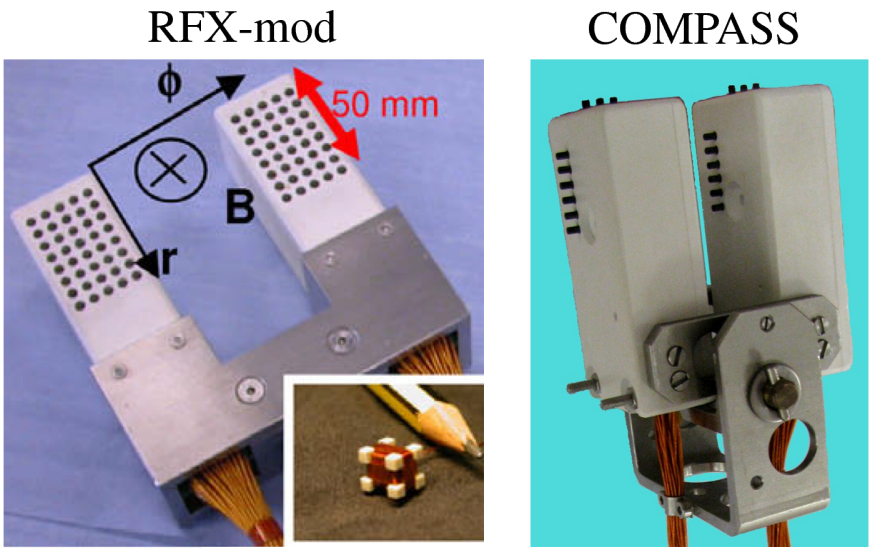

Figure 4.8: U-probe of the RFX-mod (left) and COMPASS (right).

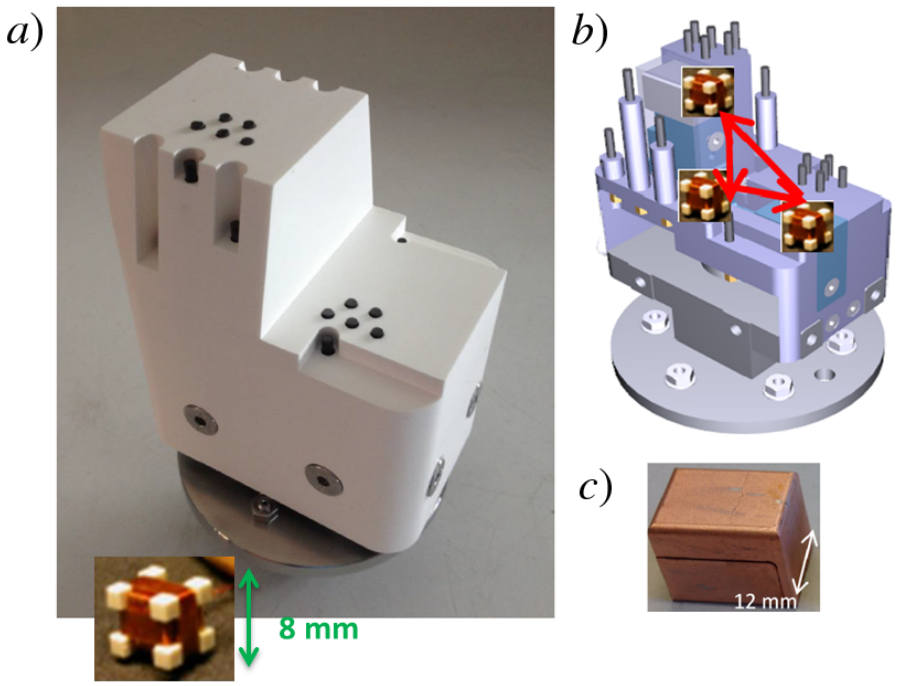

Figure 4.9: L-probe of W7-X: a) photo showing the probe head with the set of 5-tips, Mach probes, and one 3-axial pick-up coil ; b) three 3-axial pick-up coil in the triangle configuration, minimum set for measuring the parallel current density; c) copper shield for coils. Figure adapted from [240].

Another type of filamentary probe based on L-design has been used in TJ-II [247] and TORPEX [87, 88]. This probe has the advantage of being more compacted than the U-probe. A L-probe type was designed for W7-X, the High Resolution Probe (HRP) head [6]. This probe is composed of two set of 5-pins radially spaced (Fig. 4.9 a), configured to measure ion saturation current, floating potential, and temperature from the 5-pin balanced triple probe configuration [266]. In addition, the probe is equipped with four Mach probes aimed to measure the radial profile of the parallel flow. The magnetic field fluctuation is measured with three pick-up coils radially and poloidally spaced (Fig. 4.9 b). This configuration is the minimum set for measuring the parallel current density [268]. The probe body is made of boron nitrite (BN). The 3-axial magnetic coils were calibrated before operation, where the effective area of each component was determined. This value is important to obtain the magnetic field fluctuation with proper physical units. One of the challenging for the probe design is the straight radiation from the ECRH system of W7-X, where the working frequency is $f = 140$ GHz with power up to 7 MW in a pulse length within the range 10-20 s. On the other hand, the relevant plasma fluctuation typically is within the range: 0-1000 kHz. Therefore, it was necessary to cover the magnetic coils with a proper shield able to filter out high-frequencies (in the range of the ECRH straight radiation), but keeping low-frequencies (in the plasma turbulent range). The shield material employed was copper and the shield thickness (or skin depth) was carefully chosen since the cutoff frequency is proportional to the square of the skin depth ($f \propto \delta^2$). Therefore, the shield thickness should not be neither too thick nor too thin. The value that matched these requirements was $\delta \approx 5\ \mu m$ [6]. The probe was successfully operated during the OP1.2b campaign in W7-X, enduring large power heat fluxes in shots where the plunge duration was up 2.5 s [240].

4.2.4 ISIS

The Integrated System of Internal Sensors (ISIS) is composed of electrostatic and magnetic sensors, toroidally and poloidally spaced, installed on the wall of vacuum vessel of RFX-mod [228]. The system covers the entire torus allowing to monitor in real-time the electrostatic and magnetic fluctuation. The latter is particularly relevant for RFX-mod since it integrates the MHD feedback control system [299].

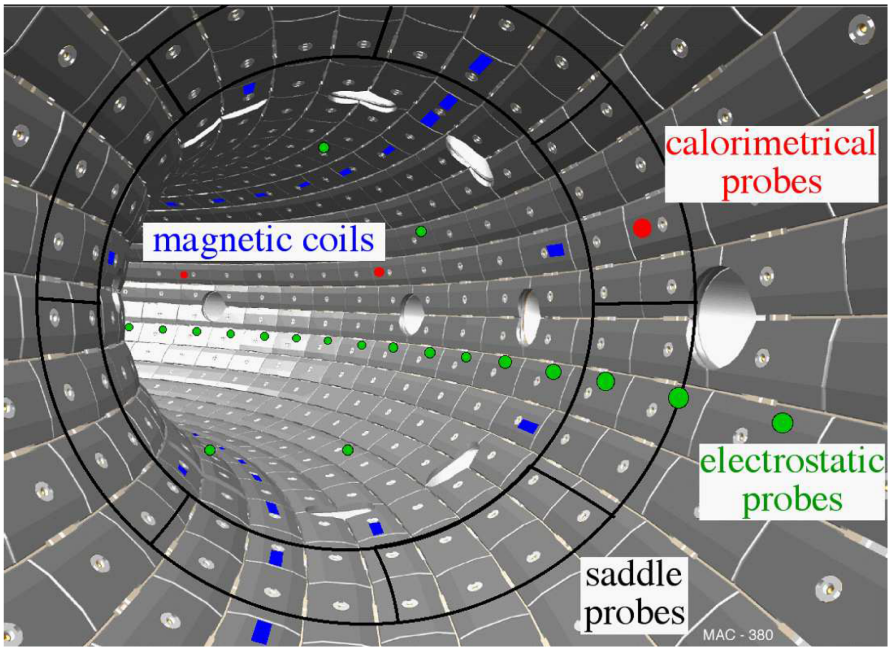

Figure 4.10: Internal System of Sensor (ISIS) in RFX-mod.

As shown in Fig. 4.10, the ISIS system is composed of: **thermal sensors**, installed behind the graphite tiles at the outboard midplane ($\theta = 6.5°$) to monitor the temperature of the wall [229]; **electrostatic sensors**, set of Langmuir probes toroidally (72 sensors) and poloidally (7 triplets sensors) spaced configured to measure floating potential [228]; **magnetic sensors**, composed of saddle and pick-up probes covering the entire torus.

4.3 Useful statistical tools for turbulence investigation

This section introduces some of the statical tools used throughout the thesis to interpreter and characterize turbulent signals.

4.3.1 Probability distribution function

Measurements with probe quite often provide time series of voltage or current at a particular position in the plasma. As discussed, the ion saturation current is typically a good proxy for the density fluctuation. The plasma edge and SOL of fusion devices is typically turbulent and so the time trace of ion saturation current signals exhibit large fluctuations around the mean. Therefore, it is useful to study their *probability distribution function* (PDF) since it might provide some useful information regarding the nature of the instability and the transport mechanism. Considering a random variable X with PDF $P(X)$, where $P(X) \in [0, 1]$, the sampling mean and variance are [18]:

$$\bar{X} = \frac{1}{N} \sum_{i=1}^{N} X_i \tag{4.9}$$

$$\sigma^2 = \frac{1}{N} \sum_{i=1}^{N} (X_i - \bar{X})^2 \tag{4.10}$$

In addition, the standardized moments of the distribution are defined as:

$$m_k = \frac{1}{N} \sum_{i=1}^{N} \frac{(X_i - \bar{X})^k}{\sigma_X^k} \tag{4.11}$$

Where $\sigma_X^k = \sqrt{1/N \sum_{i=1}^{N} (X_i - \bar{X})^k}$, with k the degree of the distribution. Note that

from this definition, $m_1 = 0$ and $m_2 = 1$. The third and fourth moments correspond to the *skewness* and *kurtosis*, respectively.

4.3.2 Correlation function

Correlation is a technique that has been used in different areas of science, from engineer to financial. It measures the degree of linear dependence between two variables, without, however, provide any information regarding causality. The correlation between two time series, $x(t)$ and $y(t)$, is given by:

$$R_{xy}(t,\tau) = \int_{-\infty}^{\infty} y(t)x^*(t-\tau)dt \tag{4.12}$$

or equivalently

$$R_{xy}(t,\tau) \;=\; \langle y(t)x^*(t-\tau)\rangle$$

where τ is a time lag and the asterisk denotes the complex conjugate. It follows that the autocorrelation is simply,

$$R_x(\tau) = \int_{-\infty}^{\infty} x(t)x^*(t-\tau)dt = \langle x(t)x^*(t-\tau)\rangle \tag{4.13}$$

It is common to define a proper normalization for the auto and cross-correlation, in this case the sampling correlation in stationary condition is [137]:

$$C_{xy}(\tau) = \langle [x(t+\tau)-\bar{x})][y(t)-\bar{y})]\rangle \,/\sqrt{\langle [x(t)-\bar{x})]^2\rangle \,\langle [y(t)-\bar{y})]^2\rangle} \tag{4.14}$$

Where $\bar{x} = 1/N\sum_i^N x_i$ and $\bar{y} = 1/N\sum_i^N y_i$ are the mean sampling of the $x(t)$ and $y(t)$, respectively, with N the total number of points in the time series. Again, the auto-correlation can be obtained straightforwardly by substituting x to y or vice and versa. The correlation values is within the range: $-1 \leq C_{xy} \leq 1$, where 1 is for full

correlated signals and -1 is for anti-correlated signals. Note that $C_{xy} = 0$ indicates that the signals do not have a linear correlation, but they can still have some degree of non-linear relation. A different approach must be considered in this case (see chapter 6 section). The correlation time is a useful quantity in the study of turbulence and it is simply defined as the time delay at which the autocorrelation drops from $\tau = 0$ by a factor $1/e$. While the fast drop is typically related to stochastic processes [137], longer correlation time might indicate sustained memory phenomena [108] and self-similarity [40].

4.3.3 Cross power spectrum and coherence

The continuous Fourier transform of a signal represented by the function $x(t)$ is defined as:

$$X(f) = \frac{1}{\sqrt{2\pi}} \int_{-\infty}^{\infty} x(t) e^{2\pi i f t} dt \tag{4.15}$$

while the inverse transform is:

$$x(t) = \frac{1}{\sqrt{2\pi}} \int_{-\infty}^{\infty} X(f) e^{-2\pi i f t} dt \tag{4.16}$$

Considering a finite time interval, the Fourier transform in its discrete form is:

$$X = \frac{1}{\sqrt{N}} \sum_{n=1}^{N} f e^{2\pi i l n/N} \tag{4.17}$$

Where $f_l = l/(N\Delta t)$, with $l = -N/2, ..., N/2$ and Δt the time sampling. Some precautions must be carried out when one deal with a finite time interval, effects

like *leakage*, that yields an artificial enhancement in some frequency bins, can be minimized by applying a proper time window [200]. The power spectrum gives the power contribution for the signal at a given frequency bin. It can be directly defined from the Fourier transform:

$$P_x(f) = X(f)^* X(f) = |X(f)|^2 \tag{4.18}$$

The spectrogram is the running version of the power spectrum. It is calculated by subdividing a long time window of a given signal in time slices where the power spectrum is calculated in each step. Note that since the frequency resolution is related with the length of the time window, i.e. the larger is the time window the better the frequency resolution is, the spectrogram requires a relatively large time window to resolve monochromatic oscillations. Consequently, fast transient phenomenons are not well captured by spectrograms. Alternatively, the wavelet transform provides a better solution (see section 4.3.5).

Given two time series, $x(t)$ and $y(t)$, the cross-power spectrum between them is:

$$P_{xy}(f) = X(f)^* Y(f) \tag{4.19}$$

P_{xy} is typically a complex function, thus, it can also be represented by $P_{xy} = |P_{xy}|e^{i\alpha_{xy}}$, where $\alpha_{xy} = tan^{-1}\left[Im(P_{xy})/Re(P_{xy})\right]$, where Im and Re are for imaginary and real part, respectively, of the complex function P_{xy}. According to the Wiener-Khinchin theorem, the power spectrum is a Fourier pair of the correlation function (auto or cross), as long as the processes are stationary [137]. It follows that in this regime:

$$P_{xy}(f) = \int_{-\infty}^{\infty} R_{xy} e^{-2\pi f \tau} d\tau \tag{4.20}$$

where the auto power spectrum is obtained from the auto correlation function by substituting x to y or vice versa.

The coherence spectrum of two time series is defined from their auto and cross-power spectrum:

$$\gamma_{xy}(f) = \frac{|P_{xy}(f)|}{\sqrt{P_x(f)}\sqrt{P_y(f)}} \tag{4.21}$$

where $\gamma_{xy} \in [-1, 1]$.

Turbulent particle flux (Γ_r)

The growth of turbulence can eventually produce fluctuation quantities that in turns can generate transport, depending on the favourable phase relation between the transported quantity and the drive velocity. The turbulent particle flux in a give direction i can be defined as:

$$\tilde{\Gamma}_i = \langle \tilde{n}(t)\tilde{v_i}(t) \rangle \,, \tag{4.22}$$

where $\tilde{n}$ e $\tilde{v_i}$ are, respectively, the density and velocity fluctuation.

Drift wave or interchange type of instability can induce local charge polarization in the plasma that yields electric fields to compensate it. The drift caused by that is then:

$$\vec{v}_E = \frac{\vec{E} \times \vec{B}}{B^2} \tag{4.23}$$

It follows that the particle flux becomes,

$$\tilde{\Gamma}_k = \frac{< \tilde{n}(t)\tilde{E}_i(t) >}{\tilde{B}_j(t)}.$$

Keeping the radial component (since it is the one that impacts on the plasma confinement performance), the radial particle flux due to fluctuation is:

$$\tilde{\Gamma}_r = \frac{< \tilde{n}(t)\tilde{E}_\theta(t) >}{B_\phi}. \tag{4.24}$$

At this point, one can recognize the cross-correlation defined at $\tau = 0$,

$$\tilde{\Gamma}_r = \frac{1}{B_\phi} R_{nE_\theta}(\tau = 0).$$

In the stationary regime, the cross-correlation is a Fourier pair of the cross-power spectrum function,

$$\tilde{\Gamma}_r = \frac{1}{B_\phi} \int_{-\infty}^{\infty} df P_{nE_\theta}(f) = \frac{2}{B_\phi} \int_0^{\infty} df Re\{P_{nE_\theta}(f)\} \tag{4.25}$$

where $Re(...)$ is for the real part of the complex cross-power spectrum P_{nE_θ} function. The total flux is then:

$$\tilde{\Gamma}_r = \int_0^{\infty} df\ T(f) \tag{4.26}$$

where,

$$T(f) = \frac{2}{B_\phi} Re\{P_{nE_\theta}(f)\},\ f \geq 0, \tag{4.27}$$

$T(f)$ is the spectral contribution for the transport. Alternatively,

$$T(f) = \frac{2}{B_\phi} Re\{P_{nE_\theta}(f)\} = \frac{2}{B_\phi} |P_{nE_\theta}(f)| \cos \alpha_{nE}(f)$$

where by using the coherence function,

$$\gamma_{nE}(f) = \frac{|P_{nE}(f)|}{\sqrt{P_n(f)}\sqrt{P_E(f)}}$$

One can obtain,

$$T(f) = \frac{2}{B_\phi}\gamma_{nE_\theta}(f)\sqrt{P_n(f)}\sqrt{P_{E_\theta(f)}}\cos\alpha_{nE_\theta}(f) \tag{4.28}$$

where α_{nE_θ} denotes the phase delay between the density and the poloidal electric field fluctuation.

4.3.4 Wavenumber frequency spectrum - S(k,f)

Fluctuations in plasma typically have space and time dependency. However, in the practical situations is very difficult to measure the same quantity simultaneously and in a broad spatial range. Ideally, the joint wavenumber- frequency spectrum $S(k, j)$ is the desire fluctuating quantity when one wants to study fluctuations in a plasma. If one can assume that the fluctuations are described by a superposition of waves, a local $S(k, j)$ version can be deduced from signals of two spaced time series [217]. The 2-point correlation technique assumes a wave relation dispersion of $k = k(f)$, where $f = \omega/2\pi$. Considering two signals, $x(t)$ and $y(t)$, spaced (say) poloidally a distance d_θ. The spectral phase shift between the signals can be obtained from the cross-power spectrum, $\alpha_{xy} = tan^{-1}\left[Im(P_{xy})/Re(P_{xy})\right]$, where $P_{xy} = X(f)^*Y(f)$ is the power spectrum function. The wave number distribution is then:

$$k_\theta(f) = \frac{\alpha_{xy}(f)}{d_\theta} \tag{4.29}$$

where $|k_\theta| \leq \pi/d_\theta$ to avoid phase redundancy. Note that this restriction set the wavenumber resolution. The local wavenumber-frequency spectrum is defined as [17]:

$$S(k,f) = \left\langle \frac{1}{2}\left[X(f)^* X(f) + Y(f)^* Y(f)\right] \delta(k_\theta(f) - k_\theta) \right\rangle \tag{4.30}$$

where δ the delta function.

$S(k,f)$ is typically obtained by considering the contribution from several sub-time windows to enhance the robustness of the method, where the wavenumber contribution for a given frequency is collected as a histogram. Once the local $S(k,f)$ is known, one can obtain the frequency spectrum (S_f) and the wavenumber spectrum (S_k):

$$\begin{aligned} S_f(\omega) &= \textstyle\int_{-\infty}^{\infty} S(k,\omega)\frac{dk}{2\pi} \\ S_k(k) &= \textstyle\int_{-\infty}^{\infty} S(k,\omega)\frac{d\omega}{2\pi} \end{aligned} \tag{4.31}$$

In addition, the phase velocity is obtained by weight averaging all the possible phases by considering the corresponding $S(k,f)$ values:

$$\bar{v}^{ph} = \frac{\int\int(\omega/k)S(k,\omega)dkd\omega}{\int\int S(k,\omega)dkd\omega} \tag{4.32}$$

where $\omega/k \neq 0$.

4.3.5 Wavelet and local intermittency measurement (LIM)

The wavelet is a mathematical technique that allows to decompose a signal into time-frequency functions and, therefore, is a suitable technique to study fast transient events [47]. Fourier decomposition is based on oscillating sinusoidal functions that are naturally constrained by the uncertainty principle, $\Delta t \Delta f \geq 2\pi$. Therefore, fast intermittent events are represented in the Fourier space by the superposition of many waves with different frequencies, e.g. the Fourier transform of a delta function in the

real space is a constant in the Fourier space. Wavelet, on the other hand, offers a practical solution for this problem, permitting to well resolve oscillations.

The base element of the wavelet analysis is the mother wavelet:

$$\psi_{t_0,\tau}(t) = \frac{1}{\sqrt{\tau}}\psi\left(\frac{t-t_0}{\tau}\right) \tag{4.33}$$

where τ is the scale (dilation) parameter and t_0 the translation parameter. Given a signal $f(t)$, the continuous wavelet transform (CWT) is defined as:

$$W(\tau, t_0) = \frac{1}{\sqrt{\tau}}\int_{-\infty}^{+\infty}\psi\left(\frac{t-t_0}{\tau}\right)f(t)dt \tag{4.34}$$

where $f \in \mathrm{L}^2(\mathbb{R})$ and $\psi(t)$ is the mother wavelet.

The wavelet analysis depends on the type of the mother wavelet used, which in turns is conditioned by the peculiarity of the study signal. Among the most popular mother wavelets, one can find the Morlet, Paul, Shannon, and Gabor [47]. In this thesis, it was considered the Marr or 'Mexican Hat' as mother wavelet. The reason relies on the nature of the turbulent signals typically observed in the plasma edge of fusion devices [11], as will be discussed next. The 'Mexican Hat' function in real space is:

$$\psi_\tau(t) = \frac{1}{\pi^{1/4}\sqrt{3\tau}}\left(1-\frac{t^2}{\tau^2}\right)\exp\left(-\frac{t^2}{2\tau^2}\right) \tag{4.35}$$

where τ is the scale parameter. Fig. 4.11 shows the time representation of the 'Mexican Hat' wavelet function at different scaling parameter. Note that the largest τ yields a more dilated signal in the time axis, while the lowest one is represented by a more time localized signal.

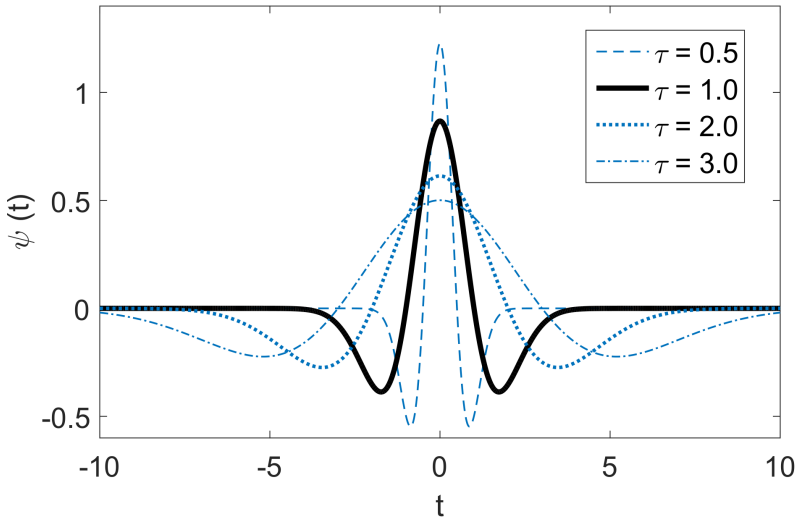

Figure 4.11: Mexican Hat function at different scale (τ).

The intermittent behaviour of turbulence in the edge of fusion devices trace of its non self-similar character [83]. Filaments emerge as structure much denser than the surrounding plasma, yielding a long PDF positive tail and large skewness. The deviation from Gaussian behaviour at different scale and time shift can be verified with the 'Local Intermittency Measure' (LIM) [73]:

$$l(\tau, t_0) = \frac{|W(\tau, t_0)|^2}{\langle |W(\tau, t_0)|^2 \rangle_{t_0}} \tag{4.36}$$

Where $\langle ... \rangle$ stands for time average over the translation parameter t_0. Deviations a pure Gaussian distribution start becoming relevant for: $l(\tau, t_0) > 1$. Besides, the flatness is defined defines as :

$$F(\tau) = \frac{\langle |W(\tau, t_0)| \rangle_{t_0}^4}{\langle |W(\tau, t_0)|^2 \rangle_{t_0}^2} \tag{4.37}$$

where pure Gaussian distribution exhibits flatness (or kurtosis) equal to 3.

Filaments can be detected unambiguously by combining the LIM with the flatness. Intermittent events at a given scale is defined as $l(\tau, t_0) > S(\tau)$, where $S(\tau)$

is the minimum threshold for which the selected ensemble of events departure from a distribution characterized by $F(\tau) = 3$, i.e. pure Gaussian. The process is done iteratively starting from a high $S(\tau)$ value that typically gives $F(\tau) > 3$. In addition, in order to avoid redundancy at a given scale, only the local maximum is considered.

4.3.6 Conditional average

Conditional sampling average is a statistical technique that has been used to characterize turbulent structures presented in fluids and plasmas [5, 132, 125]. Considering a signal $a(\mathbf{r}, t)$ measured at a certain position $\mathbf{r}$ over time t. The conditional sampling average is defined as:

$$\delta a = \langle a(\mathbf{r}, t) | b(\mathbf{r}', t') > b^* \rangle \tag{4.38}$$

where the brackets mean ensemble average and $b(\mathbf{r}', t')$ is a second signal measuring the same or a different quantity used as a reference and subjected to a condition b^* valid over the time sampling t'. Therefore, the conditional δa is performed in the time intervals corresponding to a trigger in the signal $b(\mathbf{r}, t)$. One can easily generalize equation 4.38 by adding time delays τ, i.e., $\delta a(\tau)$. Note that the reference signal can also be the conditional signal which is usually called auto-conditional average. This technique will be used in this thesis to characterize blobs in the chapters 7 and 8.

Chapter 5

Turbulence Spreading in the TJ-II stellarator

In this chapter, it is discussed the phenomenon of turbulence spreading and its role in setting and modifying the scrape-off layer (SOL) profiles in fusion devices. Owing to the importance of cross-field transport in determining the heat flux width in future fusion devices, the findings presented here can contribute to a better comprehension of the plasma nature in the edge and SOL.

5.1 Local mixing paradigm

In chapter 2, it has been discussed that the microinstabilities arise naturally in fusion devices, at different scale and location. The growth of instability is responsible for releasing free energy into the plasma that, in turns, is translated in fluctuating quantities, e.g. electric or magnetic field δE and δB, respectively, and then into a turbulent state. Turbulent fields are related to transport, either cross-field, where fluctuation is responsible for a net flux of particle and energy through $E \times B$ drift, or parallel (along the field lines), due to field line stochastization. The quasi-linear approach is the most simplified way to treat a system far from equilibrium. This refers to an

approximation where the fluxes are calculated considering the linear response of the fluctuating quantities, i.e. neglecting higher-order fluctuating terms [15]. More precisely [58], quasi-linear means that the mean distribution function ($\langle f \rangle$) of a system described by the Vlasov equation (Section 2.1) evolves slowly compared to the linear grow rate of an instability:

$$\frac{1}{\langle f \rangle} \frac{d \langle f \rangle}{dt} \ll \gamma_k \tag{5.1}$$

where $\gamma_k = \gamma_k(\langle f \rangle)$. The quasi-linear theory essentially deals with the slow depletion of the free energy by microinstabilities (resulting in turbulence) and the relaxation of $\langle f \rangle$ back to a marginally stable state. The common procedure following the quasi-linear approximation is [58]: (1) $\langle f \rangle$ is obtained from the Vlasov equation considering $f = \langle f \rangle + \delta f$, where δf is the perturbed probability function, from a given plasma initial condition; (2) the linear growth rate (γ_k) is found from the wave dispersion relation using the linear dialectic function, i.e. $\epsilon(k, \omega) = 0$; (3) the radial electric field energy is evolved ($\partial_t |E_k|^2 = 2\gamma_k |E_k|$) by plugging γ_k on it; (4) assuming linear response of δf, the diffusion coefficient ($D(|E_k|^2)$) is calculated considering the current (iteration) values of $|E_k|^2$; (5) $\langle f \rangle$ is evolved until $\gamma_k \to 0$ (the system becomes marginally stable). In the quasi-linear approach, fluctuations are $\omega = \omega(k)$ (i.e. eigenmode type), and, therefore, non-linear coupling is neglected; the saturation of the system happens by depletion of free energy source $\langle f \rangle$ for all modes.

A more general turbulence model takes into account the non-linear coupling between all modes that compose a system and the scale energy transfer between them, i.e. direct energy cascade - from bigger to small scales. This eventually leads to dissipation in the critical scale (Kolmogorov like dissipation scale [211]), where viscous damping becomes relevant, and then to the turbulence saturation. The nonlinear process occurs by nonlinear wave-wave and wave-particle interaction [58]. In addi-

tion, turbulence decorrelation by mean $E \times B$ sheared flow or fluctuating flow (see chapter 2), e.g. zonal flows [59], act as local saturation mechanism [21, 139], and so they must be included self-consistently in a more complete model.

According to the local mixing paradigm [58], turbulence is generated locally quasi-linearly and saturates as the result of the competition between linear growth (or damping) and nonlinear damping. This result is based on the Prandtl's mixing length hypothesis introduced in the context of pipe flow studies [211]. Gradients are sources of fluctuation (e.g. drift wave type of instability) that, in turns, try to reduce the gradient increasing the transport. The mixing length predicts that the local turbulence saturation happens when the growth rate of a gradient induced instability increases up to the gradient length since the induced modes try to mix (e.g. temperature hot and cold mix), causing the relaxation of the corresponding gradient (e.g. temperature profile becomes flat). By balancing the linear and non-linear terms in the density continuity equation for drift wave type of instability, one can demonstrate [58]:

$$\frac{\tilde{n}}{\langle n \rangle} \sim \frac{l_\perp}{L_n} \tag{5.2}$$

where $L_n = -n/\nabla n$ and $l_\perp$ is the mixing length. The previous formula provides an estimative for the saturation of the density fluctuation based on mixing length similar to the Prandtl's hypothesis. The free energy is assumed to be provided by the density gradient, but a similar approach can be done for the temperature gradient as well. A fair question would be, what is the nature of $l_\perp$? Typically $l_\perp$ is a complex function of nonlinear parameters and the intricate relation between damping and drive. While in the core $\tilde{n}/\langle n \rangle \ll 1$, so $l_\perp \ll L_n$, the correlation length of turbulent eddies is much smaller than the plasma extend size. In the edge and SOL one can often find $\tilde{n}/\langle n \rangle > 1$ which represents a broken of the local mixing length hypothesis, since turbulent structure becomes comparable to the plasma characteristic size (e.g.

gradient length) and so non-local interaction is expected to happen [30]. Indeed, the strong intermittency observed in the far SOL of fusion devices is an example of that [305]. In this case, non-local mixing models are required [282] and so a nonlocal length.

The diffusion coefficient related to drift-wave type of instability from the mixing length rule is $D = \gamma/k_\perp^2$ [134] (Kadomtsev 1965), where γ is the growth rate and $k_\perp$ is cross-field wavenumber of turbulence. The linear growth is balanced by diffusion at the length $\sim 1/k_\perp$. Typically, the correlation length (or turbulent cell size) is a few ion Larmor radii (ρ_i). However, in some cases mesoscale events, that is, scales that lie into the interval $\rho_i \ll l < a$, where a is the system size, might be important. Mesoscale phenomenons include transport barriers [28, 259], avalanching [193], streamers and blobs [63], zonal flows, and GAMs [85]. Long-range responses, faster than the diffusion response, i.e. before diffusive transport connects two separate plasma region have been observed experimentally [94, 164, 253]. They are clear examples of mesoscale or even macroscale events and, consequently, violate the local closure view [128] and the local mixing length hypothesis.

5.2 Turbulence Spreading

Turbulence spreading is the spatial-temporal propagation of turbulence from unstable to stable regions. Turbulence propagation is an intrinsic mesoscale phenomenon, and so turbulence spreading has been pointed out as a viable explanation for the break of the local closure schemes [128, 108]. The local growth of turbulence tends to be redistributed radially (nonlinear radial scattering) until being damped and then fades away. Global gyrokinetic simulation shows that turbulence can travel from its birth location a distance of about $25\rho_i$, while the eddy correlation length (from the two-point correlation analysis) is $\sim 7\rho_i$, that is, almost 4 times the correlation

length [157]. In addition, simulations have shown that the spreading extension does not depend on the system size ($\rho_* = a/\rho_i$) [157]. Clear evidence of spreading is the high level of transport found in regions of flat gradients, where linear instability should be absent or weak, above what would be expected from neoclassical theory [192, 138]. A direct consequence of this is that the local growth rate predicted from linear theory overestimates the actual fluctuations values obtained experimentally [120, 119, 213, 163, 49], while it underestimates in weakly linear drive regions [192, 250]. This ultimately results in a breakdown of the gyro-Bohm scaling and Fick's Law, since the local quasi-linear approach does not hold anymore and so the simple gradient-driven transport view [157, 108]. The majority of turbulent transport models rely on the local competition between linear growth rate and linear damping and nonlinear dissipation [109]. Typically, the diffusion coefficient is given by the gyro-Bohm scale according to the mixing length estimate, $D \sim (\rho_i/a)D_B$, where D_B for the Bohm scale, ρ_i is the ion Larmor radius, and a is a characteristic machine size. However, experimental results indicate that $D \sim (\rho_i/a)^{\alpha}D_B$, being α a constant usually found within the interval 0.6-0.7. The fundamental factor is the dynamics of mesoscale. Avalanching phenomenons together with turbulence spreading appear as a natural candidate for explaining this discrepancy since they are recognized as mesoscale events and so naturally yield a larger effective mixing length.

Earlier studies have shown that drift waves were able to mediate the propagation of turbulence from the core to external regions, acting as a source of edge fluctuation [172]. The larger fluctuation in the edge with respect to the core can be explained by the 'beach effect': fluctuations coming from the core looks stronger in the edge because the background density is lower. In addition, toroidal coupling was demonstrated by fluid simulations to be related to turbulence spreading by means of ballistic propagation of a turbulent front [90], while non-linear mode coupling induces diffu-

sion. These pioneer works pointed out for the importance of non-local effects on the turbulence dynamics and its potential impact on the plasma confinement predictions.

Plenty evidence of turbulence spreading has been gathered from global nonlinear gyrokinetic simulations over the last years [255, 204, 141, 156, 157, 154], with turbulence profile extending beyond the driven region, up to several times the local turbulent correlation length. Motivated by gyro-kinetic simulation, *R. E. Waltz and J. Candy* [282] have proposed a heuristic model to account for the break of gyro-Bohm scaling. The model incorporates an effective non-local linear growth rate that successfully describes the observed turbulent behaviour, with intensity drainage in strongly driven regions and turbulence enhancement in weakly driven regions. While in unstable regions non-local effects push towards Bohm scaling (i.e. breaking the gyro-Bohm), in stable (or less unstable) the breaking leads to super-gyro-Bohm since the local increase of fluctuation by non-local channels yields a larger local transport. *T. S Hahm et al.* [109] have proposed a simple reaction-diffusion nonlinear model to explain the radial propagation of turbulence. The local turbulence intensity $I \equiv \langle (e\phi/T_e)^2 \rangle$, spatial-temporal dependent, evolves under the influence of a local linear growth rate and damping ($\gamma(x)$, where positive stands for growth and negative for damping) as well as non-linear spatial interactions that leads to dissipation and scattering of turbulence energy:

$$\frac{\partial I}{\partial t} = \frac{\partial}{\partial x}\left(\chi \frac{\partial I}{\partial x}\right) + \gamma(x) I - \alpha_{NL} I^{1+\beta} \tag{5.3}$$

where $\chi = \chi_0 I^{\beta}$ is a turbulent effective diffusion coefficient, α_{NL} is a nonlinear coupling parameter, and $\beta = 1$ for weak turbulence. An equavalent equation was derived using Fokker-Planck theory [106], which includes an effective radial convective term with the fluctuation radial group velocity (v_{gr}). It follows that an equivalent of equation 5.3 in a compact form is:

$$\frac{\partial I}{\partial t} + \frac{\partial \Gamma_I}{\partial x} = S_I \tag{5.4}$$

where in this case,

$$\Gamma_I = v_{gr} I - \chi_0 I^\beta \frac{\partial I}{\partial x} \tag{5.5}$$

$$S_I = [\gamma(x) - \alpha_{NL} I^\beta] I \tag{5.6}$$

Here S_I represents a local sink and source and Γ_I the flux of the turbulence intensity composed by a convective term (first on the RHS) and a nonlinear diffusion term (second on the RHS), a Fick's law equivalent for intensity flux. The model can be extended by including explicit dependence on zonal or mean $E \times B$ flows on $\gamma(x)$, which acts as a saturation mechanism by feeding back on I. A remarkable result from the equation 5.3 is the possible turbulent patch penetration into locally stable or even damped regions. In this situation, a fluctuation front solution can be found by neglecting the second and third term RHS of Eq. 5.3 [109]. Although these simplifications are not realistic, the result highlights the role of the first term RHS of Eq. 5.3 in scattering turbulence spatially. The turbulent front eventually stops when local dissipation becomes comparable to the rate by which fluctuation is scattered into there (intensity influx by spreading exceeds the rate of local growth). Considering the influence of γ and α_{NL}, equation 5.3 becomes similar to the well known Fisher-Kolmogorov-Petrovskii-Piskunov equation [106]. In this case, numerical solution supported by semi-analytical results indicate that after the local turbulence amplitude saturates ($I = \gamma/\alpha_{NL}$), due to damping and non-linear coupling, the turbulence propagates ballistically with velocity $v = (2\gamma\chi)^{1/2}$, where energy diffusion coefficient is $\chi(x) \propto I(x)$ for weak turbulence.

The role of non-linear coupling and spatial scattering are nicely represented in Fig. 5.1. While big radial elongated structures are formed through inverse cascade process through kinetic energy transfer, internal energy tends to scatter to small scales up to the critical scale, where viscosity dissipation becomes important. The forward cascade then generates turbulence spreading until the local damping overcomes the non-linear transfer of energy. The model [105] considers similar diffusion-reaction equations 5.4, 5.5, and 5.6 for the internal and kinetic energy in the framework of Hasegawa-Wakatani approach. However, different from [109] that treats turbulent energy as single field, in this 'Two Field Model' both kinetic ($\sim \langle \nabla \phi^2 \rangle$) and internal energy ($\langle \langle (\tilde{n}/n_0)^2 \rangle \rangle$) are considered self-consistently. It is worth note that this picture is analogous to what is usually observed in the edge of fusion devices, where streamers (radially elongated structures) are broken into blobs that then travel into the SOL [195] (stable region!). *V. Naulin et al.* [190] have proposed a model that couples the turbulence spreading equation for the turbulent energy (reaction-diffusion type) with a transport equation for the mean density ($\langle n \rangle$), where, by comparing with a 2D interchange model, they pointed to the role of convective blob-like structure as agent of spreading.

The radial propagation of turbulence has been shown to slow down or even completely blocked by negative magnetic shear [294], while parallel flow shear can enhance the effect [295]. These results highlight the impact of magnetic shear in decoupling the core from turbulence coming from the edge, being the internal transport barrier (ITB) a limit case of this phenomenon [295]. The $E \times B$ shear flow, on the other hand, is a well known mechanism for stabilizing turbulence locally [259], inhibiting the local grow of turbulence [28], decorrelating turbulent cells [21], and tearing apart blobs [24]. Global gyrokinetic simulations in tokamak geometry has addressed the effect of transport barriers on turbulence spreading [285]. For this purpose, a transport barrier was placed close to the linear unstable zone (Fig. 5.2). The strength of

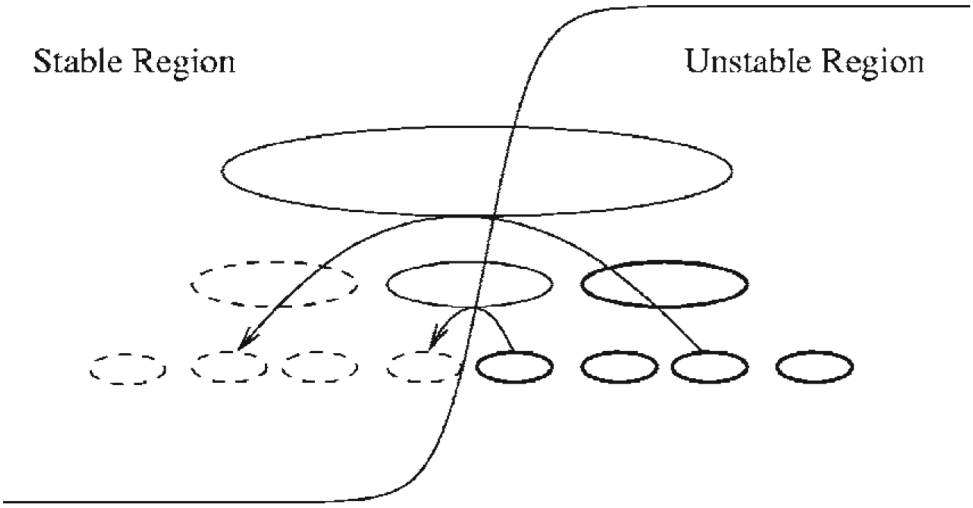

Figure 5.1: While the inverse cascade of the kinetic energy tends to concentrate in elongated cells, the forward cascade of the internal energy spreads radially easily, being damped later in the stable regions [105].

the $E \times B$ shearing rate was varied by externally modifying the radial electric profile. They have considered three configurations (Fig. 5.2, bottom), a flat profile (black), a mild well (blue), and a deep well (red). Turbulence was generated by the ion temperature gradient (ITG) instability, where its intensity was defined as $\langle \delta\phi^2 \rangle$, with the brackets meaning zonal average for steady-state fluctuation. The results show strong turbulence penetration in the linear stable zone in the absence of the transport barrier, where non-linear coupling eventually leads to turbulence saturation. In the non-negligible shear case, turbulence propagation becomes restricted, thus, reducing its penetration into the unstable zone. By increasing the shear further, the propagation is virtually quenched. In this case, the turbulence radial extension can be determined by local mixing rules. These simulations highlight an important property of transport barriers: their ability in radially decoupling turbulence. Similar results are found elsewhere [20].

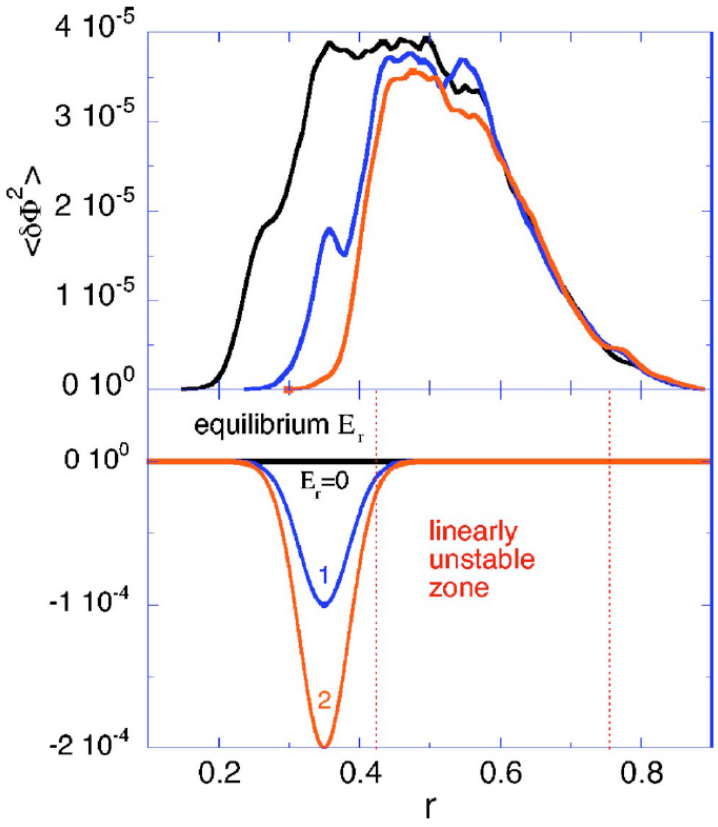

Figure 5.2: Gyrokinetic simulation showing (top) turbulence amplitude ($\langle \delta\phi^2 \rangle$) extending radially around the linear unstable zone, where ion temperature gradient (ITG) instability dominates. Three artificial radial electric field equilibrium profiles are imposed (bottom). The corresponding effect of the three cases on turbulence penetration shows that the deeper the radial electric well (or the $E \times B$ shear strength, $\omega_E \propto dE_r/dr$) the weaker is the turbulence penetration into the linearly stable zone [285].

Turbulence spreading has been observed to increase in the proximity of magnetic islands [127]. Typically, the electron temperature and density profiles are flat inside an island (in the O-point) due to the dominant parallel transport along the reconnected field lines [191]. Hence, this region is thought to be linearly stable since there is no free energy to feed instabilities. However, turbulence propagation into the O-point has been observed in simulations [210] with ballistic propagation. Non-linear mode coupling inside the island enhances the large scales energy, while reduces the energy content of small scales (microinstabilities). This results in a rise of the local ion

thermal diffusion coefficient around the island and flux surface breaking, leading to spreading [130].

Understanding the role of zonal flows and Geodesic Acoustic Mode (GAM) in the propagation of turbulence can be challenging since they are inherently coupled with turbulence [85]. Studies of the relation of turbulence spreading and zonal flows [44] have suggested that the latter is responsible for the growth of spreading. However, *Ö.D. Gürcan et al* [105] have shown that zonal flows, although connected with spreading, is not the principal agent of turbulence propagation. Alternatively, radial envelope solitons solution (traveling as a coherent structure) was shown to be able to enhance spreading. The result was obtained in a two-field drift wave zonal flow model (DW-ZF) in slab geometry [104]. While zonal flows can suppress turbulence spreading rather than generates it (this remains a discussion), GAM seems to directly mediate spreading [180].

Lastly, the modern view tends to treat turbulence spreading and avalanching as connected phenomenons, although they are conceptually different [108]. While turbulence spreading refers to turbulent front propagation, this effect happens naturally as a result of an avalanching (i.e. avalanching induces spreading). They are the most prominent approaches in dealing with non-local transport towards a more extensive global model. Avalanching is a non-linear spatial coupling phenomenon, where gradient toppling connects space-separated regions, making the transport scale-independent with typically power-law flux spectrum ($\sim 1/f$). The concept emerges from the self-organized critically (SOC) theory [14] as explosive relaxation that allows the system to return to a self-organized state by generating transient flux (intermittency). SOC transport models have the advantage of not relying on the properties of local instability to generate fluctuations, so they are more general and fundamental approaches.

5.3 Experimental observations of turbulence spreading

As mentioned before, the concept of turbulence spreading in magnetically confined plasma arises from the empirical evidence of the presence fluctuations in linear stable zones and the breakdown of Fickian local transport that ties gradient and flux. Non local effects have been observed in perturbative experiments: by laser ablation [94], pellet [164], and supersonic molecular beam injection (SMBI) [253] in the plasma periphery. The common feature of these experiments is an increase of the temperature in the plasma core and a decrease in the edge, with non-perturbed intermediate zone. The phenomenon was interpreted as non-local, since local models based on thermodynamic approach (i.e. the transport coefficients depend on the local thermodynamic variables) was not able to explain the global plasma changed observed, with higher thermal diffusivity in the edge and lower in the core. The large temperature gradient in the core was interpreted as an internal transport barrier-like phenomenon that decouples turbulence from the core to the edge and vice versa. Similarly, the phenomenon was also observed in LHD [129], suggesting that it is a more general feature of magnetized plasma rather than an exclusive tokamak property [164]. The effect was observed to nearly cease completely once the electron density rises beyond a critical limit [253]. It should be noticed that the local transport can be non-diffusive (e.g. convective), as well as non-local diffusive and non-local non-diffusive. Local here means that the transport (particle, momentum or energy) can be determined by local plasma parameters. The rise of the temperature in the core that follows the external perturbation in the plasma periphery is usually understood as a non-local diffusive phenomenon since the changes in the core happens faster than any local model can predict [128]. This result suggests that mesoscale and even macro-scales events might

be involved. Simulations considering a reaction-diffusion type model have shown that turbulence spreading can explain this effect [110].

Another evidence of turbulence spreading is shown in Fig. 5.3. The density relative fluctuation ($\tilde{n}/n$) measured by reflectometry is compared with linear growth rate predictions from a local microinstability code [192]. The experiment indicates that fluctuations and anomalous transport appear in stable regions. Fig. 5.3 (b) shows the density profile for a plasma with an internal transport barrier. One can see that even in this case, fluctuations are found in the inner zone of the barrier, where microinstabilities are linearly stable. These results show that the local mixing paradigm that usually assumes that the turbulence correlation length is shorter than the density or temperature gradient is not suitable here.

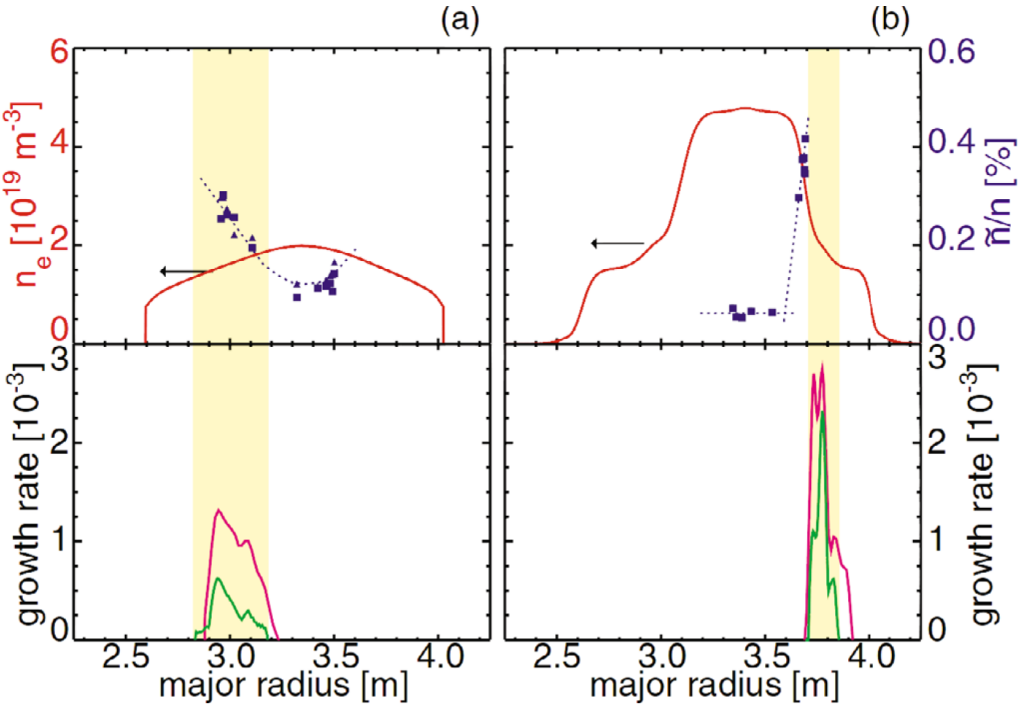

Figure 5.3: Density profile (red) and relative fluctuation (blue) from microwave reflectometer measurements in regular (a) and in the internal transport barrier plasmas (b) in reversed shear plasma in the JT-60U tokamak. On bottom, (c) and (d), are shown the linear growth rate predictions from the *FULL* code for both scenarios, respectively, with (green) and without (purple) $E \times B$ shear effects [192].

Experimental evidence of turbulence spreading in the proximity of transport barrier has been observed in TJ-II during spontaneous L-H transition [72]. Density fluctuations measured with Doppler reflectometry around a transport barrier has been shown to increase prior to the H-L back transition and barrier collapse, mainly in the regions where the shear was not so intense. This increase was almost synchronized with the relaxation of the shear layer, re-forcing the role of $E \times B$ in blocking turbulence spreading [285]. Another piece of evidence of spreading and transport barrier has been reported in DIII-D during the L-H transition [174]. Density fluctuation measured with Beam Emission Spectroscopy (BES) at the core reduces faster than the transition time. This result points out to the core-edge turbulence coupling and the role of sheared layers in cutting the non-local turbulence channel.

Spreading through magnetic islands has been observed in KSTAR from the X-point to the O-point when temperature gradient and fluctuation exceed a limit. In the opposite direction, if the limit is not overcome a convective cell around the O-point prevents cross-field transport into the center of the island [46]. Turbulence propagation ($\tilde{n}$) from the island X-point to the O-point has been observed to be faster than thermal diffusion in external ECH modulated experiments performed in DIII-D [127]. Density fluctuation was measured using Beam Emission Spectroscopy (BES), while the temperature was measured with Electron Cyclotron Emission (ECE). This effect might be particularly relevant for divertor configuration in stellarators, where magnetic islands are employed [206].

Turbulence is strong in the SOL even though profiles are usually flat, thus linear stabilities are expected to be weak. Therefore, turbulence spreading and edge-SOL coupling are natural and expected phenomenons in fusion devices. The SOL has some peculiarity which distinguishes it from other regions of plasma, namely the open field lines set a channel for energy dissipation along the field lines up to the wall (sheath dissipation). This region is usually dominated by blobs or turbulent filaments, pres-

sure structure larger than the surrounding plasma and aligned to the magnetic field (see chapter 3). Local polarization generated by interchange instability produces a potential structure (usually dipole) that propels the blob radially outward. As pointed out [166], blobs are the main candidates for being the 'agent' of turbulence spreading and edge-SOL coupling. Some preliminary analysis has shown that their dynamics are the main source of turbulence in the far SOL (by means of turbulence spreading) [201]. Global turbulence simulation, coupling the physics of the edge and SOL, have indicated the leader role of turbulence spreading [43, 154], from the pedestal to the SOL region, and how this effect can be crucial to set the SOL width in future fusion reactors [42, 154]. In TJ-II, the role of spreading and local turbulence drive was widely explored in different plasma regime and varied background shear [103]. Those results are the main subject of the next sections.

5.4 Edge-SOL model for Turbulence Spreading

A model for turbulence spreading in the edge and SOL was proposed by *P. Manz et al.* [166]. Based on $K-\epsilon$ type of model [211], the time evolution of the mean background ($\langle n \rangle^2$) and turbulent free energy ($\langle \tilde{n}^2 \rangle$) are derived, where they are shown to be coupled by a background-turbulence energy exchange term. Starting from the density continuity equation:

$$\frac{\partial n}{\partial t} + \nabla.(n\mathbf{v}) = S_n \tag{5.7}$$

where v is the fluid velocity and S_n the density source. Neglecting S_n and considering incompressible plasma in the cross-filed plane ($\nabla.\mathbf{v}_\perp = 0$), the radial part of the continuity equation, assuming that density variation in the bi-normal direction is negligible, becomes:

$$\frac{\partial n}{\partial t} = -v_r \frac{\partial n}{\partial r} \tag{5.8}$$

Considering now that the density can be written in terms of the its mean and fluctuating part, $n = \langle n \rangle + \tilde{n}$, where $\langle ... \rangle = \int dSdt$ is the zonal and time average, and the background flow velocity is negligible ($\langle v_r \rangle = 0$), it follows that the time evolution of the mean density is:

$$\frac{\partial \langle n \rangle}{\partial t} = -\left\langle \tilde{v}_r \frac{\partial \tilde{n}}{\partial r} \right\rangle = -\frac{\partial}{\partial r} \langle \tilde{v}_r \tilde{n} \rangle \tag{5.9}$$

where one can recognize $\Gamma_r = \langle \tilde{v}_r \tilde{n} \rangle$, the radial turbulent particle flux. The time evolution of the background flow energy $\left(\frac{1}{2} \frac{\partial \langle n \rangle^2}{\partial t} = \langle n \rangle \frac{\partial \langle n \rangle}{\partial t} \right)$, considering the previous expression is easy obtained:

$$\frac{1}{2} \frac{\partial \langle n \rangle^2}{\partial t} = -\langle n \rangle \frac{\partial}{\partial r} \langle \tilde{v}_r \tilde{n} \rangle = -\frac{\partial}{\partial r} \left[\langle n \rangle \langle \tilde{v}_r \tilde{n} \rangle \right] + \left\langle \frac{\partial n}{\partial r} \right\rangle \langle \tilde{v}_r \tilde{n} \rangle \tag{5.10}$$

Analogously, the evolution of the total energy $\left(\frac{1}{2} \frac{\partial [\tilde{n} + \langle n \rangle]^2}{\partial t} \right)$ is given by:

$$\begin{aligned} &\tfrac{1}{2} \tfrac{\partial \left\langle [\tilde{n} + \langle n \rangle]^2 \right\rangle}{\partial t} = -\left\langle [\langle n \rangle + \tilde{n}] \tilde{v}_r \tfrac{\partial}{\partial r} [\langle n \rangle + \tilde{n}] \right\rangle = \\ &-\langle n \rangle \tfrac{\partial}{\partial r} \langle \tilde{v}_r \tilde{n} \rangle - \left\langle \tfrac{\partial n}{\partial r} \right\rangle \langle \tilde{v}_r \tilde{n} \rangle - \left\langle \tilde{n} \tilde{v}_r \tfrac{\partial \tilde{n}}{\partial r} \right\rangle \end{aligned} \tag{5.11}$$

Where the evolution of the turbulent energy is found by subtracting Eq. 5.10 in Eq. 5.11:

$$\frac{\partial}{\partial t} \langle \tilde{n}^2 \rangle = -\left\langle \frac{\partial n}{\partial r} \right\rangle \langle \tilde{v}_r \tilde{n} \rangle - \left\langle \tilde{v}_r \tilde{n} \frac{\partial \tilde{n}}{\partial r} \right\rangle \tag{5.12}$$

Alternatively, considering: $\partial_r \langle \tilde{v}_r \tilde{n}^2 \rangle = 2 \langle \tilde{v}_r \tilde{n} \partial_r \tilde{n} \rangle$, it follows that:

$$\frac{\partial}{\partial t} \langle \tilde{n}^2 \rangle = - \left\langle \frac{\partial n}{\partial r} \right\rangle \langle \tilde{v}_r \tilde{n} \rangle - \frac{\partial}{\partial r} \langle \tilde{v}_r \tilde{n}^2 \rangle \tag{5.13}$$

In the paper by *P. Manz et al.* [166], they defined two convenient parameters based on Eq. 5.12. The rate of turbulence drive by the background (ω_D) is obtained from the first term RHS of 5.12 normalised by the local turbulence energy ($\tilde{n}^2$):

$$\omega_D = - \frac{2 \langle \frac{\partial n}{\partial r} \rangle \langle \tilde{v}_r \tilde{n} \rangle}{\langle \tilde{n}^2 \rangle} \tag{5.14}$$

Note that this term appears in the background energy equation with opposite sign, suggesting that this an exchange or transfer term between the two fields. The rate of turbulence spreading (ω_S) is defined from the second term RHS (Eq. 5.12), again normalized by the local turbulence energy:

$$\omega_S = - \frac{\frac{\partial}{\partial r} \langle \tilde{v}_r \tilde{n}^2 \rangle}{\langle \tilde{n}^2 \rangle} \tag{5.15}$$

At this point, it is natural to compare the equations 5.4 and 5.12 (reaction-diffusion model). Assuming that $I = \langle \tilde{n}^2 \rangle / 2$ and considering weak turbulence ($\beta = 1$), it follows that $\gamma_L = - \frac{2 \langle \frac{\partial n}{\partial r} \rangle \langle \tilde{v}_r \tilde{n} \rangle}{\langle \tilde{n}^2 \rangle} = I \omega_D$ and $\Gamma_I = 2 I \omega_S$, where it is neglected the linear and non-linear dissipation as well as the diffusion of the turbulence energy (which are indeed the assumptions of the model [166]). One can argue that, although dissipation is not included explicitly, it likely acts on ω_D, e.g. by inhibiting the local growth of turbulence in the light of decorrelation model [28]. In addition, turbulence propagation has been observed in simulations to be blocked by $E \times B$ shear flow [285] and by magnetic shear and toroidal flow shear [295], which in this case would act on

ω_S. The diffusion term is likely important in the edge where most of the instabilities are driven and so $\partial I/\partial x$ can be important (i.e. the radial gradient of turbulent energy in the vicinity of a strongly driven zone towards a weaker driven region is, likely, not negligible).

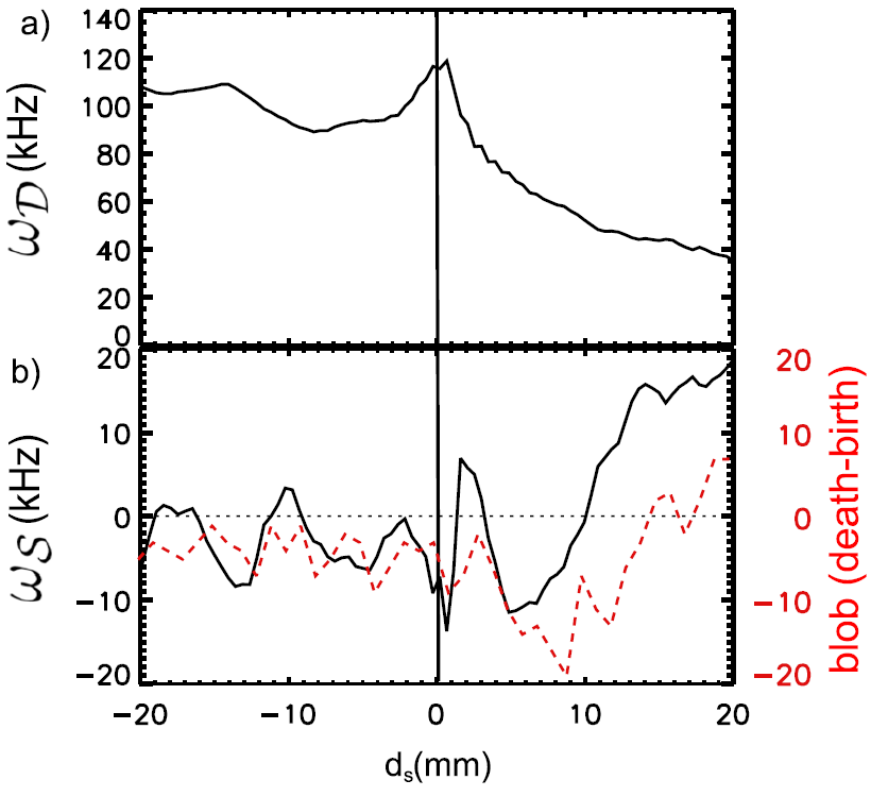

Figure 5.4: Radial profile of the rate of turbulence drive by the background gradient (ω_D) and turbulence spreading (ω_S), the latter compared to the blob death-birth rate (red curve). Results obtained self-consistently using the GEMR code [166].

The model was confronted with simulations carried out with GEMR [227], a three-dimensional gyrofluid turbulence code, where blobs are generated self-consistently. Interchange and drift waves instabilities are included in an ASDEX-Upgrade configuration. The SOL region was modeled by considering a proper current closure scheme based on perturbed Debye sheath current to take into account the effect of Conduct Wall Instabilities (CWI), which might no be negligible in ASDEX-Upgrade. Besides, the model considers finite ion temperature as well as the impact of the background,

such as shear flows (mean, zonal flows and GAM) and electromagnetic effects. In the ref. [166], they compared blob dynamics with a self-consistent calculation of ω_D and ω_S. While most of the blobs are generated in the vicinity of the $E \times B$ shear layer, the vast majority disappear in the far SOL. The blob death-birth trend resembles the turbulence spreading rate profile (Fig. 5.4), suggesting a link between them. The effective linear growth rate of turbulence represented by the ω_D parameter is higher in the edge and lower in the SOL, compatible with the density gradient variations. On the other hand, ω_S is mainly activated in the SOL, highlighting the role of spreading as a source of turbulence in this region. An interesting output of the simulations is seen in Fig. 5.4, where ω_S and ω_D become comparable in the far SOL, which strongly suggests that turbulence spreading is the dominant source of fluctuation in this location and the blobs are the main responsible for 'carrying' turbulence up to there. A drawback of this model, as discussed previously, is to neglect the turbulence diffusivity term. As discussed in section 5.2, the non-linear spatial scattering term can produce ballistic turbulence propagation into the stable zone where linear and non-linear dissipation is stronger [109, 106]. Therefore, this term is able to enhance the radial propagation of turbulence, especially close to LCFS where the gradient of fluctuation is expected to be larger.

5.5 Turbulence Spreading in the TJ-II

In this section, it is reported measurements of turbulence drive and spreading in the edge region and scrape-off layer (SOL) of the TJ-II stellarator for plasmas heated by electron cyclotron resonance heating (ECRH) and neutral beam injectors (NBI). The turbulence spreading rate (ω_S) and the rate of turbulence drive (ω_D) from the edge to the SOL were measured with a set of electrostatic probes following the technique introduced by *P. Manz et al.* [166]. In addition, it is shown how an external modulated

biasing can actively modifying those parameters and other plasma relevant quantities. These findings are reported elsewhere [103].

The experiment discussed here was carried out in TJ-II standard configuration (see chapter 4), i.e. with edge rotational transform n/m = 8/5 at $\rho \simeq 0.8$, where $\rho = \sqrt{\psi_N}$ with $\psi_N = \psi/\psi_{LCFS}$ (ψ_N - normalized magnetic flux and ψ_{LCFS} - flux at the LCFS). Hydrogen plasma was initially heated by two ECRH and sustained later by NBI co-injection. The total ECRH power delivered was $P_{ECRH} \leq 200$ kW at frequency of 53.2 GHz (X-mode), while the NBI power was $P_{ECRH} \leq 500$ kW. The switch of heating is characterized by a changed of the central line averaged density from about 0.6×10^{19} m^{-3} to 1.0×10^{19} m^{-3} (Fig. 5.5) while the central electron temperature was in the range $300 < T_e(0) < 400$ eV. In addition, an electrode biased placed in TJ-II periphery was used to modulate the edge radial electric field. Fig. 5.5, right side, shows a reference shot where a square 40 Hz biasing was applied at $r/a \approx 0.88$. Note that the modulation of the H_α only occurs during the NBI phase, suggesting an impact on the radial particle transport. The biasing scenario will be discussed in the section 5.5.2.

The plasma edge in this experiment was monitored with the probe D (Fig. 5.6). This probe is composed of a two-dimension array of electrostatic sensors (5×4), with five rows radially displaced $\sim$ 5 mm, 4 tips each, having a mutual bi-normal separation of $\sim$ 3 mm. The probe was configured to measure floating potential (ϕ_f) and ion saturation current (I_s) with three working tips in each row set as: [ϕ_f, I_s, ϕ_f]. Signals were acquired at 2 MHz. With this configuration, it is possible to estimate the radial turbulent particle flux, $\Gamma_r \simeq \langle \tilde{n}_e \tilde{v}_r \rangle \propto \langle \tilde{I}_s \tilde{E}_\theta \rangle / B$, where the brackets mean time averaging. Note that it was considered $\tilde{v}_r = \tilde{E}_\theta / B$, i.e. the radial projection of the $E \times B$ drift. The fluctuating poloidal electric field is approximated by $\tilde{E}_\theta \approx -\Delta\tilde{\phi}_f / \Delta\theta$, where the electron temperature fluctuation was neglected and $\Delta\theta$ is the tips poloidal separation. In addition, the effective radial velocity was

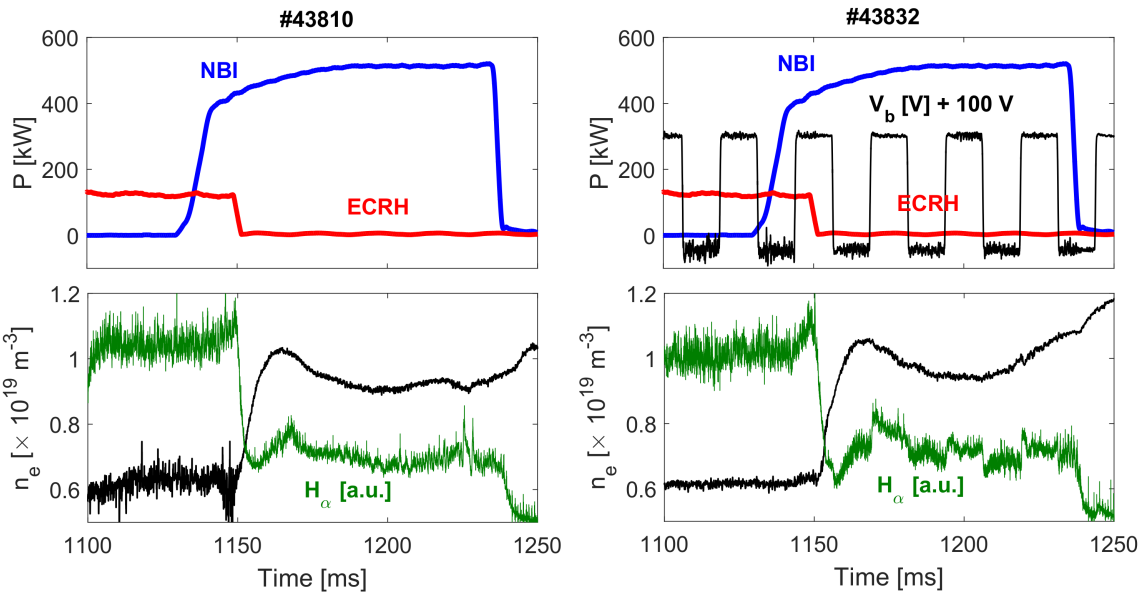

Figure 5.5: Two plasma scenarios considered in this experiment. On the left: plasma heating power in arbitrary units (top) and line averaged density and H_α (bottom) during the transition from ECRH to NBI. On the right: similar plasma scenario, but with an external square wave biasing applied in the TJ-II periphery.

defined as $v_r^{\text{eff}} = \langle \tilde{I}_s \tilde{E}_\theta \rangle / I_s B$. This a convenient manner to investigate the statistical properties of the particle radial propagation in the edge and SOL, since it is not affected by uncertainties in the probe area. The turbulence phase velocity in the bi-normal direction ($\approx$ poloidal direction) was obtained from the two-point correlation technique [217], considering two poloidally spaced floating potential signals. The technique is explained in detail in chapter 4. The experimental configuration permits to compute both the turbulence spreading rate (ω_S) and the local effective turbulence growth rate (ω_D). Again, neglecting the electron temperature fluctuation, one obtains $\omega_D \simeq -2\langle \partial I_s/\partial r \rangle \langle \tilde{E}_\theta \tilde{I}_s \rangle / (B_T \langle \tilde{I}_s^2 \rangle)$ and $\omega_S = -\partial/\partial r \langle \tilde{E}_\theta \tilde{I}_s^2 \rangle / (B_T \langle \tilde{I}_s^2 \rangle)$. Therefore, to obtain ω_D and ω_S it is necessary the simultaneous measurement of $\tilde{I}_s$ and $\tilde{E}_\theta$ at least two radial separated positions, apart from the mean value of I_s. The radial derivative is approximated by first order divided difference, i.e. $df/dx \approx (f(x_1) - f(x_0))/(x_1 - x_0)$.

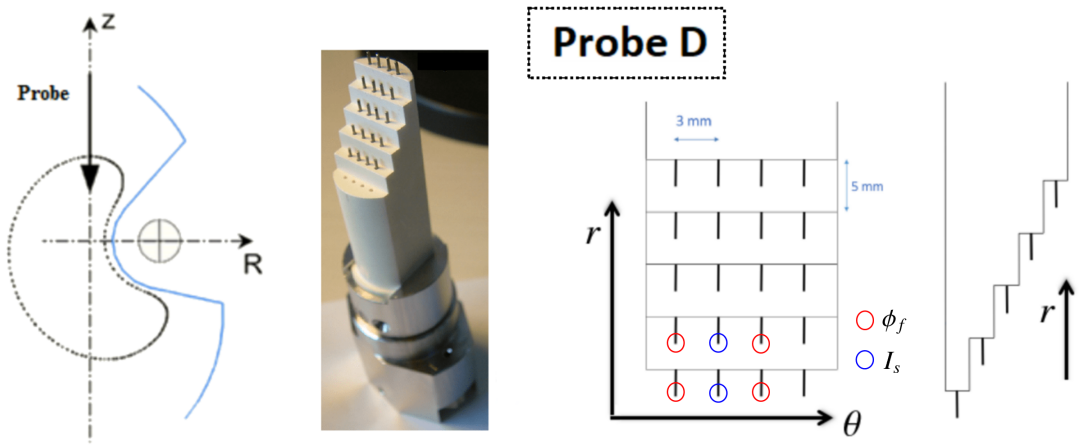

Figure 5.6: Probe D inserted from the top of TJ-II.

The radial profiles of the mentioned plasma parameters were obtained in a shot by shot basis, owing to TJ-II good reproducibility. Global parameters were kept approximately steady far from the heating overlap (Fig. 5.5, left).

5.5.1 Electron to the ion root transition

Different from tokamak, the ambipolar condition for the neoclassical electron and ion particle fluxes (i.e. $\Gamma_e = \Gamma_i$) imposes in stellarators specific radial electric field solutions [274]. While for the so-called electron root solution the radial electric field is negative ($E_r < 0$), for the ion root, the ambipolar condition imposes a positive radial electric field solution ($E_r > 0$). The electron to the ion root transition typically happens when the neoclassical viscosity increases above a certain limit. The effect is described by neoclassical theory, where one can show that the transition happens spontaneously when density increases above a critical value [275]. In TJ-II, a global potential signal is observed when the plasma heating is switched from ECRH to NBI or/and when the line average density overcomes a limit [177]. As a consequence of that, the energy confinament time increases [13], likely because of the establishment of a stepper radial electric field profile in the plasma boundary [275], resulting into a $E \times B$ shear layer and turbulence suppression [103].

Figure 5.7 shows the spatial-temporal evolution of some plasma quantities: a) floating potential (ϕ_f), ion saturation current (I_s), radial turbulent particle flux (Γ_r) and the projection of the turbulence phase velocity in the poloidal direction ($v_\theta^{\rm ph}$) when plasma heating was switched from ECRH to NBI. The profiles were built considering data from eleven shots, where the probe was moved from the SOL to the edge in a shot by shot basis. The signals were time-averaged in 2 ms time slices. The results presented in Fig. 5.7 shows how fast is the modification in the plasma edge induced by the electron-ion root transition when NBI is switched on. The change of the plasma potential (Fig. 5.7 a), ion saturation current (Fig. 5.7 b), and particle flux (Fig. 5.7 c) happen in a comparable time scale, while the poloidal phase velocity shear becomes stronger slightly later. This might be related to the enhancement of the background flow by the diamagnetic drift once the pressure gradient becomes further steeper. The floating potential (ϕ_f) changes signal in the edge ($r - r_0 \leq 0$), becoming less negative, while the scrape-off layer values do not change significantly (Fig. 5.7 a). The profile is roughly flat in the ECRH phase, but becomes steeper during NBI, with higher positive gradient near the edge. The transition is also followed by an enhancement of the poloidal phase velocity absolute value (Fig. 5.7 d), resulting in a shear layer in the near edge. Concomitantly, the turbulent particle flux decreases (Fig. 5.7 c) in the edge, roughly around the shear layer (in agreement with turbulence decorrelation by sheared flow [28]), but also further outside in the SOL. In addition, the ion saturation current slightly decreases in the edge and SOL.

Figure 5.8 displays time averages, ECRH ($1100 - 1140$ ms) and NBI ($1180 - 1220$ ms), of the parameters shown in Fig. 5.7 and a few other quantities. One can see here that the ϕ_f profile becomes steeper in the edge, while I_s SOL baseline drops during NBI with respect to ECRH, with a longer 'tail' that extends to the far SOL. The effective radial velocity supports this result, v_r^{eff} increases stronger in the SOL during ECRH, suggesting that turbulence structures penetrate easier during this phase.

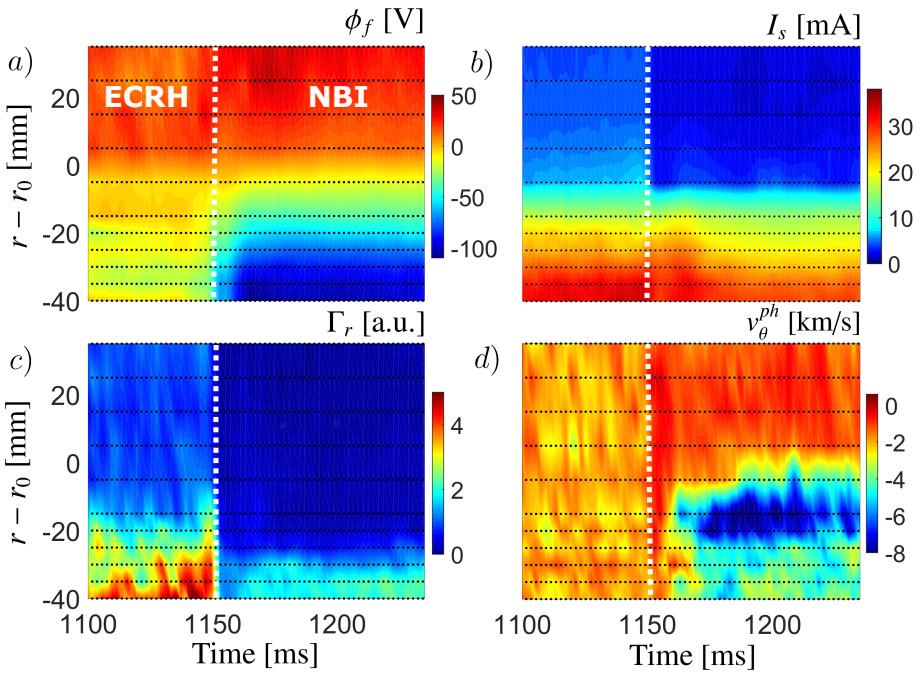

Figure 5.7: Transition from ECRH to NBI; a) the radial profile of floating potential, b) ion saturation current, c) turbulent particle flux and d) turbulence phase velocity in the TJ-II plasma boundary region. The vertical axis shows the radial position (r) relative to the the location of the Last Closed Flux Surface (LCFS, r_0). Negative values of $r - r_0$ correspond to the plasma edge, positive values to the SOL. The horizontal black lines indicate the locations of probe pins.

As noted, a shear layer develops near the edge around $r - r_0 \simeq -15$ mm during the NBI phase, as represented in the graph of $v_\theta^{\rm ph}$ Fig. 5.8 f). The shear in the poloidal phase velocity (dv_θ/dr) increaes up to $4{\cdot}10^5$ s^{-1} during this phase, in contrast with ECRH where the maximum value achieved is about $0.3 \cdot 10^5$ s^{-1} at the same position. The time evolution of the poloidal phase velocity is closed connected to the $E \times B$ poloidal rotation [117], i.e. $v_\theta^{E\times B} = E_r/B \approx -\nabla_r \phi_f/B$, in agreement with results reported elsewhere [215, 216, 115]. This notable difference impacts the radial turbulent particle flux shown in Fig. 5.8 c) in the shear layer region (in the near edge, $-15 \leq r - r_0 \leq 0$) and indirectly in the SOL, by slowing down the turbulent velocity in this region and, thus, the plasma penetration (Fig. 5.8 c). The shear strongly impacts the turbulence correlation time ($\tau_{\rm turb}$ - computed from the auto-

correlation of the floating potential) in the edge Fig. 5.8, possibly due to the increase of rotation in this region (Fig. 5.8 d), as seen in the laboratory frame, while the effect is less pronounced in the SOL. Considering this low rotation in the SOL, the radial correlation length of turbulence can be obtained by considering the Taylor's frozen turbulence hypothesis $l_r \approx \tau_b v_r^{eff}$ [259], yielding in this case $l_r^{ECRH} \approx 4$ mm (for $v_r^{eff} = 0.2$ km/s and $\tau_b \approx 18\ \mu s$) and $l_r^{NBI} \approx 1$ mm (for $v_r^{eff} = 0.05$ km/s and $\tau_b \approx 18\ \mu s$), suggesting the presence of small travelling structures in the SOL during NBI (possibly due to fragmentation) [54]. One has to note, however, that v_r^{eff} represents a mean velocity based on the effective turbulent flux and its value is substantially smaller than typical blobs velocity in TJ-II SOL [10]. Nevertheless, this result gives some import insights regarding the nature of turbulence in plasmas heated by ECRH and NBI. The larger and faster structures observed during ECRH have a direct impact on the SOL ion saturation current baseline and decay length, in agreement with stochastic models predictions [92, 181], and experimental findings in tokamaks [36]. This intuitive result, i.e. the bigger and faster (cross-field velocity) the filaments are, the further they will penetrate into SOL, assuming that the parallel transport does not change appreciably. This hypothesis does not hold, for instance, during the onset of the shoulder formation in tokamaks, where an increase of the collisionality along the field lines reduces the parallel dissipation, favoring, thus, the radial propagation of fast and big filaments [36]. In the current experiment, however, there are not strong reasons to think that a similar effect might have happened: neither the density nor the temperature change that much. In short, the spontaneous establishment of the edge poloidal velocity shear layer during NBI (ion root) affects all the monitored fluctuating and mean parameters not only locally (where the shear layer is formed), but also further outer, in the SOL region, where the $E \times B$ shearing rate is weaker.

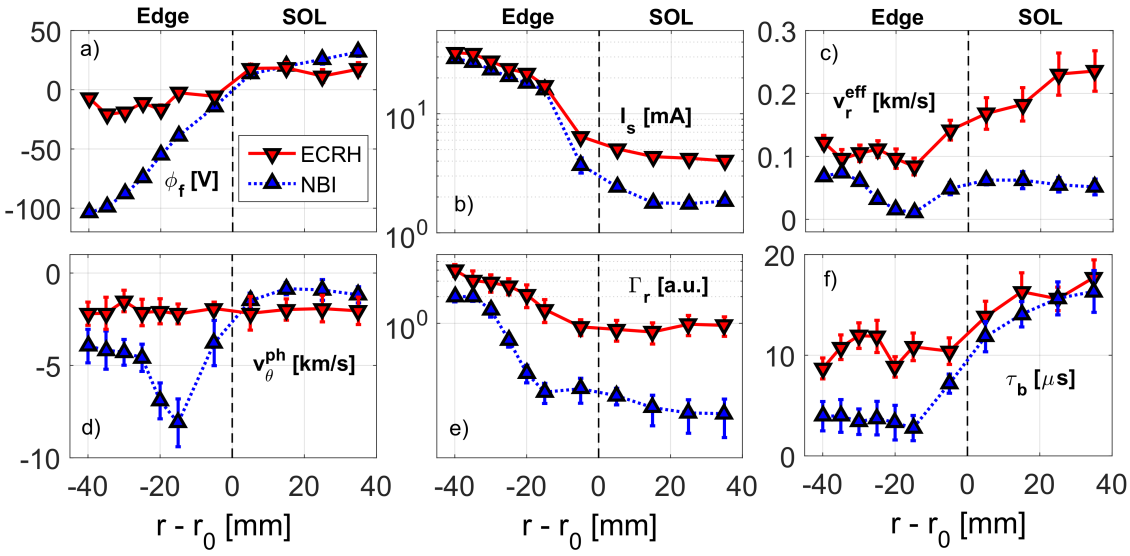

Figure 5.8: Edge radial profiles during ECRH (1100-1140 ms) and NBI (1180-1220 ms): (a) floating potential, (b) ion saturation current, (c) radial effective velocity, (d) poloidal phase velocity of the fluctuations, (e) turbulent transport, and (f) turbulence correlation time.

The turbulence drive (ω_D) and spreading (ω_S) were calculated using signals from probe D (Fig. 5.9) assuming $n \propto I_s$ and $E_\theta \simeq -\Delta\phi_f/d$, where d is the poloidal displacement between the two corresponding pins measuring floating potential. The time average was running over an interval much larger than the turbulence correlation time. Their calculation was performed in 2 ms time slices and fluctuation was taken in the range 5-700 kHz to avoid low frequency oscillations (e.g. zonal flows) and high frequency noise.

From Fig. 5.9, one can see that the local linear growth term (ω_D) is high in the edge and lower in the SOL during ECRH, roughly consistent with $\nabla_r n$ (high in the edge and low in the SOL). During NBI, ω_D strongly reduces in the edge region, around the location of the poloidal velocity shear layer, and slightly in the SOL. On the other hand, the turbulence spreading rate (ω_S) is much higher in the SOL than in the edge (especially during ECRH), reducing during the NBI heating phase. Interestingly, ω_D and ω_S become comparable in the far SOL suggesting that the turbulence spreading becomes important in this region. This result is in agreement

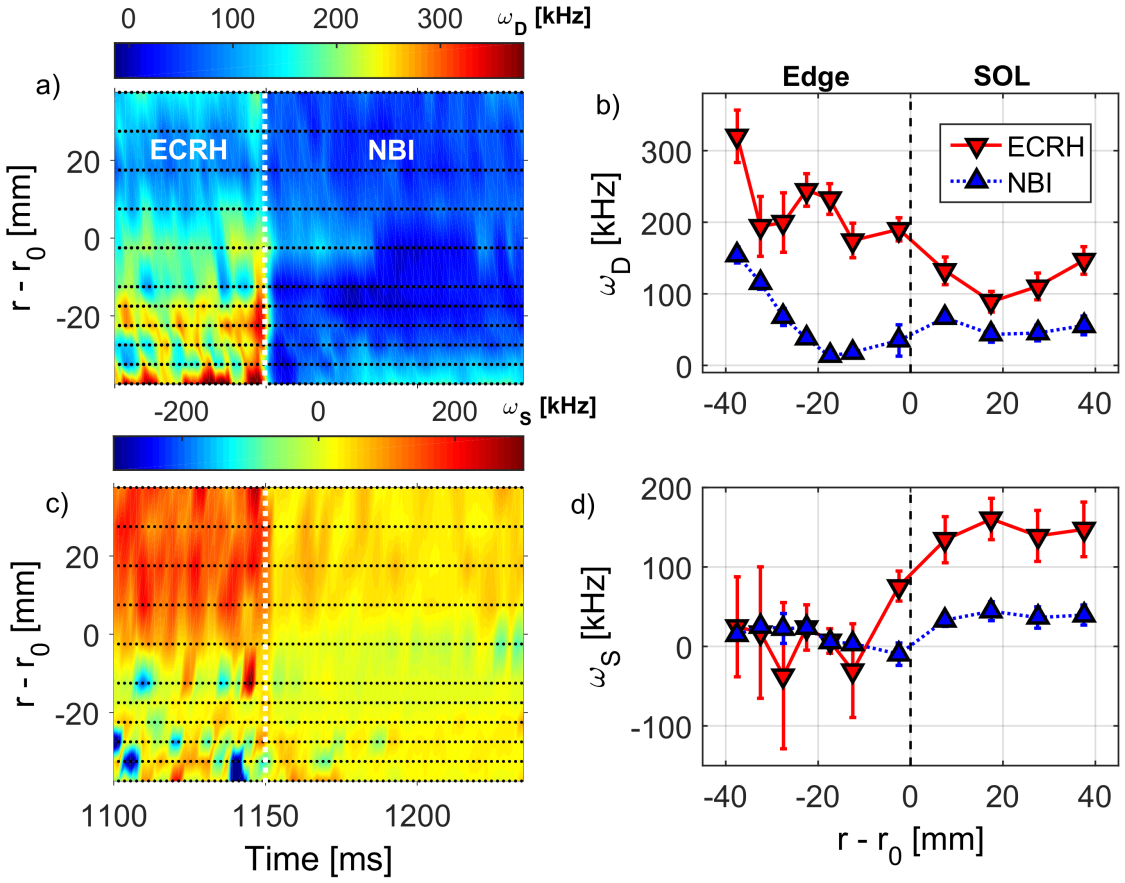

Figure 5.9: Local turbulence drive a) and b) (ω_D) and turbulence spreading c) and d) (ω_S) during the transition from ECRH to NBI. The horizontal black lines indicate the locations of the probe pins.

with the view of turbulent front penetrating in stable regions causing the enhancement of the local anomalous transport [108]. This effect is also observed during NBI, although both parameters are lower, suggesting that the spreading is fundamental in setting the far SOL, even for a stronger shear scenario.

5.5.2 NBI + biasing

In this section, it is studied the influence of an external electrode biasing during the NBI phase, in a similar plasma condition as in the previous section (Fig. 5.5). The electrode is made of graphite, with 25 mm diameter in mushroom-shaped, and 12 mm height, inserted in a boron nitride insulating body. This technique has been shown to

successfully modulate the plasma periphery of TJ-II [233], generating in some cases an edge transport barrier, with an improved plasma confinement. In the presented experiment, the electrode was inserted into the plasma edge $\rho \simeq 0.85$ from the top, delivering -350 V in a duty cycle of 50% with a 40 Hz square signal.

The plasma profiles were built (as before) in a shot by shot basis, in this case from twelve reproducible shots. Fig. 5.10 shows the evolution (1 ms time averaging) of floating potential (ϕ_f), ion saturation current (I_s), radial turbulent particle flux (Γ_r), and the poloidal projection of the turbulence phase velocity. As biasing is switched from 0 to -350 V (Fig. 5.10 a), a fast profile readjustment is observed. The negative biasing induces a ϕ_f well in the near edge (Fig. 5.10 b) and an increase of the turbulent poloidal phase rotation at the same interval (Fig. 5.10 e). In addition, turbulent particle flux strongly reduces in the shear layer and slightly in the SOL (Fig. 5.10 d). The I_s amplitude increases in the edge and reduces in the SOL at -350 V, suggesting a rise of edge transport barrier at this voltage. Notice that $V_b = 0$ does not mean unbiasing or floating potential.

These results can be summarized by taking the average over time windows at 0 and -350 V (Fig. 5.11). At -350 V, the profiles of the floating potential (Fig. 5.11 a) and ion saturation current (Fig. 5.11 b) steepen in the plasma edge region, while ϕ_f SOL values do not change much, but the I_s baseline and its decay length slightly drop. The turbulent particle flux (Fig. 5.11 d) and the effective radial turbulence velocity (Fig. 5.11 c) are reduced in both edge and SOL ($r - r_0 > -30$ mm), concomitant with a slight reduction of the turbulent correlation time (from the autocorrelation of the ϕ_f).

The phase velocity of the fluctuations v_θ^{ph} indicates that the plasma rotation enhances during the negative biasing phase. The radial gradient in floating potential profiles reaches values up to $\sim$ -8 kV/m ($v_\theta = E_r/B \approx -\Delta\phi_f/\Delta r B$, where $B \approx 1$ T), while the polidal phase velocity increases up to $\sim$ -9 km/s, showing that the measured

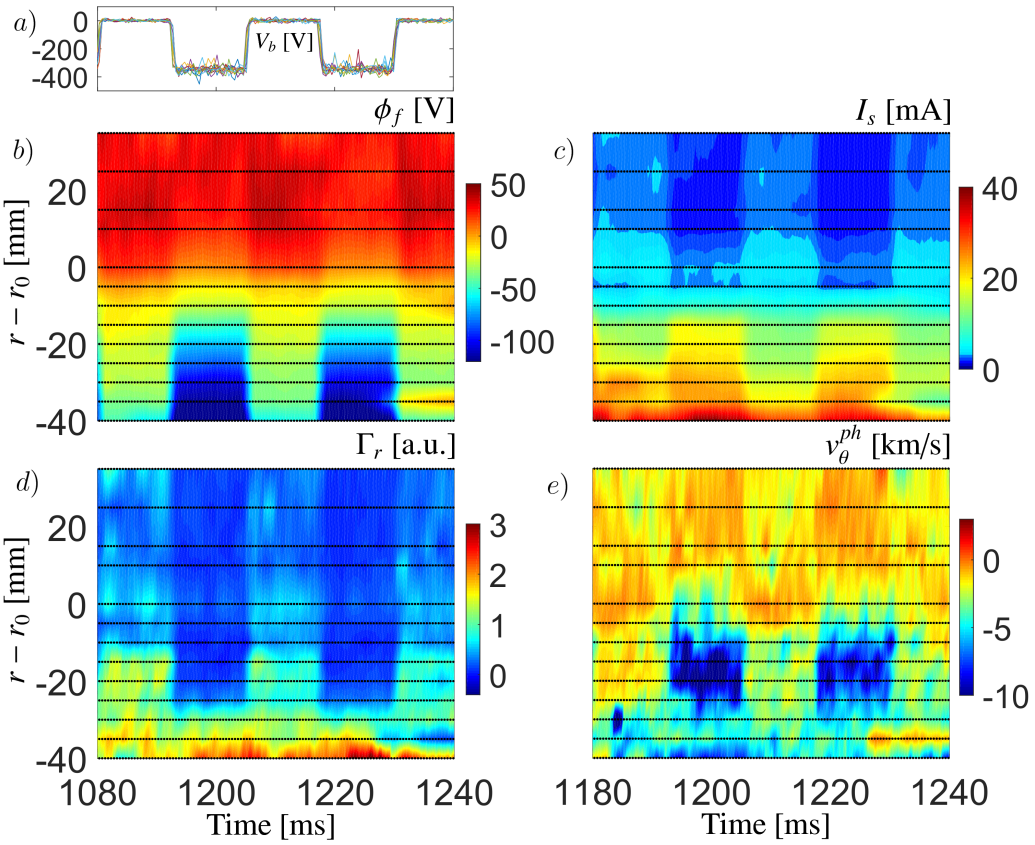

Figure 5.10: Biasing impact during NBI: a) biasing voltage, b) the radial profile of floating potential, c) ion saturation current, d) turbulent particle flux and e) turbulence phase velocity. The vertical axis shows the radial position (r) relative to the the location of the Last Closed Flux Surface (LCFS, r_0), where negative values of $r - r_0$ correspond to the plasma edge and positive to the SOL. The horizontal black lines indicate the locations of probe pins.

phase velocity is closed connected to the imposed $E_r \times B$ drift [117]. The maximum shear in the perpendicular velocity (dv_θ/dr) is of the order of $5 \cdot 10^5$ s^{-1}, i.e., close to the inverse of the turbulence decorrelation time (Fig. 5.11e). The shear reaches its maximum near $r - r_0 \simeq -10$ mm. This result agrees with [222], where limiter biasing in the LAPD device have been shown to control the turbulent particle flux, with values going to near zero when the shearing rate get close to the inverse of correlation time measured at zero shearing rate.

The local turbulence drive (ω_D) and the turbulence spreading rate (ω_S) are shown in Fig. 5.12. At 0 V biasing, ω_D is high in the edge and low in the SOL, roughly

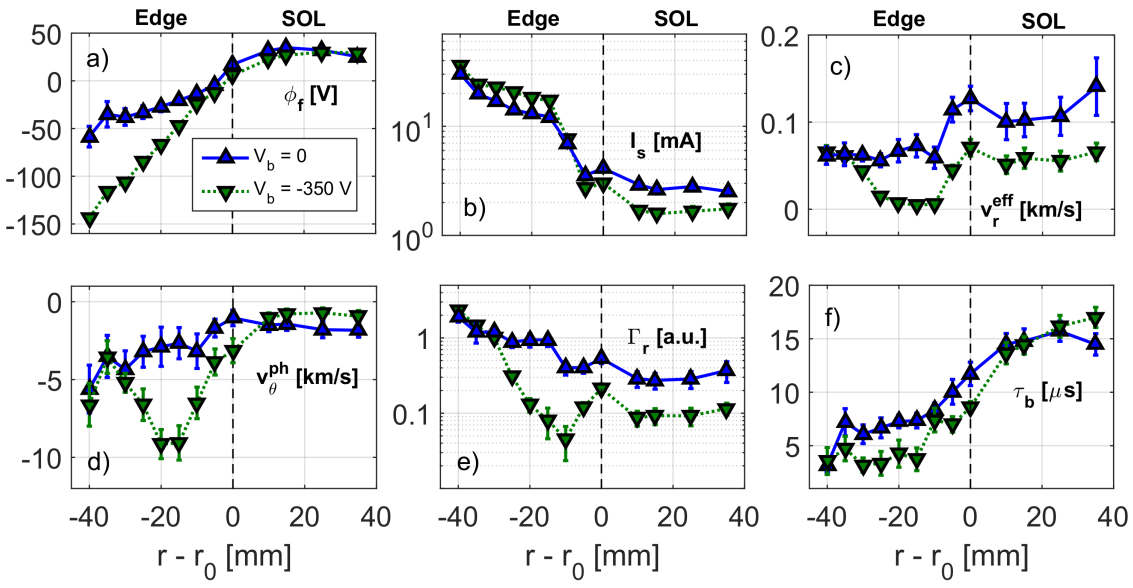

Figure 5.11: Radial profiles during biasing 0 V (up triangle) and -350 V (down triangle) of: (a) floating potential, (b) ion saturation current, (c) radial effective velocity, (d) phase velocity of the fluctuations, (e) turbulent transport, and (f) turbulence correlation time.

consistent with $\nabla_r n$ radial variation (that is, high in the edge and low in the SOL, where the profile is flatter Fig. 5.11 b). On the other hand, at -350 V, ω_D strongly reduces around the shear layer (Fig. 5.11f), consistent with turbulence stabilization induced by the $E \times B$ sheared flow [28]. The rate of turbulence spreading (ω_S) is mainly activated in the SOL at 0 V biasing, reducing at -350 V biasing (Fig. 5.12 b) and d). As observed in Fig. 5.12, both ω_D and ω_S become comparable in the SOL, suggesting that spreading becomes more relevant in the far SOL.

In short, the poloidal velocity shear layer that forms in the near edge region at -350 V (Fig. 5.11 f) establishes a transport barrier that leads to the edge-SOL decoupling [20, 295]. This is done by the combination of local turbulence suppression (represented by ω_D) and the block of turbulence propagation (ω_S). A similar conclusion can be drawn in the plasma heating transition from ECRH to NBI (Fig. 5.8 and Fig. 5.9). In this case, the radial electric field profile is modified spontaneously due to the electron to the ion root transition [177]. A shear layer is also formed in the ion root phase,

similar (although less intense) to the negative biasing case. Note that the zero-bias has a deleterious effect on the plasma confinement compared to the unbiasing case (pure NBI) or -350 V bias. Since the edge potential in the ion root phase is typically negative, increasing towards the plasma boundary, the imposed zero biasing makes the potential profile flatter. This ultimately has an impact on the $E \times B$ poloidal rotation and so the shear flow. Naturally, one can expect that the edge-SOL decoupling leads to a reduction of the SOL width (the SOL decay length), assuming that the parallel transport remains constant.

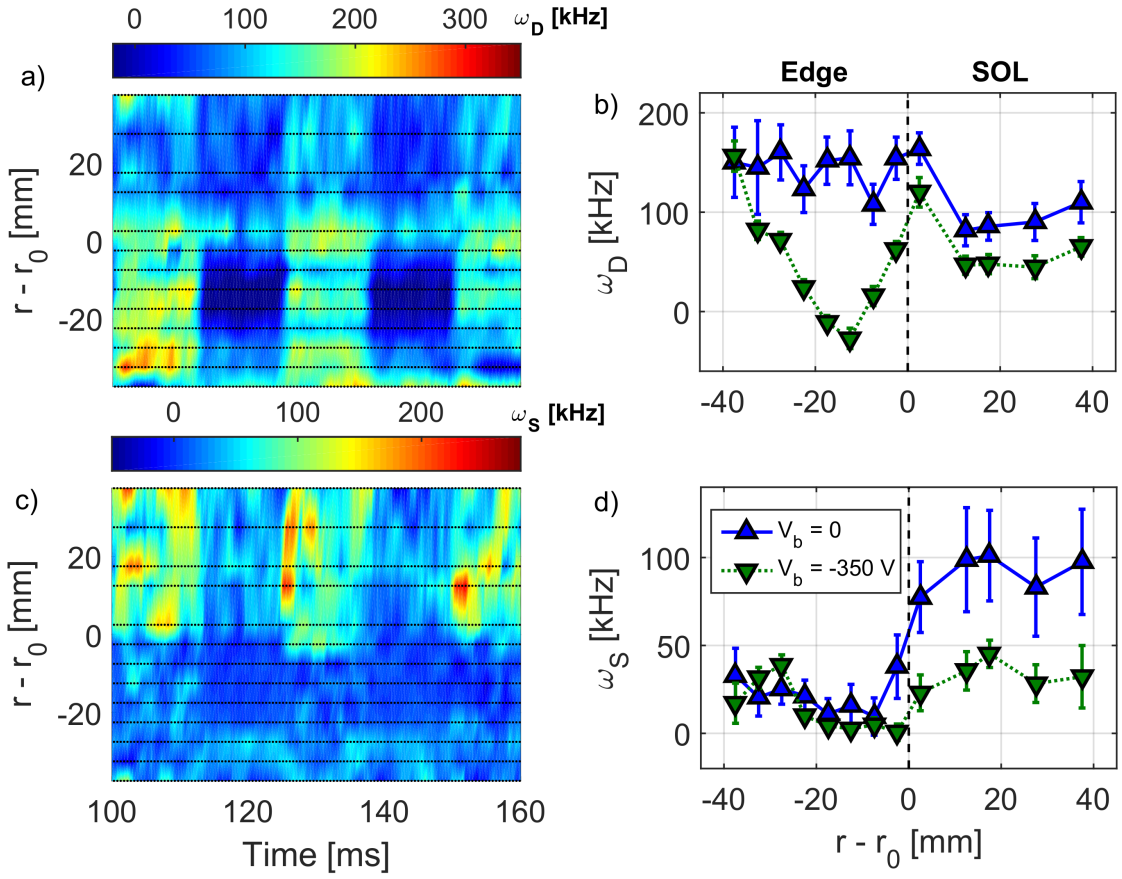

Figure 5.12: Local turbulence drive a) and b) (ω_D) and turbulence spreading c) and d) (ω_S) at 0 and -350 V electrode biasing. The horizontal black lines indicate the locations of the probe pins.

5.6 Conclusion

This chapter addressed one of the most challenging and fundamental questions regarding turbulence in fusion devices: its nonlocal nature and the impact of this effect in the scrape-off layer (SOL). Although the classical turbulence quasilinear approach, where gradients are assumed to evolve slowly and so microinstabilities growth linearly until the free gradient energy becomes depleted, is able to explain the growth of turbulence observed experimentally fairly well. Important disagreements suggest that this approach has limitations. Non-linear models are more successful to describe the transport in fusion devices since they take into account the self-organized behavior of turbulence. However, most of them rely on local assumptions, i.e. turbulence saturates by local linear and non-linear damping. Mixing length rules [134] predict that turbulence correlation length is typically a few ion Larmor radii (ρ_i) and, thus, the diffusion coefficient scales as gyro-Bohm. Experimental results, however, indicate that turbulence tends to scale as Bohm in a strongly driven region and super-gyro-Bohm in weakly driven [108]. The most prominent explanation for this discrepancy relies on the fact that turbulence tends to propagate radially. Indeed, predictions from reaction-diffusion models based on turbulence spreading seem to agree very well with both experiment and global simulations [109, 190, 106]. In short, the propagation of turbulence decreases the level of fluctuation locally, affecting the predictions from linear theories, while increases the level of turbulence in regions linearly stable. Therefore, the turbulence in fusion devices is intrinsically non-linear and non-local, where non-linear dissipation and spatial mixing are key elements. Therefore, turbulence spreading demands global models.

The main focus of this chapter was to present some novel experimental findings on turbulence spreading in the edge-SOL region of TJ-II [103]. Since the near edge is linearly unstable, while the SOL, where gradients are flatter, is thought to be stable, turbulence spreading is believed to be important. This potentially has an impact on

the SOL width (a crucial parameter for the future fusion reactors) as spreading can feed cross-field transport that, together with parallel transport, is responsible for the SOL maintenance. In this scenario, edge-SOL turbulence is thought to be coupled.

A dedicated experiment was carried in TJ-II to address this point. Two plasma conditions were considered 1) plasma started with ECRH and then sustained with NBI; 2) NBI + biasing. The latter is based on the electrode biasing technique [258, 116]. The experimental results are in good agreement simulations from a three-dimensional gyro fluid turbulence model [166]. In both cases, the rate of turbulence spreading (ω_S) is mainly activated in the SOL region. It was observed that the ECRH to NBI transition is characterized by a reduction of the spreading in the SOL, while the rate of turbulence drive (ω_D) strongly reduces in the near edge where a poloidal shear flow layer was established. In addition, it was shown how both ω_D and ω_S can be controlled with an external edge biasing. Particularly, when biasing turned negative, a shear layer was formed in the plasma edge, followed by the reduction of ω_D and ω_S (in the SOL). At zero biasing, however, the background $E \times B$ flow reduces compared to the pure NBI case (i.e. without biasing) and so both ω_D and ω_S increase. The edge-SOL decoupling was observed to happen when the $E_r \times B$ shearing rate reaches values comparable to the inverse of the turbulence correlation time in the vicinity of the LCFS [96].

Therefore, these findings indicate that sheared radial electric fields are able not only to suppress turbulence locally (a well know result), but also to reduce non-local effects (i.e. turbulence spreading). Although a similar effect has bee seen in global gyrokinetic simulations [285], this is the first time it was demonstrated experimentally.

Chapter 6

Edge-SOL turbulence coupling

The propagation of turbulence from unstable locations to stable ones, a phenomenon known as turbulence spreading, was discussed in chapter 5. In the referred chapter, the rate of turbulence spreading [166] was measured in the plasma edge and scrape-off layer (SOL) of TJ-II in different regimes. This quantity has shown to be mainly activated in the SOL and being impacted by $E \times B$ shear flows. Particularly, high shear levels achieved with the aid of an external electrode biasing has led to a partial edge-SOL decoupling, as well as local turbulence suppression around the shear layer. These results further confirm that sheared radial electric fields suppress turbulence locally, but also indicates that the rise of an edge transport barrier prevents the propagation of turbulence from the edge to the SOL in agreement with simulations [285, 43]. In addition, a growth piece of evidences from simulations [42, 43, 154] have pointed out for the leading role of turbulence spreading in setting the SOL width in ITER and beyond. The power fall-off length is defined from: $q(r) = q_{\|} e^{-r/\lambda_q}$, where $r = R - R_{sep}$, with R_{sep} the separatrix position at the outboard midplane. Turbulence propagation from the pedestal and near edge regions can provoke an increase of λ_q [43, 154], by enhancing the turbulent cross-field transport in the SOL, beyond predictions from data-based regression [67]. Therefore, the proper understanding of the underlying

mechanisms that set the SOL became an important requirement for future fusion devices. Although the great development of turbulence codes (coupling with transport codes) has permitted to study turbulence properties in the edge and SOL with an unprecedented level of detail. Experimental validations necessary. This is important in order to make reliable predictions for ITER. In this chapter, the propagation of turbulence will be studied by a novel technique called transfer entropy [270] applied to floating potential signals from a multi-pins probe placed in the TJ-II boundary. The impact of radial electric fields (E_r) on edge-SOL coupling will be investigated in TJ-II by relying on a fundamental property of stellarators: the neoclassical root transition, in which E_r changes its sign in a controlled and continuously way. In addition, the role of self-organized phenomenons will be also addressed.

6.1 Statistical tools

Before discussing the main experimental results of this chapter, this section introduces some of the statistical tools employed. The techniques are: the mutual information, the transfer entropy, and the biorthogonal decomposition. Since they are not so widespread among the fusion community, they were introduced in this chapter instead of 4, where some general techniques were discussed. Their applications in this thesis were also restricted to the present chapter.

6.1.1 Mutual information

Entropy is a fundamental concept in physics, historically related to the study of thermodynamics and statistical mechanics, and commonly understood as the amount of disorder in a system [264]. The concept is particularly important in the field of information theory. In this context, entropy can also be viewed as the amount of information stored in a time series with a defined probability distribution (PDF) [137].

The Shannon entropy [231] measures the number of bits required to encode a signal represented by a PDF $p(i)$:

$$H_I = \sum p(i) \log_2 p(i) \tag{6.1}$$

The mutual information (MI), on the other hand, is a non-linear technique that measures the amount of information shared between two signals or the quantity of information generated by (naively) assuming that the two signals are independent [226]. MI can be seen as a non-linear extension of the linear correlation [137]. Roughly speaking, MI measures how much one can know about a signal $x(t)$ by using information from a second signal $y(t)$ or vice versa. If $p(i)$ and $p(j)$ are the probability distribution function of two processes and $p(i,j)$ is the joint probability, the mutual information is defined as [2]:

$$M_{IJ} = \sum p(i,j) \log_2 \frac{p(i,j)}{p(i)p(j)} \tag{6.2}$$

Equivalently, the mutual information can be written as: $M_{IJ} \equiv H_I + H_J - H_{IJ}$, where $H_I = \sum p(i) \log_2 p(i)$ is the Shannon entropy and $H_{IJ} = \sum \sum p(i,j) \log_2 p(i,j)$ is the joint entropy [231]. It follows that $M_{II} = H_I$, since $H_{II} = H_{JJ} = 0$, i.e. the auto mutual information is equal to the single entropy. Note that $M_{IJ} = M_{JI}$, i.e., the mutual information is symmetric.

6.1.2 Transfer Entropy

Although very powerful, the mutual information technique does not deal with dynamics - it is not possible to know the direction by which information flows between two processes by knowing only the mutual information between them. Worth noting that time lags can also be introduced in the mutual information [226]. On this purpose, a

more powerful technique for studying Edge-SOL coupling in plasmas is the Transfer Entropy (TE) [270]. First introduced in the Information Theory context [226], this technique allows studying the causal relationship between two signals by measuring the amount of information exchanged between them in a defined direction and time delay. The transfer entropy of two processes, e.g. X and Y, measures in bits how much they are causal connected or how much X depends on Y or Y depends on X (they are nonsymmetric by construction). A time-series $x(t)$ has a causal relation with $y(t)$ if it is possible to predict its next step by using the history of both signals: the auto-transfer entropy is zero by definition. In this case, the transfer entropy can be defined in a simplified version as [226]:

$$\mathrm{T}_{X\to Y} = \sum p(x_{n+1}, x_{n-k}, y_{n-k}) \log_2 \frac{p(x_{n+1}|x_{n-k}, y_{n-k})}{p(x_{n+1}|x_{n-k})} \tag{6.3}$$

Where $p(...)$ is the probability density function and $p(a|b) = p(a,b)/p(b)$ is the conditional version a on b. The probability density function is built by using 'course graining', that is, by selecting a low bin number 'm' that gives statistically significant results. The number of points necessary to build the PDF is then m^d, where d is the PDF dimension or the number of arguments. Typically, the transfer entropy values are significant if they are larger then the values assumed by considering two random noises at the same bin m (see Fig. 1 of reference [271]).

6.1.3 TE and blob 'toy model'

The edge and SOL of fusion devices are dominated by filaments or blobs, coherent pressure structures align to the magnetic field and propelled by $E \times B$ drift. Blobs are mesoscale phenomenons, which means that their size is typically substantially larger than the local ion Larmor radius but shorter than the machine characteristic size (e.g. minor radius). Typical blob size is ~ 1 cm. In addition, those structures can be

tilted with respect to the propagation direction due to magnetic and/or $E \times B$ shear flow [76]. These two ingredients (finite size and tilt) make difficult the measurement of cross-field velocity based on 2-points correlation technique. Travelling structures with cross-field extension larger than the distance between pins can yield a fictitious projected velocity. In a limit case, a rotating blob in the bi-normal direction, but almost completely aligned radially, can yield an almost infinite 'radial' velocity when measured by two probes radially displaced a distance shorter than the blob radial projection length.

Since blobs are stochastic [92] and time-prolonged phenomenon with a well-defined velocity distribution function at a given position, one can study their dynamics by using transfer entropy (TE). As discussed in section 6.1, TE measures the amount of information flowing between two signals. Blobs are sustained memory events or, in statistical terms, a time series ($X(t)$) in a interval T dominated by bursts (related to blobs) has Hurst exponent in the interval $1/2 < H < 1$ [108], where $\langle [X(t+T) - X(t)]^2 \rangle = T^{2H}$.

To verify the robustness of using TE to study the dynamics of coherent structures travelling ballistically, periodic elliptical shape blobs were artificially created with a well-defined velocity and shape. Merge and suppression are not allowed. An artificial one dimension probe in a slab geometry (X-Y plane) was set to measure the signal in time. Apart from the simplifications involved, the aim of this 'toy model' is to demonstrate that TE is indeed able to perceive the dynamics of coherent structures. The TE technique can also be used to detect ballistic events as well as diffusion ones [269]. The simulated blobs are described by a two-dimension Gaussian function:

$$Z(t) = Z_0 e^{-\left[(x')^2/a^2 + (y')^2/b^2\right]} + Z^{noise}(x, y) \tag{6.4}$$

with

$$x' = [(x - x_0) - v_x t]\, cos(\alpha) - [(y - y_0) - v_y t]\, sin(\alpha)$$
$$y' = [(x - x_0) - v_x t]\, sin(\alpha) + [(y - y_0) - v_y t]\, cos(\alpha) \tag{6.5}$$

where α is a tilt angle with respect to the horizontal direction, v_x and v_y are, respectively, the horizontal and vertical velocities, and Z^{noise} is a random noise set to be ten percent of the maximum amplitude of the generated blob to avoid the long tail reminiscence that might influence in the TE calculation. The time coordinate was set as sawtooth wave to generate repetitive blobs and, thus, increasing the sampling for computing TE with more precession. Fig. 6.1 shows on the left a 45° tilted blob travelling along the x-axis together with the set of artificial probes all aligned along the horizontal direction at y = 25. On the right is shown the transfer entropy starting from the reference signal (the leftest, indicated by an open circle) to the other signals. The long-time correlation due to the periodicity of the generated signal, i.e. the correlation between two successive events, are not shown. A TE plume with an almost constant positive slope indicates that the propagation is towards increasing x (outward considering that x is equivalent to the radial coordinate). Note that TE is almost zero close to the reference point around $x_p = 24$. Therefore, as pointed out before, the transfer entropy, different from the 2-point cross-correlation, is zero when there is not propagation and so time delay is null. This effect happens here because the coherent structure is larger than the distance between two close artificial probes.

As a second example, Fig. 6.2 shows coherent structures travelling perpendicularly with respect to the artificial probe pins disposition. This example is particularly common in experimental situations, where rake or reciprocating probes measure the

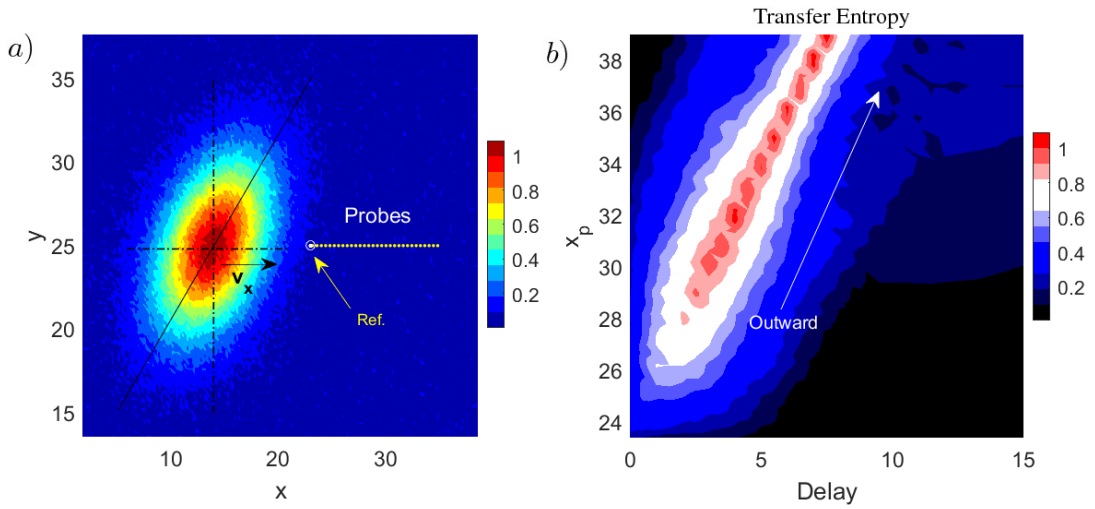

Figure 6.1: Gaussian shape blob travelling outward (increasing x) in a 'toy model'. The transfer entropy (TE) capture the blob dynamics, where the plume slope gives the correct blob velocity.

plasma boundary in several radial positions simultaneously in a region where the plasma poloidal rotation is typically larger than the radial one. Again, the reference is chosen to be leftest indicate by an open circle. Fig. 6.2 a) shows a coherent tilted structure travelling downwardly (decreasing y). The corresponding transfer entropy is shown in Fig. 6.2 b), where one can see a less intense plume of propagation with a positive slope as before. Hence, the plume shape suggests that the propagation is outward, i.e. increasing x, although the velocity is vertical downward by definition. This spurious effect is due to the combination of a tilted structure and the short distance between probes (smaller than the structure characteristic size). These two conditions are sufficient to yield a time delay and so a not negligible TE. The effect is absent for 0 or 90° tilted structure or for a distance between probe larger than the blob size (e.g. beyond the probe at $x_p \approx 34$, where TE drops sharply). Fig. 6.2 c) and d) show again a 45° tilted structure, but travelling upward (increasing y). Note that in this case, the delay leads to the misinterpretation of a structure travelling inwardly (decreasing x). A similar conclusion could be drawn from the first example,

i.e. structure travelling downward, but with a negative tilt. In short, these simple examples help obtaining some intuition on practical experimental examples when only one-dimension set of probes is available, besides of showing that the TE is a suitable to detect coherent structures with ballistic propagation.

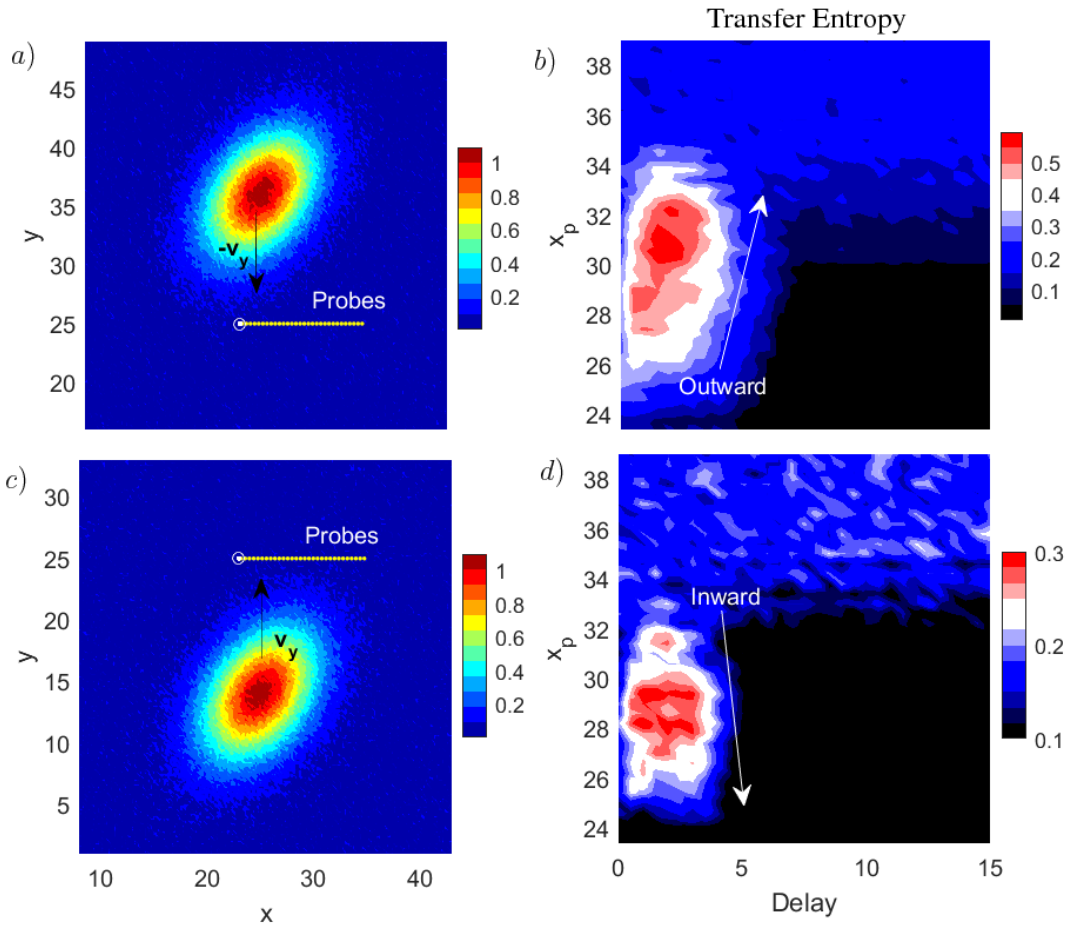

Figure 6.2: Two examples of Gaussian shape blobs travelling vertically downward (a) and upward (c). The transfer entropy, in this case, yields a plume that might be interpreted as if the blob was propagating outwardly (b) or inwardly (d).

6.1.4 Biorthogonal decomposition

The biorthogonal decomposition (BOD) is a convenient way to extract informations regarding the spatial and temporal behaviour of a set of signals displaced in the space and measuring the same quantity simultaneously (e.g. plasma potential or

temperature). The method was pioneered used in fusion plasmas by *Dudok de Wit, T., et al.* [64] and is based on the decomposition of an array of signals in orthogonal spatial-temporal functions. Given a matrix of data $Y(i,j)$, where $i = 1, ..., N$ stands for time and the index $j = 1, ..., M$ represents the number of detectors in different positions, the decomposition is given by:

$$Y(i,j) = \sum_{k}^{K} \lambda_k \psi_h(i) \phi_k(i) \tag{6.6}$$

Where K is the number of modes, $K = min(N, M)$. The temporal function ψ_k is called '*chrono*', while the spatial function ϕ_k is known as '*topo*'. The functions are orthogonal:

$$\sum_{i} \psi_k(i) \psi_l(i) = \sum_{j} \phi_k(j) \phi_l(j) = \delta_{kl} \tag{6.7}$$

The mode amplitude λ_k is given in the signal units or, alternatively, one can normalize it as: $\lambda_k^* = \lambda_k / \sqrt{NM}$. Worth noting that time is acquired experimentally at a constant sampling rate, while the sensors can be displaced in an irregular grid.

The decomposition can be done by using the single value decomposition (SVD) [263]. The method consists in decomposing a $m \times n$ matrix in the product of three matrices of the same dimension:

$$Y = USV^{\dagger} \tag{6.8}$$

Where S is a diagonal matrix composed of real positive values in descending order, and U and S are unity matrix: $VV^{\dagger} = \mathbf{I} = UU^{\dagger}$, where $\mathbf{I}$ is the identity matrix. Following the SVD approach, the matrix U can be identified as the 'chrono' functions

in the BOD analysis and V the 'topo' one, while S is the eigenvalue matrix of the amplitude of the modes (λ_k). Therefore, the BOD and SVD are formally equivalent.

Given two displaced signals, the covariance between them is:

$$\mathrm{Cov}(j_1, j_2) = \frac{1}{N} \sum_i Y(i, j_1) Y(i, j_2) \tag{6.9}$$

substituting $Y(i, j)$ by its decomposed form (6.6) and considering the orthogonal condition (6.7), it follows that:

$$\mathrm{Cov}(j_1, j_2) = \frac{1}{N} \sum_k \lambda_k^2 \phi_k(j_1) \phi_k(j_2) \tag{6.10}$$

The covariance between two displaced signals measuring the same quantity at the same time interval is the sum of the product of their topos for each mode weighted by the corresponding mode amplitude. A more relevant quantity for the purpose of this chapter, the correlation between the same two signals, measured by two displaced sensors, can be easily obtained from the covariance function defined in (6.10):

$$C_{12}(j_1, j_2) = \frac{\mathrm{Cov}(j_1, j_2)}{\sqrt{\mathrm{Cov}(j_1, j_1)\mathrm{Cov}(j_2, j_2)}} \tag{6.11}$$

By substituting Eq. 6.10 into 6.11, it is clear that the correlation function depends only on the topos. If the two sensors are remotely separated, one can calculate the long-range correlation (LRC) between them [9]. Particularly, the correlation for a given mode is simply:

$$C_{12}^k(j_1, j_2) = \frac{\lambda_k^2 \phi_k(j_1) \phi_k(j_2)}{\sqrt{\mathrm{Cov}(j_1, j_1)\mathrm{Cov}(j_2, j_2)}} \tag{6.12}$$

The method has been used in TJ-II to detect zonal flows unambiguously [272]. Those are characterized global oscillations with very long (poloidal and toroidal) wavelengths, typically associated with low-frequency oscillation ($f < 1$ kHz). While the standard two-point cross-correlation method [150] requires that the mode stays roughly stationary since any movement might result in a loss of correlation. The BOD analysis, on the other hand, extracts information of a single dominant global mode by decomposing it spatial-temporally with contribution from multiple signals.

6.2 Divertor heat flux width (λ_q) in fusion devices

One of the most relevant issues nowadays that will potentially have an impact on the feasibility of ITER and beyond is the heat flux width (λ_q) and the mechanism that set it. In the ITER standard configuration (Q = 10), the heat power from the bulk plasma to the SOL is foreseen to be ~ 100 MW ($P_{total} - P_{rad,core}$, where P_{total} is the total input power into the plasma and $P_{rad,core}$ is the core radiated power) [158]. Such high power level has to be exhausted somewhere. While a substantial part will be irradiated by impurity seeding [158], some will end up in the plasma wall, and the remaining will be conducted along the field lines onto the divertor plates. The power that will arrive at the wall has to be controlled to avoid overload, which might cause wall contamination as well as its damage. The power load on the wall must be below 4.7 MW/m^2 in steady state condition [121]. Such an important requirement set a limit for the intensity of the SOL cross-field transport. However, the most critical point is the power that will arrive on the divertor. It is not clear yet whether the divertor targets will be able to withstand the coming power in steady-state condition for a long period. The material power threshold is ≈ 10 MW/m^2, which reduces drastically the

operating margins for ITER. A possible solution for that is to increase the impurity irradiation contribution by impurity seeding up to the so-called detachment or partial detachment regime [135], where the heat flux and pressure along the field lines up to the divertor reduce strongly. However, the impurity seeding has to be carefully tailored to avoid that density increases beyond the limit where radiative collapse might be activated [148].

Experimental results from several machines, including JET, DIII-D, ASDEX Upgrade, C-Mod, NSTX and MAST, indicate that $\lambda_q \sim B_p^{-\gamma}$, where $\gamma \approx 1.1 - 1.3$, or equivalently $\lambda_q \sim I_p^{-\gamma}$ since $B_p \propto I_p$ [67]. This result was obtained by infrared tomography. Typically, this diagnostic is composed of a set of cameras designed to measure the infrared radiation coming from the divertor plates that, in turns, allows to measure the surface temperature and so the heat flux (by assuming stationary condition) with a good spatial-temporal resolution. The footprint of the power over the divertor has a characteristic pattern during inter-ELM H-mode as observed in several machines, with a heat flux peak at the target position that faster decreases towards the private zone than to the flux expansion direction. This motivated a fitting formula first proposed by *Eich T.* [68] that successfully describes the data of several machines. Fig. 6.3 shows λ_q as a function of the poloidal magnetic field at the midplane, clearly indicating that the heat flux becomes narrower regardless of the machine size. The dependence $\lambda \sim 1/B_p$ suggests that the heat flux width in ITER baseline H-mode (Q = 10), $I_p = 15$ mA with $q_{95} = 3$, in attached condition will be $\lambda_q \leq 1$ mm.

The 'Eich scale' is largely supported by the Goldston heuristic model [97]. *R.J. Goldston* has proposed a model that estimate the heat flux width for tokamaks in inter-ELM H-mode regime based only on neoclassical drifts, i.e. neglecting the cross-field transport contribution from turbulence. The basic idea behind this model is that the magnetic curvature and ∇B make the gyro-center of ions and electrons to move

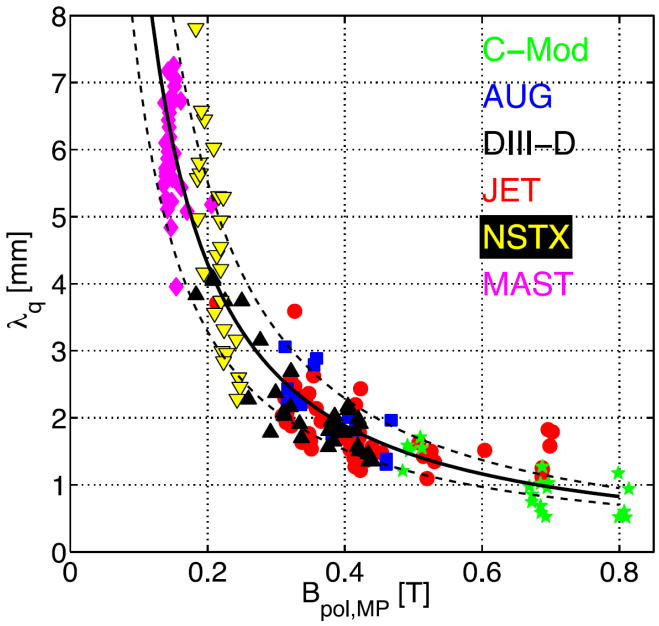

Figure 6.3: Eich scale: heat flux width (λ_q) as function of the poloidal magnetic field at the outer midplane (for several devices). The black line represents the data fitting curve [67].

vertically. In average, some ions will escape the confinement region towards the SOL with velocity $\langle v_{\nabla B+curvB} \rangle = 2T/eZBR$, where T is the temperature in eV. According to the model, the effective cross-field drift is balanced in the SOL by parallel flows into the divertors and also to counter Pfirsch-Schlüter parallel flow. By assuming that $T_e = T_i = T_{sep}$ on the drift and by balancing with the parallel flow to the divertor, and considering that the velocity is $c_s/2$ (half of the total contribution), one can demonstrate that $\lambda \approx 2a\rho/R$, where a is the minor radius and ρ is the ion Larmor radius. This formula has been shown to agree very well with the data from present operation tokamaks. Worth noting that the argument just described neglects explicitly any contribution from turbulent transport, which might be fine at some extend for inter-ELM H-mode, but is clearly not suitable for L-mode.

Gyrokinetic simulations with XGC1 have shown that λ_q in ITER baseline configuration might be $\lambda_q \sim 6$ mm [42], therefore deviating from the Eich's scale. This fortuitous result would give some margin for the ITER divertor design. Those simulations

neglect electromagnetic effects, i.e. consider that fluctuations are pure electrostatic. Nevertheless, simulations have shown good agreement with experimental results and the Eich's scale for DIII-D, C-mod, and NSTX. XGC1 is a full $-f$ particle in cell gyrokinetic code, able to perform global plasma simulations in diverted geometry, including plasma-wall physics [48].

Following this result, several simulations were carried out to verify the validity and extension of those findings [290, 257, 214, 194]. As an example, BOUT++ is a framework for non-linear fluid plasma simulations that can accommodate many different models. Among them, a nonlinear three-dimensional turbulence code that considers two-fluid and 6-fields has been used to simulate the physics of the edge and SOL [290]. The code assumes that the plasma in this region can be described by a set of Braginskii equations (i.e. plasma is treated as fluid), including also electromagnetic effects and finite Larmor radius, gyro-Landau fluid. The code has been shown to successfully predict the properties of the quasi-coherent mode observed in the EDA H-mode in C-Mod [43]. This mode acts to enhance the cross-field transport in this machine [151]. Such a result points out to the importance of the underlying instability to the transport and, consequently, to the SOL width. *Myra et al.* [186] have further confirmed the key role of the underlying instabilities and turbulent transport and their impact on the SOL properties, as well as the role of the turbulence saturation mechanism.

Some turbulence codes [214, 257, 251] consider that the turbulence that contributes to the SOL anomalous cross-field transport is generated in the near edge and scrape-off layer. Thus, those codes naturally neglect that a portion of the turbulence in the SOL might actually come from the pedestal region. However, a growth piece of evidence has shown that this effect might be presented and could be crucial for ITER and beyond [42, 43, 154, 292]. Fig. 6.4 shows simulations from BOUT++ [154] of the plasma edge and SOL in ITER baseline condition (I_p = 15 MA). Note that

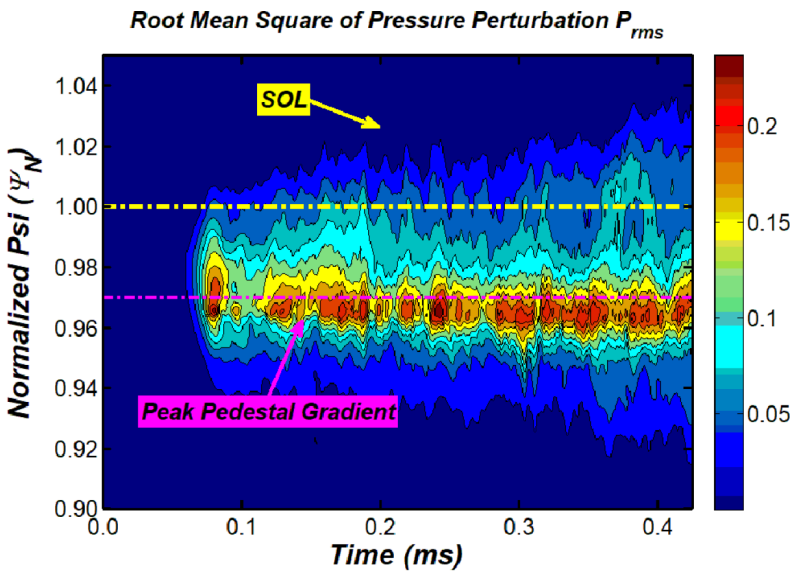

Figure 6.4: Simulations from BOUT++ in ITER condition: root mean square of the pressure perturbation shows as color map where the vertical axis is the normalized flux coordinate and the horizontal axis represents the time evolution [154].

most of the turbulence (represented by the root mean square of the pressure perturbation) is generated at the maximum pedestal gradient region, but penetrates into the SOL, affecting, thus, the local turbulence feature of this region. The simulations reported in Ref. [154] have shown two cross-field transport regimes: a dominated by neoclassical drift (in agreement with the heuristic model) and a turbulent dominant regime. The parameter that yields this deviation was pointed out to be the level of SOL thermal diffusivity $\chi_\perp$. The critical value ($\chi_{\perp,crit}$), however, depends on the machine parameter. In relatively small machines (basically all the present tokamaks), the threshold between the two regimes is larger than the expected anomalous cross-field transport and, thus, the neoclassical drift dominates the cross-field transport. In bigger machines, like ITER and CFETR [291], the turbulent cross-field transport contribution becomes dominant, and, therefore, turbulence is expected to set λ_q. This result is likely related to the combination of the diminished importance of neoclassical drifts, that decrease with the major radius and the magnetic field strength, with an enhancement of turbulent transport (with a leading role of turbulence spreading).

The latter seems to be in accordance with a relaxed $E \times B$ shear layer. Indeed, cross-field turbulence transport and turbulence spreading can be regulated by radial electric field or its shear [285, 43]. The $E \times B$ shear in ITER and beyond is expected to be weaker [143], and wider, $\Delta r \sim (\alpha a \rho_i)^{1/2}$ [42], where α depends on the magnetic equilibrium. This favours the cross-field transport of bigger structures (streamer-type) towards the SOL. Therefore, while SOL turbulence in the present tokamaks is thought to be dominated by blob-type structures, streamers might be dominant in ITER and beyond. These structures are more efficient to transport plasma outward and, hence, might have a significant impact on the SOL width. Therefore, the divertor heat flux width in ITER and beyond can be fully dominated by turbulence processes with the combined contribution of local and non-local effects. Turbulence spreading intensity and the edge-SOL coupling level are strongly dependent on sheared radial electric fields as shown in [103] and discussed in the previous chapter. These results were obtained with fast switch biasing experiments. In the next section, the propagation of turbulence will be studied for slowly-varied radial electric fields in TJ-II during the spontaneous electron-ion root transition. Although TJ-II is a stellarator, the basic idea of the SOL been set by the competition of cross-field and parallel transport remains. Therefore, turbulence spreading is also expected to be relevant in stellarators.

6.3 Slow electron-ion-electron root transition in TJ-II

Radial electric fields in stellarator are set by the interplay between neoclassical and turbulent mechanisms. The ambipolar condition requires a balance of the electrons and ions flux ($\Gamma_e = Z_i \Gamma_i$), that, in turns, is locally dependent on the density and temperature gradients as well as on the radial electric field itself [274]. This stellara-

tor property differs profoundly from tokamaks, where the radial electric field is set independently from the neoclassical ambipolar condition, that is, $\langle j_r \rangle = 0$ for any E_r solution. Deviations from the axisyemmetry (e.g. toroidal field ripples) in tokamaks or turbulence effects can yield $\langle j_r \rangle \neq 0$, turning the ambipolar flux tied to local E_r and vice versa. In stellarators, the electrons and ions mobility depends strongly on the level of colissionality ν^* (also called neoclassical viscosity), that defines different plasma confinement regimes, e.g. banana, plateau or Pfirsch-Schlüter. But also on the local radial electric field, which in turns, impacts on the ambipolar condition and so back on E_r. This makes the radial electric fields intrinsically non-linear in stellarators. Therefore, local ambipolarity in stellarator is only consistent with specific E_r solutions [112]. The so called electron root is the positive radial electric stable solution ($E_r > 0$) that typically appears in low collisionality regimes and for $T_e \gg T_i$. In higher density regimes and for $T_i \sim T_e$, negative stable solution ($E_r < 0$), called ion root, becomes dominant. In TJ-II, the 'root transition', i.e. when the radial electric field locally or globally flips the sign, typically happens when the central averaged line density overcomes a critical value at constant heating rate [275]. The transition has been observed experimentally in TJ-II with Heavy Ion Beam Probe (HIBP), as global potential sign [177]. A stepper radial electric field profile in the plasma edge is an observed consequence of the transition [71, 275]. Substantial improvement in the plasma confinement time during the ion root phase [13] is consistent with an enhanced $E \times B$ shear layer in the plasma edge [275] that drives turbulence suppression [103]. In addition, the radial electric field can also be set by turbulence mechanisms, although there is some controversy regarding this point [112]. This because turbulent transport is also ambipolar in stellarators, so the neoclassical transport, on scales larger than gyroradius, is thought to be the dominant factor that sets the radial electric field. The turbulence self-regulation acts to saturate turbulence locally by creating fluxes through Reynolds stress mechanism [60] and thus inhibiting the further growth

of the turbulence. In this process, turbulence events feed the growth of low scales, i.e. zonal structures, in an inverse cascade process [59]. The rise and fall of turbulence amplitude occurs in low frequency ($\sim$ 1kHz) in a limit cycle oscillation (LIM), thought as a 'predator pray' mechanism [139]. This self-regulation process generates zonal flows that is characterized by larger m = n = 0 structures, which is commonly observed experimentally in TJ-II with a high long-range correlation (LRC) (at zero delay) [207] and as global slow oscillating mode [272]. In stellarators, zonal flows become enhanced with the decrease of the neoclassical viscosity when the density approaches the limit beyond the root transition [275]. The viscosity, that acts to damp low-frequency oscillation, goes to zero in the transition, permitting the growth of low-frequency modes such as zonal flows. Its contribution to the local flow can be critical, beyond the neoclassical contribution, especially in high turbulent regions.

To study the impact of radial electric field on turbulence propagation, a dedicated experiment was considered [102]. Thanks to the special root transition property in stellarators, the radial electric field can be varied continuously and slowly, making those devices ideal to study the relationship between turbulence and radial electric fields. In chapter 5, it was demonstrated through the electrode biasing technique that sheared radial electric fields are able to suppress turbulence locally (a well-known result [28]), but also its radial propagation [103]. The consequences of this is a partial turbulence edge-SOL decoupling, with a direct effect on the edge and SOL profiles, e.g. the ion saturation current SOL decay length becomes reduced. The root transition can be achieved in TJ-II by varying the plasma density by external gas feed control, keeping the heating rate constant. The heating here was provided by electron resonance heating (ECRH) at a frequency of 53.2 GHz (X-mode). The transition happens in this situation when density overcomes a critical value [275]. During this process, the main instability that drives most of the turbulence remains the same, as has been shown recently in global gyrokinetic simulations [219]. The dominant

microinstability in TJ-II is the trapped electron mode (TEM), mainly driven by the electron temperature rather than density gradient. This is an important requirement since one can guarantee that the modifications in the turbulence properties is mainly provided by the varying radial electric field.

Deuterium plasmas with magnetic field on axis $B_0 < 1.2$ T was initialized and sustained by two gyrotron, delivering a total power of $P_{ECRH} = 150$ kW. The line averaged density was varied in the range $\bar{n}_e \approx 0.3 - 1.0 \times 10^{19}$ m^{-3}. The empirical critical density in this case is $\bar{n}_e^c \approx 0.6 \times 10^{19}$ m^{-3}, beyond the electron-ion root transition occurs. The core electron temperature was observed in the interval: $300 < T_e(0) < 400$ eV.

The plasma edge and SOL were monitored with two electrostatic probes toroidally displaced (Fig. 6.5). The probe B was inserted from the top vessel at the toroidal cross-section $\phi = 195°$, while probe D was installed at the bottom at $\phi = 38°$. All the eight radially aligned pins of probe B, with a radial mutual separation of ~ 2 mm, were set to measure floating potential (ϕ_f). Probe D is composed of a two-dimension array of tips (5x4), with five rows ~ 5 mm radially separated and four tips by row, having a mutual bi-normal (or approximately poloidal) separation of ~ 3 mm. The probe was set to measure at each row: $[\phi_+,\ \phi_f,\ I_s,\ \phi_f]$, where I_s is ion saturation current and ϕ_+ is a positive potential with respect to the wall (at ground connection). The positive potential is set to have the same magnitude by opposite signal to ϕ_-, the biasing potential for the ion saturation current measurement. Both potential voltage were around ± 150 eV and so $\phi_+ - \phi_- \gg T_e$ [eV]. With this configuration, the electron temperature (T_e) can be estimated, $T_e = (\phi_+ - \phi_f)/\log(2)$ [133], as well as the radial turbulent particle flux $\Gamma_r \simeq \langle \tilde{n}_e \tilde{v}_r \rangle \propto \langle \tilde{I}_s \tilde{E}_\theta \rangle / B$, assuming that $\tilde{n}_e \propto \tilde{I}_s$ and $v_r = E_\theta / B \approx -\nabla_\theta \phi_f / B$ [217]. The signals of both probes were acquired at 2 MHz. In addition, the plasma boundary was monitored with two channels of Doppler reflectometry [71]. The system permits to measure, with good spatial-

temporal resolution, the plasma cross-field velocity ($u_\perp$) and the density fluctuation. The perpendicular velocity in the plasma periphery is $u_\perp = v_{E\times B} + v_{ph}$, where $v_{E\times B} = B^{-2}\vec{E}\times\vec{B}$ and v_{ph} is the intrinsic phase velocity of the fluctuation. By considering that the poloidal $E\times B$ rotation is dominant over the phase velocity, which is a good approximation for the plasma edge of TJ-II [71, 219], one can obtain the local radial electric field $E_r \approx u_\perp / B$.

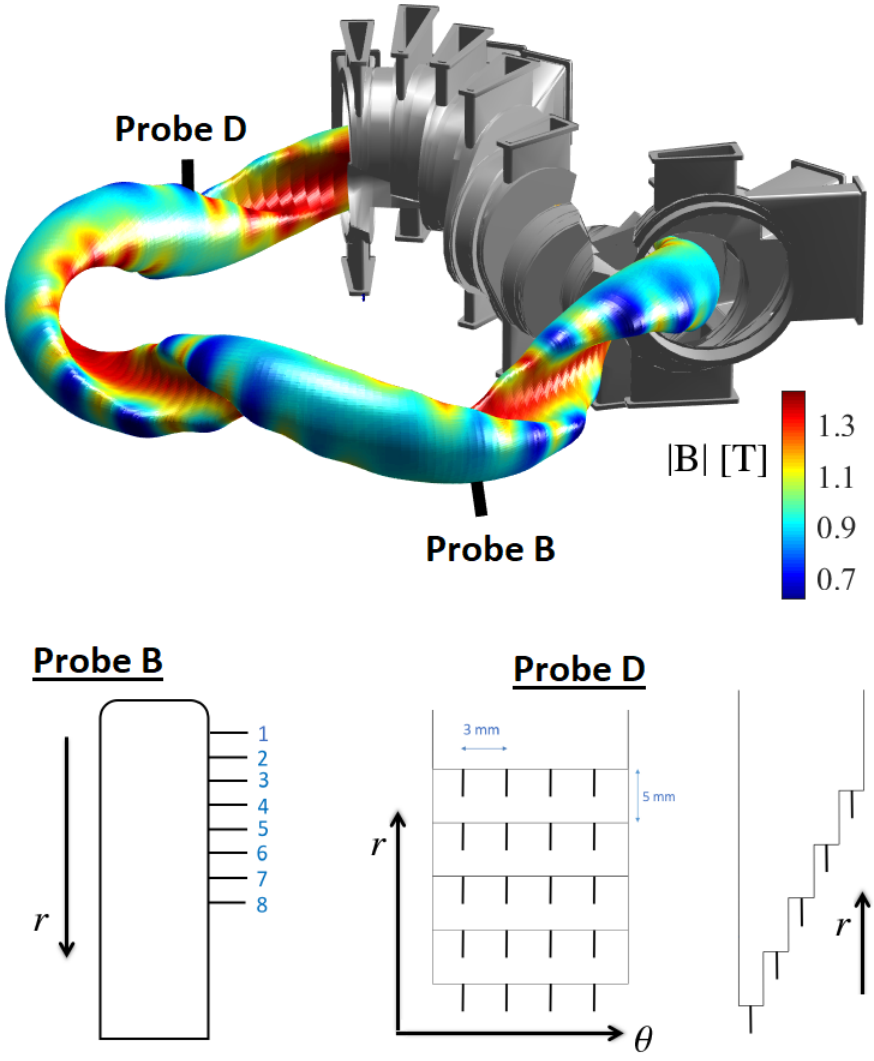

Figure 6.5: Schematic view of the TJ-II last closed flux surface (LCFS) magnetic field strength $|B|$, and the toroidal position of the two probes. The probes B and D are shown in detail at the bottom.

Figure 6.6 shows: a) the time evolution of the central line averaged density together with the two gyrotron power (in arbitrary units); b) the radial electric field at $\rho = r/a \approx 0.8$ measure with Doppler reflectometry; c) averaged floating potential profile (in sub-time windows of 2 ms). In the first phase ($1100 \leq t \leq 1160$ ms), the plasma density increases slowly from around 0.4×10^{19} m^{-3} to 0.6×10^{19} m^{-3}, while E_r reduces roughly following the density variation. The floating potential profile during the same phase exhibits a peaked in the edge ($r - r_0 < 0$) dropping towards the SOL ($r - r_0 > 0$). The slope of the profile is negative, suggesting that the radial electric field is also positive, since $E_r = -\nabla_r \phi_p \approx -\nabla_r \phi_f - 3\nabla_r T_e$ and $\nabla_r T_e > 0$ in the edge and SOL. In this phase, the plasma edge is in the electron root. Between approximately 1160-1190 ms, the density increases over 0.6×10^{19} m^{-3} and the radial electric changes sign, becoming negative. The floating potential profile now exhibits a valley in the edge that increases towards the SOL. In this phase, the plasma edge is consistent with the ion root solution that becomes dominant once the density overcomes its critical value [275]. In the latter phase ($1190 \leq t \leq 1250$ ms), the plasma density decreases and the radial electric turns positive again. The floating potential has the same peaked profile as in the first phase, but with larger values in the edge than before. In this phase, the plasma returns to the electron root dominated solution after the density decreases below the critical value.

Figure 6.7 shows some plasma relevant parameters during the electron-ion-electron root transitions in the plasma edge ($\rho \approx 0.9$) measured with the probe D. The radial gradient of the floating potential (Fig. 6.7 a) exhibits a similar behaviour to the radial electric field measured with Doppler reflectometry (Fig. 6.6), i.e. signal flip sign in the ion root phase, suggesting that $-\nabla_r \phi_f$ is a good proxy for E_r. The ion saturation current (I_s) and the electron temperature (T_e) show roughly opposite trend, while I_s slightly increases during the first phase ($1100 \leq t \leq 1160$ ms), T_e decreases. Both quantities are tied through the density, since $I_s \propto n_e/\sqrt{T_e}$. During the ion root phase,

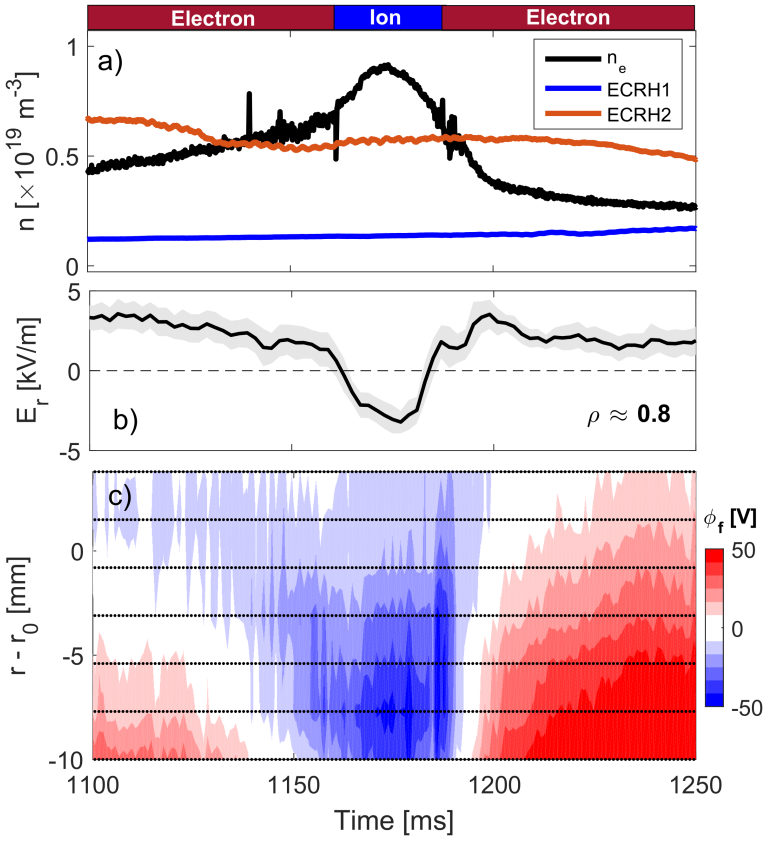

Figure 6.6: Electron-ion-root transition in TJ-II: a) central line density and ECRH power (arbitrary units); b) radial electric field (E_r) measured with Doppler retometry at $\rho \approx 0.8$; c) spatiotemporal evolution of the floating potential, measured with the probe B, where the innermost pin is placed at $r - r_0 \approx -10$ mm or $\rho \approx 0.9$, where r_0 is the LCFS position.

the ion saturation current reaches its maximum value, while the electron temperature reaches its minimum. After the back transition (ion to electron root), the situation returns roughly to what it was before, $-\nabla_r \phi_f$, I_s and T_e assume similar values as in the first electron root phase, with the last two slightly lower and higher, respectively. As has been shown in chapter 4, the turbulent particle flux can be computed from the I_s and E_θ fluctuations preferentially measured at the same location. This requirement is necessary to avoid non-physical phase delay between the two quantities. In practical situations, however, the poloidal electric field can be deduced from two tips measuring plasma potential (or floating potential, by neglecting temperature fluctuation). Other

diagnostics, e.g. heavy ion beam probe (HIBP), one can measure the two quantities simultaneously and at a close position [176]. Nevertheless, some precautions must be taken by using probes in order to obtain good and reliable results. The most

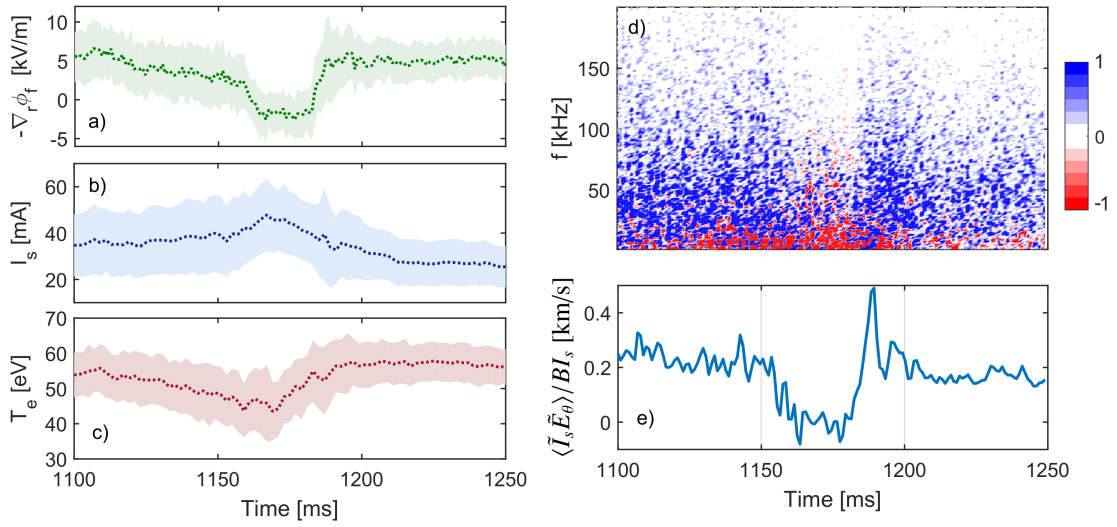

Figure 6.7: Some plasma relevant parameters during the electron-ion-root transition in TJ-II: a) minus the radial gradient of the floating potential; b) ion saturation current; c) electron temperature; d) spectral contribution for the transport ($T(f)$); d) radial particle normalize by mean ion saturation current. All parameters are measure at $\rho \approx 0.9$.

critical one is that the distance between tips measuring potential must be shorter than the eddy poloidal size [17], but larger than at least three Debye lengths to avoid any cross-talk between pins. The tip measuring I_s should be placed between the two potential, which limits the achievement of this requirement. The poloidal electric field was measured in this experiment with two floating potential signals, $d \sim 6$ mm poloidally displaced, where d is shorter than typical turbulence size ~ 1 cm. The ion saturation current was measured with a tip between them. From this configuration, the turbulent particle flux is approximately $\Gamma_r \propto \left\langle \tilde{I}_s \Delta\tilde{\phi}_f \right\rangle / (Bd)$. As discussed in the chapter 4, the turbulent flux can be decomposed in frequency: $\Gamma_r = \int_0^\infty T(\omega) d\omega$, with: $T(\omega) = 2/B|P_{n\phi}(\omega)|k_\theta(\omega)\sin\alpha_{n\phi}(\omega)d\omega$, where $S_{n\phi}$ and $\alpha_{n\phi}$ are, respectively, the cross-power spectrum and the cross-phase between density and plasma potential (or

between ion saturation current and floating potential considering the approximations above), and $k_\theta = \Delta\alpha/d$, where $\Delta\alpha$ is the phase delay between the two floating potential spaced d. Note that $|k_\theta| \leq \pi/d$, where $\pi/d \approx 5.2$ cm^{-1}. In addition, as it was defined in the previous chapter, the effective radial velocity is: $v_r^{\text{eff}} = \langle \tilde{I}_s \tilde{E}_\theta \rangle / I_s B$. Fig. 6.7 d) shows that the spectral contribution of transport comes mainly from frequencies lower than 100 kHz, although the higher frequency contribution is not negligible. The transport is essentially outward with some input of inward in low frequency (< 10 kHz). The overall transport (averaged over all frequencies) is outward in the first electron root phase, reducing sharply in the ion root phase due to a combination of decreased high-frequency contribution and expansion of the inward transport band in lower frequencies. In the last phase (electron root), the spectral contribution of transport returns roughly as it was before, showing that the two-electron root phases share similar transport properties. The normalized transport by the background ($\langle \tilde{I}_s \tilde{E}_\theta \rangle / B I_s$) or effective radial velocity is nearly constant during the two-electron root phase, with a value around ~ 0.2 km/s, but reduces strongly in the root phase to almost zero. This result suggests that the electron to the ion root transition has a substantial impact on the turbulent transport, in accordance with the ECRH to NBI root transition seen in chapter 5.

The cross-correlation is a linear technique that measures the level of similarity between two signals at a given time delay (see chapter 4). The technique has been used to characterize the properties of coherent structures both in the edge and SOL of plasma devices. The radial and poloidal correlation length of fluctuating plasma density or potential are useful quantities to infer on the turbulence cross-field extension and the role of background flows. During the two transitions (Fig. 6.6), the edge radial electric field is modified continuously, going from positive to negative and then to positive again. The effect on the turbulence radial correlation length is obtained here by using the auto and cross-correlation technique. The probe B, with 7 pins

$\sim$ 2 mm radially spaced, was used for this purpose. The reference is a pin roughly 5 mm inside the plasma. The choice is convenient since this is the region where one can usually observe the E $\times$ B shear layer in TJ-II [103] and, thus, the process of streams turning into blobs is expected to happen [195]. Therefore, by measuring the plasma simultaneously in the edge and SOL, it is possible to study how the effective turbulent size changes when the plasma transits between different roots. The signals were band-pass filtered ($2 - 600$ kHz) to eliminate the signal trend, thus highlighting its fluctuating part. The calculation was performed in 4 ms time slices in a long time window covering the two transitions.

To study the radial correlation length, two approaches were considered. In the first one, the turbulence extension is deduced from the cross-correlation at zero delay, which can be thought as an averaged snapshot of the turbulence projected in the radial direction. In the second approach, the maximum of cross-correlation is considered instead, where the aim is to take into account for the fact that the turbulence might be propagating. Note that the maximum can appear at any time delay. Fig. 6.8 a) shows the spatiotemporal map of the maximum of correlation, where the reference (auto-correlation) is indicated by the white dashed line. One can see that the high correlation range get narrower in the ion root phase, becoming broader again in the electron root back transition, with high correlated structures penetrating further the SOL. The map can be fitted in time by two exponential functions starting from the reference position in the inner part towards the core, and towards the SOL. The final radial correlation length is defined as the sum of the two exponential coefficients. Fig. 6.8 b) shows the radial correlation defined from the maximum correlation (L_r^{max}) and at zero time delay (L_r^0, where the corresponding map is not shown here); the former is larger by definition. Both L_r^{max} and L_r^0 slowly decrease as the electron-ion root transition approaches. The result suggests that not only the local size of turbulence (represented by the correlation at zero delay) is affected by the transition

or the evolution of the radial electric field, but also the turbulence radial spread (L_r^{max}) becomes more restricted. During the electron root after the back transition, both quantities increase again, reaching values comparable to the first electron root phase. Although both quantities become comparable in some time interval, suggesting that either the propagation becomes less important or the turbulence radial size largely overcomes the pins separation, in most of the time, $L_r^{max} > L_r^0$. This result indicates that the propagation yields an effective correlation length larger than the standard local correlation length. One can argue that travelling coherent structures make the correlation length non-local. This can ultimately affect the SOL profiles [181].

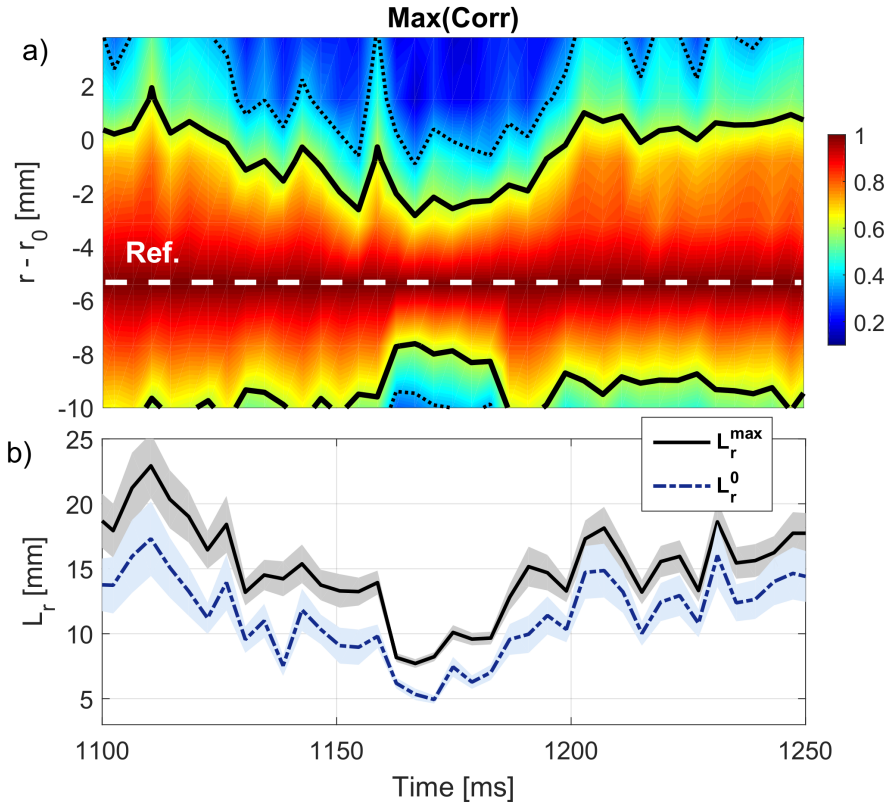

Figure 6.8: Turbulence correlation length during the electron-ion-electron transition: a) spatiotemporal map of the maximum of correlation; b) radial correlation length for the maximum correlation (L_r^{max}) and at zero time delay (L_r^0) defined from the sum of decay coefficients of two exponential functions starting from the reference.

Turbulence self-regulation benefits from the turbulence-free energy, by creating bigger structures such as zonal flows in inverse cascades. In this process, turbulence can feedback the flow thus altering the radial force balance and ultimately the local radial electric field. Zonal flows traces are identified here by two methods: long-range correlation (LRC) based on two-point cross-correlation and biorthogonal decomposition (BOD).

LRC refers to the cross-correlation between two signals (measuring the same quantity) that are far enough spaced in the plasma (several correlation lengths), but preferentially at the same magnetic surface. A typical length for the LRC is the device characteristic size. In TJ-II, high levels of LRC have been observed between two remote toroidal spaced probes measuring floating potential [207]. The same is not observed for ion saturation current measurement. Those results have shown that the radial electric field evolution is connected with the rise and fall of the potential LRC. To verify the role of LRC in the edge-SOL turbulence coupling during the electron-ion-electron root transition, the probes B and D (see Fig. 6.5), remotely separated $\Delta\phi \approx 157^{\circ}$ (toroidal angle), were used to compute the floating potential LRC over time. The typical global potential structure that yields a significant LRC is thought to be the zonal flows. The structure is characterized by m = n = 0 and low frequency oscillation (typically $f \leq 1$ kHz). Fig. 6.9 a) shows the radial derivative of two radial spaced ϕ_f signals in the probe D located at $\rho \approx 0.9$. Note that $-\nabla_r \phi_f$ time evolution is similar to E_r, measured using Doppler reflectometry (Fig. 6.6), particularly, both flip sign from about 1160 to 1190 ms. Hence, $-\nabla_r \phi_f$ is a good 'proxy' for edge radial electric field in this experiment. Fig. 6.9 b) shows the LRC between a fixed pin in the probe D with the eight pins of probe B, with mutual radial separation of ~ 2 mm. The LRC is defined here as the cross-correlation between remotely separated probes at zero delay. One can see that the largest long-range correlation is with the pins located in the near edge during the electron root phase. Near the transition, from

1150-1160 ms, the LRC reaches its maximum value (~ 0.8), dropping sharply later during the ion root phase (1160-1190 ms). Note the LRC pattern has a clear radial profile. After the back transition, LRC increases again in the edge, but with lower values than before. Taking the innermost pin of the probe B and performing the cross-correlation with the reference pin in the probe D, the result in time is shown in Fig. 6.9 c) for a wide range of time delays. Note that in the first electron root phase there is a plume of high correlation around the zero delay, suggesting that the two remote separated potential is roughly synchronized. The correlation intensifies close to the transition and then decreases in the ion root phase. The plume returns strong in the second electron root phase but slightly shifted towards positive delay. Fig. 6.9 d) shows the time evolution of the LRC between the two pins in c). It is interesting to note that the LRC is over $1/e$ almost all the time (used as a lower limit for long-range correlation [162]). In the ion root phase, LRC drops by a combination of lower amplitude and shift to $\tau \neq 0$. Therefore, the long-range correlation effect is more intense in the electron root phase, reaching its maximum during the electron to the ion root transition, in agreement with theoretical predictions [275]. This effect is likely related to zonal flows.

The identification of global structures can be done by using the biorthogonal decomposition, as described in section 6.1. It has been shown in TJ-II, from measurements of two remote probes [272] in the plasma edge, that this technique can identify global structures presenting high levels of long-range correlation and low frequency ($\sim$ 1 kHz) oscillation. Given that those are precisely the properties of zonal flows, they were identified as such. In Fig. 6.9 is shown that the LRC is higher in the electron root phase and becomes further amplified in the electron-ion root transition. Besides, the high LRC range has a clear radial dependence, therefore, any radial displacement of the global structure can yield a lower LRC if one considers the correlation between only 2-points, as shown in Fig. 6.9 c and d). The BOD extracts information from

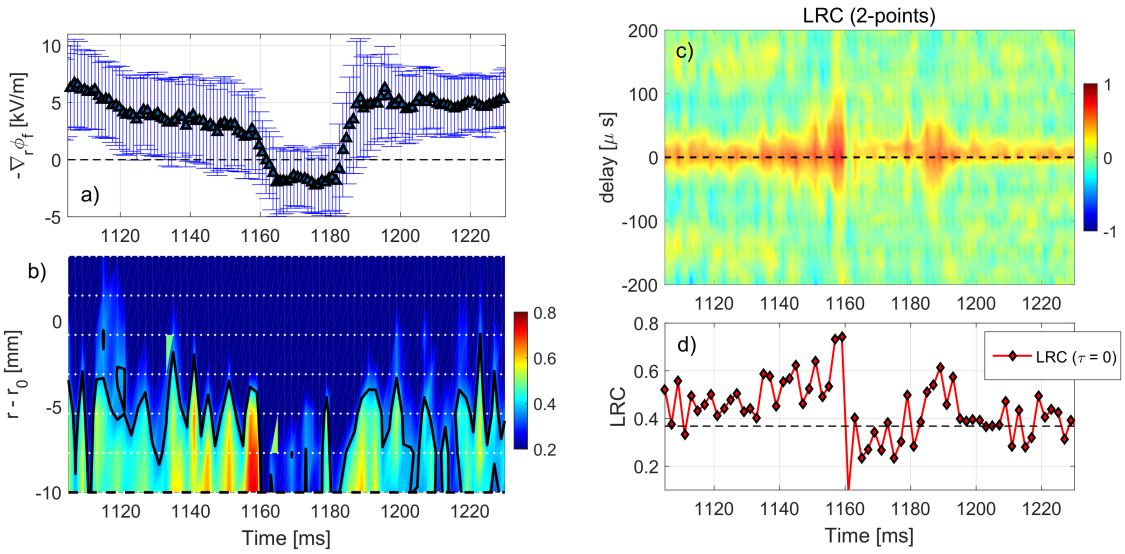

Figure 6.9: Long distance correlation during the electron-ion-electron root transition. The radial gradient of the floating potential ($-\nabla_r \phi_f$), considered as proxy for E_r in this experiment, is shown in a), while the cross-correlation at zero time delay between a reference pin in the probe D with al the pins in the probe B is shown b) as time evolution. The correlation between the innermost pin in the probe B with the reference in the probe D is shown in time for wide range of time delay. The LRC between these two pins is shown in d).

all signals included in the analysis, thus, it is less depended on whether the structure moves or not, as long as this displacement is covered by the probe resolution. The biorthogonal decomposition is built here by considering all the signals in the probe B, covering a range of about 1.5 cm, and 6 pins in the probe D, two per row with mutual separation of 5 mm. The radial range covered by the two probes presents some overlap. All pins were set to measure floating potential ϕ_f. The array of signals in a long time window: 1100-1250 ms, is subdivided into smaller time windows of 4 ms where, by using SVD, the 'topo' and 'chrono' functions for all modes and their respective coefficients are obtained. It has been shown in section 6.1 that the correlation, or the LRC, can be obtained directly from the topos of remotely separated signals.Fig. 6.10 shows the result of this procedure. For sake of comparison, $-\nabla_r \phi_f$, a proxy for the local radial electric field, was plotted again. Fig. 6.10 b) shows the amplitude of the three most dominant modes in time. The λs are normalized by the

square root of the product between the chromo and topo dimensions. Note that λ_1 sharply drops in the ion root phase ($-\nabla_r \phi_f < 0$). The long-range correlation for the three modes is shown in Fig. 6.10 c). Mode 1 presents the largest LRC, with higher values in the electron than the ion root phase. Note that the $C_{LRC}^{\lambda_1}$ peaks in the electron-ion root transition, dropping later, and increasing again in the ion root phase. The time behaviour of the three modes is depicted by the corresponding chrono functions. Fig. 6.10 d) shows the spectrogram of the three modes. Note that a high spectrum contribution appears for low-frequency ~ 1 kHz near the transition, as seen by the chrono of the mode 1. Similar behaviour is observed in the mode 2, but with higher frequency (around 5 kHz) and lower amplitude, while it is virtually absent in the mode 3. The combination of low-frequency oscillation with a relatively high long-range correlation are strong signatures of zonal flows. Therefore, the results present in the graphs of Fig. 6.10 indicate that zonal flows are amplified in the transitions, but it is more intense during the electron-ion root transition, in agreement with theoretical predictions [275]. Note that the time evolution of λ_1 is a good proxy for zonal flows strength, it peaks in regions where both $C_{LRC}^{\lambda_1}$ and the low-frequency spectrum are significant.

Following the approach presented in the Fig. 6.8, one can also study the turbulence extension and how it evolves in time during the roots transitions by using the mutual information (MI), discussed in section 6.1. The technique quantifies the level of dependency or shared information between two process. Different from the correlation that is based on linear dependency, MI is nonlinear and based on Shannon entropy [137]. Given that the plasma edge is a strong nonlinear environment, where different processes, such as mode coupling and self regulation, together with breaking of streamers [195] and merging/breaking of blobs, all happen simultaneously, this technique can provide some complementary knowledge about the turbulent coupling between the edge and SOL. The MI was computed by considering the same reference

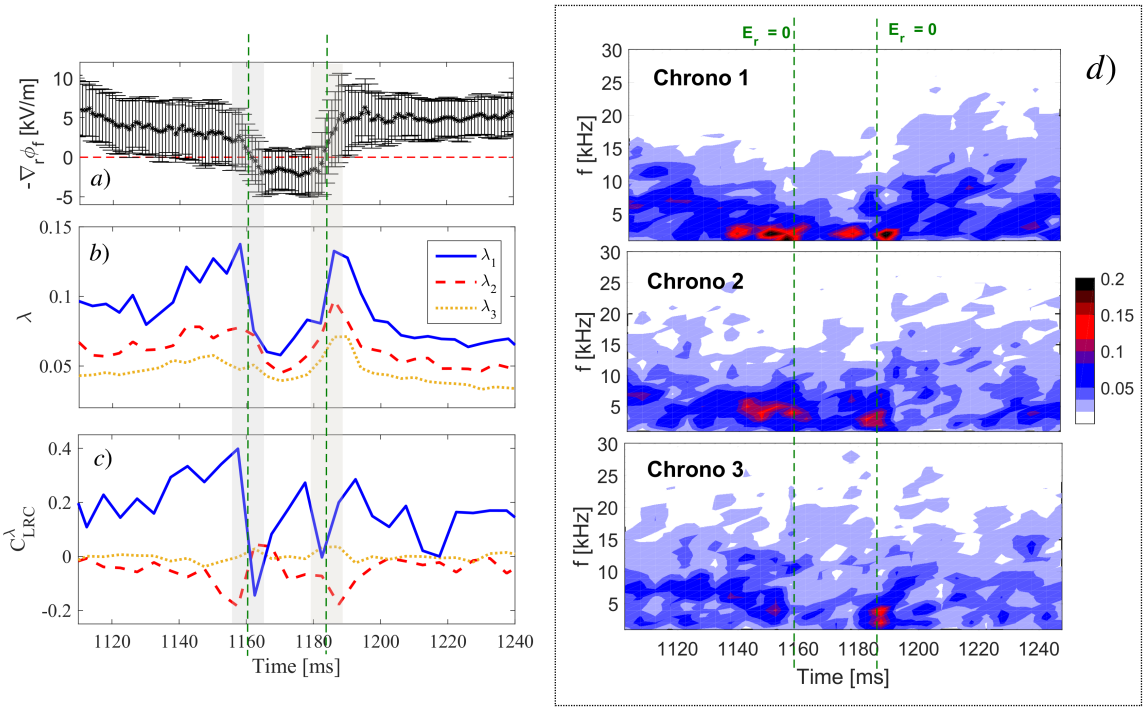

Figure 6.10: Biorthogonal analysis: time evolution of a) $-\nabla_r\phi_f$, b) amplitude of the three most dominant modes, and c) long range correlation. The spectrogram of the chronos corresponding to the three dominant modes is shown in d).

in the probe B as before: $r - r_0 \approx -5$ mm, around the TJ-II shear layer location. The result is shown in Fig. 6.11, where is plotted the maximum MI value (on logarithmic scale) at any delay. The MI single contribution from the raw floating potential signals over the time window: $1100 - 1250$ ms was evaluated in 4 ms time slices. The MI radially extension reduces in the ion root phase ($1150 \leq t \leq 1190$ ms) when the highest values of MI become constrained in a short radial range around the reference location. In the electron root phases, this range becomes extended up to near SOL. The depicted behaviour is similar to the correlation maps shown in Fig. 6.11, where they all follow roughly the density time evolution and the correspondent root transitions. The result suggests that during the ion root, the structures become less nonlinear dependent over the correlation length, possibly due to the $E \times B$ break of turbulent cells (Fig. 6.7 d) and e).

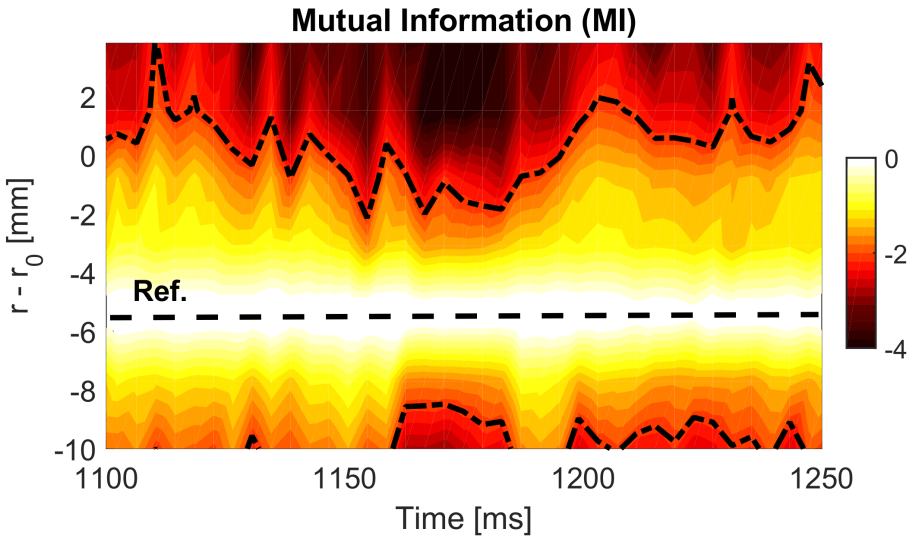

Figure 6.11: Mutual information (MI) on logarithm scale over time during the electron-ion-electron transitions. The dashed white line indicates the reference location while the thick black line represents the level $\log(\mathrm{MI}) = -2$.

As discussed in section 6.1, the mutual information technique does not tell any information regarding propagation. Transfer Entropy (TE), on the other hand, offers a way to compute the information flowing between two signals [270]. This can be a powerful tool for studying the turbulent edge-SOL coupling. TE provides a novel way to directly quantify the propagation of turbulence, or turbulence spreading, without relying on the mechanisms that might drive this propagation [101]. Turbulence spreading has been observed in global simulations [255, 204, 141, 156, 157, 43, 154], but experimental evidences of the phenomena are still scares [72, 127, 101]. Global simulations coupling the plasma edge and SOL [43, 154] suggest that turbulence that arises and growths in the region of maximum pedestal pressure spreads towards the SOL. The increase of turbulence level in the SOL can enhance the cross-field transport in this region and ultimately the SOL width. As discussed in section 6.1, although in most of the present tokamaks the heat flux width seems to be mainly set by neoclassical effects [67, 97], in ITER and beyond turbulence is expected to play a leading role [42, 154]. The strength of the $E \times B$ shear layer, that depends on ρ_i/R, where

ρ_i is the ion Larmor radius and R is the major radius, seems to be the key factor. In chapter 5, it has been shown that the turbulence can control the level of local turbulence (represented by the ω_D parameter) and the level of turbulence spreading (ω_S). This effect is studied here by using the transfer entropy technique during the spontaneous electron-ion-root transition using probe B measuring floating potential.

Figure 6.12 shows the transfer entropy between two pins (2 and 4), $\sim$ 5 mm radially displaced and located in the plasma edge ($r - r_0 \approx -5$ mm). According to the adopted reference, T_{2-4} refers to propagation from the pin 2 to 4, while T_{4-2} is the opposite, i.e. from 4 to 2. The analysis was done in sub-time windows of 10 ms and bin number m = 5. The radial gradient between the two potentials is shown at the top of Fig. 6.12, where the flip of signal characterizing the root transitions is well depicted. In the first electron root phase ($1100 \leq t \leq 1150$ ms), the net propagation is outwards, i.e. the information flows predominately from the pin 2 (inner) to the 4 (outer) at $\sim$ 1 km/s (deduced from the probe separation and the TE time delay). Near the transition, T_{2-4} reduces, but T_{4-2} exhibits an increment in long time delays. This effect happens concomitantly with the observed enhancement of zonal flows (Fig. 6.9 and 6.10). But, the TE technique requires long roughly stationary time windows, thus, one has to be careful drawing any conclusion from transient events. In the ion root phase ($1160 \leq t \leq 1190$ ms) the propagation ceases nearly completely in both directions. In the back transition, T_{2-4} increases again, initially in a wider range of time delay, similar to the first transition. The maximum TE shifts from higher to lower time delays, suggesting a variation of velocity. In the electron root, far from the transition ($1200 \leq t \leq 1250$ ms), the pattern of propagation resembles to the first phase, with an effective radial propagation of about 1 km/s.

The extension of propagation in the three phases can be better visualized by computing the TE from a reference signal with the remaining. Taking the innermost pin in the probe B ($r - r_0 \approx -10$ mm) as the reference, the outward TE propagation

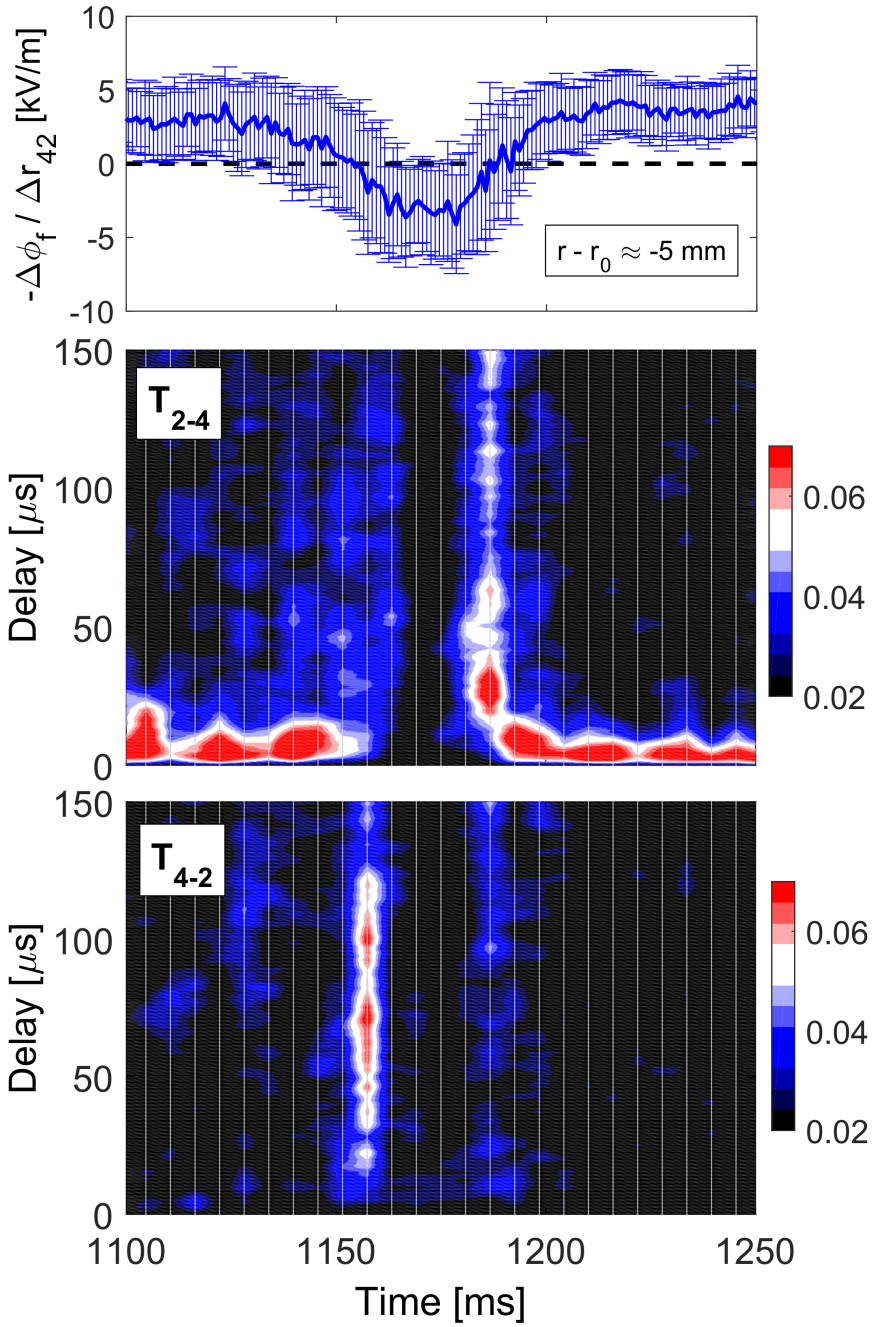

Figure 6.12: At the top: $\nabla_r \phi_f$ between the pin 2 (inner) and 4 (outer) in the probe B, placed at the plasma edge $r - r_0 \approx -5$ mm and with mutual separation of ~ 5 mm. At the bottom is shown respectively, the transfer entropy from 2 to 4 (T_{2-4}), and from 4 to 2 (T_{4-2}).

is shown in Fig. 6.12 in three-time slices corresponding, respectively, the electron-ion-electron root phases (also shown in the time evolution of central line averaged density).

The vertical axis of the three frames shows the probe position with respect to the LCFS and the horizontal one the time delay. In the first phase, electron root, a plume of propagation starting from the reference is evident, extending up to the near SOL. Note that the slope of the plume gives the velocity of propagation in each position and that seems to slow down near the plasma boundary ($r - r_0 = 0$). During the ion root, frame number 2, the plume almost disappears, being restricted to a narrow range around the reference. In frame 3, the plasma edge returns to the electron root again, the plume comes back even more intense than before, penetrating further into the SOL. Near the plasma boundary, the plume is broader in the horizontal axis, suggesting the presence of a transport barrier in this region that slows down the propagation and reduces its amplitude.

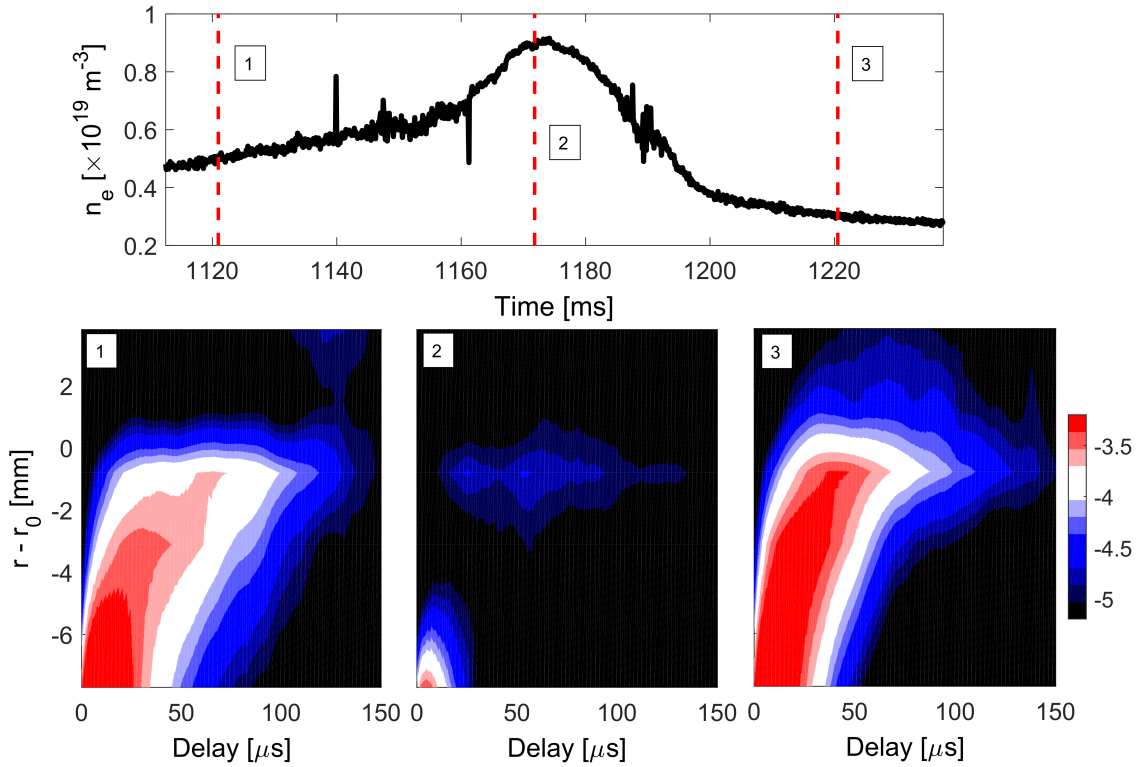

Figure 6.13: At the top: time evolution of the central line averaged density. At the bottom: radial profile of the transfer entropy (on logarithm scale) starting from a reference at $r - r_0 \approx -10$ mm in three time moments shown at n_e at the top.

The results obtained through the transfer entropy indicate a strong reduction of turbulence propagation during the ion root phase ($E_r < 0$). In the electron root ($E_r > 0$) phases, a plume of propagation of about $\sim$1 km/s from the edge towards the SOL suggests that the turbulence in this two regions is connected. The partial decoupling during the ion root seems to be related to the time evolution of the radial electric field. Since the level of turbulent transport in the SOL impacts on the SOL width and consequently on the heat flux width (λ_q), those finds provide an important piece of information to better understand the mechanisms that set the SOL in fusion devices.

6.4 Conclusion

Propagation of turbulence from the pedestal or near the edge to the SOL region is one of the candidate for the larger λ_q observed in some recent simulations for ITER condition [42, 43, 154]. In this chapter, it was discussed the impact of a varied radial electric field on turbulence propagation in TJ-II. The results presented here were based on spontaneous electron-ion-electron root transition, where the edge radial electric field flips sign slowing from positive to negative, and back to positive again. From the biorthogonal analysis, considering multiple floating potential signals from two remotely separated probes, it was shown that the amplitude of the dominant global mode is related to zonal flows [272] and becomes amplified in the transitions, in agreement with simulations [275]. In the ion root phase (where an enhanced shear layer has been observed [101]) the turbulent particle flux and radial correlation length reduced compared to the electron root phase. While these results indicate that turbulence is locally affected in the ion root phase, the transfer entropy [226] applied to radially spaced signals around the LCFS gives information on the turbulence propagation. This analysis shows that turbulence propagation is

predominant outward with a typical velocity of 1 km/s in the electron root phase, but it nearly ceases completely during the ion root phase, suggesting the edge-SOL turbulence becomes decoupled. These findings present an experimental validation of the turbulence spreading phenomenon and how radial electric fields could impact its velocity and intensity.

Chapter 7

Cross Field Transport in the RFX-mod tokamak

The RFX-mod is a Reversed Field Pinch (RFP) device that started operating in Padova, Italy, in 1992, and it has been through major updates since then [239]. The machine has major radius $R_0 = 2.0$ m and minor radius $a = 0.46$ m, and maximum plasma current up to 2 MA. Owing to its peculiar configuration in which the plasma confinement relies strongly on self-organization properties [161], the device is a formidable laboratory for studying MHD instabilities. A variety of magnetic perturbations (e.g. tearing/resistive kink mode) are found in the RFP standard configuration. While their growth can induce line stochastization and chaos [70], their presence is determinant for the *Dynamo Effect* [32]. Besides, the machine typically operates in very high plasma current (up to 2 MA) that, in turns, yields high plasma betas that ultimately drives resistive wall mode (RWM) [16]. Given these drawbacks of the reversed field configuration in terms of performance, active control of magnetic boundary is necessary to avoid that the instabilities take over rapidly and lead to the plasma disruption. On this purpose, RFX-mod is equipped with external magnetic coils (192: 48 toroidally by 4 poloidally) installed on the plasma wall, covering the

full torus. This system permits the MHD active control in real-time. In addition to the actuator coils, the machine is also composed of saddle coils that are aimed to monitor the plasma current and magnetic field, i.e., they are the sensors of the MHD feedback control system of RFX-mod [299].

Thanks to its flexibility, RFX-mod can also operate as low current tokamak in both circular and single null configuration. In this chapter and the subsequent one, the focus will be on RFX-mod operating as single-null tokamak with plasma current $I_p \leq 50$ kA, toroidal magnetic field $B_0 \leq 0.55$ T, and deuterium as working gas. In this configuration, the edge safety factor is $q_0 = 3 - 4$ and the central line averaged density is within the range (2-6)$\times 10^{18}$ m^3.

As discussed in the chapter 2, the biasing electrode technique has been used in tokamaks and stellarators to induce high confinement regime, however the application of this technique on a D-shaped tokamak plasma represents a novelty. The method relies on the key role played by radial electric fields (or its shear) in suppressing turbulent transport that is the main obstacle for the further growth of the pressure gradient in the plasma edge. The induced radial current by the electrode is able to enhance the radial electric field in a short time scale, before the radial force balance and ambipolar condition take over [52]. Even in bigger machines where H-mode is achieved by external heating, a minimum value of radial electric field is necessary to trigger the transition [221]. The electrode used in this experiment is made of graphite in an ellipsoid shaped (115 x 25 x 65 mm^3). It was inserted into the plasma from the bottom (Fig. 7.1). The bias is applied with respect to the plasma wall, that is in ground connection, in a squared 200 ms pulse. The electrode biasing circuit is shown in Fig. 7.1 b). In addition, the biasing power was real time controlled to avoid overload and transient effects such as electric arcs. Fig. 7.1 a) shows the electrode characteristic curve (Langmuir curve) as measured accounting for several shots with similar parameters in single-null configuration. One can recognize the ion

saturation current branch for voltage lower than -200 V and the exponential growth up to positive voltage where the electron saturation current begins to settle. The biasing configuration with positive voltage was not able to induce a substantial improvement in the plasma confinement within the performed experimental campaign. A similar effect was observed in TJ-II in NBI plasmas [103]. The most plausible explanation is that the biasing in those cases act to reduce the local or ambipolar radial electric field [52], making the E_r profile less steep and thus reducing the $E \times B$ shearing rate. The negative biasing, on the other hand, makes the radial electric field profile even more stepper (increasing the plasma poloidal rotation), which enhances the shearing rate leading to turbulence suppression. Positive biasing can yield improved plasma confinement as well, depending on the background radial electric field [26, 101]. The results presented in this chapter is for biasing at -400 V with electrode inserted 8 cm at the plasma edge ($\rho \approx 0.83$, with $\rho = r/a$, where r is the radial position from the plasma center). Such experimental condition has been shown to induce a stable and reproducible H-mode transition in RFX-mod [243].

The plasma periphery was monitored with the U-probe (Fig. 7.2). This probe is composed of a set of electrostatic and magnetic sensors displayed in a two-dimension array covering $\sim 112 \times 24$ mm in the cross-field plane. Each tower is equipped with 40 graphite tips (5x8 array), 5 per row roughly aligned poloidally (or in the bi-normal direction) and displaced 3 mm from each other, and 8 tips each column roughly aligned in the radial direction with mutual separation of 6 mm. The probe is also equipped with seven 3-axial magnetic coils installed in each tower, with radial and poloidal separation of about 6 mm and 88 mm, respectively, allowing the simultaneous measurement of the fluctuation of three components of the local magnetic field. Based on the filamentary probe concept analogous probes have been built and used in TORPEX [87], TJ-II [247], COMPASS [144, 244], and more recently in Wendelstein 7-X [6, 240]. The U-probe probe was inserted into the plasma edge of RFX-mod from

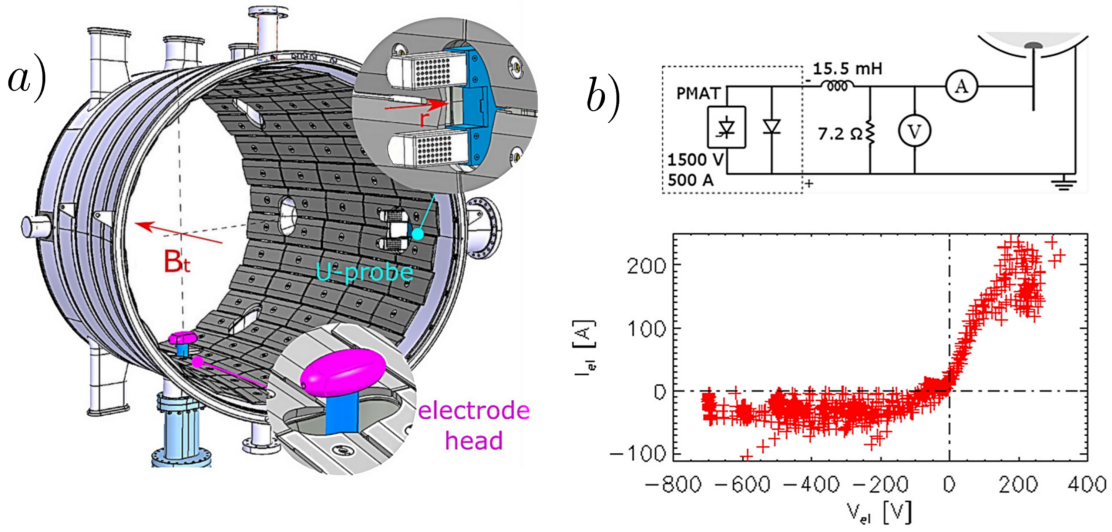

Figure 7.1: Schematic view of RFX-mod a), showing the toroidal magnetic field (counter-clockwise by looking from the top), the U-probe (inserted from the equatorial plane) and the electrode biasing (inserted into the plasma from the bottom). The correspondent electric circuit of the external electrode is shown in b), with its characteristic curve (or Langmuir curve) at the bottom for similar shots in RFX-mod operating as tokamak in single null configuration. Figure adapted from [243].

the midplane in a shot by shot basis. In the configuration reported in this chapter, the U-probe was set to measure simultaneously floating potential (ϕ_f), ion saturation current (I_s), and the positive potential (ϕ_+, with ϕ_+ = -ϕ_-, where ϕ_- is the biased voltage for measuring the ion saturation current) in the 5-pins balanced triple probe (see chapter 4). Fig. 7.2 shows in more detail the measured signals and how they were arranged in the two towers. In addition, the simultaneous measurement of the cross-field components of the magnetic field $\tilde{B}_r$ and $\tilde{B}_\theta$ permit to calculate the local parallel current density in different positions as will be discussed in section 7.5. The data were acquired at 2 MHz sampling rate.

7.1 L-H transition in the RFX-mod tokamak

High confinement mode (H-mode) induced by an external electrode biasing in ohmic discharges in the RFX-mod operating as tokamak has been reported recently [243].

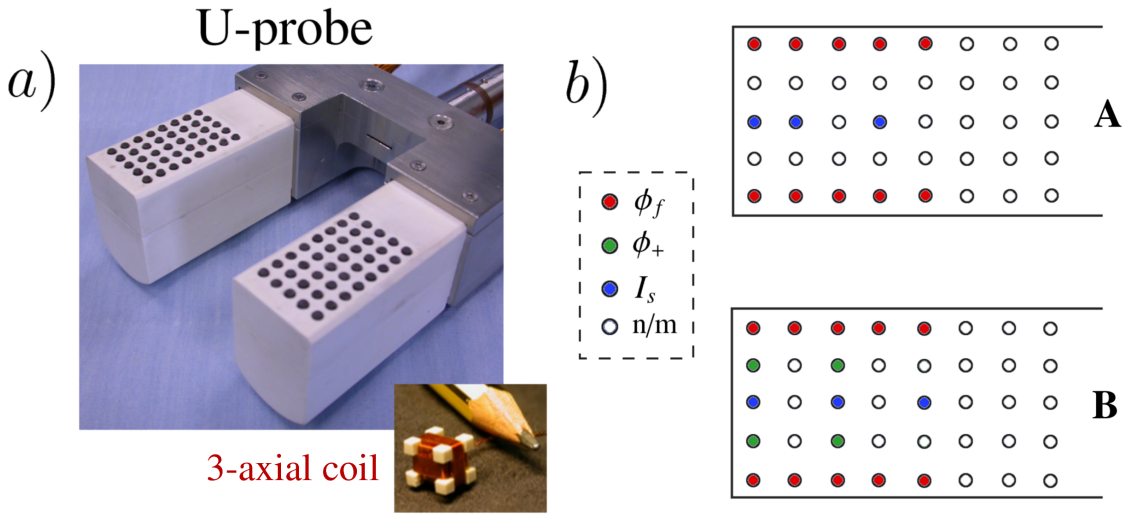

Figure 7.2: U-probe: a) picture showing the two towers with 40 graphite tips installed in each and one of the fourteen 3-axial coils; b) experimental configuration to measure floating potential (ϕ_f), ion saturation current (I_s), and the positive potential for measuring the electron temperature according to the 5-pins balanced triple probe configuration.

Different from the classic H-mode obtained when the external power heating overcomes a threshold [279], that in turns, depends on the characteristics of the plasma and the confinement fields, in biasing experiments the plasma is not necessarily heated [258, 101]. This technique relies on the key role of edge radial electric fields on induce L-H transition [221], by stabilizing turbulence in this region and thus allowing the steepness of the pressure profile and the enhancement of the energy confinement time [273, 116]. The typical feature of this experiment is a fast and intense drop of the D_α line (midplane) followed by an increase of the central line density. Fig. 7.3 shows three similar shots. The maximum achieved density is below $0.8n_G$, where n_G is the Greenwald density, which provides a relatively safe margin for high triangularity below the limit for triggering MARFE [100]. In the shot #39140, however, the density increases beyond $0.8n_G$, which is the possible reason for a disruption around 750 ms. Similar behaviour is also seen in the #39143, but the price to pay in this

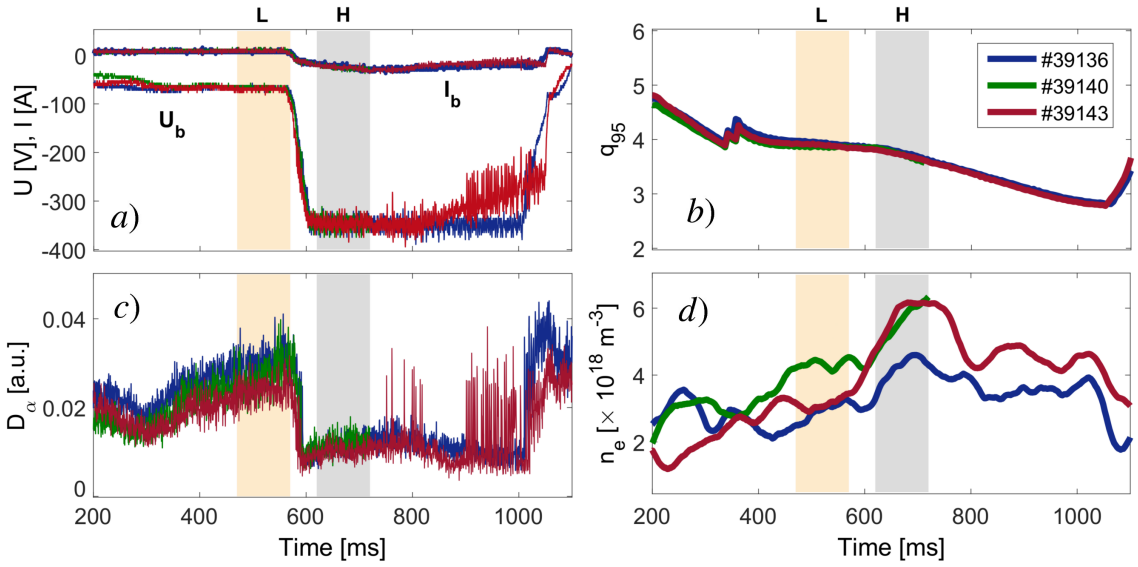

Figure 7.3: L-H transition in RFX-mod running as tokamak induced by an external electrode biased inserted 8 cm into the plasma edge. a) biasing voltage and drained current, b) edge safety factor, c) D_α line signal, and d) central line averaged density for three shots: #39136, #39140 and #39143. The two colourful areas behind each graph represent the time windows considered in the following analysis of filaments dynamics.

case was the rise of an ELM-like instability. This shot will be studied in more detail in the next chapter.

The effect of biasing on some of the electrostatic signals of the U-probe can be seen in Fig. 7.2. When biasing is applied around 600 ms, I_s increases in the edge ($r - r_0 \approx -2.9$ mm, where r_0 is the last closed flux surface position), and decreases in the near SOL ($r - r_0 \approx 0.5$ mm), suggesting that the plasma density profile becomes steeper, since $I_s \propto n_e\sqrt{T_e}$. The floating potential, $\phi_f \approx \phi_p - \alpha T_e$, where ϕ_p is the plasma potential and α is a constant that is approximately 3 for deuterium plasmas, becomes less negative in the edge (reaching values similar to the biasing voltage) and varies slightly in the SOL. When biasing is switched off, around 1000 ms, the parameters return as they were before biasing, i.e. the plasma returns to L-mode.

The radial and poloidal magnetic field fluctuation are shown in Fig. 7.4 within the range 20-1000 kHz. These signals were obtained by numerically integrating the

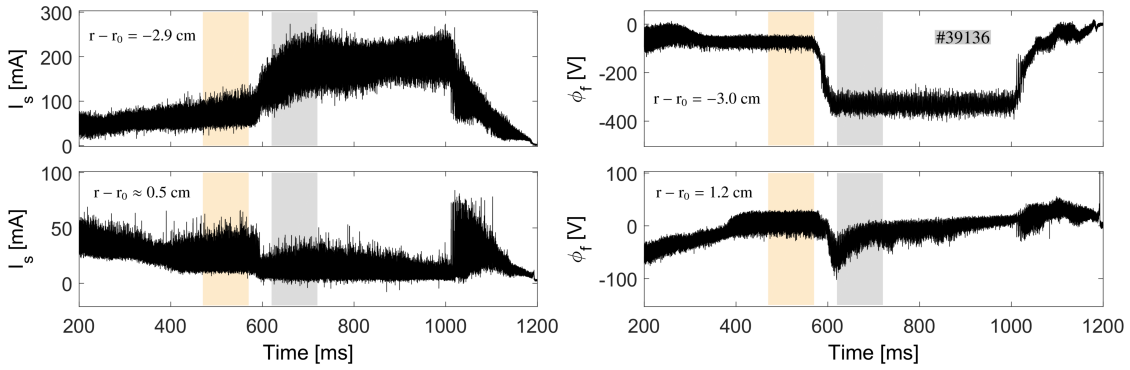

Figure 7.4: Ion saturation current (I_s) and floating potential (ϕ_f) time series in the edge and SOL during the biasing transition.

coil signals in time, $B_i = 1/A_i \int \dot{B}_i dt$, where A_i is the coil effective area orthogonal to the magnetic field component corresponding to the index i. Fig. 7.4 shows $\tilde{B}_r$ and $\tilde{B}_\theta$ in time for a coil in the edge and SOL before and during biasing. In addition, it is shown the corresponding spectrogram computed in time slices of 2 ms. During biasing ($600 \leq t \leq 1000$ ms), the spectral contribution of the magnetic field fluctuation in high-frequency becomes further enhanced, particularly one can see some traces of high-frequency bands in the poloidal component of the coil in the edge. The signals of the coil placed in the SOL also presents some high-frequency activities (lower than the one in the edge), with both components behaving quite similarly. As shown in the Ref. [243], the enhancement of high-frequency activities during biasing is very reproducible over several shots (even in circular configuration). As will be discussed in the next chapter, such behaviour is likely related to electromagnetic instabilities.

The main goal of using a biasing electrode is to modify the radial electric field and ultimately the level of $E \times B$ shear flow. In Fig. 7.6 a), it is shown the floating potential represented as a two-dimension map in L and H-mode. The signals were averaged in time windows before and during biasing (shaded area shown in the Figures 7.3 and 7.4), and the graph was built by using 2D quadratic interpolation to make the data visualization clearer. The dashed lines in both figures represent the last closed flux surface (LCFS) position, separating the plasma edge (lower part) from the SOL

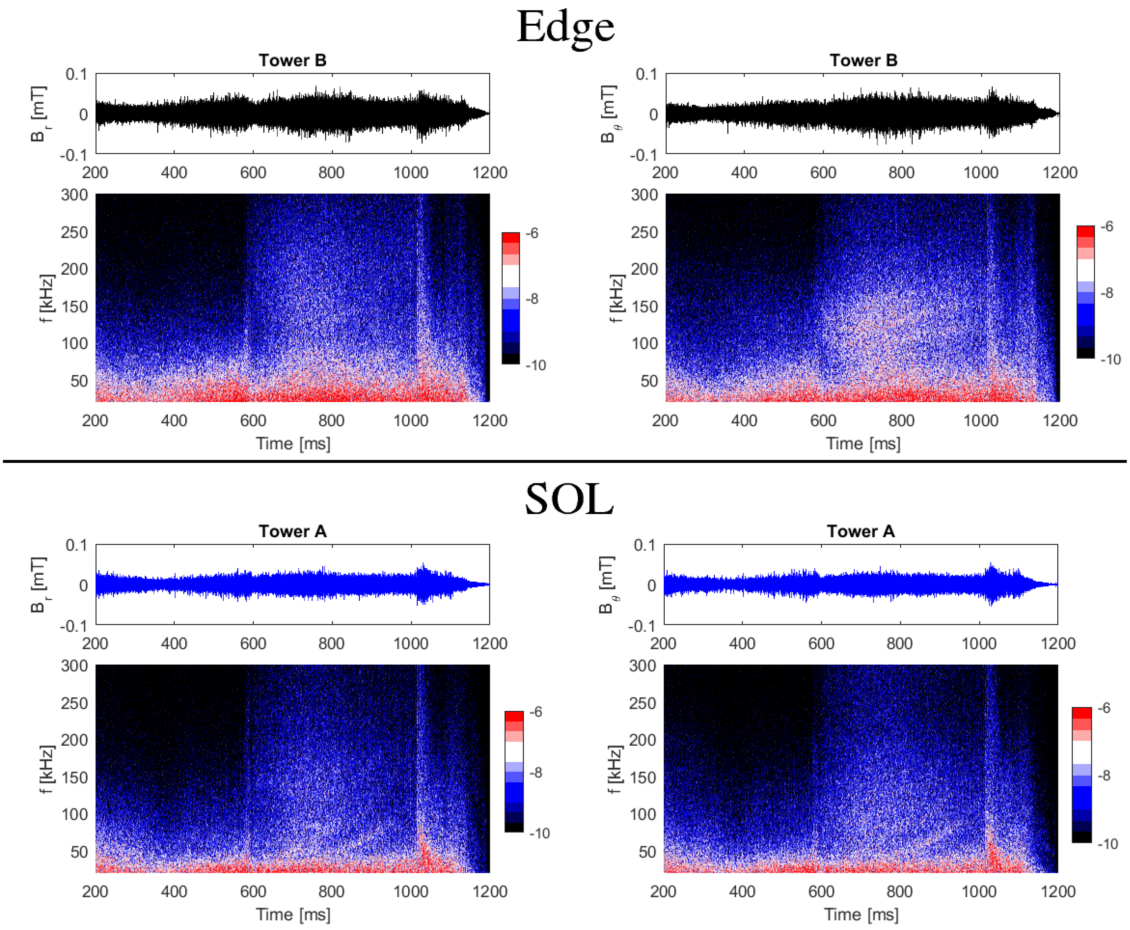

Figure 7.5: Radial (left panel) and poloidal magnetic (right panel) field fluctuation: time series and spectrogram for a coil placed in the edge (top) and in the SOL (bottom).

(upper part). In addition, the white arrows represent the $E \times B$ flow deduced from $\vec{v}^{E\times B} = \vec{E}\times\vec{B}/B^2 \cong -\vec{\nabla}\phi_f \times \vec{B}/B$, i.e. neglecting the temperature contribution. One can see clearly from the absolute values that the floating potential change strongly in the edge. The already presented potential well becomes further enhanced while in far SOL the values do not change much. The arrows pattern indicates that the flow in both cases is mainly downward and stronger around the LCFS. Fig. 7.6 b) shows the radial profile of the floating potential before (L-mode) and during biasing (ELM-free H-mode). One can see the strong impact induced by the biasing on the profile, especially near the plasma boundary where it becomes much steeper. In the far SOL,

beyond $r - r_0 = 20$ mm, the potential is similar in both regimes. This result suggests that this range is already located in the wall shadow (or limiter shadow) region. This point will be further discussed later. The ϕ_f data in both cases is interpolated with a third order Savitsky-Golay filter [137]. The steeper potential profile indicates larger radial electric field or poloidal rotation since $v_\theta^{E\times B} = E_r/B$. Fig. 7.6 c) confirms that, where $v_\theta^{E\times B}$ is obtained from the derivative of the interpolated curves. The errors are estimated from the derivative operation, i.e., propagation of uncertainty, where the error of the position was neglected, together with the ensemble error since the derivative was performed in ever 2 ms. In Fig. 7.6 c) is shown that during H-mode, $v_\theta^{E\times B}$ becomes enhanced around the LCFS, with values up to -20 km/s. It is worth noting that this values is overestimated due to the absence of the temperature correction that yields $-3\nabla_r T_e/B > 0$. Following the same procedure, the $E \times B$ shearing rate can be obtained from the derivative of $v_\theta^{E\times B}$, $\gamma_{E\times B} \approx dv_\theta^{E\times B}/dr$. One can note in this case a shear layer around the LCFS, with a positive and negative shear zone with values up to $|\gamma_{E\times B}| \approx 1 \times 10^6$ s^{-1}.

In chapter 4, it was discussed how one can evaluate the wavenumber-frequency spectrum ($S(k,\omega)$) from the measurements of two displaced signals. $S(k,\omega)$ is a fundamental quantity that provides information on the dispersion of waves in a medium that not necessarily obeys $k = k(\omega)$, i.e., with a deterministic dispersion relation. In a turbulent medium, the dispersion relation is typically broader, that is, one might have several ω's for a single k and vice versa. Intuitively, the broader is the $S(k,\omega)$ spectrum, more turbulent the medium is. The difference of phase between two displaced signals is: $\alpha_{12} = \text{phase}(P_{12})$, where P_{12} is the cross-power spectrum between them. Therefore, the wavenumber is defined in the range: $|k| \leq \alpha_{12}/d$, where d is the distance between the two signals. Fig. 7.7 a) and b) show the wavenumber-frequency spectrum for two poloidal displaced signals in the near edge ($r - r_0 \approx -2$ mm), measuring floating potential before (a) and during biasing (b). The calculations were

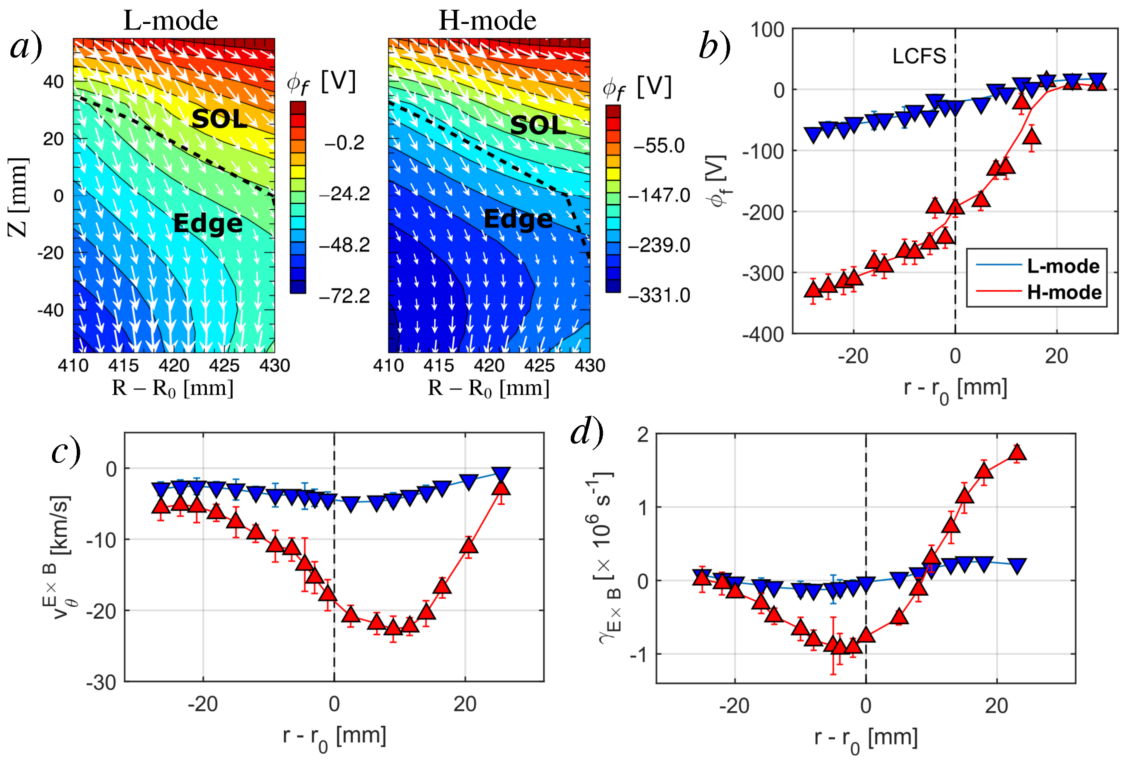

Figure 7.6: Two-dimension floating potential map in a) L and H-mode. The arrows represents the $E \times B$ flow, $\mathbf{v}^{E\times B} = -\nabla\phi_f \times \mathbf{B}/B^2$. The ϕ_f radial profile in both scenario are shown in b), together with c) the poloidal projection of the $E \times B$ flow and d) the shearing rate.

restricted to the fluctuations of ϕ_f in the range 20-700 kHz to avoid the influence of low-frequency modes and high-frequency noise. The poloidal projection of pins equally displaced at the same tower depends on the radial position with respect to LCFS since the magnetic curvature is not negligible (Fig. 7.14): it varies within the range $d_\theta \approx 1.7-2.7$ cm. Besides, to avoid spatial aliasing, the maximum wavenumber $k_{max} = \pi/d_\theta \approx 1.0 - 1.4$ cm^{-1} should be greater than the largest possible wavenumber found in the system. Although in H-mode (Fig. 7.7 b) the criterion is fairly satisfied, in L-mode the spectrum is broader in k_θ and so the requirement is not so easily matched. The wave phase velocity ($v_{ph} = \omega/k$), as discussed in chapter 4, can be deduced from $S(k,\omega)$. Each point in the maps of Fig. 7.7 a) and b) corresponds to a phase velocity (poloidal projection) that, in turns, is weighted by $S(k,\omega)$. The

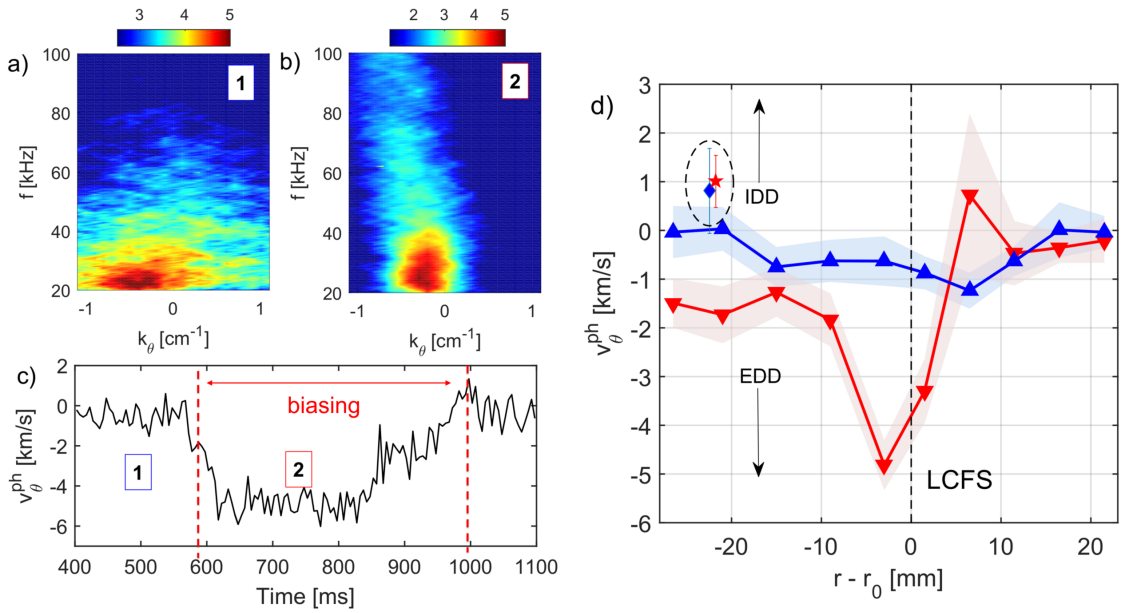

Figure 7.7: Wavenumber-frequency spectrum analysis: a) $S(k,f)$ in L-mode, b) $S(k,f)$ in ELM-free H-mode, c) poloidal phase velocity in time ($r - r_0 \approx -2$ mm), and d) v_θ^{ph} radial profile in L-mode (blue) and H-mode (red). The ion diamagnetic direction (IDD) and the electron diamagnetic direction (EDD) are indicated in the graph.

mean phase velocity is: $\bar{v}^{ph} = \int\int(\omega/k)S(k,\omega)dkd\omega / \int\int S(k,\omega)dkd\omega$, where $k \neq 0$ and $\omega = 2\pi f$. Fig. 7.7 c) shows the mean poloidal phase velocity (v_θ^{ph}) in time before, during, and after the external biasing (applied approximately in the interval $\sim 600 - 1000$ ms). The analysis was performed ever 5 ms, split into sub-windows of 0.5 ms with 50% of overlap to increase the robustness. The absolute value of the phase velocity increases sharply during biasing, from around 1 to 5 km/s. The phase velocity as seen from the laboratory frame is thought to be set by $E \times B$ and diamagnetic drifts. In some cases, the poloidal projection of the phase velocity agrees very well with the $E_r \times B$ drift, where E_r is main radial electric field [215, 115], indicating that the turbulence intrinsic velocity is negligible compared the background velocity. The radial profile of the poloidal phase velocity in L and H-mode are shown in Fig. 7.7 d). For sake of comparison, the ion diamagnetic velocity ($v_D^i = \hat{\mathbf{b}} \times \nabla p_i/(en_iB)$) was also plotted in both regimes, but only in the edge region where temperature

measurements were available. During H-mode, a clear shear layer in the phase velocity is formed around the LCFS (red curve). As seen before, the poloidal projection of the $E \times B$ velocity around the last closed flux surface during H-mode is $v_\theta^{E\times B} \cong -\nabla_r \phi_f / B \approx -[80\ \text{V}/(10\ \text{mm} \times 0.5\ \text{T})] \approx -16$ km/s. Since the average temperature profile decays towards the SOL in this range, the contribution from the temperature for the $E \times B$ flow is $\sim -3\nabla_r T_e / B > 0$. Therefore, it acts to reduce the $-\nabla_r \phi_f / B$ term. Considering that the phase velocity shown in Fig. 7.7 could be set solely by $E \times B$ flow, i.e. $v_\theta^{ph} \approx -\nabla_r \phi / B - 3\nabla_r T_e / B$. The gap of ~ 10 km/s between the two velocities (the largest difference) would require a temperature variation of $\Delta T_e \approx 16$ eV in 10 mm, which is not so easy satisfied (Fig. 7.8 b). Therefore, the poloidal phase velocity is possibly set by other mechanisms, e.g., by a turbulence intrinsic phase velocity. The ion diamagnetic drift is a natural candidate together with the $E \times B$ flow, as has been observed for specific turbulent modes elsewhere [262]. Although the non-negligible difference between the $E \times B$ flow (without taking into account temperature corrections) and the phase velocity, they could be comparable elsewhere. This point will be further explored later in the section in 7.5.

The radial profile of I_s becomes steeper in the edge during the biasing H-mode (Fig. 7.8 a), with the innermost point reaching values almost three times larger than in L-mode. Around the LCFS, however, I_s barely change, while in the SOL its baseline drops significantly with respect to the L-mode. This reflects in a faster decay of I_s towards the wall. The electron temperature (T_e) was calculated by using the five pins balanced triple probe and the result is shown in Fig. 7.8 b). Due to technical problems, it was not possible to measure T_e in the SOL. The temperature does change much during biasing, even in regions where the I_s changes dramatically: T_e slightly drops in H-mode. Since $n_e \propto I_s / \sqrt{T_e}$, one can conclude that the biasing induces an increase of the plasma density in the edge, suggesting the rise of a particle transport barrier in this region. The mild effect on the temperature profile compared to density is quite

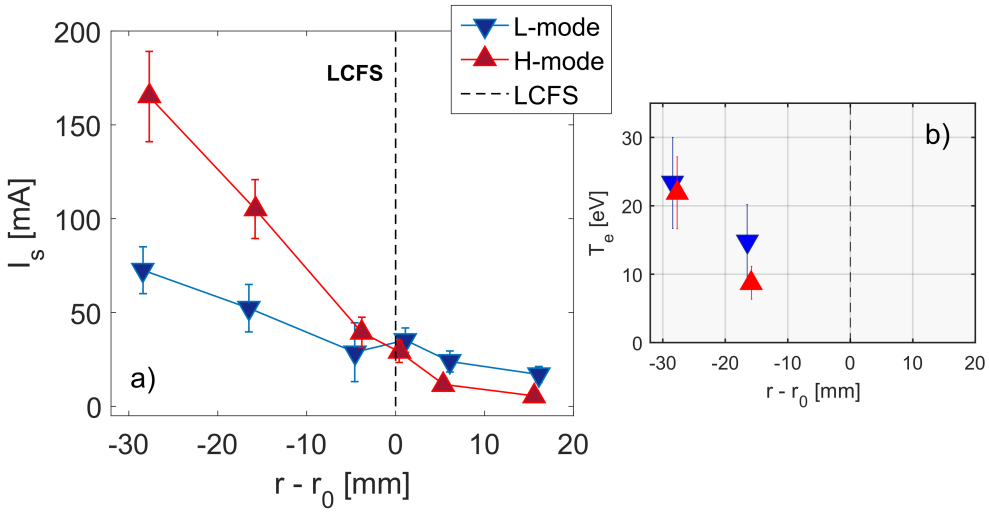

Figure 7.8: Mean profiles in L and H-mode: a) ion saturation current; b) electron temperature.

recurrent in biasing experiments [26, 116, 101] and it is often related to radiation losses and impurity contamination.

Figure 7.9 shows the radial profile of the I_s spectral decomposition in the range 1-300 kHz. The graphs a) and b) of Fig. 7.9 shows the power spectrum of I_s in L-mode and H-mode, respectively, from the edge to the SOL. One can see that fluctuations are higher in the edge than in the SOL in both cases and concentrated in low frequency range ($f \leq 100$ kHz). In H-mode, the level of fluctuation in the SOL reduces compared to L-mode over the whole spectrum range, with dominant low-frequency activities. However, in the plasma edge, the level of fluctuation does not change much. Fig. 7.9 c) shows the radial profile of the ion saturation current relative fluctuation ($\delta I_s / \langle I_s \rangle$) in L and H-mode, where δI_s and $\langle I_s \rangle$ are, respectively the sampling standard deviation and mean. While in the edge the fluctuation normalized by the mean is higher in L-mode than H-mode, in the SOL this trend is reversed. Worth noting that $\delta I_s / \langle I_s \rangle$ is substantially larger near the LCFS in L-mode, with spectral contribution from a broad frequency range. This seems to be a region of strong turbulence driven that, however, reduces during H-mode, possibly because of the larger $E \times B$ shear in

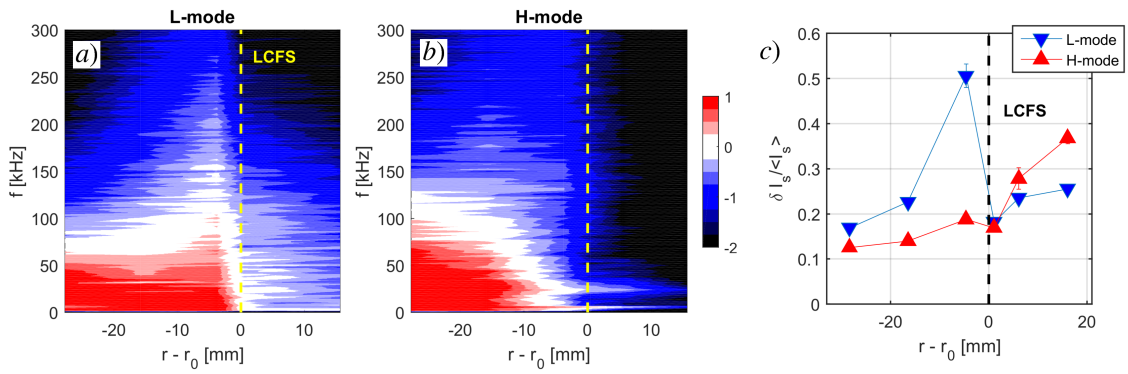

Figure 7.9: Radial profiles of the power spectrum of the ion saturation current fluctuation (a, L-mode and b, H-mode) and c) the relative fluctuation ($\delta I_s / \langle I_s \rangle$) in L and H-mode.

this phase. Besides, the reduced I_s SOL baseline during H-mode results in a larger $\delta I_s / \langle I_s \rangle$ in this phase.

As discussed in the chapter 4, the turbulent particle flux can be estimated considering three probes, with one measuring the I_s fluctuation (used as proxy for the density fluctuation) and the other two displaced poloidally measuring the plasma potential where one can deduce the poloidal electric field ($E_\theta = -\nabla_\theta \phi_p$). The reference potential here is the floating potential, where it is assumed that $\nabla_\theta T_e$ is negligible over $\nabla_\theta \phi_f$. It follows that the turbulent radial particle flux is: $\Gamma_r \propto \left\langle \tilde{I}_s \tilde{E}_\theta \right\rangle$, where the brackets means time averaging. Equivalently, one can demonstrate (see chapter 4) that $\Gamma_r(t) \propto \int_0^\infty T(t,f) df$, where $T(t,f) = \mathrm{Re}\,(P_{IE})$, with P_{IE} the cross-power spectrum between the ion saturation current signal and the poloidal electric field. Fig. 7.10 a) shows the spectrum contribution for the transport ($T(t,f)$) before and during biasing at the position $r - r_0 \approx -5$ mm. The graph at the bottom shows the total turbulent flux (integral over all the frequencies at a given time) in arbitrary units computed in 2 ms time slices. Before biasing, the transport is predominant outward and concentrated in frequencies below 100 kHz. When biasing is switched on, the turbulent transport reduces over the whole spectrum, impacting on the total flux that drops sharply in this phase. Fig. 7.10 b) shows the radial profile of the tur-

bulent particle flux decomposed in frequency and averaged over a time window before biasing (L-mode) and during biasing (H-mode). The dashed white line represents the LCFS position, while the magenta one indicates the position of the signal showed in Fig. 7.10 a). The effect of the biasing on the transport is clearer in the range that goes from the near edge (-10 mm $\leq r - r_0 \leq 0$ mm) up to the far SOL. The level of transport decreases mainly in the range of steeper floating potential profile. The reduction happens especially in the low-frequency range ($f \leq 100$ kHz) where the contribution for the total flux is dominant. Note that the fluctuation for the innermost point is virtually unchanged. The total flux profile is shown in Fig. 7.10 c). The strong reduction is indeed confirmed in the interval from the near edge to the SOL. Fig. 7.10 d) shows the total flux normalized by the mean I_s, which, as discussed in chapter 4, can be interpreted as effective turbulent radial velocity. The normalization by the background rules out the geometry dependence on the density from the ion saturation current. In H-mode, the effective radial velocity reduces in almost ever radial position, tending to zero near the LCFS.

The reduction of the turbulent transport around the LCFS followed by a decreasing of the I_s SOL baseline in the H-mode, with a faster profile decay towards the wall, suggest a reduction of the edge-SOL coupling during this phase. As has been demonstrated in TJ-II recently [103], sheared radial electric fields are able not only to suppress turbulence locally but also to reduce its propagation. This has an effect on the SOL turbulence characteristic and, ultimately, on the SOL profiles. The level of turbulence penetration into the SOL can be studied by using the cross-correlation technique. On this purpose, five pins located in the SOL all measuring floating potential were considered, where the innermost one (about 6 mm outer from the LCFS) was chosen as reference. Typically, the turbulent correlation length is usually defined as the interval where the correlation is higher than 1/e from the reference (autocorrelation) at zero delay, i.e. it is a snapshot of the turbulent fluctuation projected

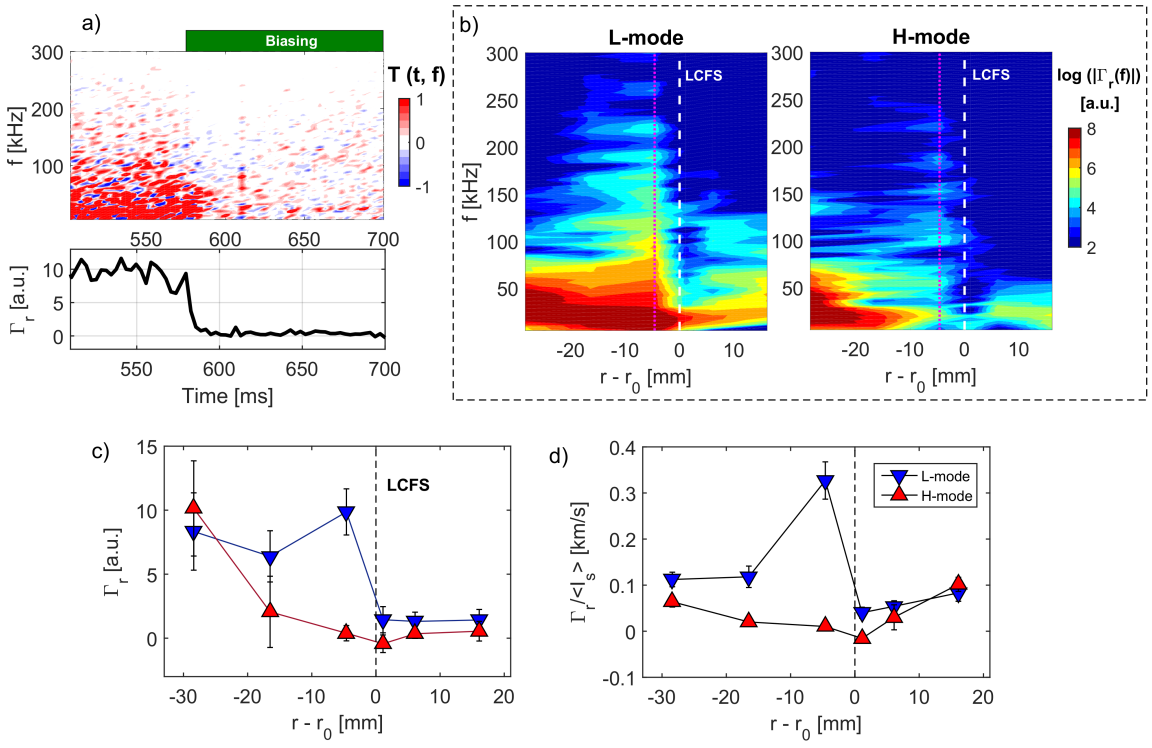

Figure 7.10: Turbulent transport in L and H-mode: a) spectral contribution for the transport ($T(t, f)$) at top and total flux at the bottom at the position $r - r_0 \approx -5$ mm; b) radial profile of radial flux decomposed in frequency in L and H-mode (the dashed and dotted lines are, respectively, the LCFS position and the position of the signal shown in a); c) radial profile of the total flux and d) effective radial velocity in L and H-mode.

in the radial direction. Since the SOL is dominated by travelling structures, the maximum correlation captures better the properties of this region because it takes into account for the fact that the turbulence might be propagating. Note that the maximum correlation might occur at different time delay, including, of course, zero time lag. The signals were bandpass filtered ($15 < f < 800$ kHz) to eliminate the influence of high-frequency noise as well as low-frequency modes, e.g., tearing mode. The calculation was performed in a large time window that covers the entire transition and divided into time slices of 4 ms. The result is shown in the top graph of Fig. 7.11. Before biasing, the high-correlation band extends up to the far SOL, with visible intermittent events. When biasing is switched on around 600 ms, the high-correlation

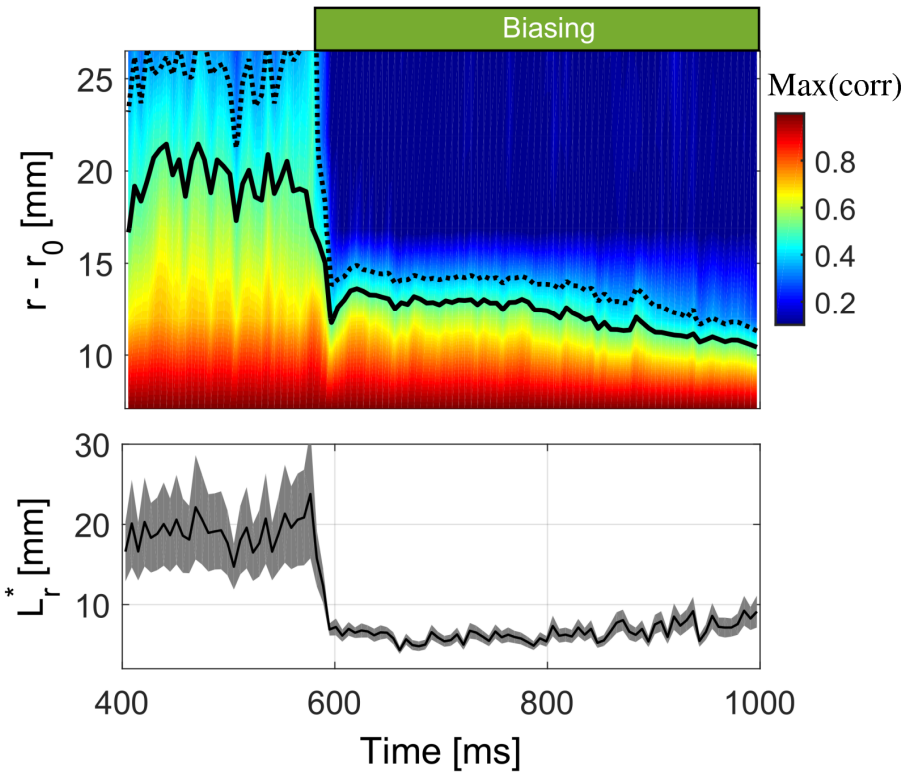

Figure 7.11: Top: maximum $\tilde{\phi}_f$ correlation where the reference is located in the SOL ($r - r_0 = 6$ mm). The full line represents the correlation at 0.5, while the doted 1/e. Bottom: correlation length (L_r^*) calculated from an exponential fitting starting from the reference position.

range becomes reduced to a short interval around the reference. The effective radial correlation length was calculated from an exponential fitting function starting from the reference, where L_r^* was defined as the exponent parameters. Fig. 7.11 (bottom) shows that after the transition, L_r^* goes from around 20 mm to about 8 mm. This result suggests that the turbulence does not penetrate the SOL so freely as in L-mode. The stronger flow during the biasing H-mode creates a transport barrier that prevents the propagation from the near edge and SOL into the far SOL.

7.1.1 Plasma-wall interaction

The Integrated System of Internal Sensors (ISIS) is composed of electrostatic and magnetic sensors, toroidally and poloidally spaced, installed on the wall of the RFX-mod [228] (see chapter 4). The focus here was, however, the poloidal electrostatic array composed of 7 tungsten pins with 2 mm of diameter, Fig. 7.14 a). All the pins are set to measure floating potential, which can be used for monitoring the plasma-wall interaction. Fig. 7.12 shows an example of how ISIS poloidal array can perceive the column shape evolution up to the null point formation. The red lines in the four small charts represent the LCFS reconstruction obtained in the RFX-mod tokamak in real-time ($\sim$1 ms) by extrapolating both poloidal magnetic flux and magnetic field measurements in the vacuum region [147]. In the middle graphs are shown the mean floating potential time evolution (top) and its standard deviation (bottom) as a function of the poloidal angle as defined in Fig. 7.14 a). Both quantities were computed in 4 ms time slices. In the two first frames (1 and 2), the plasma column is approximately circular, but in the second one the LCFS intercepts the wall in two regions, at the top and bottom. At $\theta \approx 100^\circ$ and $\theta \approx -100^\circ$ the ISIS detects an increase of ϕ_f and $\delta\phi_f$. In the frame 3, the plasma shape changes, with the null point starting to emerge, but the LCFS at the bottom still intercepts the wall, which is detected by ISIS. The higher ϕ_f and $\delta\phi_f$ are likely related to a hotter plasma (with higher plasma current) in this phase (not shown here). In 4, the null point is already formed and the LCFS does not intercept the wall anymore (within the reconstruction error bar). However, a strong point of interaction appears at the outboard middle plane. As will be further discussed next, the emergence of this point is likely related to a combination of cross-field and parallel transport.

The full equilibrium reconstruction has been calculated in RFX-mod operating as tokamak with a free boundary version of the IET code [3] The estimation of IET free parameters was performed by using an iterative scheme trying to minimize the

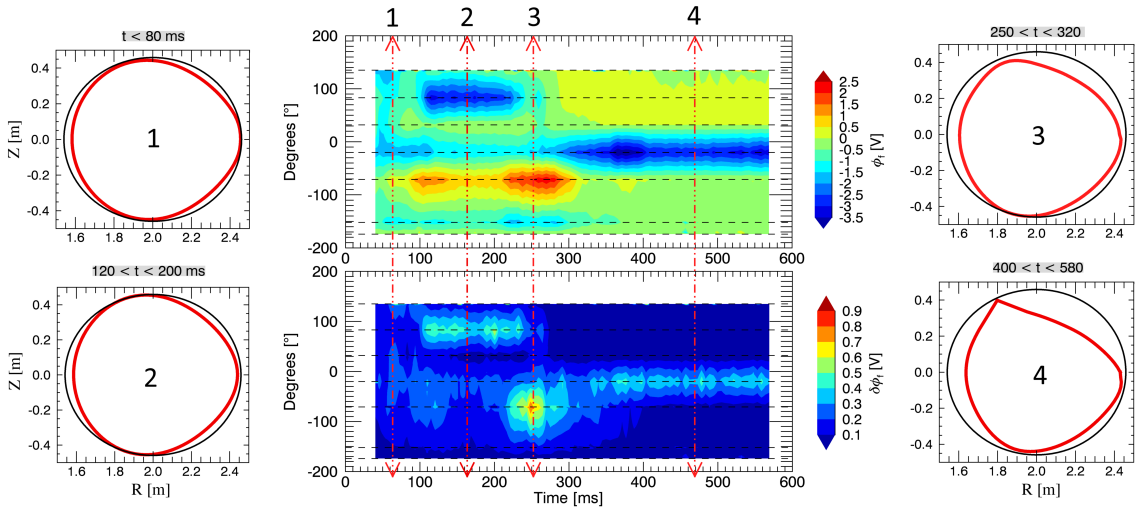

Figure 7.12: The last closed flux surfaced (LCFS) reconstruction in four moments (or phases) prior to the null point formation. At the middle, mean (top) and standard (bottom) floating potential in time (4 ms time slices) from ISIS poloidal array as function of the poloidal angle, counter-clockwise from the equatorial plane (see Fig. 7.14 a).

discrepancy between the poloidal magnetic field experimentally measured by pick-up coils and the simulated one [1]. The reconstruction provides results in a good agreement with the real time reconstruction [147]: less than 1 cm of disagreement at the outboard midplane. From the full reconstruction, the SOL parallel connection length ($L_{\parallel}$)was obtained with the field line integration code NEMATO [81]. $L_{\parallel}$ is defined from the sum of the forward and backward field line integration starting from a location at the SOL up to the field line intercepts a material surface. Fig. 7.13 a) shows the result of this procedure iteratively over a cross-field section at the outboard midplane near where the U-probe was placed during the experiment. The $L_{\parallel}$ radial profile at the equatorial plane (Z = 0) is shown in Fig. 7.13, left, together with the 2D map of $L_{\parallel}$ over the full cross-section. As a peculiar result of this experiment, the connection length varies strongly over a relatively short range near the LCFS. The map of Fig. 7.13 shows that $L_{\parallel}$ varies from about 30 m neat the LCFS (dark red) to 10 m further outer (light red). The two clearly distinguishable layers are related to the fact that field lines are connected to the strike point like at the top vessel, near

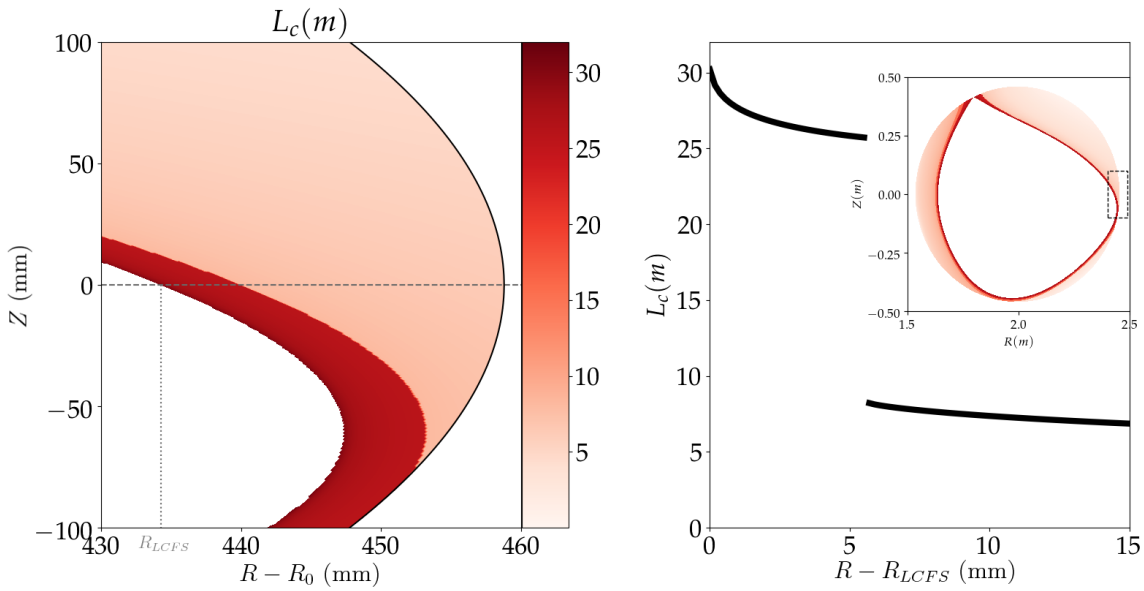

Figure 7.13: On the left, parallel connection length ($L_\parallel$) represented as 2D map at the outboard midplane region. On the right, $L_\parallel$ radial profile at the outboard midplane (Z = 0). The small chart show the 2D map over the entire cross-section.

the LCFS, and to the outboard midplane wall (and still at the top vessel) in the far SOL - wall or limiter shadow region. The $L_\parallel$ radial profiles show that the change of layers occurs in a short-range that is comparable to the range covered by the U-probe. This likely affects the properties of turbulence in the SOL [250]. However, one has to note that since the error in the LCFS reconstruction can be up to 1 cm, the thickness of the two layers can be different. Note that the tokamak configuration here differs from standard tokamaks [36, 265], where the gap between the LCFS and the wall at the outboard midplane is larger.

The scrape-off layer is typically established from the net result of the competition between cross-field and parallel transport [250]. While the cross-field transport tends to enlarge the SOL, the parallel dissipation goes to the opposite direction. The parallel dissipation occurs typically at the time scale $\tau_\parallel = L_\parallel / v_\parallel$, where $v_\parallel$ is in the sound speed range ($c_s = \sqrt{T_e/m_i}$, where m_i is the mass of the ion specie). Fig. 7.13 shows that the field lines intercept the wall at outboard midplane, opening a new channel for parallel dissipation in a range where turbulent cross-field transport is still expected to

be important. Fig. 7.14 b) and c) shows the time evolution of the mean and standard floating potential measured with the ISIS poloidal array during the biasing transition (calculated in 4 ms time slices). The D_α line is plotted at the top as a proxy for the L-H transition. Before and after biasing, in the ohmic L-mode phases, a strong plasma-wall interaction is observed at the outboard midplane ($\theta \approx -10°$). During biasing, however, this level of interaction decreases significantly. As observed before (Fig. 7.10 and 7.11), during L-mode the turbulent cross-field transport is higher, therefore, the larger interaction in this phase can be due to the simple fact that the plasma is cross-field transported to that point. Competing with that, the parallel transport can carry plasma along the field lines up to that point as well. Hence, in any case, cross-field transport seems to be the key ingredient for the plasma-wall interaction. Therefore, the reduction of the wall floating potential observed during biasing is likely due to the partial turbulence suppression in this phase and the consequent decreases of the cross-field transport. Nevertheless, as will be discussed in section 7.5, if the parallel collisionality increases, that can affect the parallel transport, which in turns might have an impact on the plasma-wall interaction.

7.2 Blobs detection and characterization

7.2.1 Threshold criterion

The positive bursts in the ion saturation current signal located in the SOL is a mark of the intermittent behaviour of this region. Indeed, the cross-field transport in the far SOL is widely dominated by convective transport provided by blobs or turbulent filaments [63]. These structures are characterized by a higher density with respect to the background with typical cross-field size of a few centimeters, i.e., several times larger than the local ion gyroradius, $\rho_s = \sqrt{T_e m_i}/eB \approx 0.8 - 1.0$ mm. Since their size is typically smaller than the machine size, they are considered mesoscales

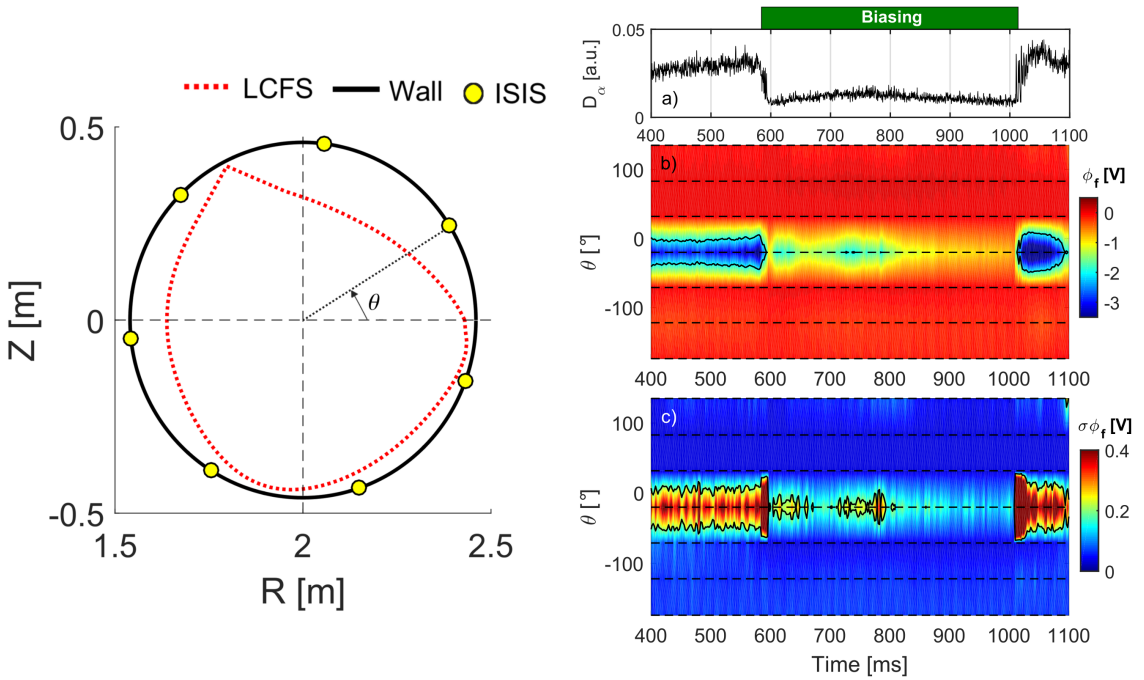

Figure 7.14: On the left, the last closed flux surface (LCFS) reconstruction showing the ISIS poloidally symmetric array. On the right, ISIS poloidally array measurements: a) the D_α line (midplane) is shown as a proxy for the L-H transition together with the time evolution of seven ISIS sensors measuring floating potential (ϕ_f), showing its b) mean, c) and standard deviation calculated in 4 ms time slices.

events [108]. The implications of mesoscales phenomenons on the transport were discussed in chapter 5. As an example, Fig. 7.15 shows the ion saturation in time (considered here as a proxy for the density fluctuation) for a probe located in the SOL (approximately 6 mm outer from the LCFS). It is quite visible that the signal presents larger positive bursts that occur randomly over time. Such behaviour can be better visualized by looking at the $(I_s - \langle I_s \rangle)/\sigma$ probability distribution function (PDF), where $\langle I_s \rangle$ is the sampling mean and σ is the standard deviation. The 'fat positive tail' is a sign of intermittency that yields to a deviation from a Gaussian distribution towards power laws [108]. The skewness in the present case is $S \approx 1.5$. The threshold criterion (considered elsewhere [35, 265]) selects those extreme events that provoke the large skewness of I_s PDF. This is done by choosing a convenient threshold in the I_s amplitude. Several works have been demonstrated that the blob feature is not

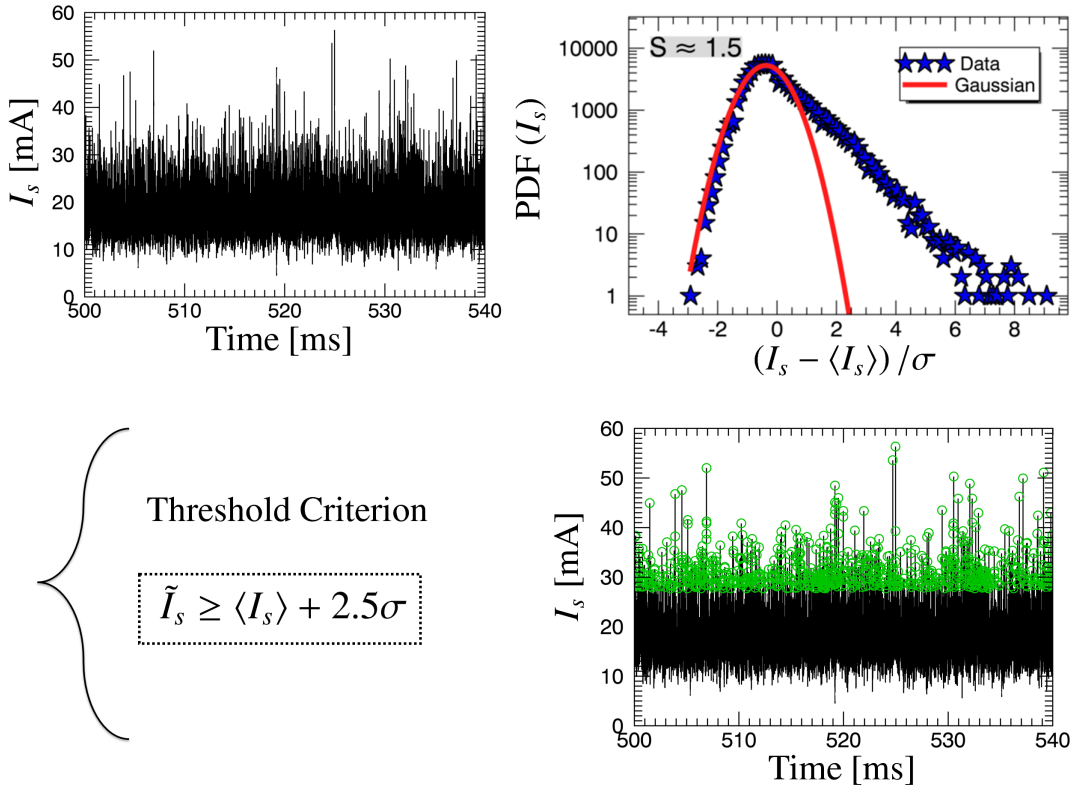

Figure 7.15: The ion saturation current signal in the SOL is mainly dominated by positive bursts that skew its probability distribution function (PDF), creating a 'fat tail'. S indicates the corresponding skewness and the red line represents a Gaussian fit. The threshold criterion selects the extreme events in the ion saturation current signal larger than $\langle I_s \rangle + 2.5\sigma$, where $\langle I_s \rangle$ and σ are, respectively, the sampling mean and standard deviation.

so sensitive to the threshold choice [63], as long as it is sufficiently larger than the mean sampling. Here it is considered the threshold as the extreme events larger than $\langle I_s \rangle + 2.5\sigma$. Note from the PDF of $(I_s - \langle I_s \rangle)/\sigma$ that this threshold selects the points that belong to the non-Gaussian long tail. Note that the criterion is applied only in the amplitude of the signal, therefore it does not distinguish time scales. In the chapter, it will be discussed a different criterion for detecting intermittent events based on wavelet decomposition. The local intermittency measure (LIM) selects events based on its amplitude (or wavelet power) and time scale.

After selecting a reference signal convenient for detecting blobs (here an ion saturation current signal located in the near SOL) and separating the extreme events that cause the signal PDF to deviate from a Gaussian distribution, one can use statistical techniques to study those events in more detail. The conditional average (see chapter 4) is a convenient tool for that. The technique is used to perform averages in a portion of the signal subject to a criterion or condition [132]. It follows that the conditional average of the ion saturation current signal shown in Fig. 7.15 subject to the threshold criterion is given by:

$$\delta I_s = \left\langle I_s(t) | I_s(t') > I_s^{threshold} \right\rangle \tag{7.1}$$

The conditional average applied to the reference I_s signal ($r - r_0 \approx 6$ mm) together with two neighbor signals (radially outer and inner from the reference probe) in a time slice of 40 μs around each peak is shown in Fig. 7.16. The three probes present a peak (Fig. 7.16 a) but in different time instants. The inner probe in black perceives the peak first than the reference one in red ($\tau = 0$) and the outer (blue), that exhibits a peak at $\tau \approx 3$ μs. Such behaviour can be better visualized in Fig. 7.16 b) where it is shown a contour plot with the color indicating δI_s, the x-axis the time delay, and the y-axis the probe radial position with respect to the LCFS. One can see that the hot color plume that characterizes the conditional average I_s peak is slightly tilted, which suggests radial propagation. The effective radial propagation can be deduced from its slope. The term 'effective' is more appropriated here because, as discussed in chapter 6, tilted poloidal rotating structures can yield a fictitious radial propagation that can be inward or outward depending on the poloidal velocity direction and tilt. This effect becomes less important when the structure size is smaller than the distance between probes. However, this does not seem to be the case here, Fig. 7.16 a) shows an overlap between the detected δI_s of all probes, that is especially accentuated for the two innermost. Hence, the I_s structure seems to be larger than the distance between

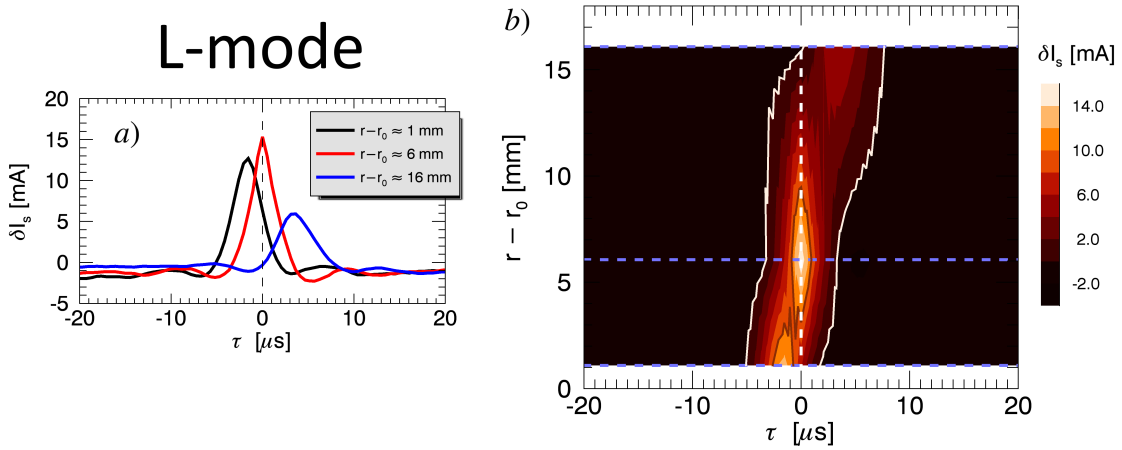

Figure 7.16: Conditional average of ion saturation current (I_s) for three probes in the SOL: a) amplitude (δI_s) as function of time delay, and b) contour plot showing the amplitude in a color scheme as function of the time delay (x-axis) and the probe position with respect to the LCFS (y-axis).

pins and, therefore, the velocity deduced from the slope of Fig. 7.16 b) is coupled with the structure dimension and velocity. There are several ways to decouple the system and, thus, obtain the proper radial velocity, but all techniques require at least three measuring probes displaced radially and poloidally [35, 78].

The conditional average can be extended to other signals at different positions in the plasma as well as to different quantities. Keeping the same reference, i.e. a probe at near SOL measuring ion saturation current, and using the threshold criterion to detect the blobs in I_s, one can use the floating potential (ϕ_f) signals to depict their 2D nature. The ϕ_f array is composed of 20 probes displaced in a cross-field plane covering a range of 88x20 mm. The result is represented in a two-dimension map at 16-time frames (Fig. 7.17). The conditional averaged floating potential ($\delta\phi_f$) array was interpolated with the two dimension quadratic interpolation technique, i.e. by fitting a quadratic function ($y = a + bx + cx^2$) in ever three neighbour points. The white arrows represent the $E \times B$ flow, $\vec{v}^{E\times B} \approx -\vec{\nabla}\phi_f \times \vec{B}/B$. One can see initially a dipole potential structure arising near the LCFS (dashed line). The position of the three ion saturation current signals of the Fig. 7.16 is represented in the map by

filled circles with the corresponding color. At zero time lag, i.e. when the reference signal shows a peak in δI_s (at the red circle position), the potential structure exhibits a dipole around the reference, with the dipole mid-distance lying roughly at the red circle position. It is worth noting that this result is very similar to the classic view of a density blob surrounded by a dipole potential [63]. In the subsequent frames, the potential structure detaches from the plasma edge moving towards the SOL. Therefore, both conditional I_s and ϕ_f agree, indicating that the blob travels from the edge to the SOL. In addition, the arrows pattern follows the potential suggesting an enhanced vortex structure in the SOL. Note that the $E \times B$ velocity from the dipole does not point in the radial direction, as one might expect from curvature effects [146]. The background shear flow together with magnetic shear effects could account for this apparent discrepancy [184, 76]. Besides, as discussed before, the electron temperature fluctuation can modify the plasma potential and so altering the dipole observed in Fig. 7.17. However, the reasonable agreement between the dipole dynamics and the I_s blob suggests that such correction might be small in L-mode.

7.2.2 2D cross correlation technique for cross-field filament detection

The potential structure obtained from the conditional average exhibits a clear dipole structure near the LCFS that later becomes a monopole in the SOL, possibly due to the lack of spatial resolution. However, as will be discussed in section 7.5, constructive and destructive interference with the background $E \times B$ flow is foreseen in some cases, i.e. vortex selection [168]. Since the negative pole captures well the dynamics of the potential structure and possibly the density blob (since they are believed to be coupled) [63], the potential provides the boost for the density blob, the negative pole was chosen as reference for the cross-field filament motion and shape. The two-dimension cross-correlation technique was used for the image pattern recognition of

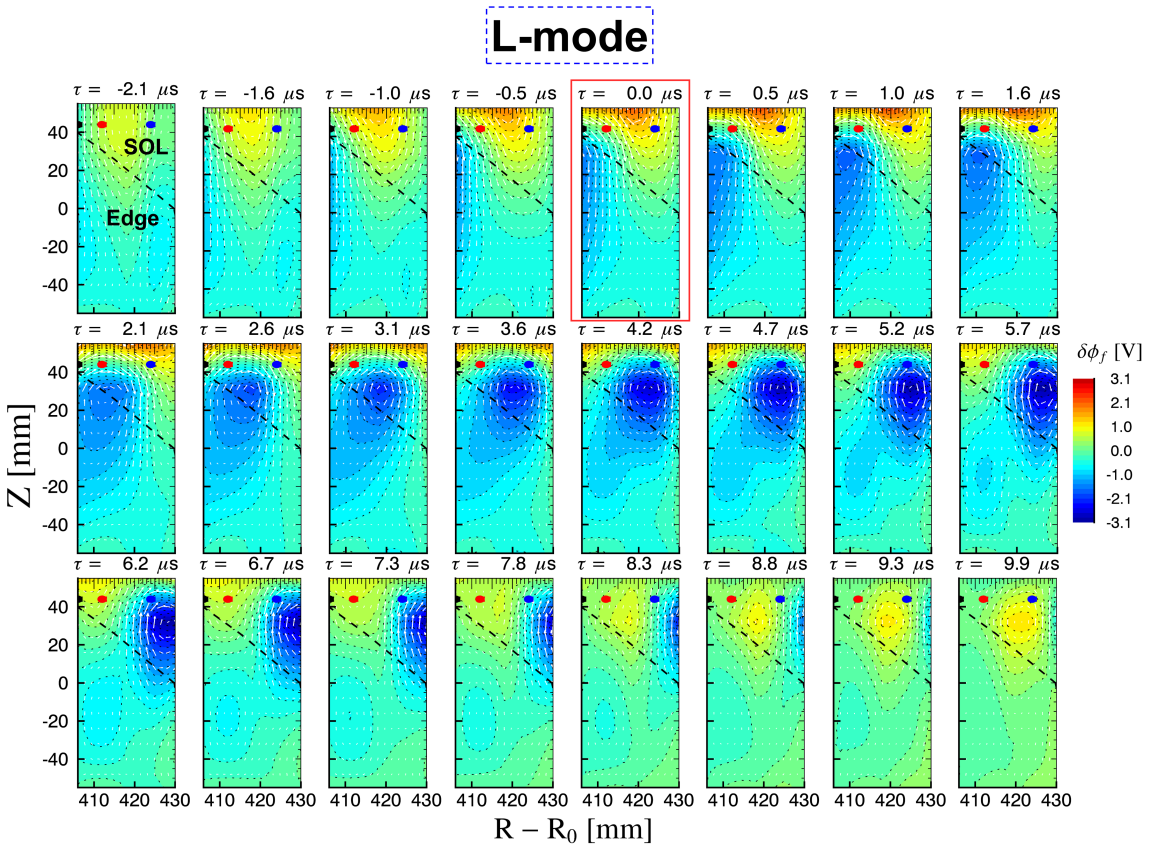

Figure 7.17: Two dimension map of the conditional average floating potential ($\delta\phi_f$) in 18 frames during L-mode. The dashed lines represent the LCFS, while the black, red, and blue dots the position of the three ion saturation signals displayed in Fig. 7.16. The white arrows represent the $\mathbf{v}^{E\times B} = -\nabla\phi_f \times \mathbf{B}/B^2$.

subsequent frames. The technique is based on computing the sum of the element-by-element product of two superposed array of signals. The arrays do not need to have the same size. When there is no overlap between the two arrays, the term is set to zero and, therefore, does not contribute to the total correlation. Given two matrix, X (M x N dimension), and Y (P x Q dimension), the correlation between them is given by:

$$C(a,b) = \sum_{m=0}^{M-1}\sum_{n=0}^{N-1} X(m,n)Y^{\dagger}(m-a,n-b) \tag{7.2}$$

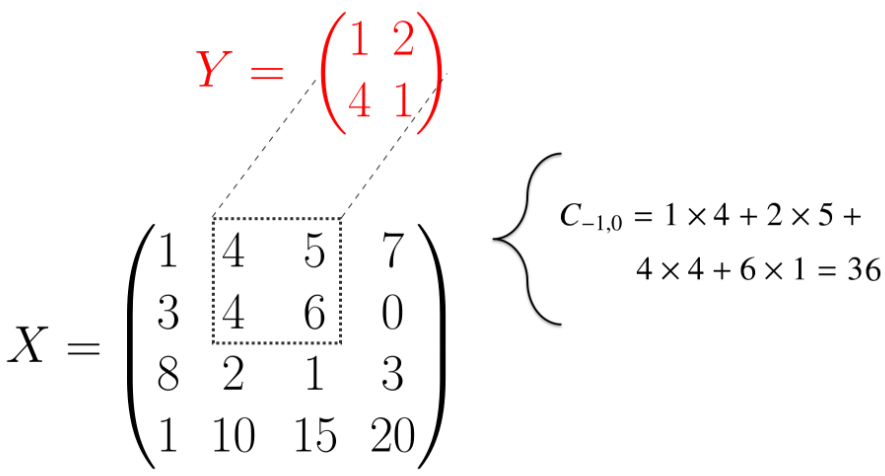

Figure 7.18: Example of the calculation of one term of 2D cross-correltaion matrix.

Where $-(P-1) \leq a \leq (M-1)$ and $-(Q-1) \leq b \leq (N-1)$ and $Y^{\dagger}$ is the complex conjugate of Y. Alternatively, one can normalize C [254]:

$$c(a,b) = \frac{\left\langle \left[X(m,n) - \bar{X}\right] \left[Y^{\dagger}(m-a,n-b) - \bar{Y}\right] \right\rangle}{\sqrt{\left\langle \left[X(m,n) - \bar{X}\right]^2 \right\rangle \left\langle \left[Y^{(}m,n) - \bar{Y}\right]^2 \right\rangle}} \tag{7.3}$$

Where $\langle ... \rangle = \sum_{m=0}^{M-1} \sum_{n=0}^{N-1} [...]/(MN)$ with $\bar{X}$ and $\bar{Y}$ the mean matrix.

Figure 7.18 shows an example of the technique applied for two matrices of different sizes (X: 4×4 and Y: 2×2), where the 2D correlation matrix dimension between them is 5×5. In the Fig. 7.18 is shown how the term $C_{-1,0}$ is calculated. The indexes -1 and 0 indicate the corresponding shift of one matrix with respect to the other in the horizontal and vertical direction, respectively. Note that the term $C_{-1,2}$ is simply $C_{-1,2} = 1 \times 7 + 4 \times 0 = 7$, since there is no overlap for the remaining terms of matrix Y with respect to X.

Coming back to the blob potential structure, each frame can be represented by a 2D matrix M-by-N in which the elements are the potential at a given position. The

2D cross-correlation (2D-CC) between two subsequent frames is then represented by a matrix $(2M-1)\times(2N-1)$. The M and N dimension are provided by the number of interpolated points, in the present case: M = N = 15. The technique can be particularly useful for calculating the blob 2D displacement between frames. Fig. 7.19 a) shows an example for two closed frames where the negative pole appears clearly, and one can note a slight displacement. Fig. 7.19 b) shows the normalized 2D cross-correlation between them represented in a contour plot. The shift of one frame with respect to the other was translated into the actual geometric scale in both axes. The term $C_{0,0}$ is represented by $\Delta R = \Delta Z = 0$, that is, the full superposition between the two images. The cross-correlation indeed is able to perceive the motion of the potential between frames: the maximum 2D-CC occurs for $\Delta R = \Delta Z \neq 0$ (yellow diamond). It should be noticed that this procedure is more reliable than simply taking the extreme point of the map as the reference in each frame (the minimum of the potential in this case). In the example shown in Fig. 7.19 a), the minimum does not move between frames, although the structure is clearly shifted (as the 2D-CC indicates). Knowing the structure displacement between subsequent frames, the velocity is obtained straightforwardly. However, the probe is located in a region where the LCFS is slanted, so the vertical and horizontal velocity in this 'geometric' frame does not correspond to the radial and poloidal velocity in a proper plasma frame. On this purpose, it was defined a new system of coordinate given by $r = \sqrt{(R-R_0)^2 - (Z-Z_0)^2}$ and $\theta = \tan^{-1}[(Z-Z_0)/(R-R_0)]$, where (R,Z) is the coordinates in the geometric frame and (R_0,Z_0) is the LCFS position that minimizes r.

7.2.3 Eigendecomposition of a covariance matrix

The blob size is defined here from the 2D auto-cross correlation. This function is easily obtained from Eq. 7.3 by replacing Y by X. The motivation in using the auto

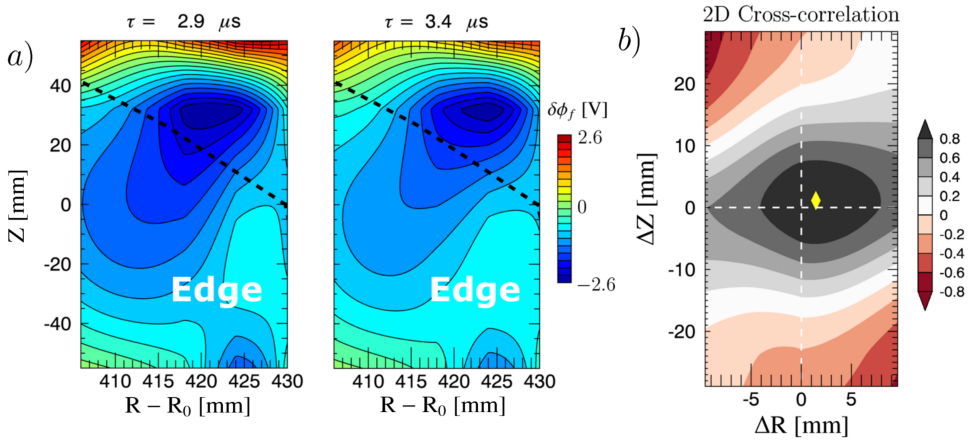

Figure 7.19: Two dimension map of the conditional average floating potential (ϕ_f) in 18 frames.

instead of the cross-correlation function to determine the structure size is because in the latter the blob motion can distort its shape. Considering that the potential blob can be fitted by a two-dimension Gaussian function, it is natural to assume that the blob extension is within the range 2D-AC$\geq$ 0.5, i.e. larger than Full Width at Half Maximum (FWHM) of 2D-AC. However, the constraint from the spatial frame size does not allow to fully visualize the structure, i.e. up to the 2D-AC approaches to the FWHM boundary layer. To deal with this issue, the blob extension was determined from a 2D-AC value high enough to depict the blob shape entirely, avoiding eventual distortions, e.g. from the boundary. Following this requirement, a convenient value is 2D-AC = 0.8. The 'real' size is then obtained by extrapolating the value from 0.8 to 0.5 (FWHM), assuming, therefore, a Gaussian decay, which in the practice yields a factor $\sqrt{\log(0.8)/\log(0.5)}$ on the blob size obtained at 0.8.

The points of the autocorrelation map that satisfy the criterion 2D-AC $>$ 0.8 are converted from the geometric to the defined plasma frame (see Fig. 7.21 a). The distribution of points can be fitted by an ellipse curve (red). The ellipse tilt and ellipticity parameters are obtained by the eigendecomposition of the covariance matrix from the distribution of points. The technique finds in the space the direction

of the maximum covariance, which turns to be the principal axis of an ellipse. The covariance matrix is given by:

$$\Sigma = \begin{bmatrix} c_{xx} & c_{xy} \\ c_{yx} & c_{yy} \end{bmatrix} \tag{7.4}$$

where the sample covariance is $c_{xy} = 1/(N-1)\sum_{k=1}^{N}(x_k - \bar{x})(y_k - \bar{y})$, with N the number of point with the coordinates x_k and y_k ($k = 1, 2..., N$) and $\bar{x}(\bar{y}) = \sum_{k=1}^{N} x_k(y_k)/N$. Through a linear transformation, one can write Σ as:

$$\Sigma V = VL \tag{7.5}$$

V and L are, respectively, the eigenvectors and the eigenvalues matrices of Σ. It follows that the covariance matrix can be rewritten as:

$$\Sigma = VLV^{-1} \tag{7.6}$$

By using now the single value decomposition (SVD) [263], one can recognize V as a rotation matrix and $\sqrt{L}$ as a scale matrix.

Fig. 7.20 shows an example of the technique apply to a generated Gaussian blob with well-known tilt and ellipticity = (major axis)/(minor axis). The 2D auto-correlation of the map of Fig. 7.20 a) is shown in b). The 2D-AC captures the shape of the structure even for a limited range in both x and y-axis. Keeping only the points that satisfy the criterion 2D-AC ≥ 0.8, the result is shown in Fig. 7.20 c), where the distribution of points is plot around the center of mass of the Fig. 7.20 a), i.e. $(X^{CM}, Y^{CM}) \approx (3, 3)$. The red curve is the fit by the eigendecomposition method. The tilt and ellipticity are well captured and so the fitting function is:

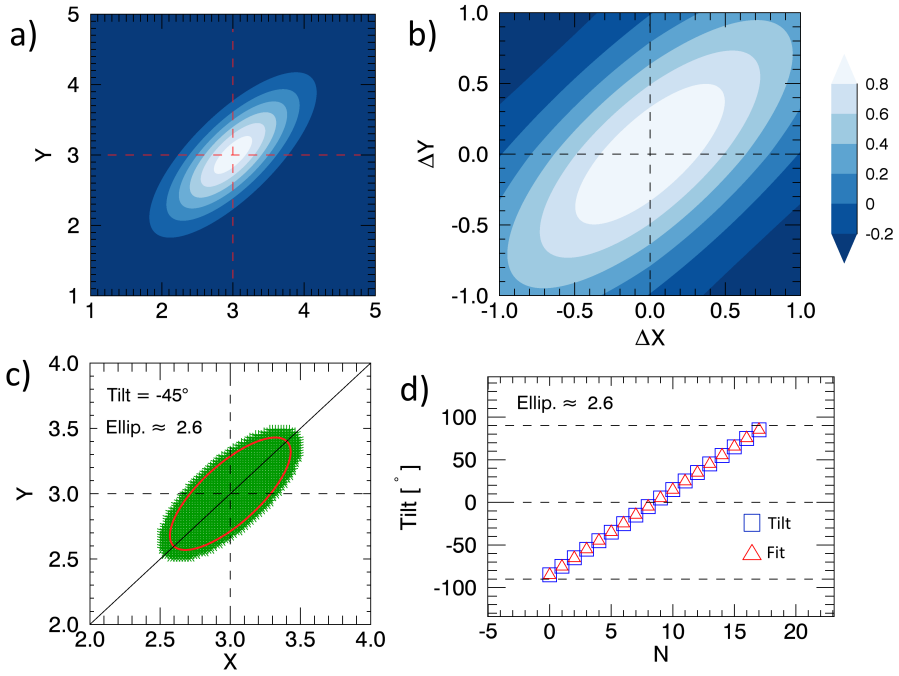

Figure 7.20: Test for the blob fitting method: a) generated 2D Gaussian blob, b) 2D autocorrelation, c) points that satisfy the criterion 2D-AC ≥ 0.8 are fitted by an elliptic curve using the eigendecomposition method, and d) the test is extend to a large range of tilt with constant ellipticity (Ellip. ≈ 2.6).

$Z = \left[X^* sin(\text{Tilt}) + Y^* cos(\text{Tilt}) + X^{CM},\ X^* cos(\text{Tilt}) - Y^* sin(\text{Tilt}) + Y^{CM}\right]$ where $X^* = \sqrt{L_2} cos(\theta)$ and $Y^* = \sqrt{L_1} sin(\theta)$, with $\theta \in [0, 2\pi]$, where $\sqrt{L_1}$ and $\sqrt{L_2}$ are, respectively, the ellipse major and minor axis. Fig. 7.20 d) shows the sensibility of the fitting at different tilt, keeping the ellipticity constant. The remarkable agreement shows the reliability of the technique. Intuitively, the method is expected to fail when the ellipticity approaches to the unity, i.e. for circular blob. However, it was observed that even for ellipticity ≈ 1.1, the agreement is very good.

The eigendecomposition method applied to 10 subsequent frames of the potential structure in Fig. 7.19 is shown in Fig. 7.21 from the edge to the SOL. Fig. 7.21 b) shows the fitted ellipses at each frame from the points that satisfy the criterion 2D-AC > 0.8. While in the edge region the potential structure is stretched in the poloidal direction, near the transition to the SOL it becomes less wide and tilted with respect

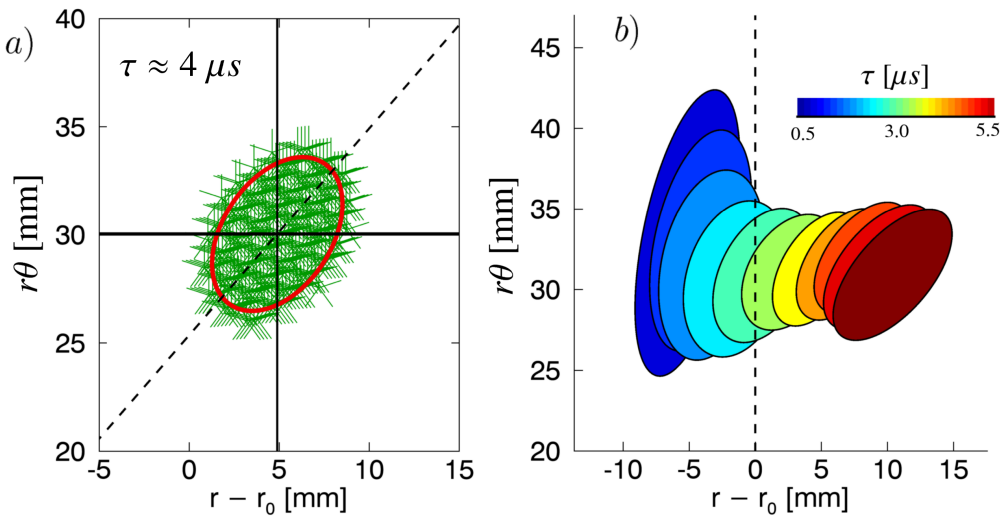

Figure 7.21: Points that satisfy the criterion 2D-AC > 0.8 are fitted by an ellipse, b) ellipse fitting over time (radial position).

to the radial direction. The structure size and shape have a clear radial dependence, which suggests an interplay between the blob and the background.

7.3 L-mode filaments

The combination of the 2D correlation with the ellipse fitting, through the eigendecomposition method, permits to track the conditional potential structure from the plasma to the scrape-off layer. As said before, blobs are defined from the extreme events of a reference ion saturation current located in the near SOL (see Fig. 7.16 and 7.17). A threshold criterion based on the I_s amplitude was considered for distinguishing the blobs (intermittent events) from the Gaussian background. In this section, the image pattern recognition introduced in the previous section will be further explored to track filaments during the ohmic L-mode phase of RFX-mod operating as a tokamak. Three reproducible shots were considered for this analysis in the time window 480-580 ms (Fig. 7.3 and 7.4), i.e. right before the biasing beginning. The blob detection and tracking were performed in sub-windows of 50 ms with 50% of overlap

for the three shots. In each time slice, the blob radial and poloidal velocity were evaluated from the 2D cross-correlation technique (as described in the previous section), where the velocity was assumed to be at the center of mass position of the prior frame. Hence, the position of the next frame is: $(R^{CM}(\tau) + \delta\tau v_R, Z^{CM}(\tau) + \delta\tau v_Z)$, where $\delta\tau$ is the time between frames (sampling period $\sim 0.5\ \mu s$ in this case), v_R and v_Z are the blob velocity in the geometric frame, and R^{CM} and Z^{CM} are the blob position in the previous frame obtained by the same procedure. However, the first reference position (for the blob tracking) was obtained from the minimum of the potential. The time reference for the first (R^{CM}, Z^{CM}) in all the shots during L-mode was $\tau = 1.0\ \mu s$ since at this time delay one can clearly distinguish the negative pole of the potential structure. At each frame, the blob size is obtained from fitting an ellipse over the 2D correlation points that satisfy 2D-AC ≥ 0.8. The radial and poloidal sizes are defined as the maximum projection of the fitted ellipse over the radial and poloidal direction, respectively. The final sizes are then corrected with the factor discussed in the previous section that corresponds to an extrapolation up to 2D-AC = 0.5 (Full-Width Half Maximum - FWHM). Besides, another relevant parameter, the potential blob amplitude, was obtained in each frame from the minimum potential. In the graph of Fig. 7.22 is shown the blob: a) radial size, b) poloidal size, c) ratio between the poloidal and radial sizes, d) minimum potential, e) radial velocity, and f) poloidal velocity for the three reference shots. Each point (at a given position) is obtained by averaging over the contribution from the sub-time windows at particularly time delay. Hence, eventual radial displacement and variations on the measured parameter over the sub-time windows is translated into the error bars (corresponding to the standard deviation). The black thick line and the grey shadow area in each graph correspond, respectively, the mean and the error of the parameter for all the shots along the blob trajectory.

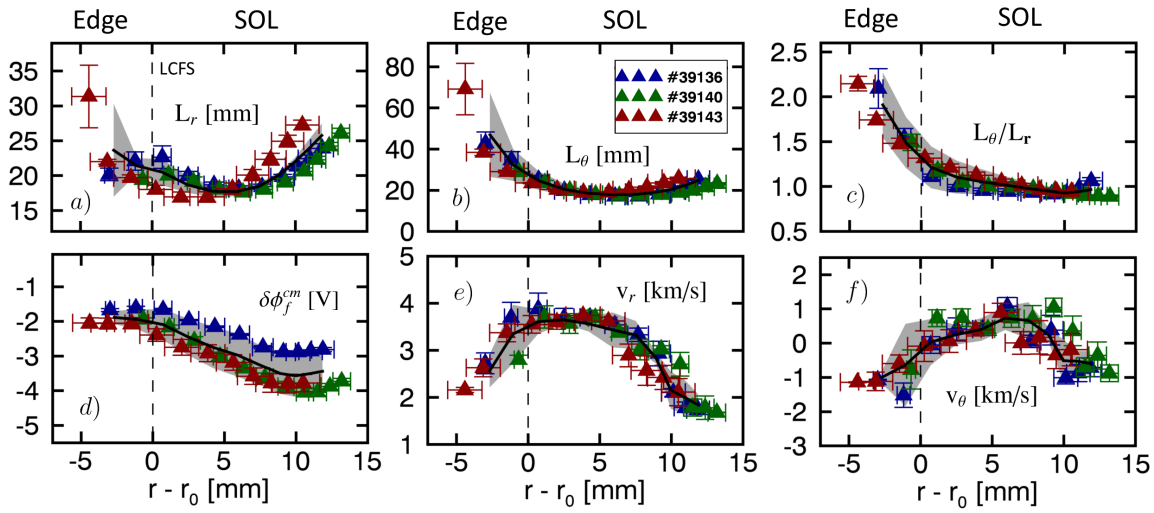

Figure 7.22: Blob parameters from the edge to the SOL during L-mode: a) radial size, b) poloidal size, c) ratio between the poloidal and radial size, d) potential amplitude, e) radial velocity, and f) poloidal velocity. The full black line indicates the average of the parameter over the three shots and the grey area the corresponding standard deviation.

In the plasma edge ($r-r_0 < 0$), the potential structure is rather aligned poloidallly than radially ($L_\theta/L_r > 1$). The blob poloidal size reaches values close to 70 mm, while the radial at the same position is $\sim$ 30 mm. The poloidal rotation is in the electron diamagnetic direction, $v_D^e = -\hat{\mathbf{b}} \times \nabla p_e/(en_eB)$, where $\hat{\mathbf{b}} = \mathbf{B}/B$, the same direction of the background $E \times B$ poloidal projection. As the structure approaches the LCFS, its radial velocity increases from around 2 km/s to up to 4 km/s, where the structure detaches from the plasma edge. During the transition to the SOL, both the radial and poloidal sizes drop, becoming comparable in the SOL ($L_\theta/L_r \approx 1$). In addition, the poloidal velocity approaches to zero. Further out, the radial size increases slightly, while the poloidal size remains roughly the same. Concomitantly, the radial velocity decreases, and the poloidal one turns negative again. The blob amplitude becomes less negative, saturating later on.

The blob tilt (clockwise with respect to the radial direction), ellipticity, area, and parallel vorticity (computed from $\omega_\parallel = \nabla_\perp \times \vec{v}^{E\times B}$, where $\vec{v}^{E\times B} = -\nabla_\perp \phi_f \times \vec{B}/B^2$) are

shown in Fig. 7.23. While in the near edge the structure is mainly aligned poloidally with a tilt closed to 90°, the transition to the SOL is followed by a change of the tilt that saturates roughly at 140°, i.e. the structure becomes rather aligned radially than poloidally in the SOL. The ellipticity is larger than 1 in the entire trajectory, indicating that structure remains stretched on the way from the edge to the SOL. In both near edge and far SOL, the ellipticity is slightly larger, which might suggest a stronger impact of the background on the blob characteristic in these positions. The two quantities: tilt and ellipticity are typically interpreted as the result of the competition between several factors, from the drive turbulence mechanism to the one responsible for its saturation, where the local $E \times B$ shear flow together with the magnetic shear play a decisive role [31, 76]. Distortions in the blob potential structure can, under certain condition, induce residual Reynolds stress [184], where the enhancement or not of the background flow depends on the eddy tilt orientation [77]. Fig. 7.23 c) shows how the blob area changes as the structure moves from the edge to the SOL. The variations of the parallel vorticity (Fig. 7.23 d) roughly follow that of the blob area in an inverse trend: the vorticity is lower in the edge when the area is larger and high in the SOL when the area is smaller. The enhancement of the vorticity that varies from $0.1{\times}10^6\ s^{-1}$ to $0.4{\times}10^6\ s^{-1}$ seems to be connected with not only the area but also to the blob potential amplitude variation (Fig. 7.22). Besides, variations on the cross-field blob shape has been show to impact on the blob velocity [197].

7.4 H-mode filaments

As discussed in the section 7.1, the external electrode biasing deeply modifies the radial floating potential profile (Fig. 7.6) that becomes further steeper around the LCFS, thus, increasing the poloidal rotation ($v_\theta^{E\times B} \approx -\nabla_r \phi_f \times B/B^2$). On the other

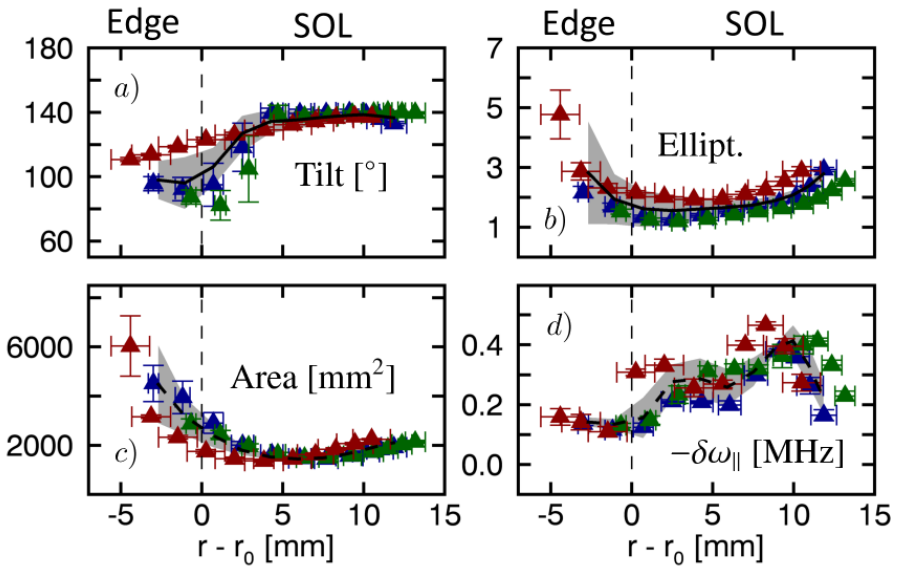

Figure 7.23: Blob parameters from the edge to the SOL during L-mode: a) tilt (with respect to the radial direction), b) ellipticity, c) area, and d) parallel vorticity. The full black line indicates the average of the parameter over the three shots and the grey area the corresponding standard deviation.

hand, the ϕ_f values remain roughly constant in the far SOL. As a consequence, the stronger $E \times B$ shear in this range is the main candidate for the observed turbulence suppression that characterizes the H-mode. As a particular result corroborating with that, Fig. 7.11 shows that the turbulence radial correlation length strongly drops in the SOL region during biasing, suggesting that coherent structures do not easily penetrate the SOL as in L-mode. Since cross-field transport is responsible for setting the mean SOL profiles (together with parallel transport), the reduction of the SOL baseline during biasing seems to be a direct consequence of that. In this section, the focus is on the bloby or filamentary transport in the edge and SOL during the biasing ELM-free H-mode. On this purpose, it was exploited the same blob detection approach introduced in the previous section. Blobs or filaments were defined as the extreme events from an ion saturation current time series located in the near SOL ($r - r_0 \approx 6$ mm). The same threshold criterion employed in the previous section was considered here, .i.e. blobs are defined as the events larger than $\langle I_s \rangle + 2.5\sigma$, $\langle I_s \rangle$

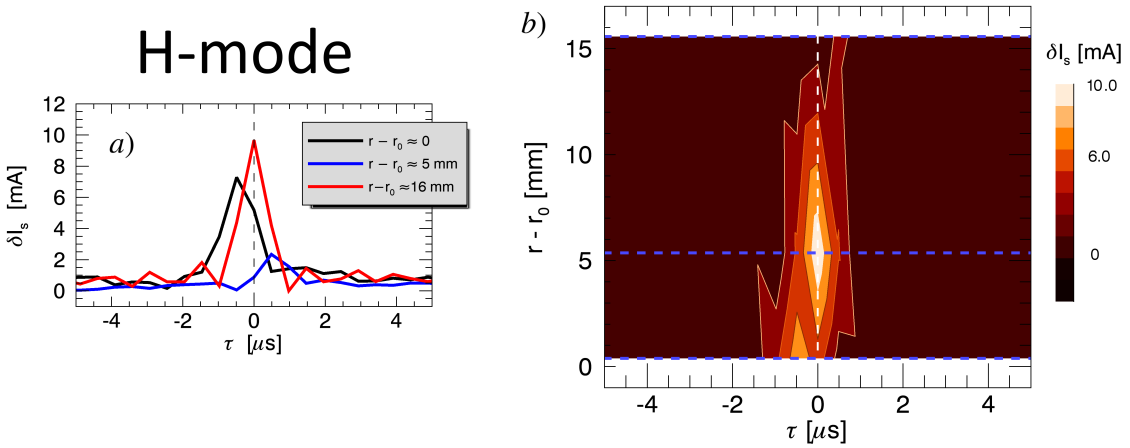

Figure 7.24: Ion saturation current conditional averaged (δI_s) for three probes in the SOL during H-mode: a) amplitude (δI_s) as function of time delay, and b) contour plot showing the amplitude in a color scheme as function of the time delay (x-axis) and the probe position with respect to the LCFS (y-axis).

and σ are, respectively, the sampling mean and standard deviation. Applying the conditional average on three I_s located in the SOL, the result (Fig. 7.24) indicates that the peaks are smaller and narrower in time with respect to the L-mode. The time delay between the reference signal (in red) and the innermost one (in black) suggests an effective radial propagation of about 5 km/s. The much smaller amplitude of the third signal, the outermost one (in blue), implies that the structure either does not reach that point with the same shape or its trajectory is deflected. In the first case, the structure would be affected by the background shear flow (possibly suppressed by it) before travelling up to the outermost point that is roughly 16 mm outer from the LCFS. Fig. 7.24 b) shows the δI_s structure projected over the radial direction for the signals shown in a). The almost vertical strip could suggest fast propagation, however, as discussed before, the combined effect of the blob size with poloidal rotation can yield such high effective radial velocity.

With the same I_s reference and criterion, the conditional floating potential ($\delta\phi_f$) can be calculated and the result is shown in Fig. 7.25. The 2D contour map captures the potential structure dynamics shown in 23 frames, with the arrows indicating

the $E \times B$ flow. The position of the three ion saturation current signals displayed in Fig. 7.25 is represented by filled circles with the corresponding color. In the first frames, from $\tau = -1\ \mu s$ up to $\tau = 0$, a dipole potential structure is evident, becoming later a negative monopole. The transition from the reference frame ($\tau = 0$) to the next frame is marked by a fast ejection and to the detachment of the structure from the plasma edge. In the subsequent frames, the dominant-negative pole takes over. This indicates that either the positive pole becomes squeezed (because of the lack of spatial resolution) or fades away. The implications of the second hypothesis for the blob dynamics will be discussed in the next section. As evident from Fig. 7.25, the potential structure does not propagate so ease as in L-mode. Instead, the structure becomes nearly 'trapped' in the SOL, remaining roughly at the same position over several frames. The vortex flow is evident, especially from the fifth frame on. The potential blob amplitude gradually decreases until fades away completely at $\tau \approx 13\ \mu s$. One can conclude that blobs exist during the ELM-free H-mode in RFX-mod, but their properties are substantially different from those in L-mode. There are some similarities, at least qualitatively, to the hot filaments observed during ELMs in the KSTAR tokamak [297], measured with electron cyclotron emission imaging (ECEI). Hot filaments can develop a finger shape [185] that, in turns, can be stabilized by sheared flows. In this case, the blob would spin rather than propagate. This is in qualitative agreement with the potential in Fig. 7.25, although the blob temperature is unknown.

Considering as reference again the negative pole, the potential blob was tracked by using the same image pattern recognition employed in the previous section. The same three shots in Fig. 7.3 were considered, in the time window: 620-720 ms. Fig. 7.26 shows the blob: a) radial size, b) poloidal size, c) ratio between the poloidal and radial sizes, d) minimum potential, e) radial velocity, and f) poloidal velocity. These parameters were computed in time slices of 50 ms with 50% of overlap. Each point of

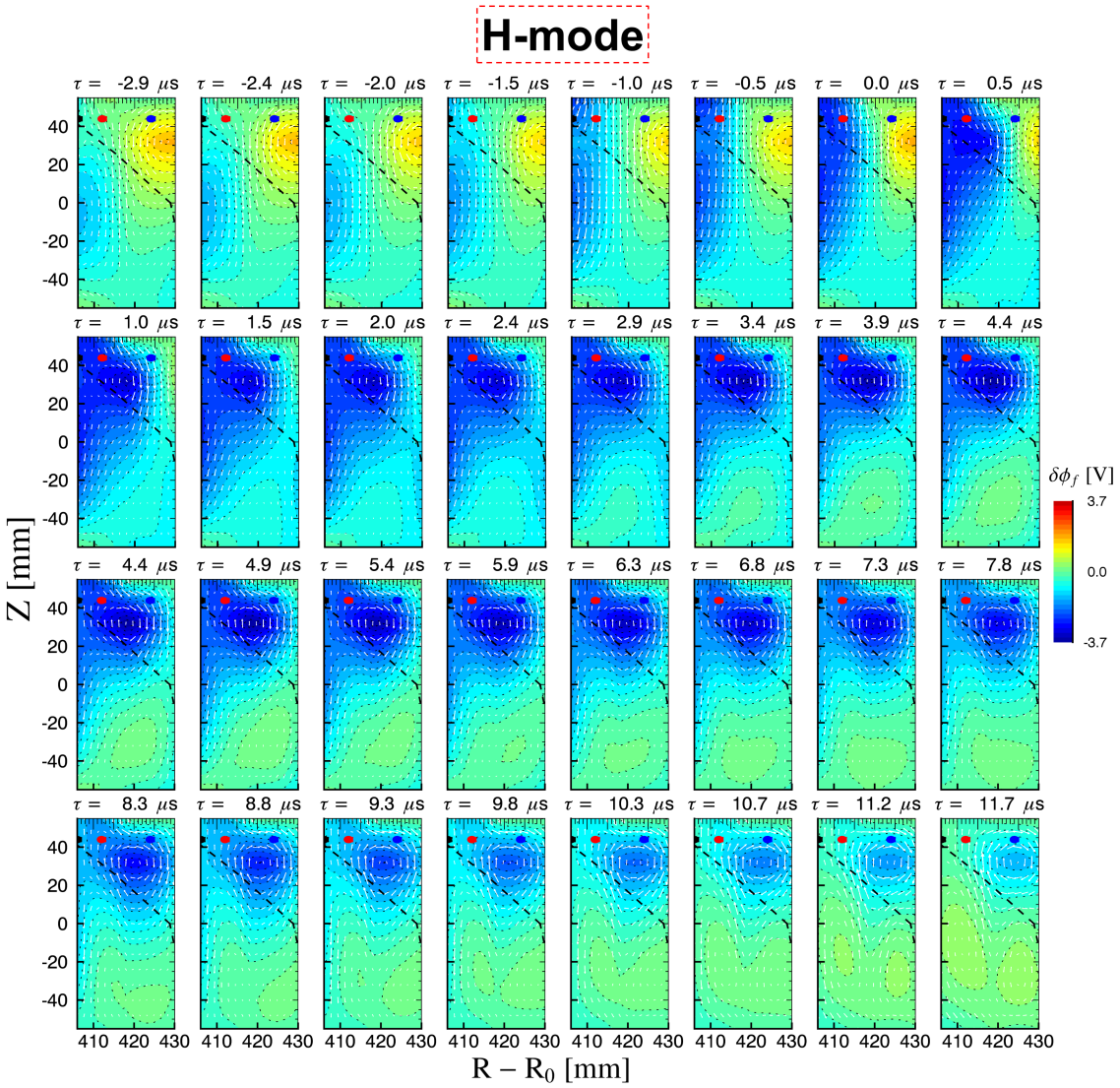

Figure 7.25: Two dimension map of the conditional average floating potential (ϕ_f) in 18 frames during H-mode. The dashed lines represent the LCFS, while the black, red, and blue dots the position of the three ion saturation signals displayed in Fig. 7.24. The white arrows represent the $\mathbf{v}^{E\times B} = -\nabla\phi_f \times \mathbf{B}/B^2$.

Fig. 7.26 is the result of the average of the corresponding parameter over the sub-time windows at the same time delay. The tracking begins in the SOL, so the parameters are constrained to this range. Near the LCFS, the structure appears more stretched poloidally than radially, with ($L_\theta/L_r > 1$). The poloidal size in this region reaches values up to 60 mm, while the radial 40 mm. Further outside, the poloidal size drops while the radial size slightly increases, yielding a more radially stretched structure in

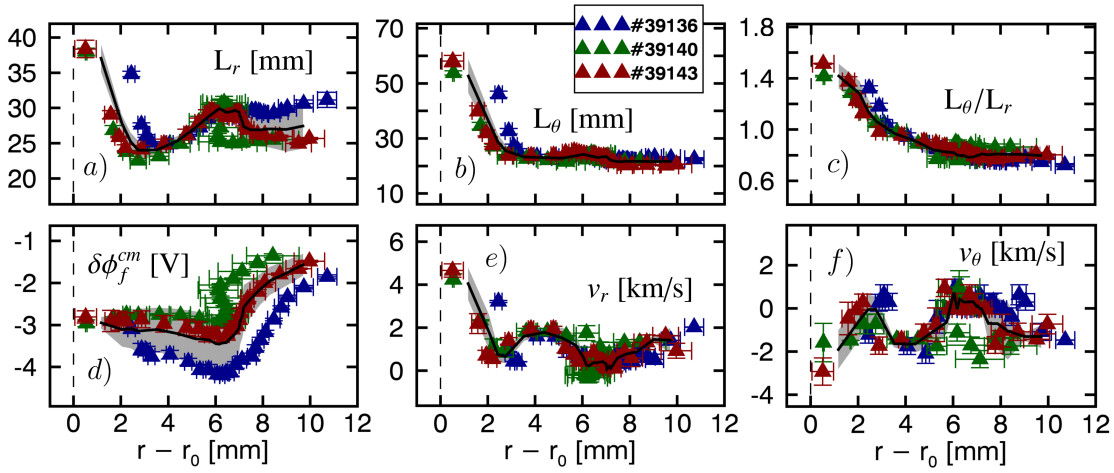

Figure 7.26: Blob parameters from the edge to the SOL during H-mode: a) radial size, b) poloidal size, c) ratio between the poloidal and radial size, d) potential amplitude, e) radial velocity, and f) poloidal velocity. The full black line indicates the average of the parameter over the three shots and the grey area the corresponding standard deviation.

this region. The blob poloidal rotation (Fig. 7.26 f) is positive close to the LCFS, in the ion diamagnetic direction: $v_D^i = \hat{\mathbf{b}} \times \nabla p_i/(en_iB)$ (opposite to the $E \times B$ poloidal flow). The radial velocity is substantially larger near the LCFS, leading to the observed blob ejection (Fig. 7.25), with values up to 5 km/s (equivalent to the velocity deduced from the time delay and radial separation of the two innermost I_s in Fig. 7.24). However, the poloidal and notably the radial velocity go almost to zero further outside, confirming the 'trapping' effect observed in Fig. 7.25. The potential amplitude gradually goes to zero (Fig. 7.26 d) after the structure stops to propagate, suggesting its depletion. The steeper profiles and the larger $E_r \times B$ shearing rate in H-mode are likely that key ingredients that keep filaments restricted to the near SOL.

In Fig. 7.27 is shown the blob: a) tilt angle with respect to the radial direction (clockwise), b) ellipticity, c) area and d) vorticity in ELM-free H-mode. The radial variation of the tilt suggests that the structure is aligned poloidally near the LCFS, becoming less tilted (or radially aligned) in the SOL. In this process, the ellipticity changes from almost 6 in the near SOL, saturating around 2 in the trapping region.

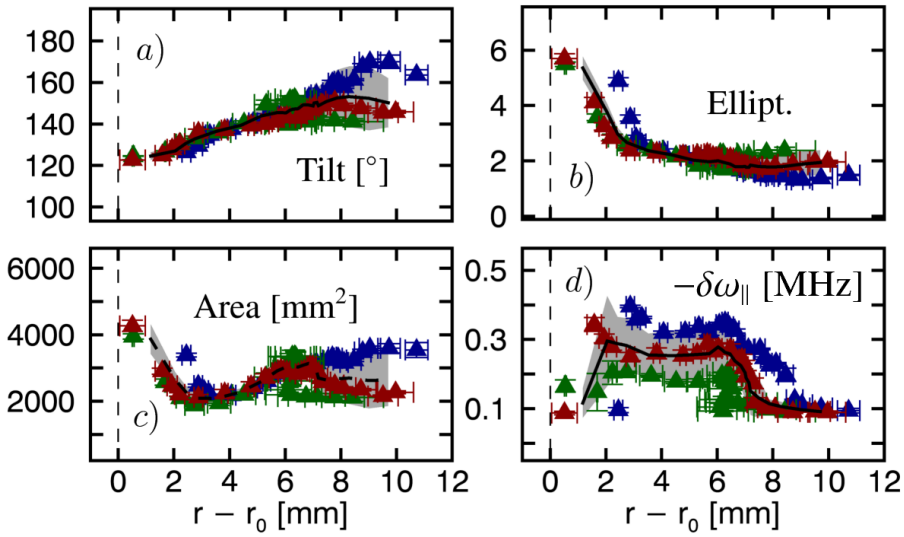

Figure 7.27: Blob parameters from the edge to the SOL during H-mode: a) tilt (with respect to the radial direction), b) ellipticity, c) area, and d) parallel vorticity. The full black line indicates the average of the parameter over the three shots and the grey area the corresponding standard deviation.

After the structure being detached from the plasma edge, the vorticity increases sharply, while the blob area decreases. Already in the trapping region, the area starts to increase when the structure begins to fade away, with a slight variation of the vorticity. Later on, the vorticity drops abruptly concomitantly with a strong potential amplitude variation (Fig. 7.27 d) that leads to the blob suppression.

7.5 L-H mode filament comparison

Up to now, potential blobs in L and H-mode were tracked and characterized along their trajectory from the edge to the SOL. Those structures are substantially different in these two regimes, underlining the impact of the plasma environment on those structures and, consequently, on the cross-field turbulent transport in these regions. In this section, this comparison will be extended to include magnetic effects and the role of parallel transport. In addition, it will be discussed the possible mechanism

behind the 'trapping' effect in H-mode that ultimately leads to blob depletion. Lastly, the blobs velocity and size in both regimes will be compared with analytical models.

7.5.1 Magnetic fluctuations and parallel current density

The U-probe belongs to the category of the filamentary probes, i.e. probes that allow measuring simultaneously the filament electrostatic and magnetic fluctuation. In RFX-mod in the Reversed Field Pinch (RFP) configuration, the U-probe combined with Gas-Puffing image (GPI) was used to correlated pressure blobs with magnetic fluctuations [245]. Particularly, it was observed a parallel current density ($\mathrm{J}_{\parallel}$) monopole associated with pressure blobs through conditional average. Further analyses in different devices have revealed that the $\mathrm{J}_{\parallel}$ can be very complex [248, 144, 244]. In the TORPEX device, those analyses were extended to a 2D view, where current density maps computed with a filamentary probe and with a 2D Langmuir probe array [87] have shown a very good agreement.

In chapter 3, it was shown that the current divergent free condition leads to a vorticity equation for filaments in the SOL. The parallel current closure set different filament regimes [145, 91, 188]. Particularly, if the current flows freely up to the sheath of a material surface, e.g. the divertor plates, the regime is called sheath-limited (SL). In the closure region the current is given by Bohm's boundary condition: $j_{\parallel} = j_s[1-exp(-e\phi_f/T_e)]$, where j_s is the ion saturation current. On the opposite direction, if the parallel resistivity becomes so high that the current along the field lines becomes negligible, the closure happens by the ion polarization drift current (see chapter 3). This regime called inertial (IN) typically happens when the collisionality along the field lines ($\nu_{\parallel}^{*} \propto nT^{-2}$) increases beyond a certain limit [188], while the filament cross-field size plays a significant role since it influences on the dominant current closure [65]. The two regimes are valid if the turbulent filaments are electrostatic, i.e. magnetic fluctuations are negligible. Electromagnetic effects become important typically when

$\beta > (m_e/m_i)$, where $\beta = n_e T_e/(B^2/2\mu_0)$ [146]. This is thought to be the case of the filamentary phase of the edge-localized mode (see chapter 8). In addition, high beta devices, e.g. reversed field pinches, can also exhibit electromagnetic filaments [245]. In the present experiment, RFX-mod running as low current tokamak, this effect is expected to be negligible. However, the condition $\beta \ll (m_e/m_i)$ during ELM-free H-mode is not so easily satisfied since the magnetic field is relatively low (~ 0.5 T), while the plasma pressure can increase sharply during biasing (Fig. 7.8).

The set of magnetic sensors installed in each tower of U-probe permits to measure simultaneously $\dot{B}_r$, $\dot{B}_\theta$ and $\dot{B}_t$, where the 'dot' stands for the time derivative. The sensors are displaced radially and poloidally (Fig. 7.28 a). The parallel current density fluctuation can be deduced from the magnetic field fluctuation according to the Amperes's Law in the slab geometry approximation:

$$j_\parallel \approx j_t = 1/\mu_0 \left[\partial_r B_\theta - \partial_\theta B_r\right]. \tag{7.7}$$

This method was borrowed from atmospheric sciences, where it has been used to measure the properties of the magnetosphere [268], and was first used in hotter plasmas in the RFX-mod [246]. Besides, the probe has been used to study magnetic reconnection in RFX-mod in RFP configuration [303]. As said before, the magnetic field fluctuation can be obtained by numerically integrating the coils signals, $B_i = 1/A_i \int \dot{B}_i dt$, where A_i is the coil effective area orthogonal to the magnetic field component of index i.

Figure 7.28 shows the magnetic perturbations related to the I_s conditional averaged blobs shown in Fig. 7.16. The circle shape depicted in the hodogram of $\tilde{B}_r$-$\tilde{B}_\theta$ Fig. 7.28 b) is a signature of parallel current density perturbation [245]. The wider is the circle the larger is the current flowing through the region. The parallel current density fluctuation is shown in Fig. 7.28 c). One can see that the peak or valley of δj_t does not appear at $\tau = 0$, i.e. when the I_s blob amplitude is maximum. This

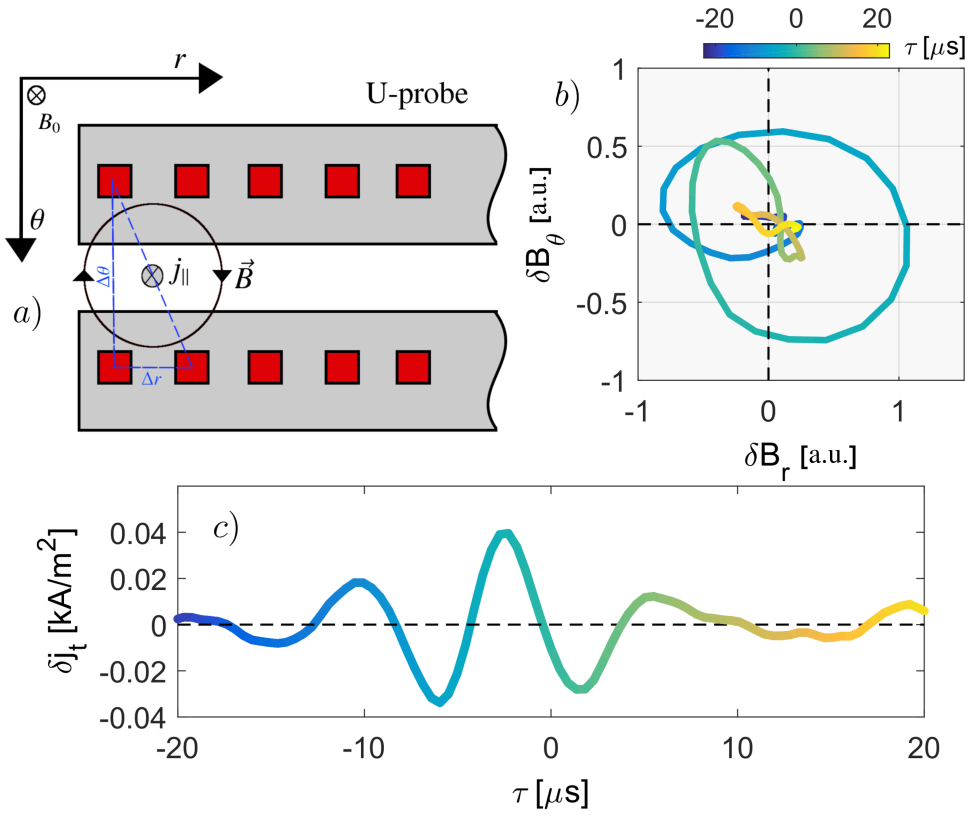

Figure 7.28: Magnetic fluctuations related to the I_s conditional averaged blob of Fig. 7.16. a) Cartoon showing the magnetic sensors, b) hodogram of the poloidal vs radial magnetic field fluctuation, and c) parallel current density fluctuation (j_t).

not-synchronized behaviour is likely related to the displacement between the two signals, as will be discussed next. Besides, the presence of both positive and negative oscillations suggest a multi-polar behaviour of δj_t.

By combining the signals of the coils from the two towers in groups of three sensors (see Fig. 7.28 a), radially and poloidally displaced, one can build a two-dimensional map of the parallel current fluctuation. The reference position of each combination is defined as the barycenter of the triangle formed by the coils. Five magnetic sensors in each tower were considered, which results in a 4x2 grid. The current density signals are related to I_s blobs by means of conditional average. In the Fig. 7.29 are shown the 2D maps of j_t related through conditional average with the I_s references shown in Fig. 7.17 and Fig. 7.25 in L (top) and H-mode (bottom). The corresponding ϕ_f

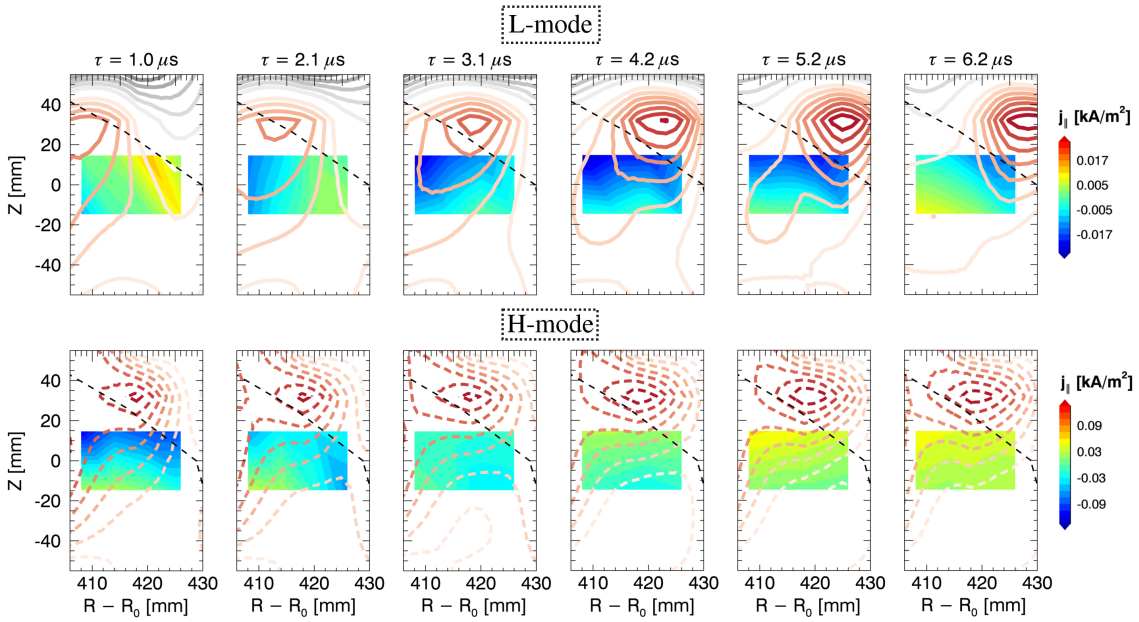

Figure 7.29: Parallel current density map in L (top) and H-mode (bottom) related to the conditional averaged I_s shown in Fig. 7.12 and 7.24. The overplotted contours represent the conditional averaged floating potential of Fig. 7.17 and Fig. 7.25. According to the colorscheme, negative is represented by 'red' and positive by 'black'..

conditional averaged contour maps are over-plotted for each case, where, from the color scheme, the negative potential is represented by 'red' and positive by 'black'.

In L-mode (top panel of Fig. 7.29), the j_t evolution seems to be connected with the propagation of the floating potential structure. Both present an almost synchronized negative structure that propagates radially outward towards the SOL. The result seems to be in qualitative agreement with the sheath-connected regime [88, 205], in which parallel transport is the main mechanism responsible for the filament depletion. During H-mode, the parallel current density appears stronger near the edge, with values almost five times larger than in L-mode. This result agrees with the higher beta environment during H-mode [248]. In the first frame displayed in Fig. 7.29, j_t assumes its largest absolute value, with a wide structure that covers a range from the edge up to the near SOL. In the next frame, the structure becomes more constrained in a narrower range around the edge. In the subsequent frames, the δj_t decreases

sharply, roughly around the potential blob becomes trapped. The results indicate that filaments in ELM-free H-mode emerge in a more intense magnetic fluctuation environment with a larger parallel current density compared to the L-mode. However, this current strongly reduces when the potential structure spreads out over the SOL in a short time window.

7.5.2 Blob suppression

As discussed in chapter 3, sheared flows are the most important mechanism for suppressing turbulence in plasma fusion devices. Analytical models suggest that blobs can be destroyed by high $E \times B$ shear flows [95], result also observed in seed blob simulations [296]. According to Ref. [23], radially elongated turbulent structures, known as streamers, or blobs can be torn apart by an external shear if their effective convective time exceeds the local shearing time:

$$\tau^{blob} = L_r/(|v_r|) > L_\theta/(L_r|\gamma^{E\times B}|) \tag{7.8}$$

where $\gamma_{E\times B} \cong B^{-1}dE_r/dr$ and L_r and L_θ are, respectively, the blob radial and poloidal size. The background shear flow selects structures based on its size and velocity, analogous to the well-known eddy decorrelation criterion [21]. To verify this effect, the $E \times B$ shearing rate was estimated from the floating potential ($\gamma_{E\times B} \approx B^{-1}\nabla_r^2\phi_f$) around the range where the filament is detected (Fig. 7.6). Considering the blob side and velocity obtained in the previous sections, the criterion can be tested for the L and ELM-free H-mode regimes.

Figure 7.30 compares the shearing rate profile in both scenarios with the inverse of the effective turbulent characteristic time ($1/\tau^{turb} = v_r L_\theta/L_r^2$). The blue dashed line represents $\gamma_{E\times B}$ during L-mode while the red dashed line is for H-mode. In addition,

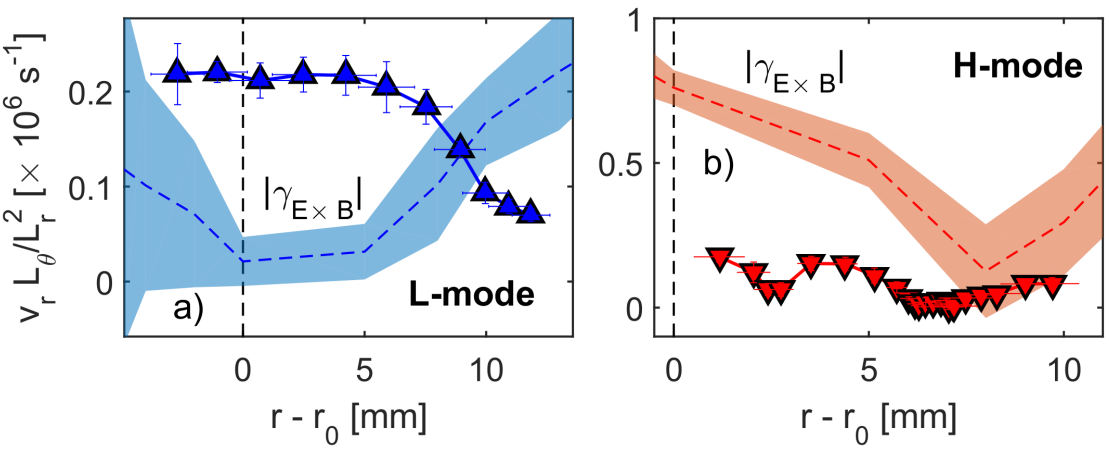

Figure 7.30: Comparison of the $E \times B$ shearing rate and the blob effective time ($v_r L_\theta / L_r^2$) for a) L-mode, and b) H-mode scenario. The parameters are result of the average over three shots (#39136, #39140 and #39143). The two colourful areas represent the shearing rate uncertainty.

the up and low triangle curves represent $1/\tau^{turb}$ in L and H-mode, respectively. The curves displayed in Fig. 7.30 a) and b) are the result of the average over the three considered shots (Fig. 7.3) in L and H-mode. In L-mode, $1/\tau^{turb}$ is higher than the background shear over the practically the whole trajectory, only in the outermost regions, they become comparable. Therefore, according to the suppression criterion (Eq. 7.8), the L-mode filaments are expected to withstand the background $E \times B$ shear. On the other hand, during biasing the shear flow increases sharply, way above the limit where the L-mode blobs would survive. In H-mode, filaments do not propagate as in L-mode, instead the potential blob becomes trapped in the near SOL for a relatively long period. The blob is not instantaneously suppressed as the criterion (Eq. 7.8) might suggest.

Studies of vortex structures embedded in a sheared flow background indicate that while the 'prograde' (i.e., when vorticity and shear have the same sign) is stable, the 'adverse' (i.e., when vorticity and shear have an opposite sign) are unstable and tend to fragment [168]. Therefore, the shear selects the vortex accordingly to the sign of its vorticity, changing then the relative population of positive and negative

pole [241]. Fig. 7.31 a) shows a cartoon of a background flow (v_θ) represented by a parabolic curve. The corresponding shearing rate is shown in Fig. 7.31 b) as a line, with negative values for $\rho < 0$ and positive for $\rho > 0$. The shear selects the 'prograde' vortexes in each region, resulting in vortexes with agreed vorticity signal with respect to the background shear (Fig. 7.31 b)) [168]. This effect can change the turbulent transport properties in regions where coherent structures exist, with superdiffusion transport where the population of dipolar vortex structure is the dominant [242] and subdiffusion where monopolar struct population is surplus [220]. Besides, in certain conditions, a vortex can feed the background shear or been fed by it resulting in its depletion in some cases, while background shear gets enhanced by enstrophy transfer [77]. In Fig. 7.17, it was observed that the potential structure related to the blob in L-mode has a dipole shape while in H-mode (Fig. 7.25) a monopole structure is more evident. The monopole vorticity has the same sign with respect to the background shear in the near SOL, suggesting that the vortex is 'prograde'. The positive vortex, that supposedly should be unstable, it does not indeed appear in the frame. The negative pole eventually becomes destabilized and disappear (Fig. 7.25). It is worth noting that hot filaments are also expected to have a monopole potential structure rather than a dipole [185], this can be the case of the H-mode filaments shown here, as it is for ELM filaments [297]. However, since the blob internal temperature was not measured in this experiment one can just speculate about that.

In the light of these results, one can conclude that the strong turbulence suppression observed in H-mode is mainly driven by $E \times B$ shear flow. This can happen directly: the $E \times B$ shear effectively suppresses the structure (e.g. by torn it apart, while the smaller structure is easily damped by the background), or indirectly: modifications in the potential structure (i.e. vortex selection by sheared flows) can lead to trapping effects [185] and vortex destabilization.

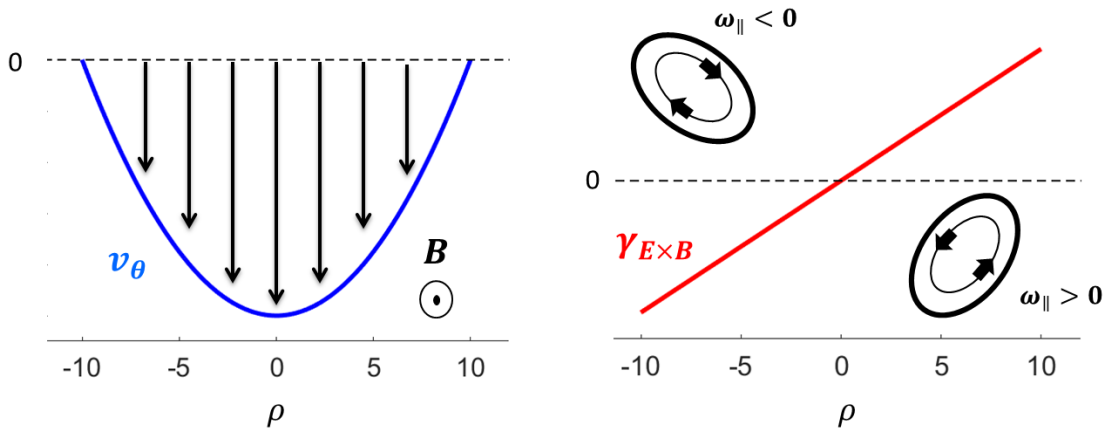

Figure 7.31: Cartoon illustrating the vortex selection mechanism. On the left: parabolic radial poloidal flow profile and, on the right, the corresponding shearing rate ($dv_\theta/d\rho$). The negative shear branch selects structures with negative vorticity, while the positive branch selects those with positive vorticity [168].

7.5.3 Filament velocity scaling

Filaments might be found in different regimes in the SOL depending on the level of collisionality along the field lines and the magnetic topology [185, 146]. These parameters determine whether filaments at the outboard midplane are or not electrically connected to a material surface elsewhere, e.g. divertor tiles or the wall.

The sheath connected or sheath-limited (SL) and the resistive balloning or inertial (IN) regimes set, respectively, a lower and an upper boundary for the blob velocity in the cold ions approximation (see chapter 3). The velocity scaling in these two regimes are:

$$v_b^{SL} = 2c_s \frac{L_\parallel}{R} \left(\frac{\rho_s}{\delta_b}\right)^2 \tag{7.9}$$

$$v_b^{IN} = c_s \sqrt{2\frac{\delta_b}{R}} \tag{7.10}$$

Where δ_b is the blob size, $\rho_s = \sqrt{T_e m_i}/eB$ is the ion gyroradius, and $c_s = \sqrt{T_e/m_i}$ is the sound speed. While in sheath-connected regime (as the name suggest) filaments found in the midplane SOL are electricity connected to the divertor (or wall) sheath, in the inertial regime they become disconnected (the closure current is through the ion polarization drift).

Figure 7.32 shows the blob cross-field velocity ($v_b \sim v_r$) normalized by the local sound speed as function of the blob radius ($\delta_b \sim L_\theta/2$) normalized by the local ion gyroradius for L and H-mode scenario. The solid and dashed red lines represent, respectively, the sheath-limited scale at $L_\parallel = 10$ m and $L_\parallel = 30$ m: approximately the parallel connection lengths evaluated in the near and far SOL (Fig. 7.13). The blue line represents the inertial regime. The electron temperature near the edge is assumed to be 15 eV in L-mode and 10 eV in H-mode, hence, the ion Larmor radius is $\rho_s \approx 0.8 - 1.0$ mm, while the sounds speed in L and H-mode are, respectively, $c_s = 22 - 27$ km/s.

In L-mode, two main trends are depicted (Fig. 7.32, left). Blobs located near to the LCFS roughly scale as predicted by the sheath connected regime at $L_\parallel = 30$ m, compatible with the expected connection length in this region. However, blobs detected farther tend to scale fairly well with the sheath connected regime at $L_\parallel = 10$ m. The result suggests that the blobs center of mass perceives the connection length variation observed in Fig. 7.13. Intermediate regimes such as the resistive X-point, ideal-interchange, or the neutral-friction [261] can also be important.

During the ELM-free H-mode phase (Fig. 7.32, right), two regions scaling in different way are observed. While close to the LCFS blobs seem to scale as the inertial regime, further outside they approach to the sheath limited case, that is, they become electrically connected to the wall. However, the impact of the background shear likely plays a role in their dynamics (Fig. 7.30), which is not foreseen by the model [185].

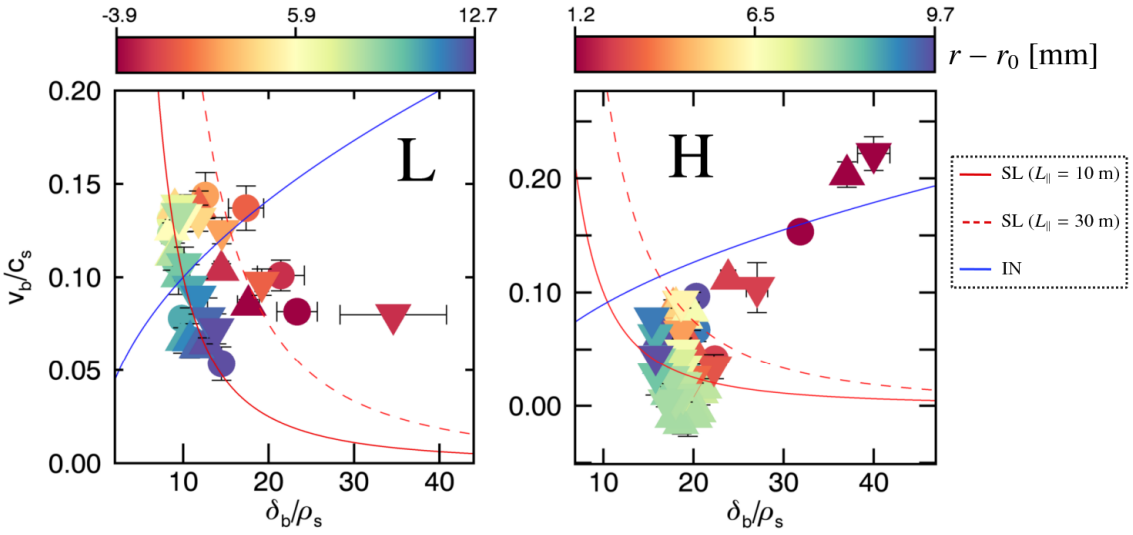

Figure 7.32: Blob normalized velocity as function of the normalized size in L (on the left) and H-mode (on the right). The symbols represent the three reference shots: circle (#39136), up-triangle (#39140), and down-triangle (#39143). The red lines stands for the sheath limited velocity scale (SL) at $L_\parallel = 10$ m (full line) and $L_\parallel = 30$ m (dashed line), the blue curve represents the inertial scale (IN). The colorbar refers the position of the detected blob with respect to the separatrix position in millimetres.

The larger $E \times B$ shear during biasing acts as saturation mechanism. Filament velocity scales that incorporate the blob amplitude with respect to the background [260, 165] seem to be more appropriate for this case. However, how a sheared background flow impacts a potential structure and how this affects the blob motion and so the velocity scaling prediction is not yet fully understood in the literature.

7.6 Conclusion

In this chapter, it was discussed the effect of a biasing electrode placed in the edge of RFX-mod operating as a single-null tokamak. This technique has been shown to induce H-mode in several devices [258, 26, 116, 101], and recently in RFX-mod tokamak in both single-null and circular configuration [243]. The biasing effect in the edge and SOL of RFX-mod was studied with a set of electrostatic and magnetic sensors. It was shown that the level fluctuation decreases in the biasing phase, when the ion

saturation current and floating potential profiles become steeper (Fig. 7.6 and 7.8), and, consequently, the plasma poloidal rotation (Fig. 7.6 c) and Fig. 7.7 d). The I_s fluctuation and the turbulent radial flux decrease in this phase around the LCFS (Fig. 7.9), while the ϕ_f fluctuation level drops close to the wall (Fig. 7.14). This is further corroborated by the smaller radial correlation length in the SOL (Fig. 7.11), suggesting that the turbulence does not penetrate the SOL so easily in this phase. Since transport in this region is dominated by filaments or blobs, the second part of this chapter was dedicated to study of these structures in two scenarios in the RFX-mod operating as tokamak: regular L-mode and ELM-free H-mode. In both cases, potential coherent structures related to ion saturation current bursts by means of conditional average were successfully detected, tracked, and characterized. 2D dynamic pattern recognizing based on the combination of cross-correlation and eigenvalue decomposition of the covariance matrix was applied in each time frame to depict the blob velocity and shape. In L-mode, a dipole potential structure was perceived near the edge (Fig. 7.17), becoming less evident further out, where the negative pole dominates the frame. For that reason, the negative pole was considered as the reference for the filament cross-field properties, e.g. shape and velocity. While this structure was mainly aligned and stretched poloidally near the LCFS, in the SOL it becomes more circular and less tilted. Fast radial ejection from the edge was observed. The blob radial velocity increases as the structure approaches to the LCFS, decreasing in the SOL where values were typically ~ 2 km/s. Its amplitude and vorticity also increase in this process, slightly reducing later in the far SOL. The blob poloidal velocity was observed to be in the electron diamagnetic direction in the near edge, the same direction of the $E \times B$ background poloidal projection velocity.

On the other hand, in the high biasing scenario, ELM-free H-mode, blobs appear mainly in the SOL. The potential in this case seems to be a negative monopole rather than a dipole. Near the LCFS, the potential blob is stretched along the poloidal

direction, reaching the highest radial velocity (~ 4 km/s). The poloidal rotation is in the ion diamagnetic direction in this region, in the opposite direction to the $E \times B$ background drift. Further outside, the structure becomes trapped and its amplitude is drastically reduced, which suggests its suppression. This result is supported through the comparison of the inverse of the blob characteristic time ($1/\tau^{turb} = v_r L_\theta / L_r^2$) with the local $E \times B$ shearing rate ($\gamma_{E\times B} = B^{-1} dE_r/dr \approx B^{-1} d^2\phi_f/dr^2$) (Fig. 7.30). According to [24], streamers or blobs are broken when $\gamma_{E\times B} > 1/\tau^{turb}$, analagous to the well known eddy decorrelation models [21, 28]. While during L-mode $1/\tau^{turb}$ is always higher than $\gamma_{E\times B}$, in ELM-free H-mode, $\gamma_{E\times B}$ increases way above the L-mode values. In addition, it was pointed out that the vortex selection by the background sheared flow [168] can yield the trapping effect observed in H-mode, since dipole can turn into monopole by this process, which would make blob to spin rather than radially propagate [185]. Therefore, the potential structure can either be suppressed directly by means of the shear [24] or indirectly by vortex selection, in this case, parallel loss would be the dominant dissipation mechanism. Besides, since blobs are closely connected with turbulence spreading phenomenon in the edge and SOL, the findings report here indirectly suggest similar edge-SOL decoupling effect discussed in chapter 5.

Finally, blobs dynamics in the two scenarios were discussed in the framework of analytical models and velocity scaling [146, 93, 188]. In the regime called sheath connected, blobs are typically electrically connected to a sheath along the field lines, where parallel dynamics are responsible for the potential depletion. On the other hand, in the so-called inertial regime, blobs become disconnected, with the ion polarization current largely overcoming the parallel one. Blobs in RFX-mod tokamak during L-mode were better described by the sheath connected regime (Fig. 7.32). Besides, the parallel current density and potential structure are roughly synchronized (Fig. 7.29, top). However, due to the strong variation of the parallel connection length

over the radial range covered by the probe, filaments scale roughly in two regimes. While near the LCFS they are better described by the sheath connected scale at $L_{\parallel} \approx 30$ m, in the far SOL the better match happens at $L_{\parallel} \approx 10$ m, roughly in accordance with the predicted $L_{\parallel}$ in this region (Fig. 7.13). In the ELM-free H-mode, however, filaments near the LCFS have a better agreement with the inertial regime. Indeed, the SOL electron temperature is lower in this phase, suggesting an increase in the collision factor. The parallel current density structure reaches its maximum amplitude and size in the edge but nearly disappear later (Fig. 7.29, bottom). In the SOL region, where filaments virtually stop propagating, the model does not seem to fit properly. Models that take into account the blob relative fluctuation [260, 165] are likely more appropriate in this case. Nevertheless, the impact of the background flow on coherent potential structures (i.e. vortex selection) and how this affects the density blob velocity and stability is overlooked. The biasing effect on the blobs dynamics ultimately affects the SOL properties. The reduction of the radial turbulence correlation length (Fig. 7.11), as well as the SOL ion saturation current baseline (Fig. 7.8), and the plasma-wall interaction (Fig. 7.14) are examples of this behaviour.

Chapter 8

ELMs filaments

The transition from low to high confinement in tokamaks happens as a result of the rise of an edge transport barrier (ETB), with steeper edge pressure gradient and strong $E \times B$ shear flow around the last closed flux surface (LCFS). The high confinement mode (H-mode) is characterized by a substantial improvement in the confinement of particles and energy [279]. The strong increase of pressure in H-mode results into a 'pedestal' region in the near edge and to even larger poloidal flow. The further increase of pressure is, however, constrained by the MHD limit, that ultimately leads to instabilities, being the Edge Localized Modes (ELMs) the most common and potentially dangerous for the feasibility of the future fusion reactors [301, 153]. While the so-called spontaneous L-H transition typically happens after the injection of additional heating, e.g. neutral beam injector (NBI) or electron cyclotron resonance heating (ECRH) [279], edge transport barriers can also be induced via edge biasing technique (chapter 2) [258, 273, 189]. The resulting H-mode in both cases exhibits a similar feature, with steeper pressure gradient concomitantly with a strong turbulence suppression, leading to an improvement of the stored plasma energy. Besides, edge localized modes (ELMs) have been reported in biasing experiments [243].

The aim of this chapter is to study edge-localized modes (ELMs) and their filamentary trace in RFX-mod, running as tokamak, and the COMPASS tokamak.

8.1 Edge-Localized Modes (ELM)

The Edge-Localized Modes (ELMs) refer to a type of MHD instability in the plasma edge of toroidal magnetic fusion devices that appear during the high confinement mode (H-mode) in tokamaks [301, 50, 153], with also some evidence of their appearance in stellarators [118, 93]. The phenomenon is usually accompanied by a fast loss of energy and particles towards the SOL, in a millisecond time scale. A very similar effect happens in the solar corona, characterized by relatively fast (in the order of minutes or hours) periodic solar flares, followed by a large ejection of energy [53, 212]. Therefore, this is a more general effect in nature with important implications for telecommunications, in the latter case, and the device life-time in the case of ELMs.

The L-H transition is followed by the appearance of an edge transport barrier (ETB), resulting in steeper density and temperature profiles and massive turbulence suppression. When the pressure gradient increases beyond the ideal MHD limit, the Edge Localized Modes (ELMs) can appear. The most accepted view considers that the ELM is generated by a combination of peeling and ballooning instability, also called peeling-ballooning mode [236]. While ballooning is a typical pressure-driven instability that occurs in the 'bad curvature' region (low field side) because the large edge pressure gradient in H-mode is not proper balanced by the average curvature of the magnetic field lines [287]. The peeling instability is a current-driven type, characterized by an edge localized external kink mode [153]. The key element that couples these two distinct instabilities is the bootstrap current. As discussed in chapter 7, such current is predicted by neoclassical theory and it is related to the particle orbits at low collisionality, the so-called 'banana orbits'. When the pressure gradient

becomes steeper, larger than the certain limit, and the collisionality is low enough, then particles in a banana orbit can follow their trajectory without suffering collisions with other closer particles, i.e. $\nu_{ei} < \nu_b$ (the local collision frequency is lower than the banana bounce frequency). In this case, a projection of its trajectory along the magnetic field lines yields an effective current proportional to the pressure gradient: $j_b \propto \nabla_r p$. Since in H-mode the pressure gradient from the pedestal to outward becomes stronger, a large bootstrap current arises in this region. This phenomenon has two effects: (1) to increase the free-current in this region, which favours the growth of current-driven instabilities; (2) to make the magnetic shear profile less steep in the edge, which has a destabilizing effect on ballooning instability [153]. Fig. 8.1 shows the classical schematic diagram of the peeling-ballooning instability. The figure shows at different plasma shaping (where strong and weak referred to high and low triangularity, respectively) the boundary limit for activating the peeling and the ballooning instabilities. In the graph, j_{ped} and p'_{ped} are, respectively, the pedestal current density and radial pressure gradient. Since $j_{ped} \propto p'_{ped}$, because the bootstrap current, both quantities are coupled. However, the bootstrap current also depends on the level of collisionality. For high density, the plasma edge becomes more collisional, making difficult for a particle to complete a banana orbit without colliding with other particles. In those cases, the pressure gradient can rise without a significant increase in the bootstrap current: the dominant instability becomes the ballooning. On the other hand, in collisionless plasma, when, for instance, the plasma density is too low, the bootstrap current increases unimpeded until reaches the peeling instability boundary. In most cases, however, both quantities increase in a coupled way, reaching the peeling-ballooning boundary, where both instabilities coexist and contribute to the ELM formation and crash. Some alternative approaches consider the role of microinstabilities on driving ELMs [293]. In the EPED model [235], kinetic ballooning mode (KBM) together with peeling ballooning (P-B) are the key ingredients that determine

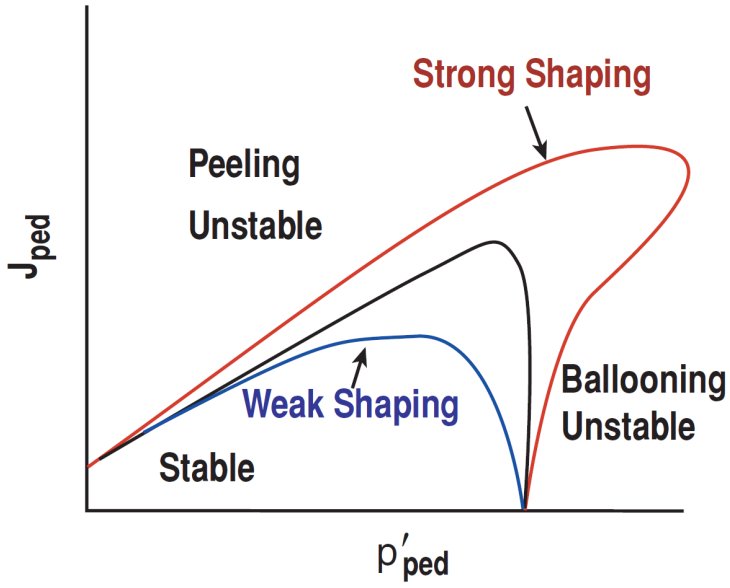

Figure 8.1: Schematic diagram illustrating the peeling-ballooning instability. The color stands for different plasma shape: blue - weak shaping; black - intermediary shaping; red - strong shaping, where strong and weak are for high and low triangularity, respectively.

the ELM rise and growth. The model is able to predict the pedestal height and width, which are important parameters for the plasma performance. Nevertheless, the non-synchronous recover of density and temperature gradient after an ELM crash [27] is not consistent with the KBM constraint in the EPED model.

Linear analysis can predict some features of the possible driven instability that generates the ELM [237, 182]. Those analyses reveal that the ELM is composed of several modes [235], characterized by a large toroidal number, with most of them concentrated at the low-field side (due to the ballooning nature of the instability). The largest mode sizes are found at the outboard midplane where the local magnetic shear is less intense. There are several types of ELMs [153] observed in different machines, but the most danger one for the plasma-facing components is the type I [160]. The type III ELM is particularly interesting, because the ELM amplitude is lower (compared to the type I), although its occurrence frequency is larger, and usually it manifests in high collisional plasmas. Besides, quasi-coherent modes in the

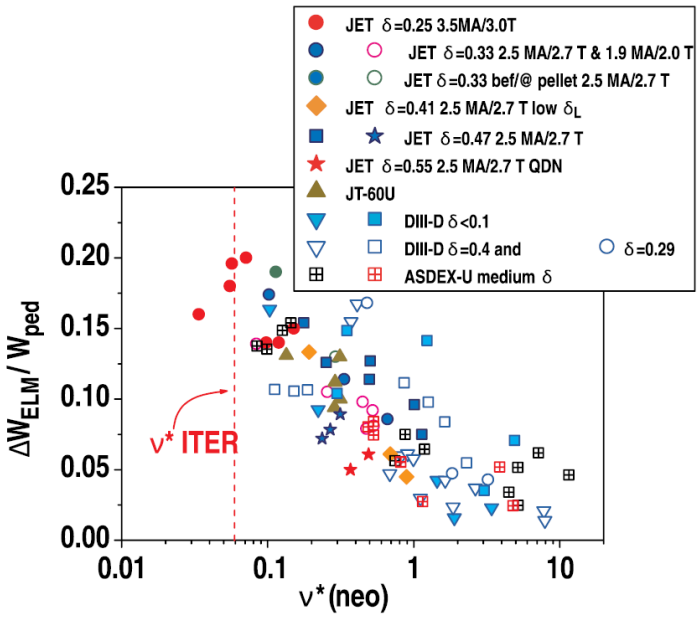

Figure 8.2: ELM energy normalized by the pedestal energy ($\Delta W_{ELM}/W_{ped}$) as function of the neoclassical viscosity for type I ELM in several devices. Image reproduced with permission from Reference [160]

.

inter-ELM phase observed during the EDA H-mode regime in Alcator C-mod [151] and HRS in JFT-2M [136] reveal an interesting regimes where ELMs are absent but particle transport is high. The amount of energy carried by a single ELM event (δW_{ELM}) is typically normalized by the pedestal energy: $W_{ped} = 3/2\ n_{ped}(T_{e,ped} + T_{i,ped})/V_{plasma}$, where n_{ped}, $T_{e,ped}$, and $T_{i,ped}$ are, respectively, the pedestal density, electron and ion temperature. V_{plasma} represents the plasma volume inside the LCFS. The relative ELM size ($\delta W_{ELM}/W_{ped}$) has been observed to depend on the neoclassical collisionality (see Fig. 8.2) for type I ELMs. At the expected ITER collisionality, the ELM lost energy can be up to 20% of the pedestal energy, which for ITER scale can represent a non-tolerable power load over the plasma-facing components [160]. Indeed, it can reduce substantially the machine life time [74].

However, once the instability arises and growths, a complex interaction between modes and the background turns the system fully non-linear. A net result of this

non-linear phase is the ejection of filamentary structures towards the SOL and wall. Different from L-mode turbulent filaments that are typically thought to be electrostatic [63] since $\beta < (m_e/m_i)$ [165], where $\beta = n_e T_e/(B^2/2\mu_0)$. ELMs filaments are electromagnetic [153] and carry a large amount of plasma current outward [244], which can locally modify the magnetic field topology in some cases. In the SOL region, where the magnetic field lines are open, the ELMs are exhausted at sound speed velocity along the field lines, but their large cross-field velocity makes the heat flux width pattern at the divertor plates much broader than in H or even L-mode [66]. Those ELMs filaments can even enhance the level of plasma-wall interaction, which can lead to erosion of the plasma wall and increase of impurities influx [208]. A strong evidence in this direction is the ELM energy fraction on the divertor plates that typically is lower than the energy lost by the pedestal. This effect intensifies with the ELM size ($\delta W_{ELM}/W_{ped}$), reducing to almost 40% at $\delta W_{ELM}/W_{ped} \approx 0.3$. Although radiation loss can account for a significant part of the energy that leads to this discrepancy [209, 84], most of the energy is lost on the wall through cross-field transport [153].

8.2 Electromagnetic filaments

The presence of filaments associated with the ELM cycle was evident from early on. Probes placed in the scrape-off layer often detect a rich and complex pattern of peaks and valleys for the density and potential measurements, related to the ELM 'fine' structure rather than a single big event [232]. Fast cameras in MAST (Fig. 8.3) have shown large filaments during ELMs, aligned to the magnetic field with a typically toroidal number in the range $5 \leq n \leq 15$. In KSTAR tokamak, the filamentary nature of ELMS is well captured through the electron cyclotron emission imaging

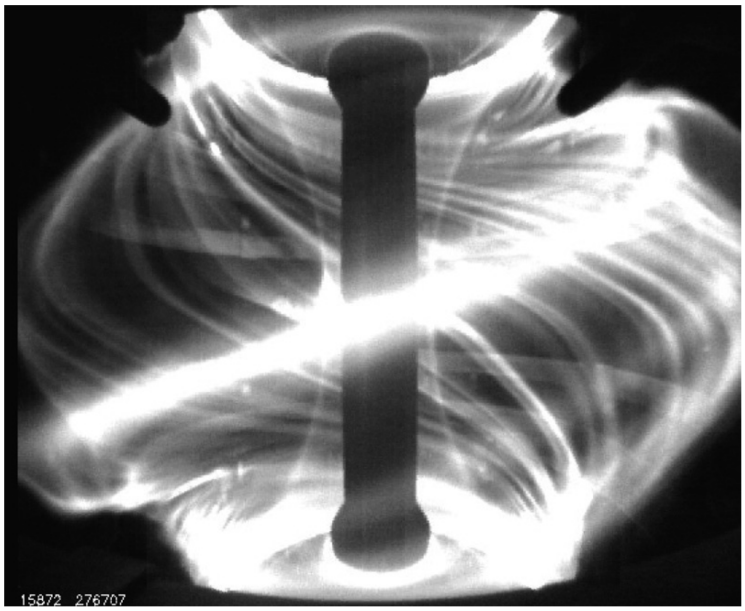

Figure 8.3: Image of ELM filaments observed with fast cameras in the MAST tokamak [140].

(ECEI) technique [297], where high-temperature structures, with finger-like shape, enhances the cross-field transport in the near edge and SOL.

ELMs are transient events related to periodic plasma relaxation, with a strong ejection of particles and energy from the pedestal to the SOL. As a consequence of that, the mean profiles, density, temperature, and potential become transiently flatter. Since ELMs are related to filamentary transport and those are affected by the plasma background (see chapter 7), it is natural to think that this relaxation favors the propagation of a broad range of blobs, with different size and velocity. A fundamental question would be: is this relationship prior to the onset of the filamentary transport or are the filaments that induce the relaxation? Field line stochastization can enhance the parallel transport along reconnected field lines [238], leading to a fast energy ejection. This process by itself can account for a large amount of energy loss from the pedestal to the divertor [124]. As a result, the profiles become less steep, reducing the $E \times B$ shearing rate, and thus enabling that filaments or blobs

to easier cross-field propagate. Experimental data from electrostatic probes show that the bursty oscillation related to the ELM fine structure occurs over a slower envelope perturbation. The latest ELM activities happen when the radial profiles are fully recovered, that is when the edge transport barrier becomes strong again. Recent experiments results suggest that the ELMs filaments at high collisionality can be mitigated by $E \times B$ shear flows [142]. This topic will be further discussed in section 8.3.

Initial ELMs simulations have treated the related filaments as pure electrostatic structures [86]. Experimental result comparing the ELMs parameters (size and velocity) measured with an electrostatic probe with analytical filament velocity scaling models in ASDEX Upgrade seems to agree inertial or restive ballooning regime [224]. However, there is plenty of evidence indicating that the ELM filaments are actually electromagnetic [140, 179, 277]. The fact that those filaments arise as a result of the non-linear saturation of an electromagnetic instability (peeling-ballooning) corroborates with that. In addition, ELM filaments are observed to carry a large amount of current towards the SOL [244]. If this current is large enough, perturbations in the magnetic topology can further enhance the cross-field and parallel transport [63]. This happens when the filament internal beta $\beta = 8\pi p/B^2$, where p is the filament peak pressure, induces field line bending ($\Delta \sim L_{\parallel}^2 \beta / R$, where $L_{\parallel}$ is the parallel connection length and R is the major radius) to such an extent that field lines become short-circuited from the near edge and SOL to the wall at the midplane. Besides, a pair of current-carrying filaments, with opposite direction, can mutual repeal, increasing substantially its radial propagation [183]. This might explain the fast filament ejection following an ELM event. Analytical models suggest that electromagnetic filaments, such as the ELMs filaments, scale differently from an electrostatic filament, but with similar dependency [165]. Indeed, experimental results suggest that the

ELM filament velocity is proportional to the square root of its size [224], which is the expected dependency for restive ballooning [188] and for electromagnetic blobs [165].

8.3 ELMs in RFX-mod tokamak

This section is devoted to the study of the ELM-like structure recently observed in the RFX-mod operating as tokamak [243]. The RFX-mod is a Reversed Field Pinch (RFP) device that has been recently operated as a low current tokamak (see chapter 7). The toroidal magnetic field is $B \leq 0.55$ T (counter-clockwise seen from the top) and the plasma current $I_p \leq 50$ kA. In this configuration, the edge safety factor is within the range: $q_a = 3 - 4$. In the previous chapter, it was discussed how an external electrode biasing can induce H-mode in RFX-mod. Particularly, it has been shown that the biasing induces a large $E \times B$ shear flow in the plasma edge, suppressing turbulence and enabling the rise of an edge transport barrier. Besides, the biasing H-mode strongly affects the cross-field transport of coherent structures in the SOL, which impacts on the mean profile of some plasma parameters and the level of plasma-wall interaction. However, strong evidence toward a major role of electromagnetic fluctuations during H-mode has been verified with the set of magnetic pick-up coils installed in the U-probe (see chapter 4). But even in this case, potential blobs were not able to propagate outwardly, being 'trapped' in the near SOL. In some discharges, however, bursty fluctuations measured by several diagnostics suggest the appearance of strong filaments. Those events are usually correlated with a relaxation of the density and potential profiles.

Figure 8.4 shows some plasma parameters during the biasing experiments in RFX-mod operating as tokamak in single null configuration (Fig. 8.5) in a shot where these strong fluctuations occurred. The figure displays the: a) biasing voltage, b) plasma current, c) central line averaged density, d) edge safety factor, e) D_α line at the

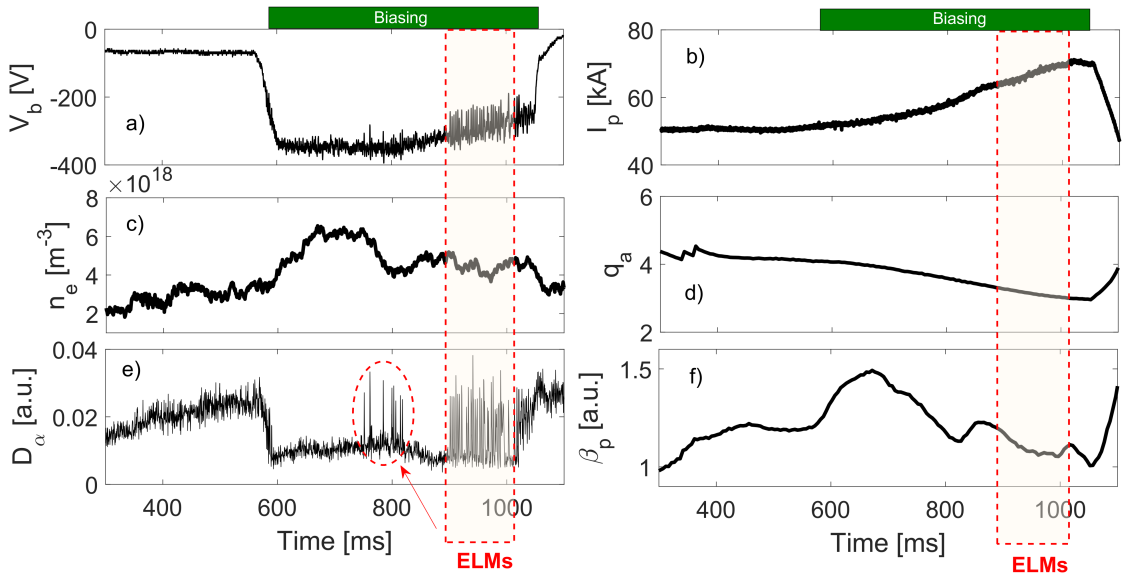

Figure 8.4: Global plasma parameters in a typical ELMy shot in RFX-mod running as tokamak with external biasing. Shot: #39143.

equatorial plane, and f) beta poloidal from plasma equilibrium considerations [147]. The fast L-H transition is observed around 600 ms and, subsequently, a stable ELM-free H-mode is formed, lasting until $\sim$ 700 ms: the plasma density increases, while the D_α line drops, followed by an increase of the beta poloidal ($\beta_p = 2\mu_0 < p > /B_\theta^2$ [287]). The latter is proportional to the plasma stored energy ($\beta_p \propto W$) since the plasma current does not vary much in this phase. Around 800 ms, both n_e and β_p decrease, while D_α detects some large amplitude spikes. Later on, those spikes become more frequents and the β_p drops further, even with the plasma current increasing up to 70 kA. At this point, the improvement on the confinement achieved thanks to the biasing is degraded on average, although it recovers in short time windows as will be discussed later. These intermittent events are very similar to the ELMs cycles observed elsewhere [301, 153]. Additional evidence of that it will be shown next.

8.3.1 Experimental evidences of ELMs in RFX-mod

The fast and large spikes observed in the D_α line suggest strong recycling during the ELMy phase, which is thought as a proxy for particle influx and plasma-wall interaction [38]. This effect is further confirmed with the ISIS poloidal array (Fig. 8.5). As discussed in chapter 4, the ISIS system is composed of a set of electrostatic and magnetic sensors installed on the wall of RFX-mod [228], covering the entire torus. Fig. 8.5 shows the measurements from the poloidal array of probes set to measure floating potential (ϕ_f) and used here to monitor the level of plasma-wall interaction. Fig. 8.5 a) shows a cross-field section of RFX-mod tokamak in single null configuration superposed with the ISIS poloidal array (not to scale) for the shot in Fig. 8.4. In Fig. 8.5 b) is shown the mean and standard deviation of the floating potential measured in all seven sensors (y-axis) in time, where those parameters were calculated in sub-windows of 1 ms. Fig. 8.5 b) confirms that right after biasing is applied ($\sim$600-700 ms), H-mode is achieved, reflecting into a reduction of the mean potential and standard deviation at $\theta \approx -20°$, i.e. outboard midplane. During L-mode, both $< \phi_f >$ and $\delta\phi_f$ are larger as measured through this sensor, which is likely due to the combination of cross-field and parallel transport (see chapter 7). However, large fluctuations are observed later on in the same position, suggesting a strong plasma-wall interaction. Note, however, that this strong interaction is only perceived in the sensor at $\theta \approx -20°$, suggesting that the potential fluctuation has a ballooning behaviour in both L and ELMy H-mode, i.e. they are stronger at the midplane low field side [302].

The effect of the biasing H-mode on the poloidal magnetic fluctuation at the wall is shown in Fig. 8.6 for two magnetic sensors of the ISIS system placed at the low ($\theta \approx 19°$) and high field side ($\theta \approx 161°$). In both cases, when the biasing is applied ($\sim$ 600-1000 ms), the time derivative of the poloidal magnetic field fluctuation ($\partial B_\theta / \partial t$) increases. From 600 to 800 ms, both signals detect an enhance of the fluctuation, with the appearance of high-frequency bands. The spectrogram of the high field side

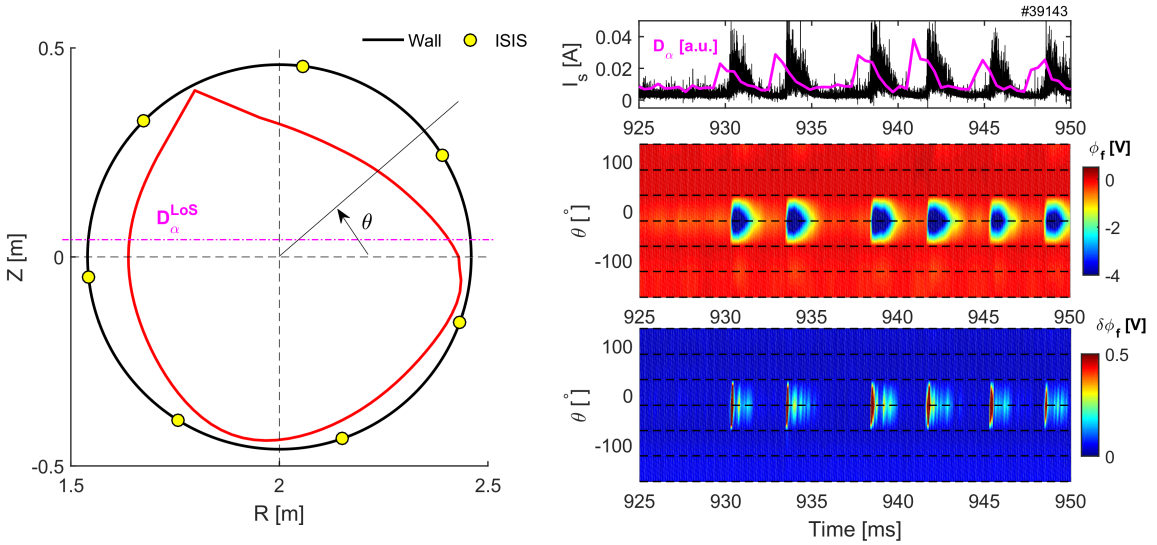

Figure 8.5: On the right, cross-field section of RFX-mod operating as tokamak in single null configuration. The ISIS electrostatic sensors are over-plotted (not to scale). On left, the measurements of the seven sensors represented as mean and standart deviation of floating potential. At he top, it is shown the D_α line (magenta) and an ion saturation current signal (black) placed in the SOL. Shot: #39143.

coil shows a mode around 100 kHz, immersed in a broadband fluctuation, while the one at the low field side exhibits high-frequency bands, from around 50 kHz up to 200 kHz. In the time interval between 800 and 900 ms, the amplitude of both signals reduce, but the high-frequency mode at HFS remains with even higher frequency. From 900 ms up to the end of the biasing phase (around 1000 ms), some enhanced low-frequency activities emerge, particularly, the LFS coil detects some positive and negative spikes in the same period when the ELM-like events are observed in Fig. 8.4 and 8.5.

The U-probe belongs to the category of filamentary probes (chapter 4). They are composed of electrostatic and magnetic sensors, allowing the simultaneous measurement of several parameters such as the electron density and temperature, as well as the three components of the local magnetic field. As shown in the previous chapter, one can estimate the local fluctuation of the parallel current density with the signals of spaced poloidal and radial 3-axial coils. Since ELMs are thought to be the

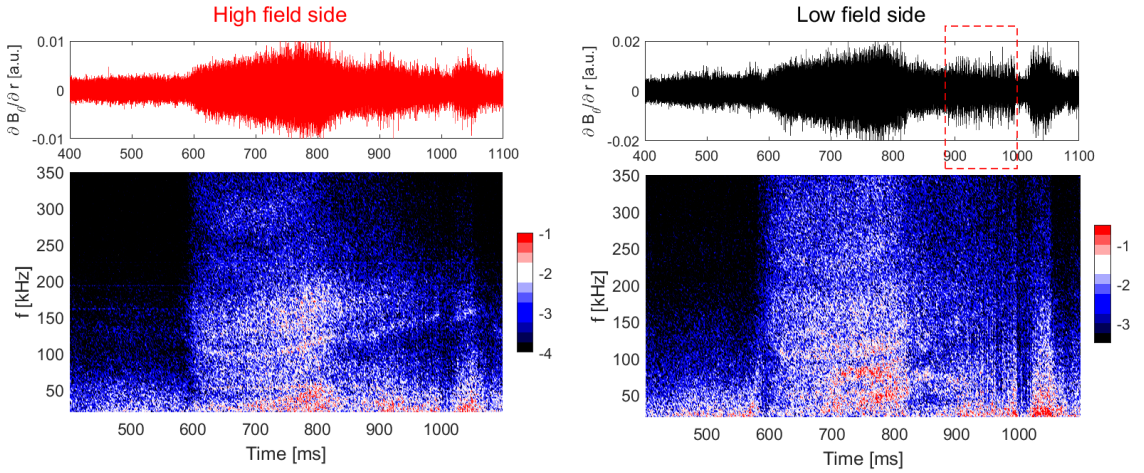

Figure 8.6: Poloidal magnetic field fluctuation at wall low and high field side. Shot: #39143.

result of an electromagnetic instability and the filaments that result from it are typically electromagnetic [63], thus, the U-probe can be a useful tool for detecting and characterizing ELM-like instabilities observed in RFX-mod tokamak during biasing experiments.

The U-probe during the reported experiment was placed in an intermediate position between the plasma edge and SOL. The probe was set to measure simultaneously the floating potential (ϕ_f), ion saturation current (I_s), and the three components of the magnetic field arranged in 2D array. Fig. 8.7 shows the time evolution of two I_s, one located in the edge ($r - r_0 \approx -28$ mm) and the other at the SOL ($r - r_0 \approx 6$ mm). The biasing was applied approximately from 600 to 1000 ms. In chapter 7, it was shown that the temperature profile does not change much during biasing, thus the ion $I_s \propto n_e\sqrt{T_e}$ is a good proxy for the density variation. Fig. 8.7 shows that when the biasing is applied, the ion saturation current in the edge increases at a level about three times its pre-biasing value, while it decreases in the SOL. As discussed in chapter 7, such behaviour is translated into a steeper density profile, as expected during H-mode. Around 800 ms, when the first evidence of ELMs appears (Fig. 8.4), the

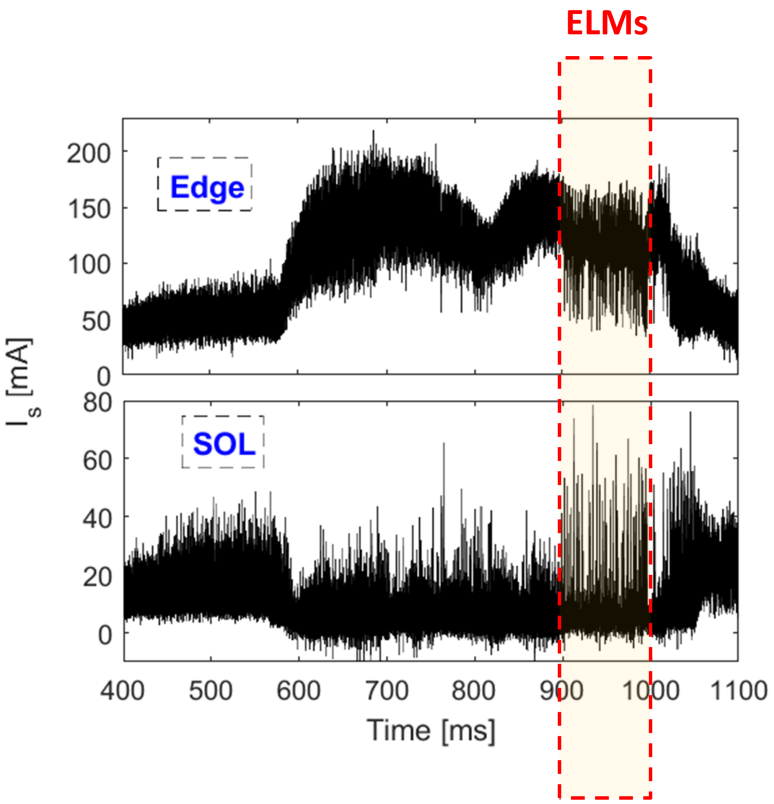

Figure 8.7: Ion saturation current (I_s) in the and edge and SOL during the L-H biasing transition. Shot: #39143.

I_s in the edge decreases on average, while the one in the SOL detects an increase of large fluctuating events. From 900 to 1000 ms, strong fluctuations are observed in both I_s signals, with negative fluctuations in the edge (hole-like) and positive in the SOL (blob-like). This result suggests a fast plasma ejection from the edge to the SOL. As seen in Fig. 8.5, a similar fluctuation is observed near the plasma wall from measurements of outboard the floating potential of ISIS poloidal array, and from the D_α line at the equatorial plane.

Poloidal magnetic field fluctuation measured with the ISIS magnetic sensor at the outboard midplane suggests that those ELMs events exhibit an electromagnetic feature. Fig. 8.8 shows the poloidal and radial magnetic field fluctuation from two pick-up coils from the U-probe located in the edge and SOL. In addition, the spec-

trogram of the four signals, where the power spectrum was evaluated in ever 1 ms, are shown below the corresponding signals. A band-pass filter was applied: 20-500 kHz, to keep only fluctuations that might be related to the ELM fine structure [152]. A broadband fluctuation right after the biasing starts is observed in the two components of the edge coil, however, the poloidal one exhibits a more concentrated (and perhaps lower) band of fluctuation. After a relatively short interval (from 800 to 900 ms), when the fluctuation from the two signals reduce over the entire spectrum, fast and large amplitude oscillation emerges in the interval from 900 to 1000 ms - during the ELMy phase. At this point, strong fluctuations are also observed from the coil in the SOL. The spectrogram of the two components from the SOL coil is slightly different from the one in the edge. In the latter case, both components exhibit a similar trend, with a broadband fluctuation around 100 kHz, but with a second band at larger frequency (slightly different for each component). This result might suggest some radial dependency of the fluctuation prior to the ELMy phase, possibly related to the nature of the driven instability [152]. The maximum magnetic field fluctuation normalized by the equilibrium magnetic field is $\delta B/B \approx 8 \times 10^{-5}$.

The parallel current density can be estimated through measurements of the magnetic field fluctuation from at least three coils of the U-probe arranged in the cross-field plane (see chapter 4). Fig. 8.9 shows the parallel current density fluctuation ($j_{\parallel} \approx j_t$) in the range: 20-500 kHz, where $\Delta r \approx 6$ mm and $\Delta\theta \approx 88$ mm. The corresponding spectrogram was calculated considering time slices of 1 ms (Fig. 8.9, below). Before the biasing starts ($t < 500$ ms), the fluctuation is concentrated in low frequencies, below 100 kHz. Some spikes are evident, possibly related to turbulent filaments. During biasing, from 600 to 800 ms, the spectrum of j_t becomes broader, although the total amplitude does not vary much. An observed reduction of the fluctuation in the interval 800-900 ms suggests damping of the current density fluctuation. At this phase, the I_s in the edge increases again. During the ELMy phase (900-1000 ms), j_t

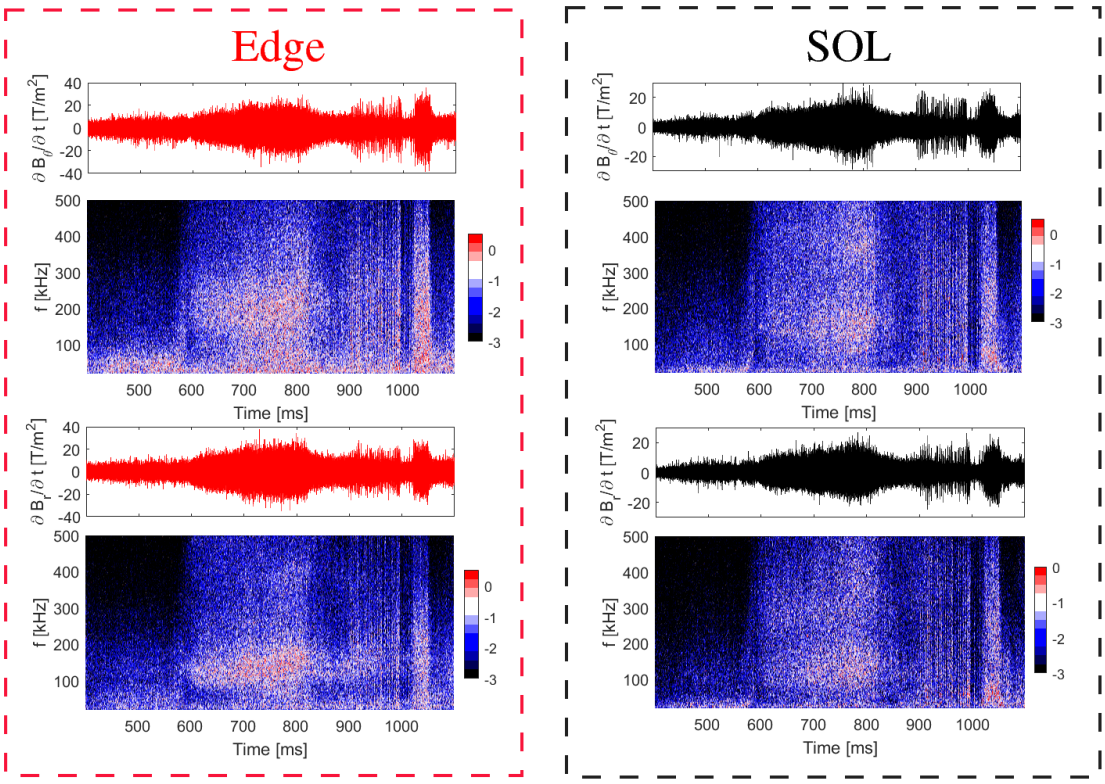

Figure 8.8: Poloidal ($\partial B_\theta/\partial t$) and radial ($\partial B_r/\partial t$) magnetic field fluctuation in the and SOL together with their corresponding spectrogram. Shot: #39143.

exhibits fast spikes (both positive and negative) with amplitude up to $|j_t| = 1$ kA/m^2. This is compelling evidence of current-carrying filaments.

Figure 8.7 suggests that during the ELMy phase, a strong plasma ejection from the edge towards the SOL occurs. This tends to make the I_s profile flatter. By focusing on the ELMy phase, the parallel current density (Fig. 8.10) is shown together with the spatial-time evolution of I_s and ϕ_f, evaluated as the average over 0.1 ms time slices. The last closed flux surface position (LCFS) is represented as a dashed line in green at $r - r_0 = 0$. The plasma edge corresponds to the region where $r - r_0 < 0$, while the SOL to $r - r_0 > 0$. The three graphs on the left of figure 8.10 (label 1) show that the ELM events affect in a synchronized way all the three parameters. During an ELM cycle, the parallel current density fluctuation increases, while the I_s drops in the edge and increases in the SOL: creating density holes in the edge and peaks in

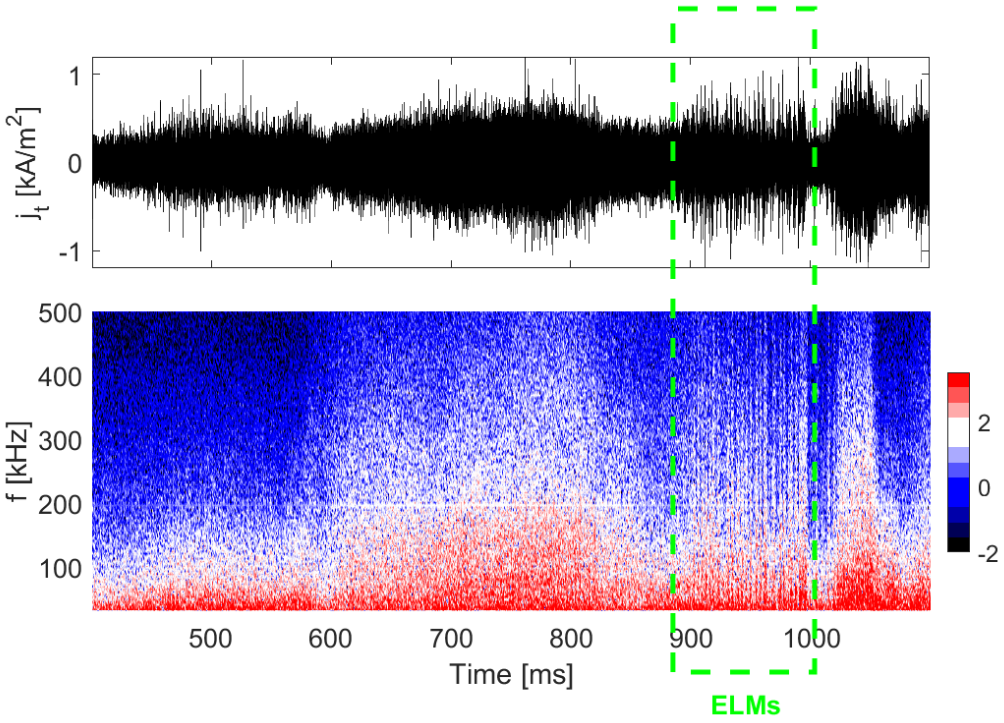

Figure 8.9: Parallel current density estimation from the magnetic sensors of the U-probe. The corresponding spectrogram on logarithm scale is shown bellow.

the SOL. Concomitantly, the floating potential in the edge, that reaches values lower than -300 V in ELM-free H-mode phase, goes to almost -200 V during the ELM cycle, propagating towards the SOL as a fast transient event. On the right of figure 8.10, it is shown two ELM cycles (zoom-in of the graphs shown on the left, grey dashed rectangle). The I_s is shown now on a logarithmic scale to highlight the impact of the fluctuation in the SOL. Note that the plasma ejection happens in a very fast time scale; the onset of the collapse of the I_s in the edge occurs almost synchronized with an increase of the I_s SOL baseline. This might suggest a streamer forming initially and then decoupling, rather than a single filament moving outwards. The same happens in the floating potential profile that becomes flatter in a very short time scale. This effect has an impact on the radial electric field profile, since $E_r \propto -\nabla_r \phi_f$ and so in the poloidal rotation. The propagation, in this case, seems to be restricted to a narrower range in the SOL, up to $r - r_0 \approx 10$ mm, in the limit transition from the

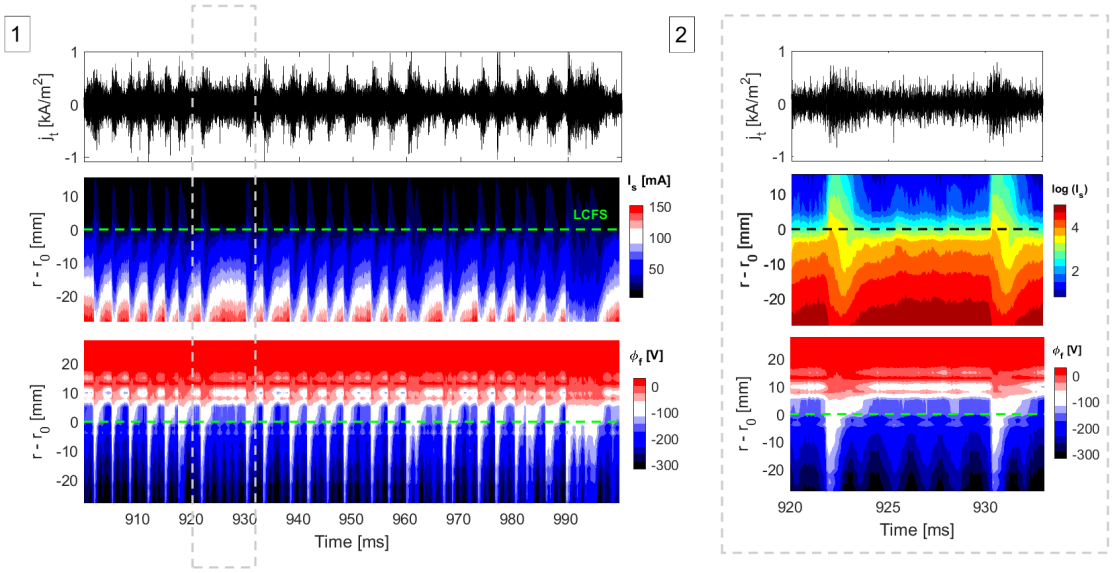

Figure 8.10: Some plasma parameters during the ELMy phase in RFX-mod tokamak: 1 - parallel current density fluctuation (j_t) and radial profiles of the ion saturation current (I_s) and floating potential (ϕ_f) in time, both calculated in time slices of 0.1 ms. 2 - it is shown a zoom in during two ELM cycles (grey dashed rectangle).

divertor like to the limiter shadow region (see chapter 7). The recover of both profiles to H-mode, i.e. with steeper profiles, occurs in a longer time window compared to the crash scale, remaining approximately steady until the next ELM event.

Figure 8.11 a) shows nine ELM events as seen from an ion saturation current signal in the edge. In addition, it is shown the b) poloidal ($\partial_t B_\theta$) and d) radial magnetic field ($\partial_t B_r$) fluctuation measured in the plasma edge. One can observe a correlation between the I_s fluctuation with magnetic perturbations, that is stronger for the radial component. Fig. 8.11 shows, respectively, the spectrogram of the c) poloidal and e) radial magnetic fluctuation on logarithm scale. High-frequency bands from 100-200 kHz and around 400 kHz is clear from the spectral decomposition of the poloidal component between ELMs, but not in the radial one. Both components present a broadband fluctuation during ELMs. Fig. 8.11 f) shows the spectrum of the radial (blue) and poloidal (red) components calculated over the time window 890-900 ms before the ELM onset. The figure further confirms that the poloidal component

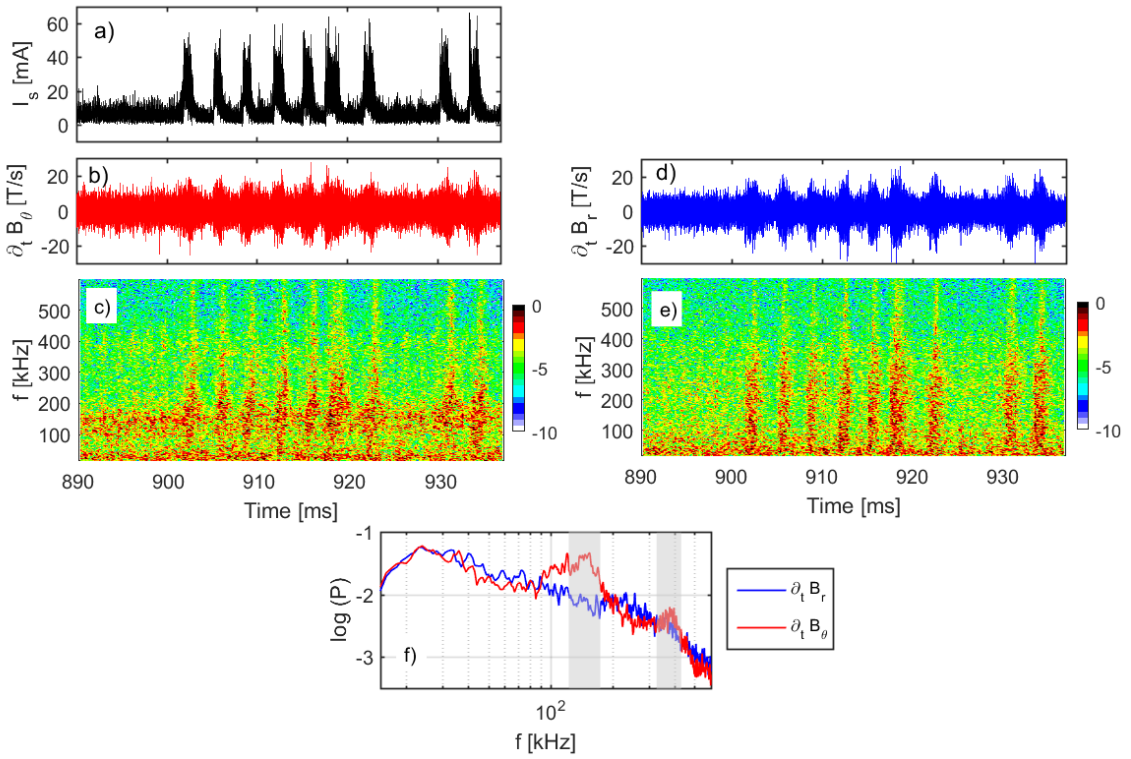

Figure 8.11: ELMy phase fluctuation: a) ions saturation current, b) poloidal ($\partial_t B_\theta$) and d) radial magnetic field ($\partial_t B_r$) fluctuation measured in the plasma edge; spectrogram of c) poloidal and e) radial magnetic fluctuation on logarithm scale; f) spectrum of the radial (blue) and poloidal (red) components calculated over the time window 890-900 ms.

is the one activated in the inter-ELM phase. Worthing noting that similar behaviour has been observed elsewhere [152], suggesting that this might be related to a more fundamental feature of this phase.

In Fig. 8.8, it was shown that when biasing is on, the magnetic field oscillation becomes larger, with fluctuations in a wider frequency range. Particularly, a high-frequency band appears around 100 kHz, which is likely a trace of the type of instability in this phase. Although in ELM-free H-mode strong turbulence suppression is observed, which reflects in a less turbulent SOL environment, electromagnetic effects become more important, especially in the plasma edge. To further investigate this effect, two coils (poloidal spaced) from the U-probe measuring the poloidal component of the magnetic field fluctuation were used to compute the wavenumber-frequency

spectrum (see chapter 4) trough the 2-point correlation technique [217]. This coil pair does not lay exactly along the same poloidal surface nevertheless useful information can be inferred accounting for their relative location. Considering that their mutual distance is $d \sim 8.8$ mm, the poloidal wavenumber is constrained within the interval $|k_\theta| < \pi/d \approx 0.36$ cm^{-1}. The data of the two coils over a large time window, 400-1100 ms, were sub-dived in time slices of 5 ms where the cross-power spectrum is evaluated over 0.1 ms with 75% of overlap. Finally, the wavenumber-frequency spectrum is obtained by considering the statistical contribution from all sub-windows with 5 ms time resolution. The spectrum in frequency, which is basically the cross-power spectrum with a proper normalization, is obtained from $S(k, f)$ by averaging it over all the wavenumbers: $S_f \propto \int_{k_{min}}^{k_{max}} S(k, f)dk$. Similarly, the wavenumber spectrum can be evaluated by averaging $S(k, f)$ over all the frequencies: $S_k \propto \int_0^{f_{max}} S(k, f)df$. Fig. 8.12 shows both spectrum in time on logarithm scale before and during biasing. While before biasing, S_f is mainly concentrated in low frequency, during the ELM-free H-mode, a broadband fluctuation appears clearly around 100 kHz, disappearing right before the onset of the ELMy phase. By looking at the wavenumber spectrum in time (S_k), a strong fluctuation is evident in the same time interval, i.e. when the broadband fluctuation appears, with a dominant wavenumber of about $k_\theta \approx 0.1$ cm^{-1}. One can calculate the fluctuation phase velocity (approximately poloidally) from the wavenumber-frequency spectrum. The phase velocity increases when the biasing is applied, reaching its maximum absolute value when the broadband fluctuation becomes more intense. The phase velocity is in the electron diamagnetic direction, the same direction of the $E_r \times B$ flow in the lab frame. During the ELMy phase, v_θ^{ph} reduces to values comparable to the L-mode phase, within the error bars. It is worth to note the similarity between this broadband oscillation observed here with the quasicoherent modes observed elsewhere [151]. Although the plasma environment is dramatically different: the magnetic field and plasma current are substantially lower

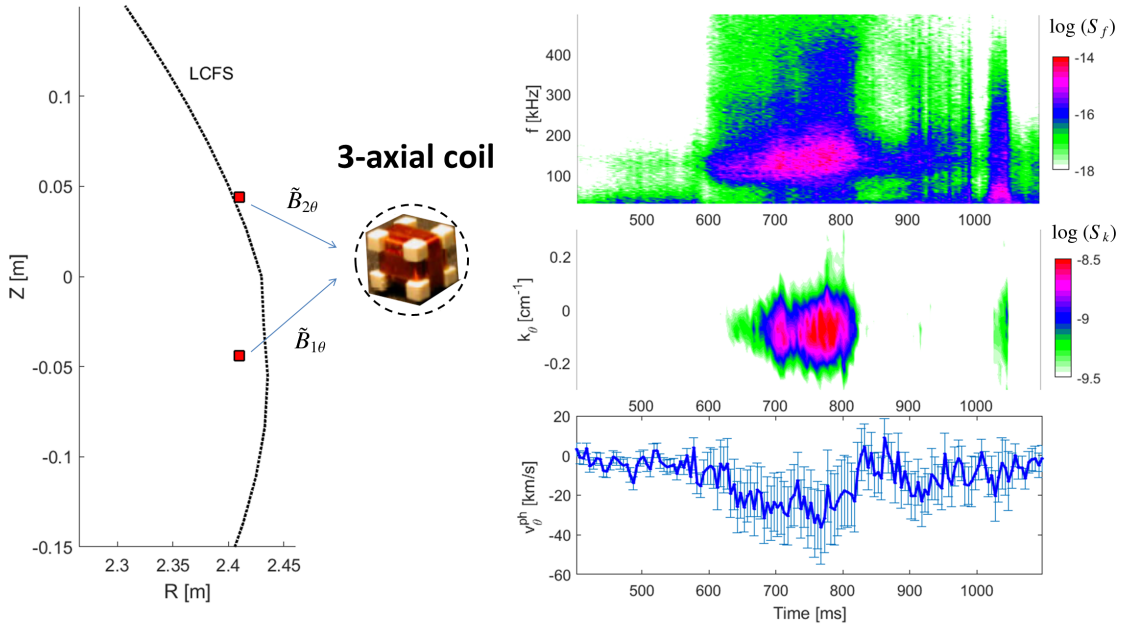

Figure 8.12: Poloidal magnetic fluctuation measured with two poloidal spaced coils installed in the U-probe body. On the left is shown the relative position of the two coils with respect to the LCFS. On the right, from the top to the bottom, are shown the frequency and wavenumber spectrum, and the poloidal phase velocity all obtained from the wavenumber-frequency spectrum ($S(k, f)$) with the 2-point correlation technique [217].

here than those experiments, the leader role of electromagnetic oscillation seems to connect all of them.

8.3.2 The ELM cycle

To study the properties of the ELM in more detail, it was defined four different phases within one cycle. The aim is to investigate the interplay between the plasma background evolution and electromagnetic fluctuation. A similar approach has been proposed elsewhere [152]. The composite structure characterizing the ELM bursts, ELM fine structure in the following, was reported in [232, 244]. In the RFX-mod case the available diagnostic set could allow a deeper investigation of the features and dynamics of the sub-structures populating the different phases of the ELM cycle, with the possibility to evaluate the effect of the plasma background all along the cycle

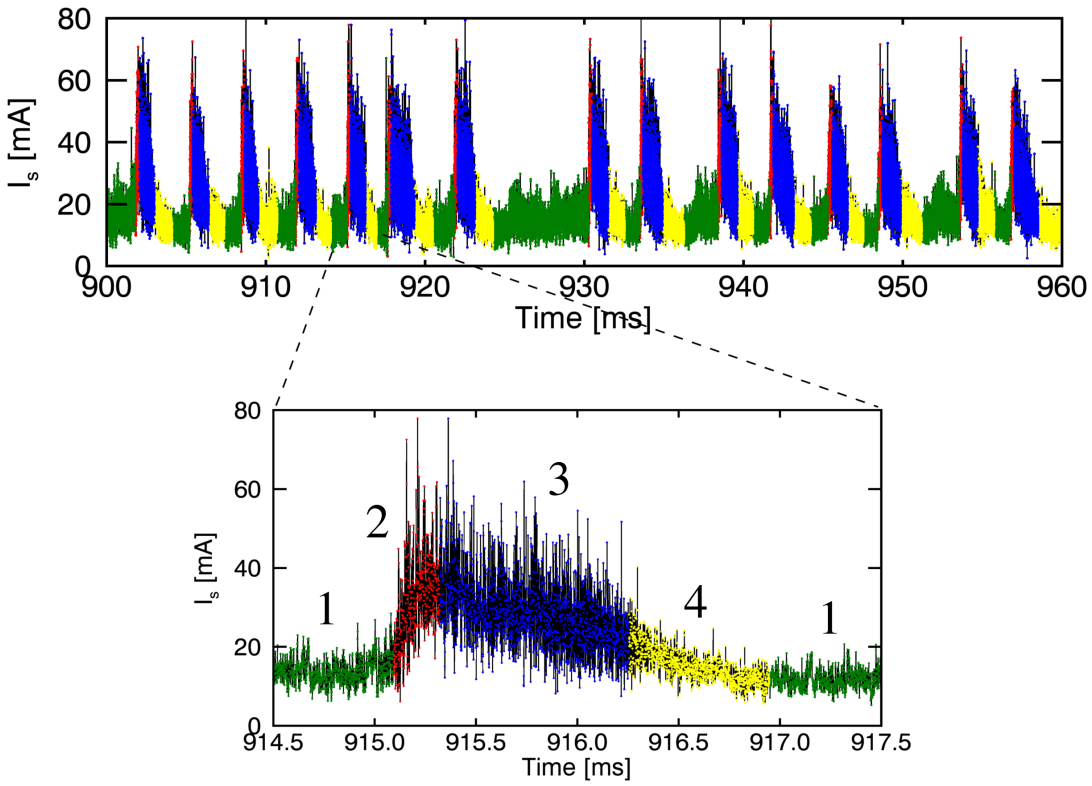

Figure 8.13: Four phases during the ELM-cycle: 1) inter-ELM phase, similar to the ELM-free H-mode discussed in the previous chapter; 2) ELM crash phase (from the fast mean growth to its saturation); 3) ELM middle phase (from the saturation up to the beginning of the profile recover); 4) ELM tail (the final ELMy phase up to the full profile recover).

itself. On this purpose four phases are defined within the ELM cycle based on the time evolution of an ion saturation current signal placed at $r - r_0 \approx 6$ mm) (Fig. 8.13). They are label as: 1) inter-ELM phase, similar to the ELM-free H-mode discussed in the previous chapter; 2) ELM crash phase (from the fast mean growth up to its saturation); 3) ELM middle phase (from the saturation up to the beginning of the profile recover); 4) ELM tail (the final ELM phase up to the full profile recover).

The mean floating potential maps corresponding to the four phases are shown in Fig. 8.14 a). The dashed line represents the last closed flux surface (LCFS) position, with the upper part corresponding to the SOL and the lower one the plasma edge. In phase-1 (inter-ELM phase), the floating potential map exhibits a negative well in

the edge, with values around -300 V, and positive in the SOL ($\approx$ 20 V). Such a feature is analogous to what has been observed during the ELM-free H-mode regime discussed in chapter 7, also characterized by a steeper floating potential profile around the LCFS (see Fig. 7.6). During phase-2 (ELM crash phase), the ϕ_f values become less negative in the edge, which makes the map and the radial profile flatter. In this phase, the potential map is in an intermediate state between L and ELM-free H-mode. In phase-3 (ELM middle phase), the profile has not fully recovered yet, but it becomes further negative in the deeper edge as compared to phase-2. Finally, in phase number 4 (the ELM tail), the profile is almost fully recovered, resembling the one corresponding the phase 1. In this phase, the transport barrier is re-established. Such a result can be seen in Fig. 8.14 b) where it is shown the poloidal projection of the $E \times B$ drift deduced from the radial derivative of the floating potential profile ($v_\theta^{E\times B} \approx -\nabla_r \phi_f$), smoothed with a third-order Savitsky-Golay filter [137]. Fig. 8.14 b) shows besides the profile of the four phases, the $v_\theta^{E\times B}$ L-mode profile. One can see that the phases 2 and 3 are indeed in an intermediate state between L-mode and the ELM-free H-mode, described by the phase 1 and roughly by the phase 4. As discussed in chapter 7, the relaxation of the potential radial profile and, thus, the radial electric field favors the emergence and propagation of slower and larger filaments (in agreement with the blob suppression criterion [24]).

The ion saturation current fluctuation in the four phases is shown in Fig. 8.15. The four maps on the left side of Fig. 8.15 show the radial profile of the Is power spectrum (on logarithm scale) in the frequency range: 20-500 kHz, to rule out the effect of low-frequency modes and high-frequency noises. While in phase-1, the fluctuations are concentrated in low frequencies (below 100 kHz) and the plasma edge ($r - r_0 < 0$), during the ELM crash phase (number 2), the level of fluctuation becomes further enhanced and spread over a wider range of frequency that penetrates (although with lower amplitude) into the SOL. In this phase, it is observed a large plasma ejection

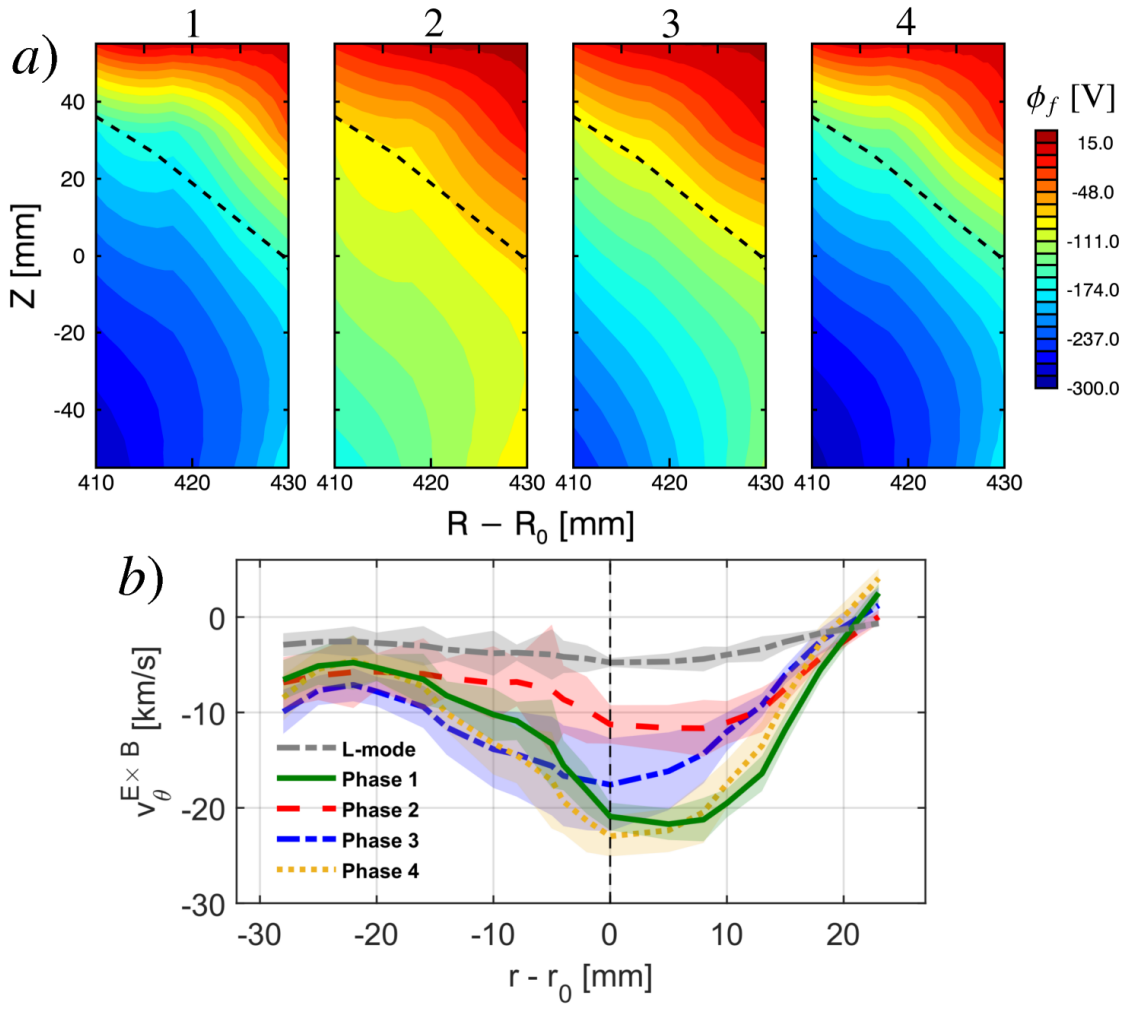

Figure 8.14: a) mean floating potential map during the four phases defined in Fig. 8.13; b) poloidal projection of the $E \times B$ background drift deduced from the floating potential of the interpolated ϕ_f profiles.

from the edge towards the SOL. In phase-3, the level of fluctuation reduces compared to phase-2, but it is still wider and stronger than phase-1. Fluctuations in this phase are more concentrated in the edge and in the range: $f < 200$ kHz. One can note, however, a frequency band around the LCFS. The phase number 4 approaches to phase-1, but fluctuations are more intense in the edge and spreader to high frequencies. Fig. 8.15, right side panel, shows the radial profiles of the I_s mean and standard deviation for the four phases. The phase-1 exhibits a radial profile of both I_s and σI_s similar the one reported in chapter 7. In this phase, the average ion saturation

current profile is the steepest (among the four phases) in the edge, with the lowest baseline values in the SOL. The fluctuation, represented by the standard deviation, is also the lowest over the whole profile compared to the other phases (as, indeed, suggested in map 1 of Fig. 8.15). The standard deviation of a given quantity is related to its RMS: $x_{RMS}^2 = \sigma_x^2$, if the mean is zero. The RMS in frequency domain can be written according to the Parseval's theorem as [200]: $x_{RMS}^2 = 1/N \sum_{l=0}^{N-1} |X[l]|^2$, where $X[l]$ is the Fourier transform of x. Hence, the integral over all the frequencies at a given position of the maps displayed on the left side of Fig. 8.15 is proportional to the standard deviation shown on the right side. In phase-2, the radial profile of I_s becomes flatter, with larger SOL baselines values. This phase presents the largest level of fluctuation over the whole profile, in agreement with Fig. 8.15, bottom right side. During phase-3, the radial profile of I_s becomes even flatter, although the fluctuation in the edge and SOL is reduced. This behaviour seems to be tied with the relaxation of the potential profile shown in Fig. 8.14, rather than the density profile (roughly proportional to the I_s), suggesting a leading role of the potential or radial electric field in regulating the I_s fluctuation. In the phase-4, the I_s profile becomes steeper again and the fluctuation reduces in the edge and SOL. This phase is similar to the inter-ELM phase.

Both Fig. 8.6 and Fig. 8.8 show that during the biasing H-mode, the magnetic fluctuation increases, with spectral contributions from the low and, mainly, high-frequency branch. Particularly, Fig. 8.8 shows that magnetic field fluctuation has a radial dependency, with higher fluctuation in the edge than in the SOL, and exhibits a high-frequency broadband fluctuation that is more pronounced in the poloidal component. From the data of 10 coils (5 in each tower), measuring the local poloidal and radial components of the magnetic field, the spectral radial profile of these quantities was evaluated. Fig. 8.16 shows the radial profile of the power spectrum of the poloidal ($\partial \tilde{B}_\theta / \partial t$) and radial ($\partial \tilde{B}_r / \partial t$) magnetic field fluctuation for the four phases. During

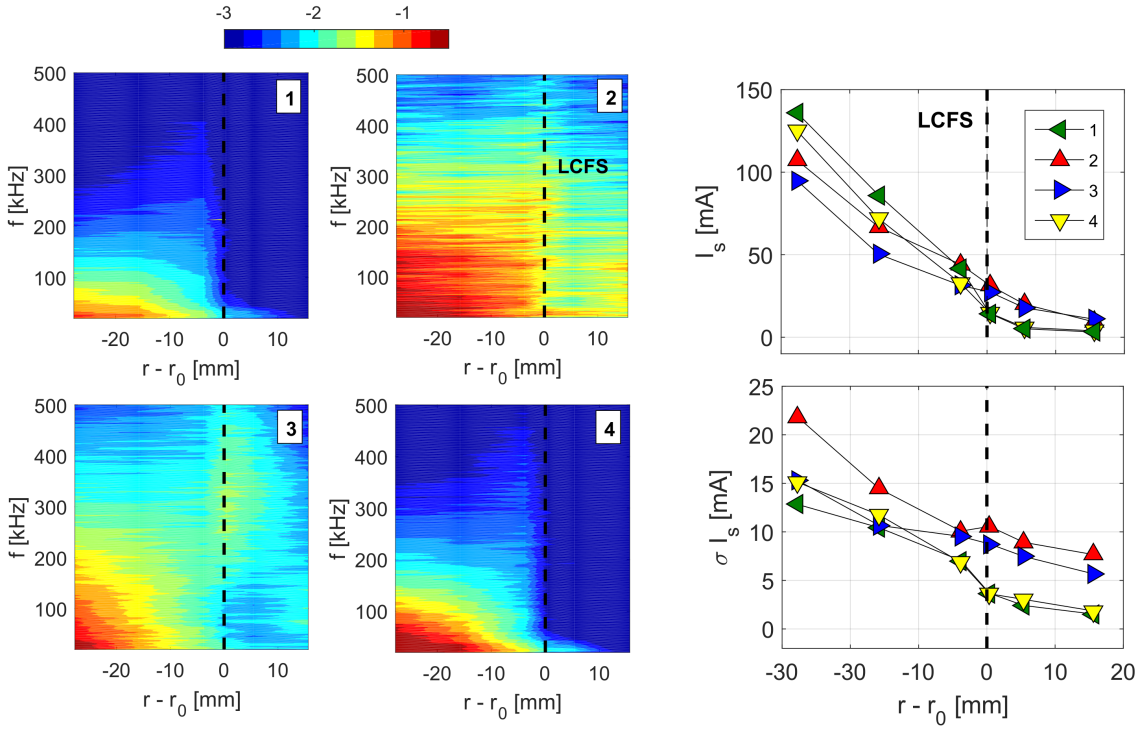

Figure 8.15: Ion saturation current in the four phases. On the left side, radial profile of the power spectrum of I_s fluctuation (20-500 kHz) for the four phases. On the right, from the top to the bottom, radial profile of the mean and standard deviation of I_s.

inter-ELM, both components present a lower fluctuation level, with the poloidal component showing a clear broadband fluctuation (100-200 kHz) in the edge that extends until roughly the LCFS. In the crash phase (number 2), the fluctuation in both components increases sharply, with a high-frequency contribution (up to ∼300 kHz). The dominant broadband fluctuation in the poloidal component is still presented, but it extends further into the SOL, merging with a strong fluctuation that emerges near the LCFS. In phase-3, the ELM middle phase, a similar trend of fluctuation as phase-2 is observed but with lower amplitude. Finally, in phase-4, the spectrum of both components become similar to phase-1, but with a slightly larger amplitude. It is interesting to note that while the spectrum of the radial component exhibits an increase of fluctuation in a wide range of frequency during the ELM phase, the poloidal one exhibits a more localized fluctuation spectrum. In the four phases, it was possible to

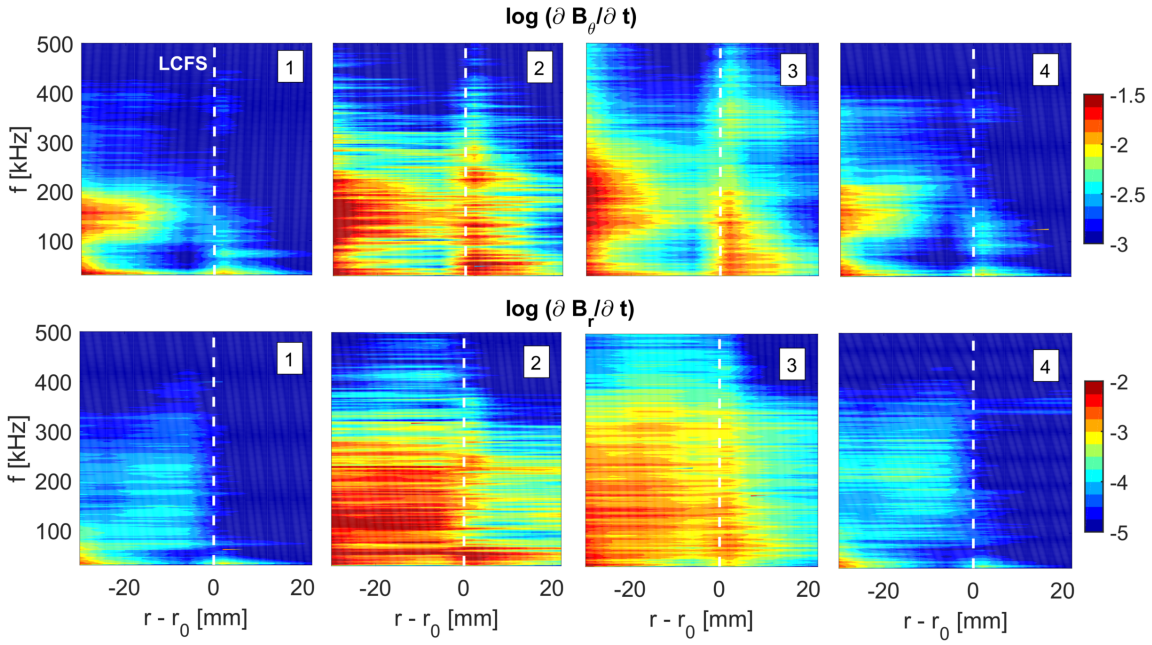

Figure 8.16: Radial profile of the power spectrum of magnetic field fluctuation: poloidal (top) and radial (bottom), in the four phases.

distinguish a broadband fluctuation in the range: 100-200 kHz, which is more evident in the plasma edge. This kind of fluctuation has been observed elsewhere [152], and is likely related to the ELM driven instability. The novelty of the results presented in Fig. 8.16 is that high-frequency mode is maintained even during the ELM ejection phase. In addition, the strong fluctuation of the magnetic field in the phases 2 and 3 might suggest an increase of the Maxwell stress ($\sim< \tilde{B}_r \tilde{B}_\theta >$) and possibly field line stochastization [182].

8.3.3 Filamentary transport during ELM cycle

Considering the four phases defined in the previous section, one can study the filamentary transport in each of them. This is the aim of this section. Fig. 8.14 and 8.15 show that the background potential and ion saturation current profiles are distinct in the four phases. Particularly, it has been demonstrated that while the phases 1 and 4 approach to the ELM-free H-mode observed in the previous chapter, with steeper

profiles (Fig. 7.6 and 7.8) and reduced magnetic fluctuation (Fig. 7.5), the phases 1 and 2 exhibit a larger fluctuation (over a wider frequency range), and flatter profiles. In this and the next section, the aim is to investigate the detected differences in terms of filamentary transport.

The bursty behaviour of the ion saturation current signals in the SOL motivated the use of the same threshold criterion considered in the previous chapter. By choosing an I_s in the SOL as reference, placed at $r - r_0 \approx 6$ mm, the threshold is: $I_s^{peak} \geq \langle I_s \rangle + 2.5\sigma$, where $\langle I_s \rangle$ and σ are, respectively, the sampling mean and standard deviation. After selecting the events that satisfy this criterion, the I_s used as reference together with two neighbourhood signals are conditional averaged: $\delta I_s = \left\langle I_s(r,t) | I_s^{reff}(r',t') > I_s^{peak} \right\rangle$. The four phases result is shown in Fig. 8.17. Note that the phases 1 and 4 present a similar behaviour as the ELM-free H-mode discussed in chapter 7. The time delay between the two innermost pins (blue and orange, respectively) suggests radial propagation; although, as discussed in the chapter 6, poloidal rotating tilted structure can yield a similar result. The almost zero amplitude in the third pin (the outermost one in yellow) is a strong indication that the blobs do not propagate easily during these two phases. The phases 2 and 3, on the other hand, exhibit clear δI_s peaks (with slightly different amplitude) and compatible mutual time delay. This might suggest that structure propagate in these phases since the radial separation between the innermost and outermost pins is larger than the typical blob radial size ($\sim$ 1 cm). Comparing the amplitude and shape of the reference conditional I_s in the four phases, one can see that the amplitude in the phases 2 and 3 is about twice higher than in the phases 1 and 4. However, the peak in phase-2 is shown to be broader in time than phase-3. By assuming that the full width at half maximum (FWHM) of each peak is related to the time that structure pass completely through the pin (τ_b), and considering the Taylor frozen turbulence hypothesis [155], the structure cross-field size can be estimated as $l_b = \tau_b v_b$, where

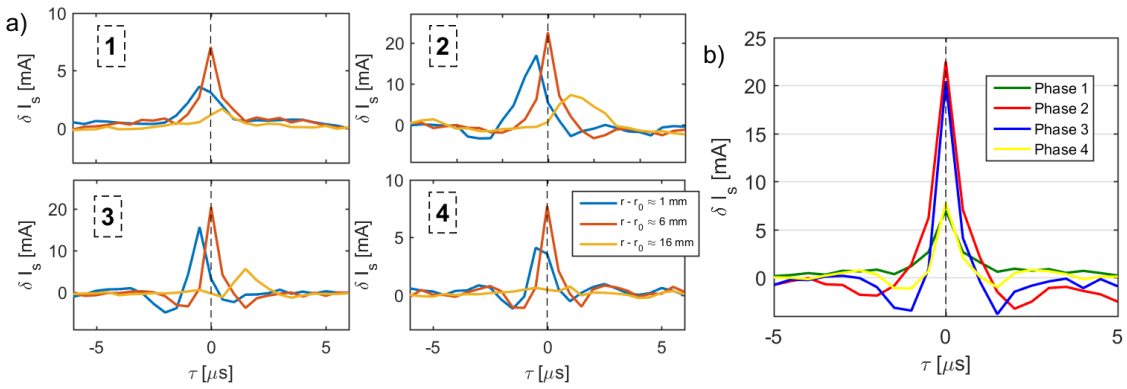

Figure 8.17: Threshold criterion: a) conditional ion saturation current (δI_s), and b) comparison of the reference peak in the four phases (Fig. 8.13).

v_b is the blob cross-field velocity. Since the time delay between the two innermost pins in the phases 2 and 3 are compatible, the cross-field velocity in both cases is similar (assuming that the poloidal projection effect is negligible). Hence, blobs in phase-2 are larger than those in phase-3. Since in the latter, the potential profile is stepper, the $E \times B$ flow can play a role in selecting blobs based on their size and velocity [24]. A similar difference is observed between phases 1 and 4, with the latter being narrower in time, which suggests the presence of smaller structures.

Current-carrying filaments induce local perturbation of the magnetic field, which is precisely how the current density is measured with the U-probe 4. Therefore, the increase of the magnetic field fluctuation can be due to the presence of current-carry filaments crossing the probe. However, the fluctuation in this case has a well defined relation between the poloidal and radial magnetic field components (for toroidal current fluctuation). Using a set of three coils from the U-probe, all placed in the SOL, the parallel current density was estimated, and then conditional averaged where the trigger was the extreme events of an I_s signal also in the edge for the four phases 8.18. While the phases 1 and 4 present a similar behaviour, with relatively low current density fluctuation, in the phases 2 and 3, i.e., when the background profiles are flatter, a larger current density is observed. This result is in agreement with the ejection of

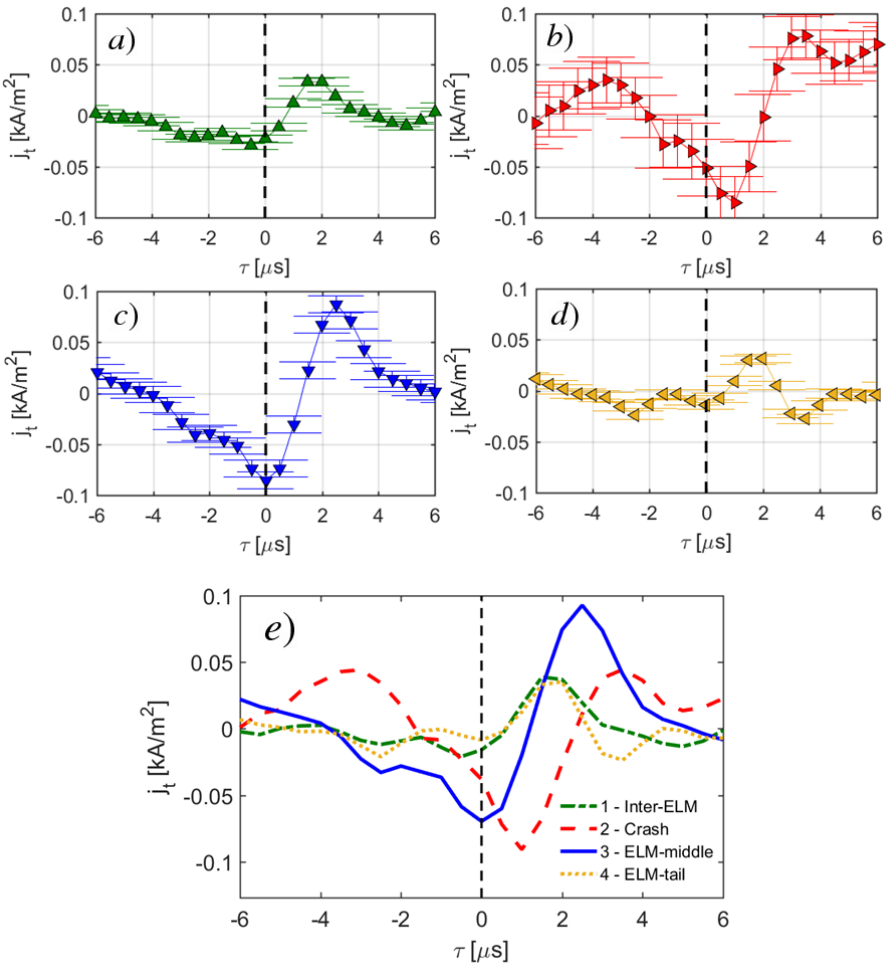

Figure 8.18: Parallel current density during the ELM-cycle: a) inter-ELM phase, b) ELM crash phase, c) ELM middle phase, and d) ELM tail obtained from the conditional average by considering the extreme events an I_s in the edge as reference. The comparison between the four phases is shown in e) where the error bar was omitted.

current-carrying filaments from the plasma in the ELM-cycle [277]. Therefore, the larger magnetic field fluctuation observed in these two phases is partially due the presence of filaments.

A noticeable piece of information is provided by the 2D array of ϕ_f collected along the cross-field plane to study the filamentary transport in the four ELM-cycle phases is by using the floating potential array. This system is composed of 20 tips arranged in a cross-field plane, covering a range of 8.8 x 2.2 cm. The dynamics of

the potential structure related to the ion saturation current peaks is obtained by conditional averaging the ϕ_f array: $\delta\phi_f = \left\langle \phi_f(r,t) | I_s^{reff}(r',t') > I_s^{peak} \right\rangle$. The result of this procedure is plotted as a 2D map, where each frame corresponds to a time instant or time delay with respect to the reference at $\tau = 0$. Fig. 8.19 shows 34 frames of conditionally averaged floating potential map from $\tau \approx -4\ \mu s$ to $\tau \approx 11\ \mu s$ during the phase-1, inter-ELM phase. Note that from $\tau \approx -4$ to $-2\ \mu s$, a dipole is visible and its negative pole (located in the plasma edge) seems to propagate upward, in the ion diamagnetic direction ($v_D^i = \hat{\mathbf{b}} \times \nabla p_i/(en_iB)$) in the lab frame, opposite to $E_r \times B$ flow. At $\tau = -1.5\ \mu s$, the negative pole starts to detach from the plasma edge and, concomitantly, its amplitude increases. At $\tau = 0$, a dipole is observed in the potential around the reference I_s (its position in the map is displayed as a red circle). In the following frames, a rapid ejection of the potential structure is observed, that subsequently spread over the near SOL. However, as noted in the previous chapter for ELM-free H-mode, the structure (negative pole) does not propagate but instead becomes nearly "trapped" until it finally fades away about $\tau \approx 11 \mu s$.

During the ELM crash phase, a strong relaxation of the I_s and ϕ_f radial profiles happens, which ultimately impacts on the level of $E \times B$ shearing rate, favouring the growth and propagation of turbulence. Indeed, Fig. 8.15 indicates that the I_s fluctuations become enhanced in the edge and SOL over a large frequency range in this phase. In addition, a strong magnetic fluctuation in both radial and poloidal components is observed (Fig. 8.16), suggesting a possible role of electromagnetic effects. Fig. 8.17 shows that the conditional I_s in the ELM crash is almost five times larger than in phase-1, broader in time, and carry larger current parallel current (Fig. 8.18). Differently from phase-1 where the δI_s amplitude measured at the third pin (the outermost) is almost zero, in phase-2 its amplitude is larger, suggesting the radial propagation of the blob. This effect is further confirmed in Fig. 8.20. One can see initially a dipole at $\tau = 0$ that rapidly propagates as a monopole. Worth noting

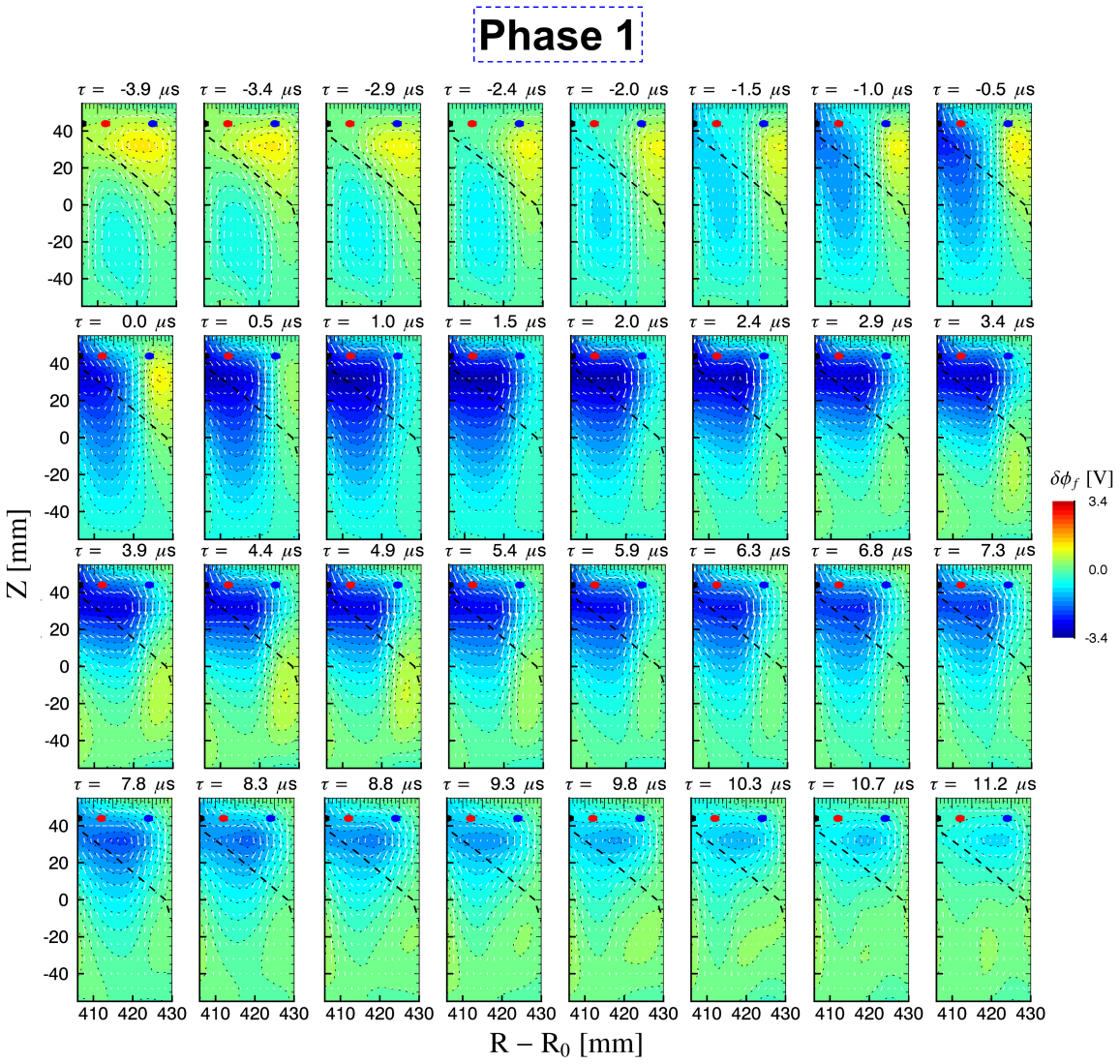

Figure 8.19: Conditional floating potential map as shown in 32 time frames during the phase-1 (inter-ELM phase). The dashed black lines represent the last closed flux surface (LCFS), separating the plasma edge (lower part) from the SOL (upper part).

that the potential increases when the structure is already in the SOL, which might suggest some interaction with the background or the merging with small blobs. The potential amplitude in this phase is almost twice with respect to phase-1, although the background potential in the latter is more negative in the edge.

In phase-3, ELM-middle phase, the background profile starts to recover, but the level of fluctuation is still high (Fig. 8.14 and 8.15), although less intense than phase-2. The conditional I_s presents a similar behavior as the phase-2, with maximum

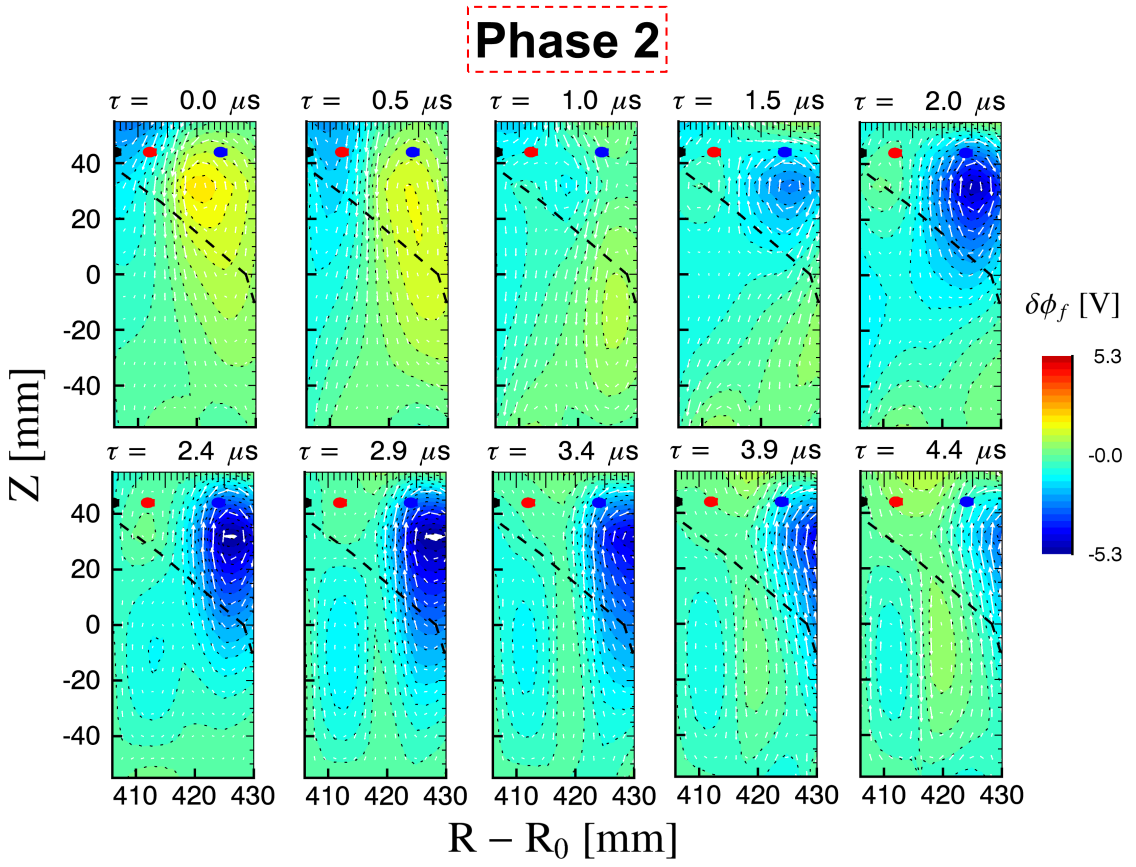

Figure 8.20: Conditional floating potential map as shown in 10 time frames during the phase-2 (ELM crash). The dashed black lines represent the last closed flux surface (LCFS), separating the plasma edge (lower part) from the SOL (upper part).

amplitude reaching $\delta I_s \approx 20$ mA and the combination time delay and amplitude in the three pins compatible with radial propagation. The radial separation between the innermost and outermost pins measuring I_s is about 15 mm, which is typically shorter than the blob radial size. Fig. 8.21 shows the conditional floating potential represented in a 2D map in 10 frames. A clear dipole is observed at $\tau = -0.5$ μs and $\tau = 0$. The subsequent frames suggest an outward radial propagation with some poloidal component (in the electron diamagnetic direction). The positive pole is either pushed outward or faded away. At $\tau \approx 4$ μs, the structure almost disappears from the frame covered by the probe, suggesting that the outward propagation is quite high. In phase-3 (similarly to phase-2), filaments propagate freely into the SOL which is

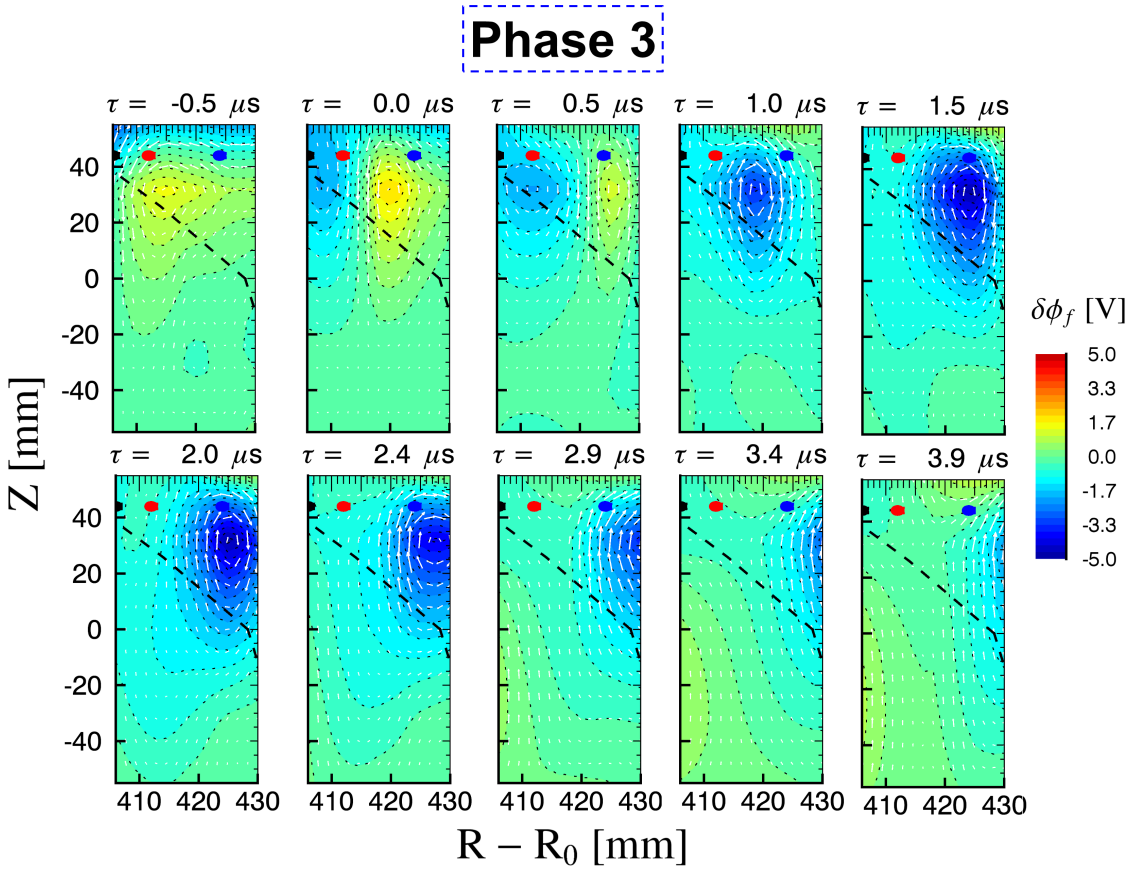

Figure 8.21: Conditional floating potential map as shown in 32 time frames during the phase-3 (ELM middle). The dashed black lines represent the last closed flux surface (LCFS), separating the plasma edge (lower part) from the SOL (upper part).

compatible with the large plasma-wall interaction observed from the ISIS poloidal array (Fig. 8.5). Note that the threshold criterion combined with the conditional average yield the most likely filament amplitude and scale. It is expected, however, a more complex and rich variety of filaments with different sizes and velocity. In the next section, the local intermittency measurement (LIM) technique will be used to address this point.

The background profiles are fully recovered in phase-4 (ELM tail) and the level of electrostatic and magnetic fluctuation reduce strongly in the near edge and SOL. The conditional I_s has lower amplitude, compatible with phase-1, and almost zero δI_s at the pin 3 (the outermost). By looking at the potential maps (Fig. 8.22) in

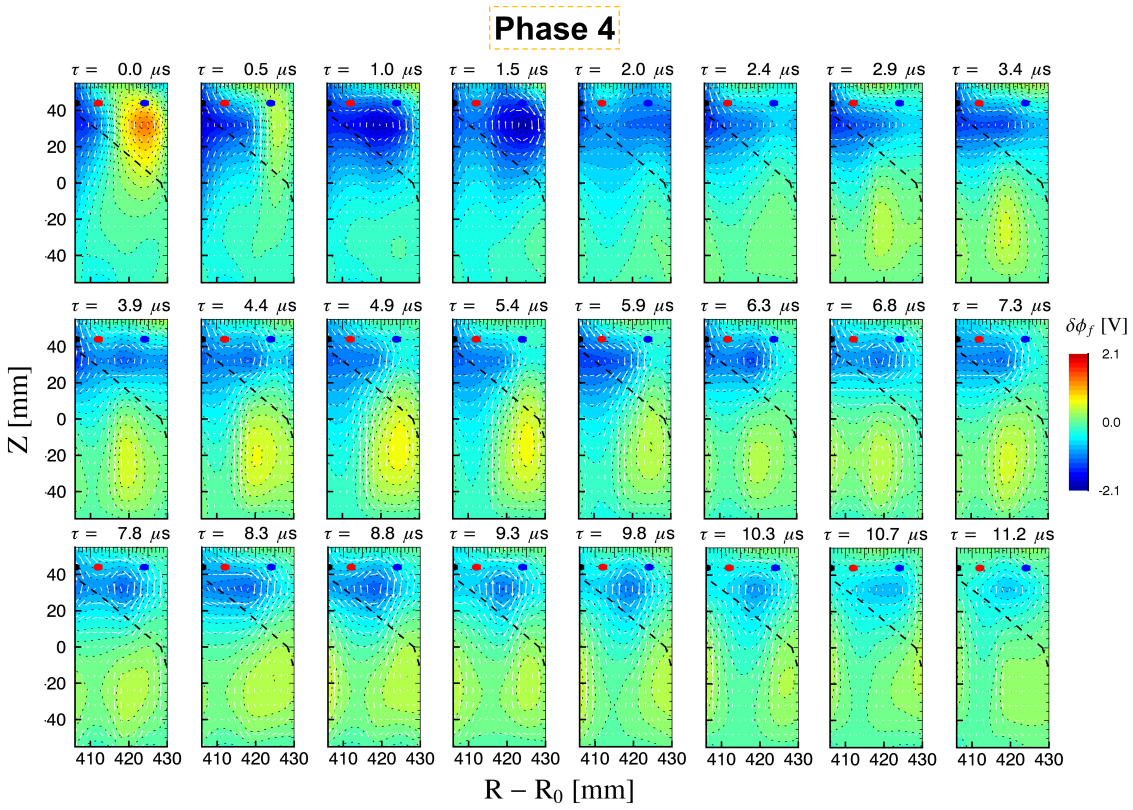

Figure 8.22: Conditional floating potential map as shown in 32 time frames during the phase-4 (ELM tail). The dashed black lines represent the last closed flux surface (LCFS), separating the plasma edge (lower part) from the SOL (upper part).

24 frames, one can see initially a dipole that rapidly turns into a spread monopole in the subsequent frames. After a fast ejection of the potential from the edge, the structure seems to be torn apart at $\tau = 1.5\ \mu s$. The larger $E \times B$ flow in this phase likely plays a role here. The negative pole remains in the near SOL, without propagating, until fades away at $\tau \approx 11\ \mu s$. Such behavior of the potential is similar to phase-1, but the $\delta\phi_f$ has lower absolute value. An important difference between these two phases is the larger amplitude of the $\partial B_\theta/\partial t$ in the range 100-200 kHz observed in phase-1. This oscillation appears in the inter-ELM phase, prior to the ELM crash. This seems to have some similarity with the quasicoherent oscillation observed elsewhere [151, 57, 89].

8.3.4 Scale dependence through the ELM cycle

The edge and SOL of fusion devices are dominated by coherent structures. They manifest as intermittent events in the ion saturation current time series [63], yielding a skewed probability distribution function. Intermittency in turbulence is identified as a deviation of a pure self-similarity behaviour [34, 11], possibly due to avalanching [14], i.e. spatially-extended excitations. While the transport resulting from avalanching is ruled by multi-scale, shear layers tend to select a set of dominant scales and induce fragmentation [195]. Therefore, the characteristic of turbulence in different scales provides a rich portrayal of its underline mechanism. As introduced in chapter 4, the wavelet decomposition technique permits to scrutinize a signal at different scales (τ) along time. Consider as an example the ion saturation signal shown in Fig. 8.23. A high-pass filter was applied to eliminate the signal trend. The continuous wavelet transform is:

$$W(\tau, t_0) = \frac{1}{\sqrt{\tau}} \int_{-\infty}^{+\infty} \psi \left(\frac{t - t_0}{\tau} \right) \tilde{I}_s(t) dt \tag{8.1}$$

Note that the wavelet coefficient at a given scale has the same size as the original signal. Fig. 8.23 b), c), and d) show the PDF (on logarithm scale) of the wavelet coefficient at three different scale, where $f \sim 1/\tau$. The black curves represent a Gaussian fit. Note that the three cases show a skewed PDF (longer positive tail), with the skewness (in red) increasing with the frequency scale. A similar trend has been reported elsewhere [11]. This is a clear trace of intermittency as well as a deviation from a self-similar turbulence behaviour (chapter 3).

As widely discussed in chapter 7, the threshold criterion is a reliable away to detect intermittent events from a time series of a given signal, e.g. ion saturation current and gas puffing imaging signal [35, 265]. By combining with statistical techniques such

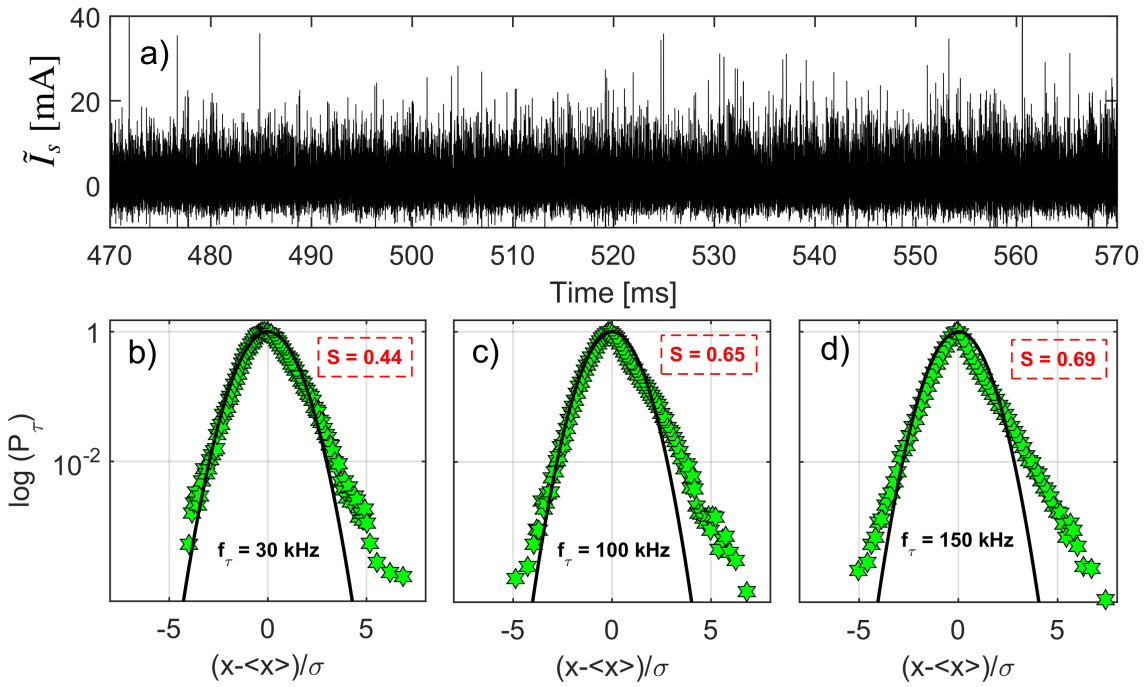

Figure 8.23: Wavelet decomposition: a) Ion saturation current signal and probability distribution function (PDF) of the wavelet coefficient at b) $f_\tau = 30$ kHz, c) $f_\tau = 100$ kHz, d) $f_\tau = 150$ kHz. The chart in red indicates the skewness value. Here $x \equiv W(\tau, t_0)$, where $< x >$ and σ are, respectively, the mean and standard deviation.

as the conditional average, one can study with a high degree of detail the properties of these turbulent structures [87]. In chapter 7 and in the previous section, it was shown how this procedure can be done for data of RFX-mod running as a tokamak. Particularly, the properties of filaments in L and H-mode have been shown to be quite different. More surprisingly, filaments during the ELM-cycle (the ELM fine structure [244]) exhibit distinct properties, possibly related to the background profile (density and potential) time evolution and the magnetic field fluctuation. In this section, the focus is still on the ELMy phase (including the inter-ELM), more precisely, the filamentary properties of the four phases by using a technique introduced in chapter 4 called: Local Intermittency Measure (LIM). This technique is based on wavelet decomposition and it has been used to select intermittent events from ion saturation current [278], floating potential [11], and gas puffing imaging signal [7].

The method selects the events, at a given time scale, that make the sampling flatness (see chapter 4) higher than 3, i.e. larger than the expected flatness of a normal distribution. Those events exhibit typically a LIM larger than 1. In addition, in order to avoid redundancy at given scale (to count twice the same structure), only the local maximum was considered. The great advantage of using this technique over the threshold criterion to select intermittent events is the possibility of selecting events based not only on their amplitude (or spectral power) but also on their time scale. In a time series corresponding to real data, e.g. an ion saturation current in the SOL, some scales can be dominant and, therefore, contribute more significantly to the overall intermittency of the signal. The conditional average of an I_s in the edge using the threshold criterion is equivalent to the weighted average over the conditional I_s at different scales, as long as the range of scales is broad enough, i.e. it must cover the maximum and minimum possible scales achieved by the time series. In other words, the LIM corresponds to approximately a scale decomposition of the threshold criterion.

It was considered again the same ion saturation current signal localized at the near SOL ($r - r_0 \approx 6$ mm) as reference, in a position where it is expected that filamentary transport becomes dominant [63]. Using the LIM in the four ELM phases, one can study in more detail the scale contribution for the filamentary transport. Fig. 8.24 a) shows the maximum δI_s from the reference signal as a function of the frequency scale. In the inter-ELM (number 1) and ELM tail (number 4) phases, the amplitude is lower and comparable between each other in all considered scales. In phase-2 (ELM crash), δI_s increases over the considered scales, saturating roughly at 300 kHz on. Phase-3, ELMy middle phase, exhibits a similar trend as phase-2, but the amplitude is lower for frequencies below 300 kHz and higher for frequencies above. The number of detected events at each scale normalized by the corresponding time window Δt is shown in Fig. 8.24 b); note, for example, that the time window of phase-2 is

shorter than the one of phase-4. In all the phases (except for 2) the number of events increases with the frequency scale. In the ELM middle phase, the frequency range 80-150 kHz presents the larger number of events, reducing at larger frequencies. Both phases 1 and 4 exhibit an increased number of events in high frequency, which might indicate blob fragmentation, although their amplitude is low (Fig. 8.24 a). In the ELM crash phase, the number of events for frequencies higher than 200 kHz is larger than in phase-3 but lower than in phases 1 and 4. Since the δI_s amplitude is large in this range, it is expected an important contribution from high-frequency events in the overall filamentary transport. Worth noting that the $E \times B$ shear might play a role here. The phases 1 and 4 are more identified as pure or ELM-free H-mode, where the larger $E \times B$ shearing rate (as suggested from the steeper radial potential profile Fig. 8.14) affects the turbulent in all scales, i.e. $\gamma_{E\times B} \gg \gamma_\tau(f)$, where $\gamma_\tau(f)$ is the turbulence growth rate [28]. The larger number of events in these phases (with substantially lower amplitude) suggests the fragmentation of the potential structure. The strong relaxation of the background potential profile also softens the previous criterion, favoring the growth of filaments. Note that this effect is less intense in low-frequency scales, but not as much as in L-mode, in qualitative agreement with the decorrelation criterion [21]. The partial recovery of the transport barrier during phase-3 is associated to a reduction of the low-frequency events at the inter-ELM phase level, while it does not affect much the high-frequency events.

The filamentary transport within the ELM-cycle was studied using the LIM analysis during phases 1 and 3 since they are longer and, therefore, offer better robustness. Fig. 8.24 shows that the majority of events during the phase 3 are concentrated in the wavelet frequency range: 50-200 kHz, although they present lower amplitude compared to the higher frequency events. On the other hand, most of the events detected in the phase 1 have lower amplitude, and they are concentrated in higher wavelet frequency range. Worth re-forcing that the frequency scale is related to events in time, as

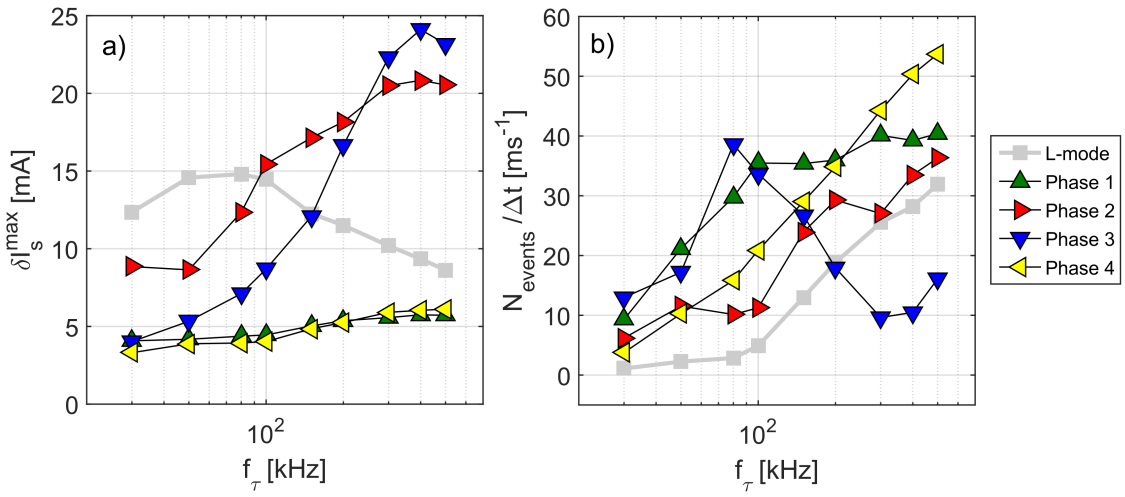

Figure 8.24: Local Intermittency Measurement (LIM) applied to an I_s signal in the SOL during the ELM-cycle: a) average δI_s^{max} and b) number of events at different frequency.

seen from a reference I_s signal. However, by employing the Taylor's frozen turbulence hypothesis, one can translate the time to spatial scale. Nevertheless, if the structure intrinsic phase velocity is larger or even comparable to the mean background velocity or if the structure is located in a strong shear flow region, this hypothesis might fail [155]. Since the ϕ_f array allows to determine the structure size directly, from the 2D map, one can study the spatial scale in both phases. On this purpose, the same I_s reference ($r - r_0 \approx 6$ mm) was considered and the LIM was employed for a wide frequency range, $f_\tau = 50 - 600$ kHz. The extreme events are conditional averaged, and the $\delta\phi_f$ can be represented in a 2D map at different time delays, and so, at different time scale. By using the same pattern recognition technique introduced in the previous chapter, based on image correlation, one can compute the potential blob size and velocity. The negative pole was taken again as reference for the blob cross-field. Fig. 8.25 shows the result of this procedure, where it is displayed the potential blob: a) radial size, b) poloidal size, c) ration between poloidal and radial size, d) radial velocity, e) poloidal velocity, and f) minimum amplitude as a function of the frequency scale for phases 1 and 3. These parameters were calculated considering the frames

where $\tau = -0.5, 0,$ and $0.5\ \mu s$ and, thus, the plotted results with the corresponding error shadow area at a given scale are the result of the mean and standard deviation over those three frames. Since the reference is placed in the SOL, the average blob potential position is around the reference position. Fig. 8.25 shows that the Taylor's hypothesis seems to hold for phase 3, both radial and poloidal size decrease with the frequency scale, but not for the phase 1. The poloidal size is larger than the radial one over the whole f_τ, yielding $L_\theta/L_r > 1$ in the phase 3, and $L_\theta/L_r \approx 1$ in the phase 1. Phase 1 confirms the trapping effect presented in the previous chapter, one can see from Fig. 8.25 d) that such behaviour occurs for the whole range of frequency scale. On the other hand, in phase 3, the radial velocity increases with the frequency scale ($\sim$size), showing that filaments at different sizes contribute to the transport in the ELM-cycle. The poloidal rotation in this phase has also a strong dependency with the scale. While filaments at low frequency scale ($f_\tau < 100$ kHz) rotate in the ion diamagnetic direction, those with larger frequency rotate preferentially in the electron diamagnetic direction (or the $E \times B$ flow direction). The largest rotation is observed in the range from 100 to 300 kHz. It is interesting to note that it occurs in the same range where L_θ/L_r is maximum. The structure amplitude, depicted by its minimum potential ($\delta\phi_f^{min}$), increases (absolute value) with the scale until saturates around 300 kHz and then decreases for larger frequencies in phase 3, while it is much lower in phase 1 for high frequency. This result shows how rich the dynamics of the ELM fine structure can be. The variety of scales with different velocity suggests some degree of filament fragmentation. The relaxation of the profiles (see Fig. 8.14) seems to favour the propagation of high-frequency filaments, while steeper $v_\theta^{E\times B}$ lead to blob trapping and dissipation.

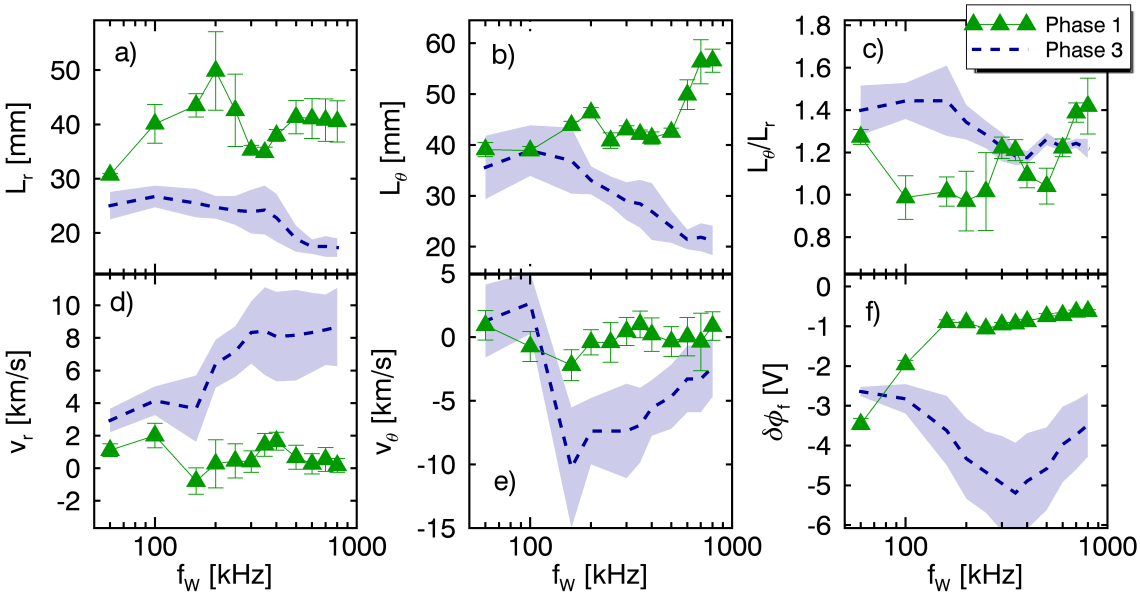

Figure 8.25: Floating potential structure at different frequency scale: a) radial size (L_r), b) poloidal size (L_θ), c) ration of poloidal by the radial size (L_θ/L_r), d) radial velocity (v_r), e) poloidal velocity (v_r), and d) minimum potential ($\delta\phi_f^{min}$) for phase 1 (green) and phase 3 (blue).

8.4 ELMs in the COMPASS tokamak

In this section, it will be discussed some experimental results from the COMPASS tokamak (see chapter 4) in NBI assisted H-mode. In the present experiment, the plasma current was in the range 250-300 kA and the magnetic field 1.25 T (clockwise from the top). The working gas was deuterium. External Co-NBI, delivering a total power of up to 280 kW on-axis, was applied when the plasma current flattop was established. Fig. 8.26 (left) shows some plasma parameter of a reference shot, where the ELMy H-mode is depicted from the periodic high amplitude bursts in D_α line signal. The plasma equilibrium is provided by EFIT and the central line averaged density is measured by a single-channel interferometer. The intense ELMy activity prevents the growth of the density, that remains approximately steady in the time NBI is on. The focus is to investigate the electromagnetic feature of the ELM filament fine structure [244]. On this purpose, a filamentary probe [144], based on the U-probe

concept, was used (see chapter 4 for more detail). The probe is composed of magnetic and electrostatic sensors, allowing the simultaneous measurement of several plasma relevant parameters, such as the floating potential (ϕ_f), ion saturation current (I_s), and the three components of the local magnetic field: $\tilde{B}_r$, $\tilde{B}_\theta$, and $\tilde{B}_\phi$. These parameters are measured in two towers (Fig. 8.27 b), displaced 4.4 cm. Owing its design, one can calculate the parallel current density from: $j_\parallel \approx (\nabla \times \mathbf{B})_\parallel / \mu_0$, from Ampere's law. The probe was inserted near the outer divertor (Fig. 8.27). The raw data from the filamentary probe are shown in Fig. 8.26 (right panel), from the top to the bottom: I_s, ϕ_f, $\partial B_\theta/\partial t$ and $\partial B_r/\partial t$. Note that all four sensors detect clearly the ELMy phase ($1080 \leq t \leq 1170$ ms). While I_s is dominated by positive peaks, which make the skewness of the corresponding PDF larger than 0, the potential and the magnetic field fluctuation (both components) exhibit positive and negative oscillations, which is a characteristic of a multi-pole structure. Besides, the strong magnetic fluctuation confirms the electromagnetic nature of the ELMs, seen as traveling filaments by the probes [244].

The parallel current deduced from measurements of three displaced coils is shown in Fig. 8.28. Before the ELMy phase starts ($t < 1080$ ms) starts, j_t oscillates in the range: $|j_t| < 10$ kA^2/m^2. In the ELMy phase ($1080 \leq t \leq 1170$ ms), periodic large amplitude events appear, reaching values of about $|j_t| \approx 50$ kA^2/m^2. Note that the amplitude of the j_t oscillation is more than ten times the one reported in section 8.3 for the ELMy phase in the RFX-mod running as tokamak. Fig. 8.28 b) shows j_t spectrogram on logarithm scale. Most of oscillation is concentrated in low-frequency before the ELMy phase (< 100 kHz), becoming spread over a wider frequency range during the ELMs.

One advantage of the filamentary probe is the possibility to measure simultaneously electrostatic and magnetic oscillation at the same location. This is particularly convenient to study electromagnetic structures as the ELMs. Fig. 8.29 shows a nar-

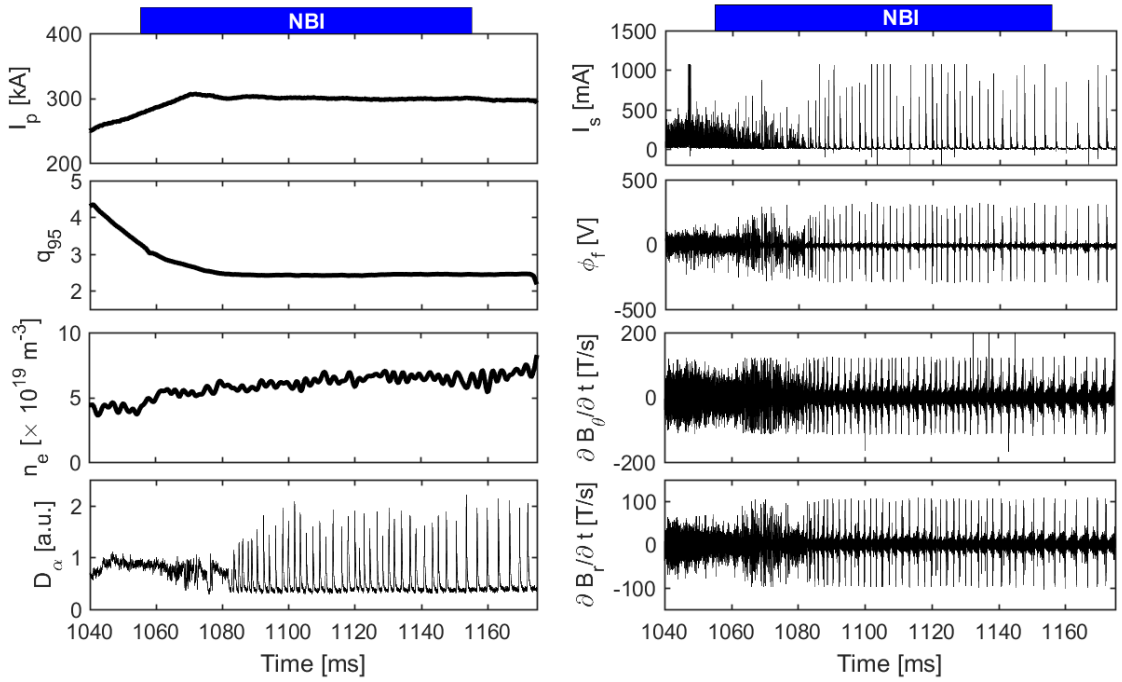

Figure 8.26: ELMy H-mode in COMPASS. Left, from the top to the bottom, plasma current (I_p), edge safety factor (q_{95}), central line averaged density (n_e), and D_α line. On the right, data from the filamentary probe, from the top to the bottom: ion saturation current (I_s), floating potential (ϕ_f), poloidal magnetic field oscillation ($\partial B_\theta/\partial t$) and radial magnetic field oscillation ($\partial B_r/\partial t$). The probe was placed at $r - r_0 \approx -4$ cm, where r_0 is the last closed flux surface (LCFS) position. Shot: #17596.

row time window of the shot depicted in Fig. 8.26, highlighting eight ELM events. Fig. 8.29 shows I_s signal placed at $r - r_0 \approx 4$ cm, where r_0 is the LCFS position. These events are related to type I ELMs [244]. Fig. 8.29 b) and c) show, respectively, the poloidal magnetic field oscillation ($\partial_t B_\theta$) and its spectrogram on logarithm scale. The peaks observed in I_s are correlated with a strong $\partial_t B_\theta$, re-forcing the electromagnetic nature of the ELM filaments. The spectral decomposition of the signal shows wide broadband turbulence from about 100 to 250 kHz preceding each event. In addition, a mode at $f \sim 50$ kHz appears before the ELM-crash, disappearing right after until appears again a few milliseconds later. A similar oscillation has been observed elsewhere [57], recognized as an ELM precursor. One has to note that al-

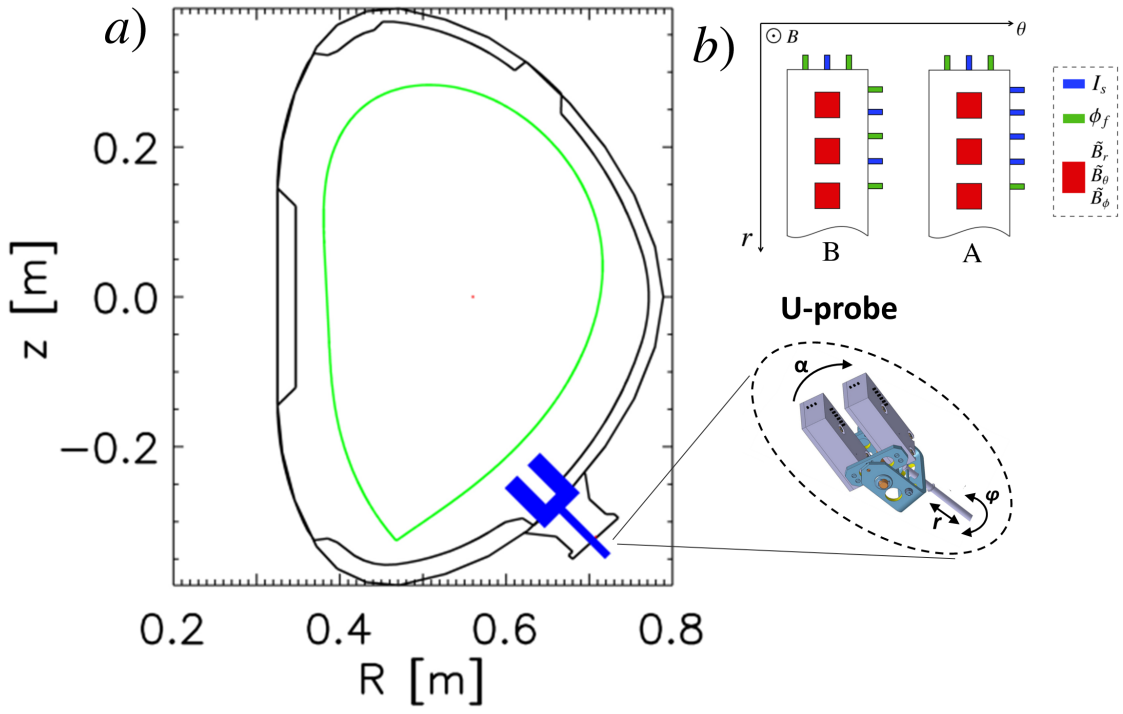

Figure 8.27: COMPASS cross-section showing (a) the U-probe inserted from a port in the lower part of the vacuum vessel. The measurement configuration in the reported experiment is shown in b).

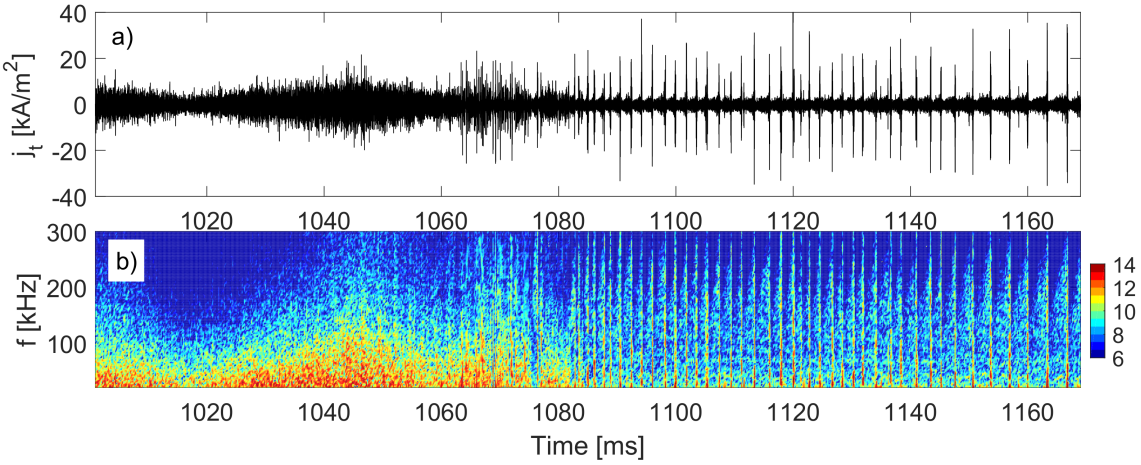

Figure 8.28: (a) Parallel current density deduced from the filamentary probe magnetic sensors. (b) corresponding spectrogram on logarithm scale. The equilibrium is provided by EFIT.

though the probe was placed in the SOL, it does not necessarily mean that the mode observed in Fig. 8.29 is local since electromagnetic fluctuation can be observed even

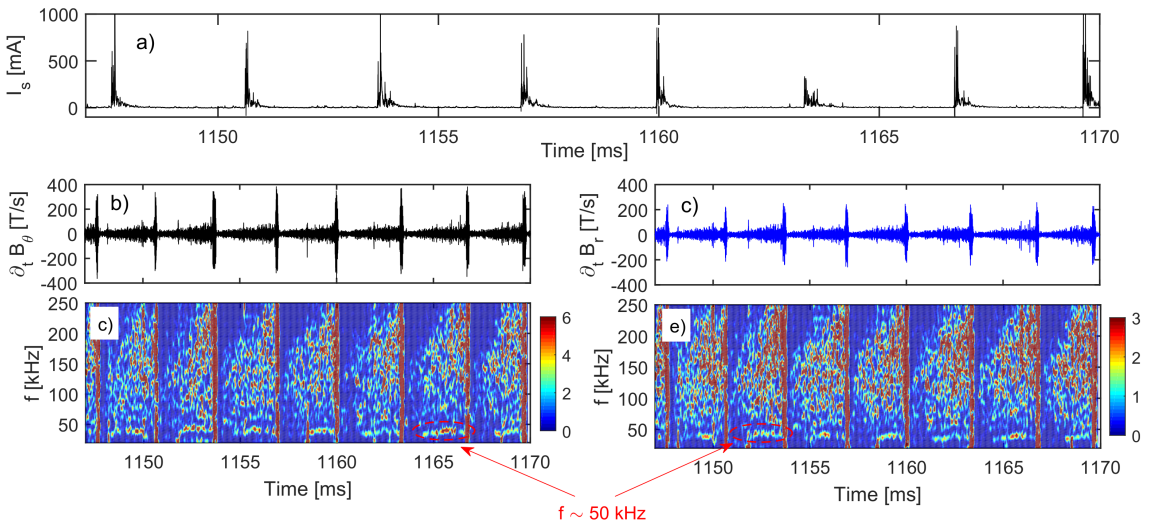

Figure 8.29: ELMy phase in COMPASS measured with the U-probe: a) ion saturation current (I_s), b) poloidal magnetic field oscillation ($\partial_t B_\theta$), c) spectrogram of $\partial_t B_\theta$ on logarithm scale, d) radial magnetic field oscillation ($\partial_t B_r$), and e) spectrogram of $\partial_t B_r$ on logarithm scale.

far from the source possibly related to toroidal coupling [56]. The radial magnetic field oscillation ($\partial_t B_r$) although lower exhibits a similar feature, with periodic strong activities correlated with the peaks in I_s and the perturbations in $\partial_t B_\theta$. A mode at $f \sim 50$ kHz is also evident from the spectrogram of $\partial_t B_\theta$ together with a strong broadband oscillation (100-250 kHz). Both, however, almost disappear right after the ELM-crash. A similar mode also appears in ELM-free H-mode in COMPASS and it has been identified as quasicoherent mode [178]. The maximum magnetic field fluctuation normalized by the equilibrium magnetic field is $\delta B/B \approx 8 \times 10^{-4}$.

Fig. 8.28 indicates that the ELM filaments are able to carry a large current (up to $|j_t| \approx 40$ kA^2/m^2) To compare the parallel current density carried by turbulent filaments in L-mode with the one measured for the ELM filaments the I_s signal was used as a reference. As discussed in the previous chapter, the ion saturation current fluctuation is a good proxy for the density fluctuation [196]. Besides, its high temporal resolution (typically limited by the data acquisition sampling rate) makes it ideal to study high-frequency turbulent events. Since blobs or filaments dominate

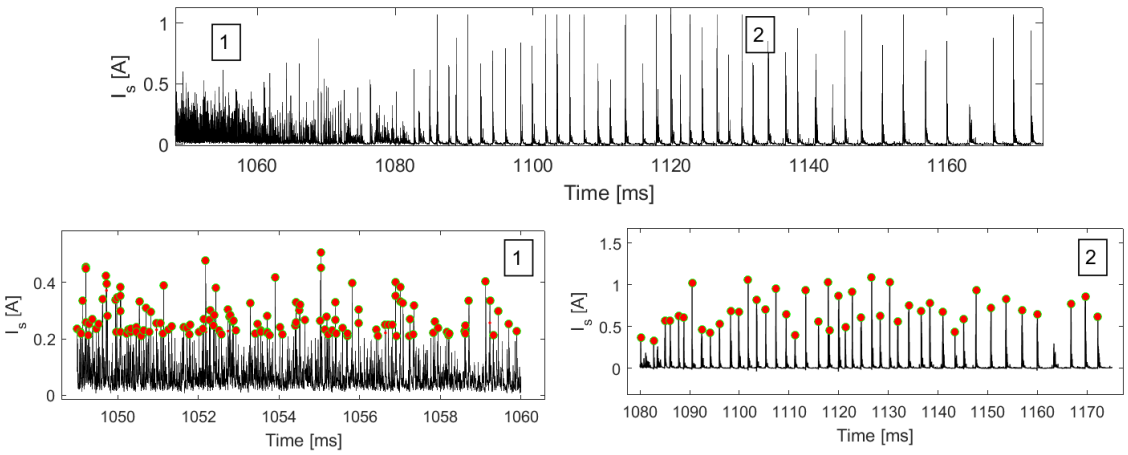

Figure 8.30: At the top: an ion saturation current signal in the SOL ($r - r_0 \approx 4$ cm) during the L-H transition. NBI was applied from 1080 ms. At the bottom are shown a time window during L-mode (phase-1) and ELMy H-mode (phase-2). The red circles indicate the peaks larger than $\langle I_s \rangle + 2.5\sigma$, where $\langle I_s \rangle$ and σ are, respectively, the sampling mean and standard deviation for each phase or time window.

the transport in the SOL, the time series of a pin measuring I_s in this region is dominated by positive oscillation that makes its probability density function (PDF) skewed. Fig. 8.30 shows an I_s signal measured at $r - r_0 \approx 4$ cm, i.e. in the far SOL. The NBI assisted heating starts approximately at 1060 ms (Fig. 8.26), inducing strong ELM filaments from 1080 ms on. The phase number 1, depicted in the bottom chart of the Fig. 8.30 indicates a time window when the plasma is still in low confinement (L-mode), while the phase number 2 indicates the ELMy phase. Filaments were defined as the I_s peaks (extreme events) that exceed a threshold. In both cases, the threshold was $I_s^{peak} > \langle I_s \rangle + 2.5\sigma$, where $\langle I_s \rangle$ and σ are, respectively, the sampling mean and standard deviation for each phase. In the ELMy phase, only the maximum peak for each ELM event was kept, as representative of the ELM cycle.

The peaks of I_s in both phases are correlated with the maximum absolute value of the parallel current density, deduced from signals of three closed magnetic sensors. Since I_s and j_t are not measured at the same location and due to their complex 2D structure [87], their maxima typically do not occur at the same time instant.

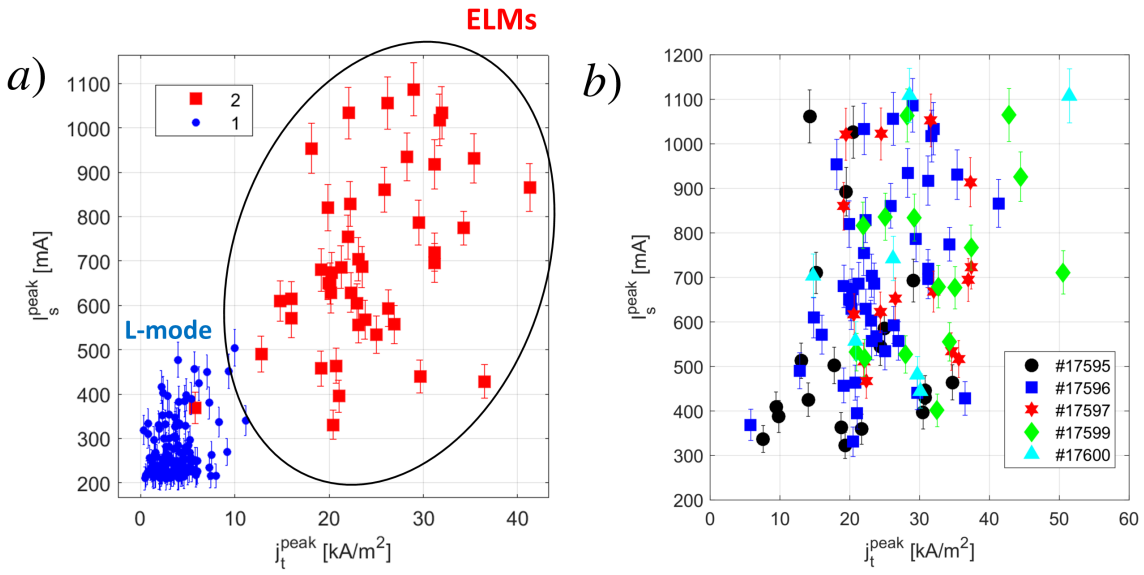

Figure 8.31: Burst events from the I_s signal are correlated with $|j_t|$ maximum: a) during L-mode (phase-1 Fig. 8.29) and ELMy H-mode (phase-2 Fig. 8.29), shot: #17596. In b) is shown I_s^{peak} as function of j_t^{peak} during the ELMy phase of five similar shots.

Therefore, for each peak of I_s, the maximum of $|j_t|$ was selected over a time window around I_s^{peak}. In L-mode, this time window was of $\sim 8\ \mu s$, which is slightly larger than the typical blob characteristic time. For the ELM filaments, the chosen time window was of the order of an ELM event ($\sim 800\ \mu s$). Fig. 8.31 a) shows the I_s^{peak} as function of j_t^{peak} (absolute value) in L-mode (blue circles) and during the ELMy phase (red squares). One can see clearly that filaments in L-mode have lower I_s amplitude and carry substantially less current. ELM filaments exhibit a wider variation in I_s and j_t, but the majority lie in the range $j_t^{peak} > 10$ kA^2/m^2. Fig. 8.31 b) shows several ELM events collected from five similar shots. The distribution of points is again quite scattered, but with comparable values among shots. Note that since the probe is placed in the far scrape-off layer, the filaments that arrive there could have been impacted by the background, which might explain in part the scattering of the data point. But, one can not neglect the fact that the instability itself after the non-linear phase can yield filaments with different characteristic.

8.4.1 Quasicoherent mode

ELM-free H-mode is frequently achieved in COMPASS, with or without auxiliary heating. In this case, quasicoherent modes (QCMs) have been observed [178], with frequency in the range $50 \leq f \leq 250$ kHz (at low-field side) and strong electromagnetic feature. While those high frequency modes typically exhibits ballooning structure, they are thought to have Alfvén nature, with frequency that roughly follows $f \sim \bar{n}_e^{-1/2}$, where $\bar{n}_e$ is the central line averaged density, i.e. with Alfvén dependency [99]. The existence of quasicoherent modes in ELM-free H-mode and inter-ELM phases have been reported in several devices [151, 57, 284], they are observed in the pedestal or the lower part of density gradient near the LCFS [262], typically rotating in the electron diamagnetic direction in both plasma and laboratory frame. Those structures are particularly important in regulating cross-field transport in ELM-free H-mode. The enhanced D_α (EDA) H-mode observed in Alcator C-Mod is an example of that, a QCM is responsible for enhancing the cross-field transport in the pedestal region towards the SOL, preventing the further growth of the pedestal pressure gradient and, thus, making the H-mode stable to ELMs [234, 43]. In this case, the underline instability seems to be resistive-ballooning for x-point geometry [173] and/or drift-Alfvén wave [187, 43].

Figure 8.32 shows some global parameter of an ELM-free H-mode shot in COMPASS. The applied NBI power (the time pulse length is indicated by the blue box) was $P_{NBI} \approx 0.3$ MW. The H-mode is characterized by a fast drop of the D_α line (Fig. 8.32 c), followed by an increase of central averaged density (Fig. 8.32 a, the strong oscillation observed is related to uncertainties of the interferometer). The transition occurs when the plasma current stabilizes around 300 kA (Fig. 8.32 b) and the edge safety factor becomes about 2.5 (Fig. 8.32).

The filamentary probe was placed again at $r - r_0 \approx 4$ cm. The measurements of the ion saturation current (Fig. 8.33 a) further confirm that the H-mode was achieved:

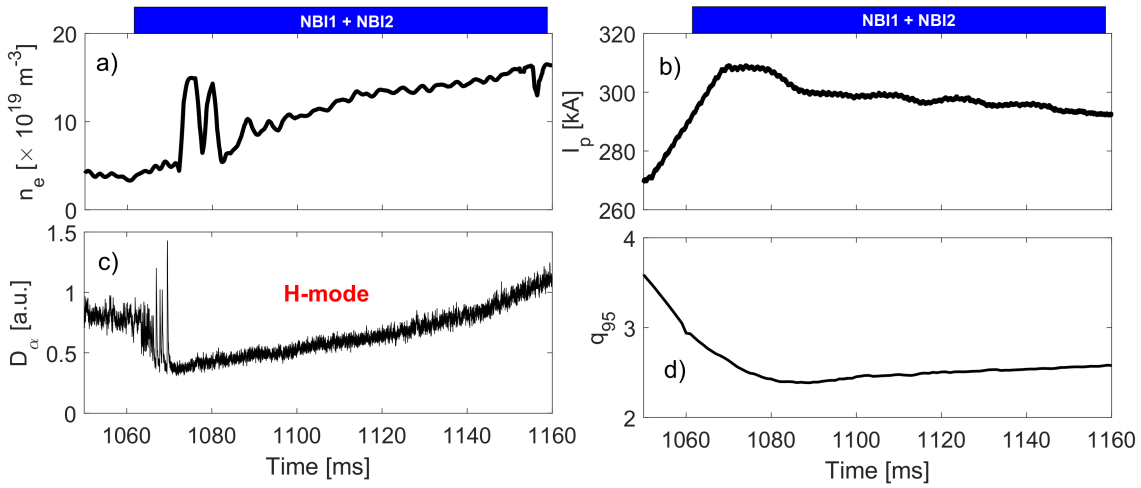

Figure 8.32: ELM-free H-mode in COMPASS: a) central line averaged density, b) plasma current, c) D_α line, and d) edge safety factor. The total NBI power was $P_{NBI} \approx 0.3$ MW. Shot: #17598.

I_s fluctuation nearly disappears in the time window $1070 < t < 1160$ ms. However, by looking at the magnetic field fluctuation (Fig. 8.33 b and d), a much more complex behaviour is manifested. Right after NBI starts ($t \approx 1060$ ms), large I_s events appear (similar to type III ELM [153]), also seen by the magnetic signals. Later, the ELM-free H-mode starts, but high frequency bands are observed in the spectrogram of both poloidal and radial magnetic field components (Fig. 8.33 c and e, respectively). The oscillations appears with high frequency bands in the range: $50 < f < 150$ kHz. Those oscillations are similar to the one reported in the article [178], where they were attributed to beta-induced Alfvén eigenmodes with ballooning character. Worth noting that this oscillation seems to be modulated by the spikes observed in both $\tilde{B}_\theta$ and $\tilde{B}_r$: when they occur, the frequency of each stripe, that was decreasing, begins to increase. Around 1100 ms, a strong oscillation in the range: 50-70 kHz develops, concomitantly with the disappearing of the high-frequency bands. Later on, however, this mode disappears and a high-frequency mode around 100 kHz becomes dominant. The low-frequency spikes are still presented, associated with a low frequency oscilla-

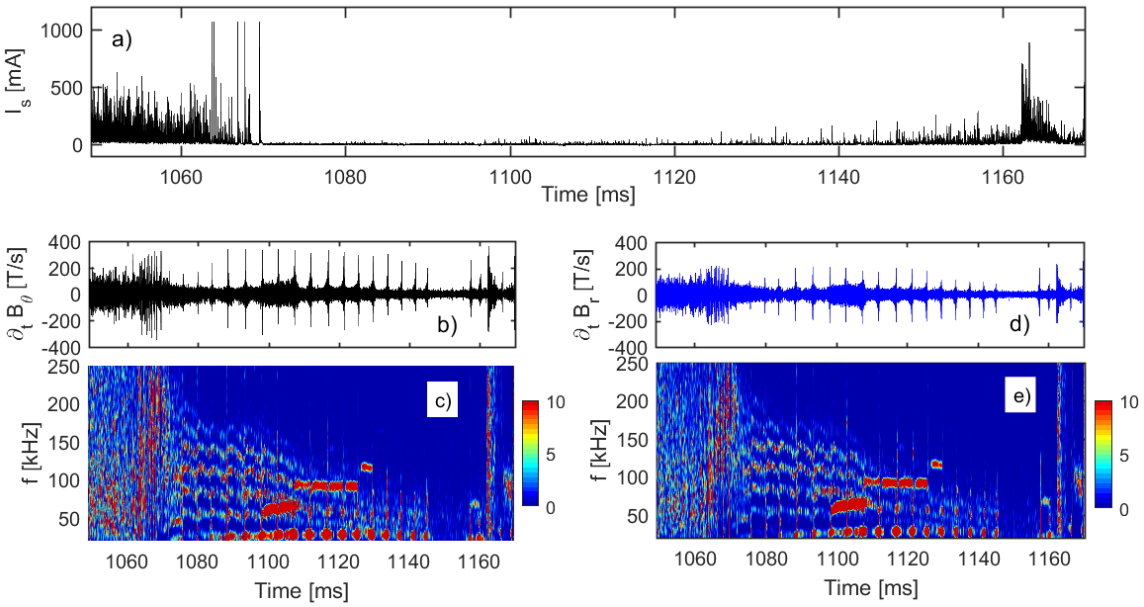

Figure 8.33: U-probe data during ELM-free H-mode of fig. 8.31: a) ion saturation current, b) poloidal magnetic field oscillation ($\partial_t B_\theta$), c) and corresponding spectrogram on logarithm scale, d) radial magnetic field oscillation ($\partial_t B_r$), and e) spectrogram $\partial_t B_r$ on logarithm scale.

tion $f < 50$ kHz. The second mode also fades away, and the spikes reduce gradually until the NBI being switched off.

To study with more detail the properties of these modes, signals of two coils, with mutual poloidal distance of d = 4.4 cm, were used. Only the poloidal magnetic field component was considered ($\partial_t \tilde{B}_\theta$). The 2-point correlation technique was applied to extract the wavenumber-frequency spectrum [217]. The maximum wavenumber detected with this method is: $|k_\theta| \leq \pi/d \approx 0.7$ cm^{-1}. The frequency (S_f) and the wavenumber spectrum (S_k) can be obtained from $S(k, f)$ by integrating over the wavenumbers and frequencies, respectively (see chapter 4). $S(k, f)$ was calculated in sub-windows of 4 ms with 50% of overlap. S_f and S_k in time are shown in Fig. 8.34 a) and b), respectively, together with the corresponding poloidal phase velocity (Fig. 8.33 c). The high frequency bands appear clearly, with a characteristic wavenumber of about $|k_\theta| \approx 0.3$ cm^{-1}, and poloidal phase velocity $v_\theta^{ph} \approx 15$ km/s in the ion diamagnetic direction (IDD) in the laboratory frame. Around 1100 ms, a

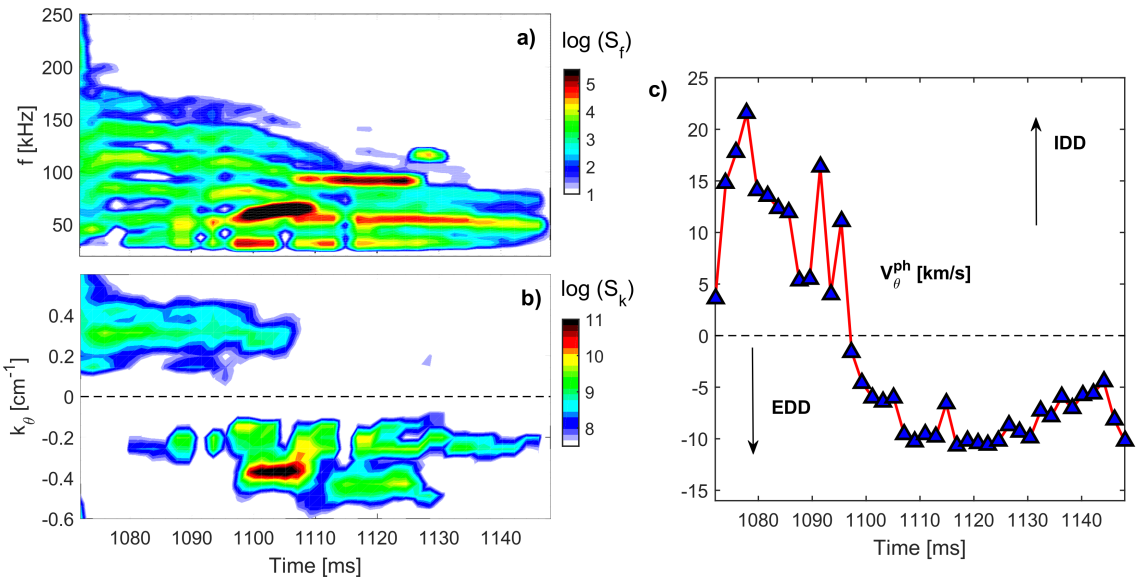

Figure 8.34: Quasicoherent mode: a) spectrogram of the frequency (S_f) and wavenumber (S_k) spectrum on logarithm scale and c) poloidal phase velocity, where IDD is for ion diamagnetic direction and EDD electron diamagnetic direction. Shot: #17598.

dominant mode in the range 50-70 kHz appears with wavenumber $|k_\theta| \approx 0.4$ cm^{-1} and opposite poloidal phase velocity $v_\theta^{ph} \approx -15$ km/s in the electron diamagnetic direction (EDD) now. From about 1110 ms, a mode around 100 kHz appears with slightly higher wave number. A mode of 50 kHz together with lower frequency oscillation $f < 50$ kHz emerge, creating a new branch in the S_k spectrum with values around $|k_\theta| \approx 0.2$ cm^{-1}. These finds suggest a very complex behaviour of the quasicoherent modes in COMPASS that typically appear in the inter-ELM or ELM-free discharges.

8.5 Conclusion

In this chapter, it was discussed the ELM instability and its filamentary nature. While this instability could allow steady-state H-mode, with periodic exhaustion of energy, the presence of high amplitude events might represent a great risk for the plasma face components in ITER and beyond [160] and, consequently, for the reactor

life time [74]. The reported results in this thesis are from the RFX-mod running as tokamak in single null configuration and the COMPASS tokamak. In RFX-mod, ELMs have been recently observed in biasing experiments [243], while in COMPASS this instability is driven with auxiliary heating and in simple ohmic discharges [202]. With a set of electrostatic and magnetic sensors, the instability and its filamentary nature are characterized in detail. A clear trace of this instability is its electromagnetic nature and the presence of current-carry filaments. In RFX-mod the parallel current associated to ion saturation current peaks in the SOL (proxy for filament density) is about 1 kA/m^2, while in COMPASS $>$ 10 kA/m^2, i.e. more than 10 times larger. The same trend has been observed for the magnetic field fluctuation $\delta B/B$, where B is equilibrium magnetic field. In RFX-mod the maximum fluctuation was $\delta B/B \approx 8 \times 10^{-5}$, while in COMPASS $\delta B/B \approx 8 \times 10^{-4}$. This, of course, reflects the different plasma environment in these two devices (Fig. 8.4 and 8.25), but also the ELM nature: while the ELMs in COMPASS are interpreted as type I, in RFX-mod they are more close to type III or grassy [153]. The U-probe in RFX-mod allowed studying with an unprecedented level of detail the ELM-fine structure, i.e. the filaments within the ELM-cycle. By looking at different phases, inter-ELM, ELM crash, ELM middle, and ELM tail (Fig. 8.13) it became evident that the background mean profiles (Fig. 8.14 and 8.15), and the magnetic field fluctuation (Fig. 8.16) play a role in the filamentary transport. Particularly, a relaxation of the profiles and a stochastization of the magnetic field are footprints of the ELM phases. The propagation or not of filaments in these phases seems to be conditioned by the potential profile, which is ultimately related to $E \times B$ flow. By using the local intermittency measurement (LIM), it was possible to study the filaments in more detail during the ELM middle phase at different time scale, which in this case can be translated in spatial scale (from the potential map), in qualitative agreement with the Taylor's frozen turbulence hypothesis. This analysis reveals that most of the filaments in this phase

are concentrated in high-frequency scales (small spatial scale), with velocities up to 8 km/s. Worth noting that since the these scales are related to the highest amplitudes, the corresponding filaments contribute more significantly for the total particle flux $\Gamma_r^{ELM} = \langle \delta I_s^{max} v_r \rangle$, observed in the plasma wall (Fig. 8.5). In both COMPASS and RFX-mod an ELM precursor were observed. They were more evident from the magnetic sensors (confirming the electromagnetic nature of the driven instability), with a broadband fluctuation around 100 kHz in both cases, but with a clear mode around 50 kHz prior the ELM crash in COMPASS. A quasicoherent mode was observed in RFX-mod (Fig. 8.12), with frequency around 100 kHz and wavenumber $|k_\theta| \approx 0.1$ cm^{-1}, rotating in the electromagnetic direction as seen from the laboratory frame. The quasicoherent mode in COMPASS has been reported before [178], with a clear ballooning feature. The COMPASS filamentary probe allowed studying the electromagnetic characteristic of this mode. The quasicoherent mode appeared in the ELM-free H-mode with no clear enhancement of the cross-field transport (the probe in the far SOL does not detect any strong fluctuation). However, the magnetic sensors exhibit a very rich and complex spectrum, with high-frequency bands, and strong high-frequency modes. The 2-point correlation technique applied for two poloidal displaced coils measuring the poloidal magnetic field fluctuation (Fig. 8.34) shows that the transition from the ballooning dominant to a more localized high-frequency fluctuation is characterized by a flip of the poloidal phase velocity, from the ion to the electron diamagnetic direction. In short, this chapter has provided some insights on the ELM-cycle (in two devices: RFX-mod running as tokamak and COMPASS) and on the electromagnetic filaments associated with it.

Chapter 9

Final conclusion

Throughout this thesis, it was investigated the properties of turbulence in the plasma edge and scrape-off layer (SOL) of TJ-II, RFX-mod, and COMPASS. Although the difference between these devices, the universal nature of turbulence permits to cross-compare their results.

The effect of turbulence propagation was studied in the TJ-II stellarator, as discussed in the chapters 5 and 6. In chapter 5, an edge-SOL turbulence spreading model was considered [166] to quantify the turbulence spreading rate and the local turbulence growth rate. These two quantities, together with some other plasma relevant parameters, were measured with a two-dimension electrostatic probe inserted into the plasma edge from the SOL on a shot-by-shot basis. TJ-II in this experiment operated with hydrogen as working gas in two regimes 1) plasma started with ECRH and then sustained with NBI; 2) NBI + external biasing (started with ECRH). The main results are summarized as follows:

- The turbulence spreading rate (depicted by the ω_S parameter) is mainly activated in the SOL region, while the local turbulence growth rate (ω_D) is larger in the edge, consistent with the steeper profiles in this region. These results are in

good agreement with simulations from a three-dimensional gyro fluid turbulence model [166];

- The ECRH to NBI transition is characterized by a reduction of the spreading in the SOL, while the rate of turbulence drive (ω_D) strongly reduces in the near edge where a poloidal shear flow layer was established;
- Biasing modulation (square 40 Hz pulse in a duty cycle of 50% with -350 V) was shown to modify the shear layer and impact on the ion saturation current, floating potential, and radial particle flux profiles. Particularly, at -350 V, a shear layer was formed in the plasma edge, followed by a reduction of ω_D and ω_S (in the SOL). At zero biasing, however, the background $E \times B$ flow reduced compared to the pure NBI case (i.e. without biasing) and so both ω_D and ω_S increased;
- The edge-SOL decoupling was observed to happen when the $E_r \times B$ shearing rate reaches values comparable to the inverse of the turbulence correlation time in the vicinity of the LCFS;
- In the far SOL, ω_D and ω_S were comparable in both regimes suggesting that the spreading becomes an important source of fluctuation in this region.

The findings presented in chapter 5 indicate that sheared radial electric fields are able not only to suppress turbulence locally but also to reduce its spreading that ultimately leads to the edge-SOL turbulence decoupling. The effect of turbulence propagation was further investigated in chapter 6 in spontaneous electron-ion-electron root transition shots, where the edge radial electric field was slowly modified from positive to negative and then to positive again. Turbulence propagation was quantified through the transfer entropy technique that measures the propagation of information between two processes [226, 271, 102]. The main results of this chapter are:

- During the transitions, zonal flows became amplified in agreement with simulations [275]. This conclusion was based on biorthogonal analysis where data from multiple floating potential signals, from two remotely separated electrostatic probes, were decomposed in orthogonal spatio-temporal functions (modes). The global dominant mode has been shown to exhibit high long-range correlation and low-frequency oscillation ($f \leq 1$ kHz), which are precisely the properties of zonal flows [85, 59];
- The electron-ion root transition was characterized by a reduction of the turbulent particle flux and radial correlation length around the LCFS, indicating that turbulence is locally impacted;
- While during the electron root phases ($E_r > 0$) turbulence propagated outwardly with a typical velocity of 1 km/s. In the ion root phase ($E_r < 0$), propagation ceased almost completely.

The results presented in chapter 6 confirms the role of radial electric fields in regulating turbulence and cross-field transport. Turbulence in the plasma edge and SOL is dominated by filaments. Hence, it is natural to think that these structures are responsible for the turbulence spreading effect described in chapters 5 and 6. The properties of filaments or blobs were studied in detail in RFX-mod running as tokamak in Single-Null (SN) configuration. The results are presented in chapter 7. In addition, biasing H-mode has been recently obtained in RFX-mod in the mentioned configuration [243]. This chapter is aimed to provide a comparison between the properties of the filaments in L-mode and biasing H-mode. For this purpose, a filamentary type of probe based on U-probe concept was used (see chapter 4). This probe is equipped with a set of two-dimension electrostatic and magnetic sensors that allows measuring the parallel current density. The main results of this chapter are:

- During the biasing phase, turbulence decreased in the edge and SOL, while the radial profiles of the ion saturation current and floating potential became steeper. This had an impact on the turbulent particle flux around the enhanced poloidal shear flow layer. Besides, the effective radial correlation length in the SOL became shorter, suggesting that the turbulence does not penetrate the SOL easily as in L-mode;
- Potential coherent structures related to ion saturation current bursts through conditional average were successfully detected, tracked, and characterized. In L-mode, a dipole potential structure was detected near the edge travelling with radial velocity ~ 2 km/s. While this structure was mainly aligned and stretched poloidally near the LCFS, it became more circular and less tilted in the SOL. Besides, its amplitude and vorticity also increased in the SOL, slightly reducing later in the far SOL. The blob poloidal velocity was observed to be in the electron diamagnetic direction in the near edge;
- In the biasing phase (ELM-free H-mode), potential blobs were detected mainly in the SOL. The potential structure, in this case, seemed to be a negative monopole rather than a dipole. Near the LCFS, the velocity was relatively high (~ 4 km/s), but it went almost to zero further outside. The potential structure became nearly 'trapped' in the SOL, disappearing later on;
- The blob suppression criterion discussed in chapter 3 predicts that streamers or blobs are broken when $\gamma_{E\times B} > 1/\tau^{turb}$. By comparing the inverse of the blob characteristic time ($1/\tau^{turb} = v_r L_\theta / L_r^2$) with the local $E \times B$ shearing rate ($\gamma_{E\times B} = B^{-1} dE_r/dr \approx B^{-1} d^2\phi_f/dr^2$) in both regimes it was shown: 1) in L-mode $1/\tau^{turb}$ was always higher than $\gamma_{E\times B}$, therefore blobs are expected to 'survive'; 2) in ELM-free H-mode, $\gamma_{E\times B}$ increased way above the L-mode values;

- It was pointed out that the vortex selection by the background sheared flow [168] can also yield the trapping effect observed in H-mode. More generally, any perturbation in the dipole that causes an unbalance between positive and negative pole can yield similar effect, i.e., the blob would spin rather than radially propagate. As suggested by [185, 281], non-thermalized blobs can produce a similar effect;

- Blobs dynamics in the two scenarios were discussed in the framework of analytical models and velocity scaling [146, 93, 188]. During L-mode, blobs were better described by the sheath connected regime, where the parallel current density and potential structure were shown to be roughly synchronized. While near the LCFS filaments are better described by the sheath connected scale at $L_{\parallel} \approx 30$ m, in the far SOL the better match happens at $L_{\parallel} \approx 10$ m, roughly in accordance with the predicted $L_{\parallel}$ in these two regions. In the ELM-free H-mode, however, filaments near the LCFS scale roughly as the inertial regime. In this scenario, the parallel current density structure reaches its maximum amplitude and size in the edge but nearly disappear later.

The chapter 7 presents measurements of potential blob around the LCFS. This quantity is important for the blob motion and usually is not available experimentally in fusion devices. While filaments described in chapter are thought to be electrostatic since $\beta < (m_e/m_i)$, where $\beta = n_e T_e/(B^2/2\mu_0)$. Filaments during edge localized modes (ELMs) are believed to be electromagnetic [153]. In the chapter 8 was discussed the ELM filaments in RFX-mod running as tokamak in single null configuration [243] and the COMPASS tokamak [202]. In both devices, a filamentary probe based on the U-probe design was used, allowing the cross-comparison between them. The main results are:

- In RFX-mod the parallel current density associated to ion saturation current peaks in the SOL, exhibiting amplitude of about 1 kA/m^2, while in COMPASS > 10 kA/m^2, i.e. more than 10 times larger;
- In RFX-mod $\delta B/B \approx 8 \times 10^{-5}$, while in COMPASS $\delta B/B \approx 8 \times 10^{-4}$ during the ELMy phase;
- ELM-fine structure in RFX-mod within the ELM-cycle showed that the background profiles and the magnetic field fluctuation play a role in the filamentary transport. Particularly, a relaxation of the profiles with higher fluctuation of the magnetic field were footprints of the ELM phases. The propagation or not of ELM filaments seemed to be conditioned by the potential profile, which is ultimately related to $E \times B$ flow;
- By using the local intermittency measurement (LIM), it was possible to study the filaments in more detail during the ELM phase at different time scale, translated, in this case, in spatial scale (from the potential map), in qualitative agreement with the Taylor's frozen turbulence hypothesis [155]. This analysis revealed that most of the filaments in this phase were concentrated in high-frequency scales (small spatial scale), with velocities up to 8 km/s;
- In both COMPASS and RFX-mod an ELM precursor was observed. They were more evident from the magnetic sensors (confirming the electromagnetic nature of the driven instability [153]), with a broadband fluctuation around 100 kHz in both cases, but with a clear mode around 50 kHz prior the ELM crash in COMPASS;
- A quasicoherent mode was observed in both devices during the ELM-free H-mode. In RFX-mod, it appeared with frequency around 100 kHz and wavenumber $|k_\theta| \approx 0.1$ cm^{-1}, rotating in the electromagnetic direction as seen from the laboratory frame. In COMPASS, this structure has been related to Alfvén in-

stanilities [178], with a ballooning character. Measurements with the U-probe in this device showed that the transition from high-frequency bands regime to a more localized high-frequency fluctuation was characterized by a flip of the poloidal phase velocity, from the ion to the electron diamagnetic direction;

Chapter 8 shows that filaments associated with ELM events share similar properties with turbulent filaments in L and ELM-free H-mode (chapter 7). Particularly, they seem to be susceptible to sheared flows. Indeed, $E \times B$ shear flow has been observed to inhibit ELM [142]. Besides, edge localized modes can be mitigated by resonant magnetic perturbation [153]. However, the underlying physics behind this process must be better understood. This is a requirement for ITER operation since ELMs can reduce the machine life-time [74]. The new MHD control system in RFX-mod 2 [169] will make this device a formidable laboratory for studying this instability.

In addition, preliminary results with the high resolution probe (HRP) [6, 240], a filamentary-type of probe (as discussed in chapter 4), has shown the robustness of this probe to investigate turbulent filaments in W7-X. These structures are thought to be determinant in setting the SOL profiles in tokamaks and stellarators [63]. The new divertor system in W7-X based on magnetic islands [206, 300] brings some physical effects that is not expected in tokamaks divertors. Particularly, the plasma-island interaction can yield a different type of turbulent filament. Besides, turbulence spreading into the island O-point might also play a role [127].

In short, the results presented in this thesis shed light on important issues regarding turbulence and its impact on cross-field transport in tokamak and stellarator.

Appendix A

List of Symbols and Abbreviations

A.1 List of Symbols

R_0	Major radius
a	Minor radius
I_s	Ion saturation current
ϕ_f	Floating potential
ϕ_p	Plasma potential
T_e	Electron temperature
$L_\parallel$	Parallel connection length
$[B_r, B_\theta, B_\phi]$	Respectively, radial, poloidal, and toroidal magnetic field components
$\mathbf{k}, k$	Wave vector, wavenumber
Γ_r	Radial particle flux
m_i, m_e	Ion and electron mass
$j_\parallel$	Parallel current density
ω_S	Rate of turbulence spreading
v_θ^{ph}	Poloidal phase velocity

ω_D	Rate of turbulence drive
$\gamma_{E\times B}$	$E \times B$ shearing rate
q	Safety factor
ι	Rotational transform
λ_q	Power fall-off length
c_s	Sounds speed
ρ_s	Ion Larmor radius
2D-AC	Two-dimension auto-correlation
2D-CC	Two-dimension cross-correlation

A.2 List Abbreviations

LCFS:	Last Closed Flux Surface
SOL:	Scrape-Off Layer
ELM:	Edge-Localized Mode
GAM:	Geodesic Acoustic Mode
LoS:	Line of sight
HFS:	High Field Side
LFS:	Low Field Side
NBI:	Neutral Beam Injector
ECRH:	Electron Cyclotron Resonance Heating
BN:	Boron Nitrite
EM:	Electromagnetic
FFT:	Fast Fourier Transform
MHD:	Magnetohidrodynamics
PDF:	Probability distribution function
RFP:	Reversed field pinch
RMS:	Root mean square
ZF:	Zonal Flow
LHS:	Left Hand Side
RHS:	Right Hand Side
LIM:	Local Intermittency Measure
MI	Mutual information
TE:	Transfer Entropy
BOD:	Biorthogonal decomposition
SVD:	Single value decomposition

IDD:	Ion diamagnetic direction
EDD:	Electron diamagnetic direction
ISIS:	Internal system of sensor
FWHM:	Full Width at Half Maximum
ETB:	Edge transport barrier

Bibliography

[1] Domenico A., G. Marchiori, and F. Villone. Modelling and experimental validation of RFX-mod tokamak shaped discharges. *Fusion Engineering and Design*, 2018.

[2] H.D.I. Abarbanel, R. Brown, J.J. Sidorowich, and L.Sh. Tsimring. The analysis of observed chaotic data in physical systems. *Reviews of modern physics*, 65(4):1331, 1993.

[3] D. Abate and P. Bettini. An inverse equilibrium tool to define axisymmetric plasma equilibria. *Plasma Phys. Controll. Fusion*, 61(10):105016, 2019.

[4] J. Adamek, J. Horacek, J. Seidl, H.W. Müller, R. Schrittwieser, F. Mehlmann, P. Vondracek, S. Ptak, and COMPASS Team and Team, ASDEX Upgrade and others. Direct Plasma Potential Measurements by Ball-Pen Probe and Self-Emitting Langmuir Probe on COMPASS and ASDEX Upgrade. *Contributions to Plasma Physics*, 54(3):279–284, 2014.

[5] R.J. Adrian. Conditional eddies in isotropic turbulence. *The Physics of Fluids*, 22(11):2065–2070, 1979.

[6] P. Agostinetti, M. Spolaore, M. Brombin, V. Cervaro, L. Franchin, O. Grulke, C. Killer, E. Martines, M. Moresco, and S. et al. Peruzzo. Design of a high resolution probe head for electromagnetic turbulence investigations in W7-X. *IEEE Transactions on Plasma Science*, 46(5):1306–1311, 2018.

[7] M. Agostini, S.J. Zweben, R. Cavazzana, P. Scarin, G. Serianni, R.J. Maqueda, and D.P. Stotler. Study of statistical properties of edge turbulence in the National Spherical Torus Experiment with the gas puff imaging diagnostic. *Phys. Plasmas*, 14(10):102305, 2007.

[8] C. Alejaldre, J. Alonso, L. Almoguera, E. Ascasíbar, A. Baciero, R. Balbín, M. Blaumoser, J. Botija, B. Brañas, and E. et al. De la Cal. First plasmas in the TJ-II flexible heliac. *Plasma Phys. Control. Fusion*, 41(3A):A539, 1999.

[9] J.A. Alonso, C. Hidalgo, M.A. Pedrosa, B.Ph. van Milligen, D. Carralero, and C. Silva. Dynamic transport regulation by zonal flow-like structures in the TJ-II stellarator. *Nucl. Fusion*, 52(6):063010, 2012.

[10] J.A. Alonso, S.J. Zweben, P. Carvalho, J.L. de Pablos, E. de la Cal, C. Hidalgo, T. Klinger, B.Ph. van Milligen, R.J. Maqueda, and M.A. et al. Pedrosa. Impact of different confinement regimes on the two-dimensional structure of edge turbulence. *Plasma Phys. Control. Fusion*, 48(12B):B465, 2006.

[11] V. Antoni, V. Carbone, E. Martines, G. Regnoli, G. Serianni, N. Vianello, and P. Veltri. Electrostatic turbulence intermittency and MHD relaxation phenomena in a rfp plasma. *EPL (Europhysics Letters)*, 54(1):51, 2001.

[12] E. Ascasíbar, D. Alba, D. Alegre, A. Alonso, J. Alonso, F. de Aragón, A. Baciero, J.M. Barcala, E. Blanco, J. Botija, L. Bueno, S. Cabrera, E. de la Cal, I. Calvo, A. Cappa, D. Carralero, R. Carrasco, B. Carreras, F. Castejón, R. Castro, A. de Castro, G. Catalán, A.A. Chmyga, M. Chamorro, A.W. Cooper, A. Dinklage, L. Eliseev, T. Estrada, M. Ezzat, F. Fernández-Marina, J.M. Fontdecaba, L. García, I. García-Cortés, R. García-Gómez, J.M. García-Regaña, A. González-Jerez, and G. Grenfell et al. Overview of recent TJ-II stellarator results. *Nucl. Fusion*, 2019.

[13] E. Ascasíbar, T. Estrada, M. Liniers, M.A. Ochando, F.L. Tabarés, D. Tafalla, J. Guasp, R. Jiménez-Gömez, F. Castejön, and D. et al. Löpez-Bruna. Global Energy Confinement Studies in TJ-II NBI Plasmas. *Contributions to Plasma Physics*, 50(6-7):594–599, 2010.

[14] P. Bak, C. Tang, and K. Wiesenfeld. Self-organized criticality: An explanation of the 1/f noise. *Phys. Rev. Lett.*, 59(4):381, 1987.

[15] R. Balescu. *Aspects of anomalous transport in plasmas*. CRC Press, 2005.

[16] M. Baruzzo, T. Bolzonella, Y.Q. Liu, G. Manduchi, G. Marchiori, A. Soppelsa, M. Takechi, and F. Villone. RWM control studies on RFX-mod with a limited set of active coils. *Nucl. fusion*, 52(10):103001, 2012.

[17] J.M. Beall, Y.C. Kim, and E.J. Powers. Estimation of wavenumber and frequency spectra using fixed probe pairs. *Journal of Applied Physics*, 53(6):3933–3940, 1982.

[18] J.S. Bendat and A.G. Piersol. *Random data: analysis and measurement procedures*, volume 729. John Wiley & Sons, 2011.

[19] M. Bessenrodt-Weberpals, F. Wagner, O. Gehre, L. Giannone, J.V. Hofmann, A. Kallenbach, K. McCormick, V. Mertens, H.D. Murmann, and F. et al. Ryter. The isotope effect in ASDEX. *Nucl. Fusion*, 33(8):1205, 1993.

[20] P. Beyer, S. Benkadda, X. Garbet, and P.H. Diamond. Nondiffusive transport in tokamaks: Three-dimensional structure of bursts and the role of zonal flows. *Phys. Rev. Lett.*, 85(23):4892, 2000.

[21] H. Biglari, P.H. Diamond, and P.W. Terry. Influence of sheared poloidal rotation on edge turbulence. *Phys. Fluids B: Plasma Physics*, 2(1):1–4, 1990.

[22] N. Bisai, S. Banerjee, and A. Sen. A universal mechanism for plasma blob formation. *Phys. Plasmas*, 26(2):020701, 2019.

[23] N. Bisai, A. Das, S. Deshpande, R. Jha, P. Kaw, A. Sen, and R. Singh. Edge and scrape-off layer tokamak plasma turbulence simulation using two-field fluid model. *Phys. Plasmas*, 12(7):072520, 2005.

[24] N. Bisai, A. Das, S. Deshpande, R. Jha, P. Kaw, A. Sen, and R. Singh. Edge and scrape-off layer tokamak plasma turbulence simulation using two-field fluid model. *Phys. Plasmas*, 12(7):072520, 2005.

[25] J.A. Bittencourt. *Fundamentals of plasma physics*. Springer Science & Business Media, 2013.

[26] J. Boedo, D. Gray, S. Jachmich, R. Conn, G.P. Terry, G. Tynan, G. Van Oost, R.R. Weynants, and Textor Team et al. Enhanced particle confinement and turbulence reduction due to E× B shear in the TEXTOR tokamak. *Nucl. Fusion*, 40(7):1397, 2000.

[27] A. Burckhart, E. Wolfrum, R. Fischer, K. Lackner, and H. et al. Zohm. Inter-ELM behaviour of the electron density and temperature pedestal in ASDEX Upgrade. *Plasma Phys. Controll. Fusion*, 52(10):105010, 2010.

[28] K.H. Burrell. Effects of E× B velocity shear and magnetic shear on turbulence and transport in magnetic confinement devices. *Phys. Plasmas*, 4(5):1499–1518, 1997.

[29] K.H. Burrell. Tests of causality: Experimental evidence that sheared e× b flow alters turbulence and transport in tokamaks. *Phys. Plasmas*, 6(12):4418–4435, 1999.

[30] J.D. Callen and M.W. Kissick. Evidence and concepts for non-local transport. *Plasma Phys. Controll. Fusion*, 39(12B):B173, 1997.

[31] Y. Camenen, Y. Idomura, S. Jolliet, and A.G. Peeters. Consequences of profile shearing on toroidal momentum transport. *Nucl. Fusion*, 51(7):073039, 2011.

[32] S. Cappello. Bifurcation in the MHD behaviour of a self-organizing system: the reversed field pinch (RFP). *Plasma Phys. Controll. Fusion*, 46(12B):B313, 2004.

[33] S. Cappello, D. Bonfiglio, and D.F. Escande. Magnetohydrodynamic dynamo in reversed field pinch plasmas: Electrostatic drift nature of the dynamo velocity field. *Phys. Plasmas*, 13(5):056102, 2006.

[34] V. Carbone, G. Regnoli, E. Martines, and V. Antoni. Intermittency and self-similarity in plasma edge fluctuations. *Phys Plasmas*, 7(2):445–447, 2000.

[35] D. Carralero, G. Birkenmeier, H.W. Müller, P. Manz, P. DeMarne, S.H. Müller, F. Reimold, U. Stroth, M. Wischmeier, and E. et al. Wolfrum. An experimental investigation of the high density transition of the scrape-off layer transport in ASDEX Upgrade. *Nucl. Fusion*, 54(12):123005, 2014.

[36] D. Carralero, P. Manz, L. Aho-Mantila, G. Birkenmeier, M. Brix, M. Groth, H.W. Müller, U. Stroth, N. Vianello, and E. et al. Wolfrum. Experimental validation of a filament transport model in turbulent magnetized plasmas. *Phys. Rev. Lett.*, 115(21):215002, 2015.

[37] D. Carralero, M. Siccinio, M. Komm, S.A. Artene, F.A. Disa, J. Adamek, L. Aho-Mantila, G. Birkenmeier, M. Brix, and G. et al. Fuchert. Recent progress towards a quantitative description of filamentary SOL transport. *Nucl. Fusion*, 57(5):056044, 2017.

[38] L. Carraro, E. Casarotto, R. Pasqualotto, M.E. Puiatti, P. Scarin, and M. Valisa. Impurity influx diagnostics on RFX. *Rev. Sci. Instrum.*, 66(1):610–612, 1995.

[39] B.A. Carreras, V.E. Lynch, D.E. Newman, R. Balbın, J. Bleuel, M.A. Pedrosa, M. Endler, B. van Milligen, E. Sánchez, and C. Hidalgo. Intermittency of plasma edge fluctuation data: Multifractal analysis. *Phys. Plasmas*, 7(8):3278–3287, 2000.

[40] B.A. Carreras, B.Ph. Van Milligen, M.A. Pedrosa, R. Balbın, C. Hidalgo, D.E. Newman, E. Sanchez, M. Frances, I. Garcıa-Cortés, and J. et al. Bleuel. Self-similarity of the plasma edge fluctuations. *Phys. Plasmas*, 5(10):3632–3643, 1998.

[41] T.A. Carter. Intermittent turbulence and turbulent structures in a linear magnetized plasma. *Phys. plasmas*, 13(1):010701, 2006.

[42] C.S. Chang, S. Ku, A. Loarte, V. Parail, F. Koechl, M. Romanelli, R. Maingi, J.-W. Ahn, T. Gray, and J. et al. Hughes. Gyrokinetic projection of the divertor heat-flux width from present tokamaks to ITER. *Nucl. Fusion*, 57(11):116023, 2017.

[43] B. Chen, X.Q. Xu, T.Y. Xia, N.M. Li, M. Porkolab, E. Edlund, B. LaBombard, J. Terry, J.W. Hughes, and M.Y. et al. Ye. Progress towards modeling tokamak boundary plasma turbulence and understanding its role in setting divertor heat flux widths. *Phys. Plasmas*, 25(5):055905, 2018.

[44] L. Chen, R.B. White, and F. Zonca. Zonal-flow dynamics and size scaling of anomalous transport. *Phys. Rev. Lett.*, 92(7):075004, 2004.

[45] J. Cheng, L.W. Yan, W.Y. Hong, K.J. Zhao, T. Lan, J. Qian, A.D. Liu, H.L. Zhao, Y. Liu, and Q.W. et al. Yang. Statistical characterization of blob turbulence across the separatrix in HL-2A tokamak. *Plasma Phys. Control. Fusion*, 52(5):055003, 2010.

[46] M.J. Choi, J. Kim, J.-M. Kwon, H.K. Park, Y. In, W. Lee, K.D. Lee, G.S. Yun, J. Lee, and M. et al. Kim. Multiscale interaction between a large scale magnetic island and small scale turbulence. *Nucl. Fusion*, 57(12):126058, 2017.

[47] C.K. Chui. *An introduction to wavelets*. Elsevier, 2016.

[48] R.M. Churchill, C.S. Chang, S. Ku, and J. Dominski. Pedestal and edge electrostatic turbulence characteristics from an XGC1 gyrokinetic simulation. *Plasma Phys. Control. Fusion*, 59(10):105014, 2017.

[49] J. Citrin, F. Jenko, P. Mantica, D. Told, C. Bourdelle, R. Dumont, J. Garcia, J.W. Haverkort, G.M.D. Hogeweij, and T. et al. Johnson. Ion temperature profile stiffness: non-linear gyrokinetic simulations and comparison with experiment. *Nucl. Fusion*, 54(2):023008, 2014.

[50] J.W. Connor. Edge-localized modes-physics and theory. *Plasma Phys. Control. Fusion*, 40(5):531, 1998.

[51] J.W. Connor, A. Kirk, and H.R. Wilson. Edge localised modes (ELMs): Experiments and theory. In *AIP Conference Proceedings*, volume 1013, pages 174–190. AIP, 2008.

[52] J. Cornelis, R. Sporken, G. Van Oost, and R.R. Weynants. Predicting the radial electric field imposed by externally driven radial currents in tokamaks. *Nucl. fusion*, 34(2):171, 1994.

[53] S.C. Cowley, H. Wilson, O. Hurricane, and B. Fong. Explosive instabilities: from solar flares to edge localized modes in tokamaks. *Plasma Phys. Control. Fusion*, 45(12A):A31, 2003.

[54] E. De la Cal, P. Semwal, A. Martín Aguilera, B. van Milligen, J.L. de Pablos, Z. Khan, and C. Hidalgo. Double imaging with an intensified visible fast camera to visualize the fine structure of turbulent coherent plasma structures (blobs) in TJ-II. *Plasma Phys. Control. Fusion*, 56(10):105003, 2014.

[55] P. Deichuli, V. Davydenko, V. Belov, A. Gorbovsky, A. Dranichnikov, A. Ivanov, A. Sorokin, V. Mishagin, A. Abdrashitov, and V. et al. Kolmogorov. Commissioning of heating neutral beams for COMPASS-D tokamak. *Rev. Sci. Instrum.*, 83(2):02B114, 2012.

[56] A. Diallo, J. Dominski, K. Barada, M. Knolker, G.J. Kramer, and G. McKee. Direct observation of nonlinear coupling between pedestal modes leading to the onset of edge localized modes. *Phys. Rev. Lett.*, 121(23):235001, 2018.

[57] A. Diallo, R.J. Groebner, T.L. Rhodes, D.J. Battaglia, D.R. Smith, T.H. Osborne, J.M. Canik, W. Guttenfelder, and P.B. Snyder. Correlations between quasi-coherent fluctuations and the pedestal evolution during the inter-edge localized modes phase on DIII-D. *Phys. Plasmas*, 22(5):056111, 2015.

[58] P.H. Diamond, S.-I Itoh, and K. Itoh. *Modern Plasma Physics: Volume 1, Physical Kinetics of Turbulent Plasmas*. Cambridge University Press, 2010.

[59] P.H. Diamond, S.I. Itoh, K. Itoh, and T.S. Hahm. Zonal flows in plasmaa review. *Plasma Phys. Control. Fusion*, 47(5):R35, 2005.

[60] P.H. Diamond and Y.-B. Kim. Theory of mean poloidal flow generation by turbulence. *Phys. Fluids B: Plasma Physics*, 3(7):1626–1633, 1991.

[61] A. Dinklage, C.D. Beidler, P. Helander, G. Fuchert, H. Maassberg, K. Rahbarnia, T.S. Pedersen, Y. Turkin, R.C. Wolf, and A. et al. Alonso. Magnetic configuration effects on the wendelstein 7-x stellarator. *Nature Physics*, 14(8):855, 2018.

[62] A. Dinklage, T. Klinger, G. Marx, and L. Schweikhard. Confinement, transport and collective effects, 2005.

[63] D.A. Dippolito, J.R. Myra, and S.J. Zweben. Convective transport by intermittent blob-filaments: Comparison of theory and experiment. *Phys. Plasmas*, 18(6):060501, 2011.

[64] T. Dudok de Wit, A.-L. Pecquet, J.-C. Vallet, and R. Lima. The biorthogonal decomposition as a tool for investigating fluctuations in plasmas. *Phys. Plasmas*, 1(10):3288–3300, 1994.

[65] L. Easy, F. Militello, J. Omotani, B. Dudson, E. Havlíčková, P. Tamain, V. Naulin, and A.H. Nielsen. Three dimensional simulations of plasma filaments in the scrape off layer: A comparison with models of reduced dimensionality. *Phys. Plasmas*, 21(12):122515, 2014.

[66] T. Eich, A. Herrmann, J. Neuhauser, R. Dux, J.C. Fuchs, S. Günter, L.D. Horton, A. Kallenbach, P.T. Lang, and C.F. et al. Maggi. Type-I ELM substructure on the divertor target plates in ASDEX Upgrade. *Plasma Phys. Control. Fusion*, 47(6):815, 2005.

[67] T. Eich, A.W. Leonard, R.A. Pitts, W. Fundamenski, R.J. Goldston, T.K. Gray, A. Herrmann, A. Kirk, A. Kallenbach, and O. et al. Kardaun. Scaling of the tokamak near the scrape-off layer h-mode power width and implications for ITER. *Nucl. fusion*, 53(9):093031, 2013.

[68] T. Eich, B. Sieglin, A. Scarabosio, W. Fundamenski, R.J. Goldston, and A. Herrmann. Inter-ELM power decay length for JET and ASDEX upgrade: measurement and comparison with heuristic drift-based model. *Phys. Rev. Lett.*, 107(21):215001, 2011.

[69] V. Erckmann, F. Wagner, J. Baldzuhn, R. Brakel, R. Burhenn, U. Gasparino, P. Grigull, H.J. Hartfuss, J.V. Hofmann, and R. et al. Jaenicke. H mode of the W 7-AS stellarator. *Phys. Rev. Lett.*, 70(14):2086, 1993.

[70] D.F. Escande, R. Paccagnella, S. Cappello, C. Marchetto, and F. D'Angelo. Chaos healing by separatrix disappearance and quasisingle helicity states of the reversed field pinch. *Phys. Rev. Lett.*, 85(15):3169, 2000.

[71] T. Estrada, T. Happel, L. Eliseev, D. López-Bruna, E. Ascasíbar, E. Blanco, L. Cupido, J.M. Fontdecaba, C. Hidalgo, and R. et al. Jiménez-Gómez. Sheared flows and transition to improved confinement regime in the TJ-II stellarator. *Plasma Phys. Controll. Fusion*, 51(12):124015, 2009.

[72] T. Estrada, C. Hidalgo, and T. Happel. Signatures of turbulence spreading during the H–L back-transition in TJ-II plasmas. *Nucl. Fusion*, 51(3):032001, 2011.

[73] M. Farge. Wavelet transforms and their applications to turbulence. *Annual review of fluid mechanics*, 24(1):395–458, 1992.

[74] G. Federici, A. Loarte, and G. Strohmayer. Assessment of erosion of the ITER divertor targets during type I ELMs. *Plasma Phys. Control. Fusion*, 45(9):1523, 2003.

[75] N. Fedorczak, Ph. Ghendrih, P. Hennequin, G.R. Tynan, P.H. Diamond, and P. Manz. Dynamics of tilted eddies in a transversal flow at the edge of tokamak plasmas and the consequences for L–H transition. *Plasma Phys. Control. Fusion*, 55(12):124024, 2013.

[76] N. Fedorczak, J.P. Gunn, J.-Y. Pascal, Ph. Ghendrih, G. Van Oost, P. Monier-Garbet, and G.R. Tynan. Electrostatic transport in L-mode scrape-off layer plasmas of Tore Supra tokamak. II. Transport by fluctuations. *Phys. Plasmas*, 19(7):072314, 2012.

[77] N. Fedorczak, P. Manz, S.C. Thakur, M. Xu, and G.R. Tynan. Zonal flow shear amplification by depletion of anisotropic potential eddies in a magnetized plasma: idealized models and laboratory experiment. *Plasma Phys. Controll. Fusion*, 55(2):025011, 2013.

[78] N. Fedorczak, P. Manz, S.C. Thakur, M. Xu, G.R. Tynan, G.S. Xu, and S.C. Liu. On physical interpretation of two dimensional time-correlations regarding time delay velocities and eddy shaping. *Phys. Plasmas*, 19(12):122302, 2012.

[79] A. Fernández, A. Cappa, F. Castejon, J.M. Fontdecaba, and K. Nagasaki. ECCD experiments in the TJ-II stellarator. *Fusion Science and Technology*, 53(1):254–260, 2008.

[80] S.J. Fielding, J.D. Ashall, P.G. Carolan, A. Colton, D. Gates, J. Hugill, A.W. Morris, and M. et al. Valovic. The H-mode in COMPASS-D. *Plasma Phys. Control. Fusion*, 38(8):1091, 1996.

[81] J.M. Finn and L. Chacón. Volume preserving integrators for solenoidal fields on a grid. *Phys. Plasmas*, 12(5):054503, 2005.

[82] J.P. Freidberg. *Plasma physics and fusion energy*. Cambridge university press, 2008.

[83] U. Frisch and A.N. Kolmogorov. *Turbulence: the legacy of AN Kolmogorov*. Cambridge university press, 1995.

[84] J.C. Fuchs, T. Eich, A. Herrmann, K.F. Mast, and Team, The ASDEX Upgrade. Radiation distribution and energy balance during type-i ELMs in ASDEX upgrade. *Journal of nuclear materials*, 337:756–760, 2005.

[85] A. Fujisawa. A review of zonal flow experiments. *Nucl. Fusion*, 49(1):013001, 2008.

[86] W. Fundamenski and R.A. et al. Pitts. A model of ELM filament energy evolution due to parallel losses. *Plasma Phys. Controll. Fusion*, 48(1):109, 2005.

[87] I. Furno, M. Spolaore, C. Theiler, N. Vianello, R. Cavazzana, and A. Fasoli. Direct two-dimensional measurements of the field-aligned current associated with plasma blobs. *Phys. Rev. Lett.*, 106(24):245001, 2011.

[88] I. Furno, C. Theiler, D. Lançon, A. Fasoli, D. Iraji, P. Ricci, M. Spolaore, and N. Vianello. Blob current structures in TORPEX plasmas: experimental measurements and numerical simulations. *Plasma Phys. Controll. Fusion*, 53(12):124016, 2011.

[89] X. Gao, T. Zhang, X. Han, S.B. Zhang, D.F. Kong, H. Qu, Y.M. Wang, F. Wen, Z.X. Liu, and C.B. Huang. Experimental study of pedestal turbulence on EAST tokamak. *Nucl. Fusion*, 55(8):083015, 2015.

[90] X. Garbet, L. Laurent, A. Samain, and J. Chinardet. Radial propagation of turbulence in tokamaks. *Nucl. Fusion*, 34(7):963, 1994.

[91] O.E. Garcia, N.H. Bian, and W. Fundamenski. Radial interchange motions of plasma filaments. *Phys. Plasmas*, 13(8):082309, 2006.

[92] O.E. Garcia, R. Kube, A. Theodorsen, and H.L. Pécseli. Stochastic modelling of intermittent fluctuations in the scrape-off layer: Correlations, distributions, level crossings, and moment estimation. *Phys. Plasmas*, 23(5):052308, 2016.

[93] I. García-Cortés, E. de la Luna, F. Castejón, J.A. Jiménez, E. Ascasíbar, B. Brañas, T. Estrada, J. Herranz, A. López-Fraguas, and I. et al. Pastor. Edge-localized-mode-like events in the TJ-II stellarator. *Nucl. Fusion*, 40(11):1867, 2000.

[94] K.W. Gentle, W.L. Rowan, R.V. Bravenec, G. Cima, T.P. Crowley, H. Gasquet, G.A. Hallock, J. Heard, A. Ouroua, and P.E. et al. Phillips. Strong nonlocal effects in a tokamak perturbative transport experiment. *Phys. Rev. Lett.*, 74(18):3620, 1995.

[95] Ph. Ghendrih, G. Ciraolo, Y. Larmande, Y. Sarazin, P. Tamain, P. Beyer, G. Chiavassa, G. Darmet, X. Garbet, and V. Grandgirard. Shearing effects on density burst propagation in SOL plasmas. *Journal of Nuclear Materials*, 390:425–427, 2009.

[96] Ph. Ghendrih, Y. Sarazin, G. Ciraolo, G. Darmet, X. Garbet, V. Grangirard, P. Tamain, S. Benkadda, and P. Beyer. Transport barrier fluctuations governed by SOL turbulence spreading. *J. Nucl. Mat.*, 363:581–585, 2007.

[97] Robert James Goldston. Heuristic drift-based model of the power scrape-off width in low-gas-puff H-mode tokamaks. *Nucl. Fusion*, 52(1):013009, 2011.

[98] D.H.J. Goodall. High speed cine film studies of plasma behaviour and plasma surface interactions in tokamaks. *Journal of Nuclear Materials*, 111:11–22, 1982.

[99] N.N. Gorelenkov, S.D. Pinches, and K. Toi. Energetic particle physics in fusion research in preparation for burning plasma experiments. *Nucl. Fusion*, 54(12):125001, 2014.

[100] M. Greenwald. Density limits in toroidal plasmas. *Plasma Phys. Control. Fusion*, 44(8):R27, 2002.

[101] G. Grenfell, I.C. Nascimento, D.S. Oliveira, Z.O. Guimarães-Filho, J.I. Elizondo, A.P. Reis, R.M.O. Galvão, W.A.H. Baquero, A.M. Oliveira, and G. et al. Ronchi. H-mode access and the role of spectral shift with electrode biasing in the TCABR tokamak. *Phys. Plasmas*, 25(7):072301, 2018.

[102] G. Grenfell, B.Ph. van Milligen, U. Losada, T. Estrada, B. Liu, C. Silva, M. Spolaore, and C. Hidalgo and. The impact of edge radial electric fields on edge–scrape-off layer coupling in the TJ-II stellarator. *Nucl. Fusion*, 60(1):014001, nov 2019.

[103] G. Grenfell, B.Ph. van Milligen, U. Losada, W. Ting, B. Liu, C. Silva, M. Spolaore, and C. et al. Hidalgo. Measurement and control of turbulence spreading in the scrape-off layer of TJ-II stellarator. *Nucl. Fusion*, 59(1):016018, 2018.

[104] Z. Guo, L. Chen, and F. Zonca. Radial Spreading of Drift-Wave–Zonal-Flow Turbulence via Soliton Formation. *Phys. Rev. Lett.*, 103(5):055002, 2009.

[105] Ö.D. Gürcan, P.H. Diamond, and T.S. Hahm. Radial transport of fluctuation energy in a two-field model of drift-wave turbulence. *Phys. Plasmas*, 13(5):052306, 2006.

[106] Ö.D. Gürcan, P.H. Diamond, T.S. Hahm, and Z. Lin. Dynamics of turbulence spreading in magnetically confined plasmas. *Phys. Plasmas*, 12(3):032303, 2005.

[107] T.S. Hahm and K.H. Burrell. Flow shear induced fluctuation suppression in finite aspect ratio shaped tokamak plasma. *Phys. Plasmas*, 2(5):1648–1651, 1995.

[108] T.S. Hahm and P.H. Diamond. Mesoscopic transport events and the breakdown of Ficks law for turbulent fluxes. *Journal of the Korean Physical Society*, 73(6):747–792, 2018.

[109] T.S. Hahm, P.H. Diamond, Z. Lin, K. Itoh, and S.I. Itoh. Turbulence spreading into the linearly stable zone and transport scaling. *Plasma Phys. Controll. Fusion*, 46(5A):A323, 2004.

[110] F. Hariri, V. Naulin, J. Rasmussen, G.S. Xu, and N. Yan. Cold pulse and rotation reversals with turbulence spreading and residual stress. *Phys. Plasmas*, 23(5):052512, 2016.

[111] A. Hasegawa and M. Wakatani. Self-organization of electrostatic turbulence in a cylindrical plasma. *Phys. Rev. Lett.*, 59(14):1581, 1987.

[112] P. Helander, C.D. Beidler, T.M. Bird, M. Drevlak, Y. Feng, R. Hatzky, F. Jenko, R. Kleiber, J.H.E. Proll, and Y. et al. Turkin. Stellarator and tokamak plasmas: a comparison. *Plasma Phys. Control. Fusion*, 54(12):124009, 2012.

[113] H.W. Hendel, T.K. Chu, and P.A. Politzer. Collisional drift wavesidentification, stabilization, and enhanced plasma transport. *The Physics of Fluids*, 11(11):2426–2439, 1968.

[114] W.A. Hernandez, Z.O. Guimarães-Filho, G.G. Grenfell, and I.C. Nascimento. Spatial inhomogeneity effects on burst temperature estimation using a triple probe configuration in Tokamak Chauffage Alfvén Brésilien tokamak. *Journal of Plasma Physics*, 85(4), 2019.

[115] C. Hidalgo, B. Goncalves, M.A. Pedrosa, C. Silva, R. Balbın, M. Hron, A. Loarte, K. Erents, G.F. Matthews, and R. Pitts. Experimental evidence of fluctuations and flows near marginal stability and dynamical interplay between gradients and transport in the JET plasma boundary region. *Journal of Nuclear Materials*, 313:863–867, 2003.

[116] C. Hidalgo, M.A. Pedrosa, N. Dreval, K.J. McCarthy, L. Eliseev, M.A. Ochando, T. Estrada, I. Pastor, E. Ascasíbar, E. Calderón, A. Cappa, A.A. Chmyga, A. Fernández, B. Gonçalves, J. Hernanz, J.A. Jiménez, S.M. Khrebtov, A.D. Komarov, A.S. Kozachok, L. Krupnik, A. López-Fraguas, A. López-Sánchez, A.V. Melnikov, F. Medina, B. van Milligen, C. Silva, F. Tabarés, and D. Tafalla. Improved confinement regimes induced by limiter biasing in the TJ-II stellarator. *Plasma Phys. Control. Fusion*, 46(1):287, 2004.

[117] C. Hidalgo, M.A. Pedrosa, L. García, and A. Ware. Experimental evidence of coupling between sheared-flow development and an increase in the level of turbulence in the TJ-II stellarator. *Phys. Rev. E*, 70(6):067402, 2004.

[118] M. Hirsch, P. Grigull, H. Wobig, J. Kisslinger, K. McCormick, M. Anton, J. Baldzuhn, S. Fiedler, Ch. Fuchs, and J. et al. Geiger. Operational conditions

and characteristics of ELM-events during h-mode plasmas in the stellarator W7-AS. *Plasma Phys. Control. Fusion*, 42(5A):A231, 2000.

[119] C. Holland, L. Schmitz, T.L. Rhodes, W.A. Peebles, J.C. Hillesheim, G. Wang, L. Zeng, E.J. Doyle, S.P. Smith, and R. et al. Prater. Advances in validating gyrokinetic turbulence models against L-and H-mode plasmas. *Phys. Plasmas*, 18(5):056113, 2011.

[120] C. Holland, A.E. White, G.R. McKee, M.W. Shafer, J. Candy, R.E. Waltz, L. Schmitz, and G.R. Tynan. Implementation and application of two synthetic diagnostics for validating simulations of core tokamak turbulence. *Phys. Plasmas*, 16(5):052301, 2009.

[121] J. Horacek, R.A. Pitts, J. Adamek, G. Arnoux, J.-G. Bak, S. Brezinsek, M. Dimitrova, R.J. Goldston, J.P. Gunn, J. Havlicek, S.-H. Hong, F. Janky, B. LaBombard, S. Marsen, G. Maddaluno, L. Nie, V. Pericoli, Tsv Popov, R. Panek, D. Rudakov, J. Seidl, D.S. Seo, M. Shimada, C. Silva, P.C. Stangeby, B. Viola, P. Vondracek, H. Wang, G.S. Xu, Y. Xu, and JET Contributors. Multi-machine scaling of the main SOL parallel heat flux width in tokamak limiter plasmas. *Plasma Phys. Control. Fusion*, 58(7):074005, 2016.

[122] W. Horton. Drift waves and transport. *Reviews of Modern Physics*, 71(3):735, 1999.

[123] M. Hron, F. Janky, J. Pipek, J. Sousa, B.B. Carvalho, H. Fernandes, P. Vondracek, P. Cahyna, J. Urban, and R. et al. Paprok. Overview of the COMPASS CODAC system. *Fusion Engineering and Design*, 89(3):177–185, 2014.

[124] G.T.A. Huijsmans and A. Loarte. Non-linear MHD simulation of ELM energy deposition. *Nucl. Fusion*, 53(12):123023, 2013.

[125] T. Huld, A.H. Nielsen, H.L. Pécseli, and J.J. Rasmussen. Coherent structures in two-dimensional plasma turbulence. *Phys. Fluids B: Plasma Physics*, 3(7):1609–1625, 1991.

[126] I.H. Hutchinson. Principles of plasma diagnostics. *Plasma Phys. Control. Fusion*, 44(12):2603, 2002.

[127] K. Ida, T. Kobayashi, M. Ono, T.E. Evans, G.R. McKee, and M.E. Austin. Hysteresis relation between turbulence and temperature modulation during the heat pulse propagation into a magnetic island in DIII-D. *Phys. Rev. Lett.*, 120(24):245001, 2018.

[128] K. Ida, Z. Shi, H.J. Sun, S. Inagaki, K. Kamiya, J.E. Rice, N. Tamura, P.H. Diamond, G. Dif-Pradalier, and X.L. et al. Zou. Towards an emerging understanding of non-locality phenomena and non-local transport. *Nucl. Fusion*, 55(1):013022, 2015.

[129] S. Inagaki, N. Tamura, T. Tokuzawa, K. Ida, K. Itoh, S.V. Neudatchin, K. Tanaka, Y. Nagayama, K. Kawahata, and M. et al. Yakovlev. Abrupt reduction of core electron heat transport in response to edge cooling on the Large Helical Device. *Plasma Phys. Controll. fusion*, 48(5A):A251, 2006.

[130] A. Ishizawa and N. Nakajima. Thermal transport due to turbulence including magnetic fluctuation in externally heated plasma. *Nucl. Fusion*, 49(5):055015, 2009.

[131] S.-I Itoh and K. Itoh. Model of L to H-mode transition in tokamak. *Phys. Rev. Lett.*, 60(22):2276, 1988.

[132] H. Johnsen, H.L. Pécseli, and J. Trulsen. Conditional eddies in plasma turbulence. *The Physics of fluids*, 30(7):2239–2254, 1987.

[133] E.O. Johnson and L. Malter. A floating double probe method for measurements in gas discharges. *Phys. Rev.*, 80(1):58, 1950.

[134] B.B. Kadomtsev. Plasma turbulence. *New York: Academic Press, 1965*, 1965.

[135] A. Kallenbach, M. Bernert, M. Beurskens, L. Casali, M. Dunne, T. Eich, L. Giannone, A. Herrmann, M. Maraschek, and S. et al. Potzel. Partial detachment of high power discharges in ASDEX Upgrade. *Nucl. Fusion*, 55(5):053026, 2015.

[136] K. Kamiya, H. Kimura, H. Ogawa, H. Kawashima, K. Tsuzuki, M. Sato, Y. Miura, and JFT-2M group et al. Observation of high recycling steady h-mode edge and compatibility with improved core confinement mode on JFT-2M. *Nucl. Fusion*, 43(10):1214, 2003.

[137] H. Kantz and T. Schreiber. *Nonlinear time series analysis*, volume 7. Cambridge university press, 2004.

[138] S.M. Kaye, F.M. Levinton, D. Stutman, K. Tritz, H. Yuh, M.G. Bell, R.E. Bell, C.W. Domier, D. Gates, and W. et al. Horton. Confinement and local transport in the National Spherical Torus Experiment (NSTX). *Nucl. Fusion*, 47(7):499, 2007.

[139] E.-j. Kim and P.H. Diamond. Zonal flows and transient dynamics of the L- H transition. *Phys. Rev. Lett.*, 90(18):185006, 2003.

[140] A. Kirk, H.R. Wilson, G.F. Counsell, R. Akers, E. Arends, S.C. Cowley, J. Dowling, B. Lloyd, M. Price, and M. et al. Walsh. Spatial and temporal structure of edge-localized modes. *Phys. Rev. Lett.*, 92(24):245002, 2004.

[141] Y. Kishimoto, T. Tajima, W. Horton, M.J. LeBrun, and J.Y. Kim. Theory of self-organized critical transport in tokamak plasmas. *Phys. Plasmas*, 3(4):1289–1307, 1996.

[142] D.F. Kong, X.Q. Xu, P.H. Diamond, J.G. Chen, C.B. Huang, T. Lan, X. Gao, and J.G. et al. Li. E× B flow shear mitigates ballooning-driven edge-localized modes at high collisionality: experiment and simulation. *Nucl. Fusion*, 59(1):016016, 2018.

[143] M. Kotschenreuther, D.R. Hatch, S. Mahajan, P. Valanju, L. Zheng, and X. Liu. Pedestal transport in H-mode plasmas for fusion gain. *Nucl. Fusion*, 57(6):064001, 2017.

[144] K. Kovarik, I. Duran, J. Stockel, J. Seidl, J. Adamek, M. Spolaore, N. Vianello, P. Hacek, M. Hron, and R. Panek. Filamentary probe on the COMPASS tokamak. *Rev. Sci. Instrum.*, 88(3):035106, 2017.

[145] S.I. Krasheninnikov. On scrape off layer plasma transport. *Physics Letters A*, 283(5-6):368–370, 2001.

[146] S.I. Krasheninnikov, D.A. D'ippolito, and J.R. Myra. Recent theoretical progress in understanding coherent structures in edge and SOL turbulence. *Journal of Plasma Physics*, 74(5):679–717, 2008.

[147] O. Kudlacek, P. Zanca, C. Finotti, G. Marchiori, R. Cavazzana, and L. Marrelli. Real time measurement of plasma macroscopic parameters on RFX-mod using a limited set of sensors. *Phys. Plasmas*, 22(10):102503, 2015.

[148] A.S. Kukushkin, H.D. Pacher, G.W. Pacher, V. Kotov, R.A. Pitts, and D. Reiter. Consequences of a reduction of the upstream power sol width in ITER. *Journal of Nuclear Materials*, 438:S203–S207, 2013.

[149] S.T.A. Kumar, D.J. Den Hartog, V.V. Mirnov, K.J. Caspary, R.M. Magee, D.L. Brower, B.E. Chapman, D. Craig, W.X. Ding, and S. et al. Eilerman. Classical confinement and outward convection of impurity ions in the MST RFP. *Phys. Plasmas*, 19(5):056121, 2012.

[150] Yu.K. Kuznetsov, I.C. Nascimento, C. Silva, H. Figueiredo, Z.O. Guimarães-Filho, I.L. Caldas, R.M.O. Galvão, J.H.F. Severo, D.L. Toufen, and L.F. et al. Ruchko. Long-distance correlations in TCABR biasing experiments. *Nucl. Fusion*, 52(6):063004, 2012.

[151] B. LaBombard, T. Golfinopoulos, J.L. Terry, D. Brunner, E. Davis, M. Greenwald, J.W. Hughes, and Alcator C-Mod Team. New insights on boundary plasma turbulence and the quasi-coherent mode in Alcator C-Mod using a Mirror Langmuir Probe. *Phys. Plasmas*, 21(5):056108, 2014.

[152] F.M. Laggner, A. Diallo, M. Cavedon, and E. Kolemen. Inter-ELM pedestal localized fluctuations in tokamaks: Summary of multi-machine observations. *Nuclear Materials and Energy*, 19:479–486, 2019.

[153] A.W. Leonard. Edge-localized-modes in tokamaks. *Phys. Plasmas*, 21(9):090501, 2014.

[154] Z.-Y. Li, X.Q. Xu, N.-M. Li, V.S. Chan, and X.-G. Wang. Prediction of divertor heat flux width for ITER using BOUT++ transport and turbulence module. *Nucl. Fusion*, 59(4):046014, 2019.

[155] C.-C. Lin. On Taylors hypothesis and the acceleration terms in the Navier-Stokes equation. *Quarterly of Applied Mathematics*, 10(4):295–306, 1953.

[156] Z. Lin, S. Ethier, T.S. Hahm, and W.M. Tang. Size scaling of turbulent transport in magnetically confined plasmas. *Phys. Rev. Lett.*, 88(19):195004, 2002.

[157] Z. Lin and T.S. Hahm. Turbulence spreading and transport scaling in global gyrokinetic particle simulations. *Phys. Plasmas*, 11(3):1099–1108, 2004.

[158] A. Loarte, J.W. Hughes, M.L. Reinke, J.L. Terry, B. LaBombard, D. Brunner, M. Greenwald, B. Lipschultz, Y. Ma, and S. et al. Wukitch. High confinement/high radiated power H-mode experiments in alcator c-mod and consequences for international thermonuclear experimental reactor (ITER) QDT= 10 operation. *Phys. Plasmas*, 18(5):056105, 2011.

[159] A. Loarte, B. Lipschultz, and A.S. Kukushkin. Power and particle control [Progress in the ITER Physics Basis (PIPB)]. *Nucl. Fusion*, 47(6):S203–S263, 2007.

[160] A. Loarte, G. Saibene, R. Sartori, D. Campbell, M. Becoulet, L. Horton, T. Eich, A. Herrmann, G. Matthews, and N. et al. Asakura. Characteristics of type i ELM energy and particle losses in existing devices and their extrapolation to iter. *Plasma Phys. Control. Fusion*, 45(9):1549, 2003.

[161] R. Lorenzini, D. Terranova, A. Alfier, P. Innocente, E. Martines, R. Pasqualotto, and P. Zanca. Single-helical-axis states in reversed-field-pinch plasmas. *Phys. Rev. Lett.*, 101(2):025005, 2008.

[162] U. Losada, A. Alonso, B.Ph. van Milligen, C. Hidalgo, B. Liu, M.A. Pedrosa, and C. et al. Silva. Influence of long-scale length radial electric field components on zonal flow-like structures in the TJ-II stellarator. *Plasma Phys. Control. Fusion*, 58(8):084005, 2016.

[163] P. Mantica, C. Angioni, B. Baiocchi, M. Baruzzo, M.N.A. Beurskens, J.P.S. Bizarro, R.V. Budny, P. Buratti, A. Casati, and C. et al. Challis. Ion heat transport studies in JET. *Plasma Phys. Control. Fusion*, 53(12):124033, 2011.

[164] P. Mantica, P. Galli, G. Gorini, G.M.D. Hogeweij, J. De Kloe, N.J.L. Cardozo, and RTP Team et al. Nonlocal transient transport and thermal barriers in rijnhuizen tokamak project plasmas. *Phys. Rev. Lett.*, 82(25):5048, 1999.

[165] P. Manz, D. Carralero, G. Birkenmeier, H.W. Müller, S.H. Müller, G. Fuchert, B.D. Scott, and U. Stroth. Filament velocity scaling laws for warm ions. *Phys. Plasmas*, 20(10):102307, 2013.

[166] P. Manz, T.T. Ribeiro, B.D. Scott, G. Birkenmeier, D. Carralero, G. Fuchert, S.H. Müller, H.W. Müller, U. Stroth, and E. Wolfrum. Origin and turbulence spreading of plasma blobs. *Phys. Plasmas*, 22(2):022308, 2015.

[167] R.J. Maqueda, D.P. Stotler, S.J. Zweben, and The, NSTX. Intermittency in the scrape-off layer of the National Spherical Torus Experiment during H-mode confinement. *Journal of nuclear materials*, 415(1):S459–S462, 2011.

[168] P.S. Marcus, T. Kundu, and C. Lee. Vortex dynamics and zonal flows. *Phys. Plasmas*, 7(5):1630–1640, 2000.

[169] L. Marrelli, R. Cavazzana, D. Bonfiglio, M. Gobbin, G. Marchiori, S. Peruzzo, M.E. Puiatti, G. Spizzo, D. Voltolina, and P. et al. Zanca. Upgrades of the RFX-mod reversed field pinch and expected scenario improvements. *Nucl. Fusion*, 2019.

[170] L. Marrelli, P. Zanca, M. Valisa, G. Marchiori, A. Alfier, F. Bonomo, M. Gobbin, P. Piovesan, D. Terranova, and M. et al. Agostini. Magnetic self organization, MHD active control and confinement in RFX-mod. *Plasma Phys. Control. Fusion*, 49(12B):B359, 2007.

[171] P. Martin, J. Adamek, P. Agostinetti, M. Agostini, A. Alfier, C. Angioni, V. Antoni, L. Apolloni, F. Auriemma, and O. et al. Barana. Overview of the RFX fusion science program. *Nucl. Fusion*, 51(9):094023, 2011.

[172] N. Mattor and P.H. Diamond. Drift wave propagation as a source of plasma edge turbulence. *Phys. Rev. Lett.*, 72(4):486, 1994.

[173] A. Mazurenko, M. Porkolab, D. Mossessian, J.A. Snipes, X.Q. Xu, and W.M. Nevins. Experimental and theoretical study of quasicoherent fluctuations in enhanced D α plasmas in the Alcator C-Mod tokamak. *Phys. Rev. Lett.*, 89(22):225004, 2002.

[174] G.R. McKee, R.J. Fonck, D.K. Gupta, D.J. Schlossberg, M.W. Shafer, R.L. Boivin, and W. Solomon. Plasma turbulence imaging via beam emission spectroscopy in the core of the DIII-D tokamak. *Plasma and Fusion Research*, 2:S1025–S1025, 2007.

[175] D. Meade. 50 years of fusion research. *Nucl. Fusion*, 50(1):014004, 2009.

[176] A.V. Melnikov, L.G. Eliseev, T. Estrada, E. Ascasibar, A. Alonso, A.A. Chmyga, C. Hidalgo, A.D. Komarov, A.S. Kozachek, and L.I. et al. Krupnik. Changes in plasma potential and turbulent particle flux in the core plasma measured by heavy ion beam probe during L-H transitions in the TJ-II stellarator. *Nucl. Fusion*, 53(9):092002, 2013.

[177] A.V. Melnikov, C. Hidalgo, L.G. Eliseev, E. Ascasibar, A.A. Chmyga, K.S. Dyabilin, I.A. Krasilnikov, V.A. Krupin, L.I. Krupnik, and S.M. et al. Khrebtov.

Plasma potential and turbulence dynamics in toroidal devices (survey of T-10 and TJ-II experiments). *Nucl. Fusion*, 51(8):083043, 2011.

[178] A.V. Melnikov, T. Markovic, L.G. Eliseev, J. Adámek, M. Aftanas, P. Bilkova, P. Boehm, M. Gryaznevich, M. Imrisek, and S.E. et al. Lysenko. Quasicoherent modes on the COMPASS tokamak. *Plasma Phys. Control. Fusion*, 57(6):065006, 2015.

[179] P. Migliucci, V. Naulin, and JET EFDA Contributors. Magnetic signature of current carrying edge localized modes filaments on the joint european torus tokamak. *Phys. Plasmas*, 17(7):072507, 2010.

[180] K. Miki and P.H. Diamond. Role of the geodesic acoustic mode shearing feedback loop in transport bifurcations and turbulence spreading. *Phys. Plasmas*, 17(3):032309, 2010.

[181] F. Militello and J.T. Omotani. Scrape off layer profiles interpreted with filament dynamics. *Nucl. Fusion*, 56(10):104004, 2016.

[182] J.A. Morales, M. Becoulet, X. Garbet, F. Orain, G. Dif-Pradalier, M. Hoelzl, S. Pamela, G.T.A. Huijsmans, P. Cahyna, and A. et al. Fil. Edge localized mode rotation and the nonlinear dynamics of filaments. *Phys. Plasmas*, 23(4):042513, 2016.

[183] J.R. Myra. Current carrying blob filaments and edge-localized-mode dynamics. *Phys. Plasmas*, 14(10):102314, 2007.

[184] J.R. Myra, W.M. Davis, D.A. D'Ippolito, B. LaBombard, D.A. Russell, J.L. Terry, and S.J. Zweben. Edge sheared flows and the dynamics of blob-filaments. *Nucl. Fusion*, 53(7):073013, 2013.

[185] J.R. Myra, D.A. Dippolito, S.I. Krasheninnikov, and G.Q. Yu. Convective transport in the scrape-off-layer by nonthermalized spinning blobs. *Phys. Plasmas*, 11(9):4267–4274, 2004.

[186] J.R. Myra, D.A. D'Ippolito, and D.A. Russell. Turbulent transport regimes and the scrape-off layer heat flux width. *Phys. Plasmas*, 22(4):042516, 2015.

[187] J.R. Myra, D.A. DIppolito, and X.Q. Xu. Drift wave instability near a magnetic separatrix. *Phys. Plasmas*, 9(5):1637–1645, 2002.

[188] J.R. Myra, D.A. Russell, and D.A. DIppolito. Collisionality and magnetic geometry effects on tokamak edge turbulent transport. I. A two-region model with application to blobs. *Phys. Plasmas*, 13(11):112502, 2006.

[189] I.C. Nascimento, Yu.K. Kuznetsov, J.H.F. Severo, A.M.M. Fonseca, A. Elfimov, V. Bellintani, M. Machida, M.V.A.P. Heller, R.M.O. Galvão, and E.K. et al. Sanada. Plasma confinement using biased electrode in the TCABR tokamak. *Nucl. Fusion*, 45(8):796, 2005.

[190] V. Naulin, A.H. Nielsen, and J.J. Rasmussen. Turbulence spreading, anomalous transport, and pinch effect. *Phys. Plasmas*, 12(12):122306, 2005.

[191] A.B. Navarro, L. Bardóczi, T.A. Carter, F. Jenko, and T.L. Rhodes. Effect of magnetic islands on profiles, flows, turbulence and transport in nonlinear gyrokinetic simulations. *Plasma Phys. Controll. Fusion*, 59(3):034004, 2017.

[192] R. Nazikian, K. Shinohara, G.J. Kramer, E. Valeo, K. Hill, T.S. Hahm, G. Rewoldt, S. Ide, Y. Koide, and Y. et al. Oyama. Measurement of turbulence decorrelation during transport barrier evolution in a high-temperature fusion plasma. *Phys. Rev. Lett.*, 94(13):135002, 2005.

[193] D.E. Newman, B.A. Carreras, P.H. Diamond, and T.S. Hahm. The dynamics of marginality and self-organized criticality as a paradigm for turbulent transport. *Phys. Plasmas*, 3(5):1858–1866, 1996.

[194] A.H. Nielsen, G.S. Xu, J. Madsen, V. Naulin, J.J. Rasmussen, and B.N. Wan. Simulation of transition dynamics to high confinement in fusion plasmas. *Phys. Lett. A*, 379(47-48):3097–3101, 2015.

[195] B. Nold, P. Manz, T.T. Ribeiro, G. Fuchert, G. Birkenmeier, H.W. Müller, M. Ramisch, B.D. Scott, and U. Stroth. Turbulent transport across shear layers in magnetically confined plasmas. *Phys. Plasmas*, 21(10):102304, 2014.

[196] B. Nold, T.T. Ribeiro, M. Ramisch, Z. Huang, H.W. Müller, B.D. Scott, and U. et al. Stroth. Influence of temperature fluctuations on plasma turbulence investigations with langmuir probes. *New Journal of Physics*, 14(6):063022, 2012.

[197] J.T. Omotani, F. Militello, L. Easy, and N.R. Walkden. The effects of shape and amplitude on the velocity of scrape-off layer filaments. *Plasma Phys. Control. Fusion*, 58(1):014030, 2015.

[198] J. Ongena, R. Koch, R. Wolf, and H. Zohm. Magnetic-confinement fusion. *Nat. Phys.*, 12(5):398, 2016.

[199] D.C. Ortiz. Electromagnetic instability studies in fusion plasmas edge. *Aerospace Engineering*, 2012.

[200] H.W. Ott and H.W. Ott. *Noise reduction techniques in electronic systems*, volume 442. Wiley New York, 1988.

[201] O. Pan, Y. Xu, J. Cheng, J.Q. Xu, L.W. Yan, K. Yao, M. Xu, Z.B. Shi, Yi Liu, Q.W. Yang, X.R. Duan, Y. Liu, and the HL-2A team. Investigation of mechanisms for the generation of blobs/holes at the boundary of the HL-2A tokamak. In *Proc. 26$^{\text{th}}$ IAEA Fusion Energy Conference (Kyoto, Japan)*, pages EX/P7–29, 2016.

[202] R. Panek, J. Adámek, M. Aftanas, P. Bílková, P. Böhm, F. Brochard, P. Cahyna, J. Cavalier, R. Dejarnac, and M. et al. Dimitrova. Status of the COMPASS tokamak and characterization of the first h-mode. *Plasma Phys. Control. Fusion*, 58(1):014015, 2015.

[203] R. Pánek, O. Bilyková, V. Fuchs, M. Hron, P. Chráska, P. Pavlo, J. Stöckel, J. Urban, V. Weinzettl, and J. et al. Zajac. Reinstallation of the COMPASS-D tokamak in IPP ASCR. *Czechoslovak Journal of Physics*, 56(2):B125–B137, 2006.

[204] S.E. Parker, H.E. Mynick, M. Artun, J.C. Cummings, V. Decyk, J.V. Kepner, W.W. Lee, and W.M. Tang. Radially global gyrokinetic simulation studies of transport barriers. *Phys. Plasmas*, 3(5):1959–1966, 1996.

[205] P. Paruta, C. Beadle, P. Ricci, and C. Theiler. Blob velocity scaling in diverted tokamaks: A comparison between theory and simulation. *Phys. Plasmas*, 26(3):032302, 2019.

[206] T.S. Pedersen, R. König, M. Jakubowski, M. Krychowiak, D. Gradic, C. Killer, T. Szepesi, H. Niemann, U. Wenzel, and A. et al. Ali. First divertor physics studies in Wendelstein 7-X. *Nucl. Fusion*, 2019.

[207] M.A. Pedrosa, C. Silva, C. Hidalgo, B.A. Carreras, R.O. Orozco, and D. et al. Carralero. Evidence of long-distance correlation of fluctuations during edge transitions to improved-confinement regimes in the TJ-II stellarator. *Phys. Rev. Lett.*, 100(21):215003, 2008.

[208] R.A. Pitts, P. Andrew, G. Arnoux, T. Eich, W. Fundamenski, A. Huber, C. Silva, D. Tskhakaya, and JET EFDA Contributors. ELM transport in the JET scrape-off layer. *Nucl. Fusion*, 47(11):1437, 2007.

[209] R.A. Pitts, G. Arnoux, M. Beurskens, T. Eich, W. Fundamenski, A. Huber, A. Loarte, J. Marki, M.F. Stamp, and P. et al. Andrew. The impact of large ELMs on JET. *Journal of nuclear materials*, 390:755–759, 2009.

[210] E. Poli, A. Bottino, W.A. Hornsby, A.G. Peeters, T. Ribeiro, B.D. Scott, and M. Siccinio. Gyrokinetic and gyrofluid investigation of magnetic islands in tokamaks. *Plasma Phys. Controll. Fusion*, 52(12):124021, 2010.

[211] S.B. Pope. Turbulent flows, 2001.

[212] E.R. Priest. *Dynamics and structure of quiescent solar prominences*, volume 150. Springer Science & Business Media, 2012.

[213] T.L. Rhodes, C. Holland, S.P. Smith, A.E. White, K.H. Burrell, J. Candy, J.C. DeBoo, E.J. Doyle, J.C. Hillesheim, and J.E. et al. Kinsey. L-mode validation studies of gyrokinetic turbulence simulations via multiscale and multifield turbulence measurements on the DIII-D tokamak. *Nucl. Fusion*, 51(6):063022, 2011.

[214] P. Ricci, F.D. Halpern, S. Jolliet, J. Loizu, A. Mosetto, A. Fasoli, I. Furno, and C. Theiler. Simulation of plasma turbulence in scrape-off layer conditions: the GBS code, simulation results and code validation. *Plasma Phys. Control. Fusion*, 54(12):124047, 2012.

[215] Ch.P. Ritz, R.D. Bengtson, S.J. Levinson, and E.J. Powers. Turbulent structure in the edge plasma of the TEXT tokamak. *The Physics of fluids*, 27(12):2956–2959, 1984.

[216] Ch.P. Ritz, H. Lin, T.L. Rhodes, and A.J. Wootton. Evidence for confinement improvement by velocity-shear suppression of edge turbulence. *Phys. Rev. Lett.*, 65(20):2543, 1990.

[217] Ch.P. Ritz, E.J. Powers, T.L. Rhodes, R.D. Bengtson, K.W. Gentle, H. Lin, P.E. Phillips, A.J. Wootton, D.L. Brower, and N.C. et al. Luhmann Jr. Advanced plasma fluctuation analysis techniques and their impact on fusion research. *Rev. Scient. Instrum.*, 59(8):1739–1744, 1988.

[218] O. Sakai, Y. Yasaka, and R. Itatani. High radial confinement mode induced by dc limiter biasing in the HIEI tandem mirror. *Phys. Rev. Lett.*, 70(26):4071, 1993.

[219] E. Sanchez, T. Estrada, J.L. Velasco, I. Calvo, A. Cappa, A. Alonso, J.M. García-Regaña, R. Kleiber, and J. et al. Riemann. Validation of global gyrokinetic simulations in stellarator configurations. *Nucl. Fusion*, 59(7):076029, 2019.

[220] R. Sanchez, D.E. Newman, J.-N. Leboeuf, and V.K. Decyk. Nature of turbulent transport across sheared zonal flows: insights from gyrokinetic simulations. *Plasma Phys. Controll. Fusion*, 53(7):074018, 2011.

[221] P. Sauter, T. Pütterich, F. Ryter, E. Viezzer, E. Wolfrum, G.D. Conway, R. Fischer, B. Kurzan, R.M. McDermott, and S.K. et al. Rathgeber. L-to H-mode transitions at low density in ASDEX Upgrade. *Nucl. Fusion*, 52(1):012001, 2011.

[222] D.A. Schaffner, T.A. Carter, G.D. Rossi, D.S. Guice, J.E. Maggs, S. Vincena, and B. Friedman. Modification of turbulent transport with continuous variation of flow shear in the large plasma device. *Phys. Rev. Lett.*, 109(13):135002, 2012.

[223] J. Schirmer, G.D. Conway, H. Zohm, and W. et al. Suttrop. The radial electric field and its associated shear in the ASDEX Upgrade tokamak. *Nucl. Fusion*, 46(9):S780, 2006.

[224] A. Schmid, A. Herrmann, and H.W. et al. Müller. Experimental observation of the radial propagation of ELM induced filaments on ASDEX upgrade. *Plasma Phys. Controll. Fusion*, 50(4):045007, 2008.

[225] A. Schmid, A. Herrmann, V. Rohde, M. Maraschek, H.W. Müller, and ASDEX Upgrade Team. Magnetically driven filament probe. *Rev. Sci. Instrum.*, 78(5):053502, 2007.

[226] T. Schreiber. Measuring information transfer. *Phys. Rev. Lett.*, 85(2):461, 2000.

[227] B.D. Scott. Edge turbulence and its interaction with the equilibrium. *Contributions to Plasma Physics*, 46(7-9):714–725, 2006.

[228] G. Serianni, W. Baker, and S. Dal Bello. High-spatial resolution edge electrostatic probe system for RFX. *Rev. Sci. Instrum.*, 74(3):1558–1562, 2003.

[229] G. Serianni, T. Bolzonella, R. Cavazzana, G. Marchiori, N. Pomaro, L. Lotto, M. Monari, and C. Taliercio. Development, tests, and data acquisition of the integrated system of internal sensors for RFX. *Rev. Sci. Instrum.*, 75(10):4338–4340, 2004.

[230] K.-C. Shaing, E.C. Crume Jr, and W.A. Houlberg. Bifurcation of poloidal rotation and suppression of turbulent fluctuations: A model for the L-H transition in tokamaks. *Physics of Fluids B: Plasma Physics*, 2(6):1492–1498, 1990.

[231] C.E. Shannon and W. Weaver. *The mathematical theory of communication*. University of Illinois press, 1998.

[232] C. Silva, B. Gonçalves, C. Hidalgo, K. Erents, A. Loarte, G. Matthews, and M. Pedrosa. Determination of the particle and energy fluxes in the JET far SOL during ELMs using the reciprocating probe diagnostic. *Journal of nuclear materials*, 337:722–726, 2005.

[233] C. Silva, B. Goncalves, M.A. Pedrosa, C. Hidalgo, K. McCarthy, E. Calderon, J. Herranz, I. Pastor, and O. Orozco. Transport and fluctuations during electrode biasing on tj-ii. *Czechoslovak Journal of Physics*, 55(12):1589–1596, 2005.

[234] J.A. Snipes, B. LaBombard, M. Greenwald, I.H. Hutchinson, J. Irby, Y. Lin, A. Mazurenko, and M. Porkolab. The quasi-coherent signature of enhanced Dα H-mode in Alcator C-Mod. *Plasma Phys. Control. Fusion*, 43(4):L23, 2001.

[235] P.B. Snyder, R.J. Groebner, J.W. Hughes, T.H. Osborne, M. Beurskens, A.W. Leonard, H.R. Wilson, and X.Q. Xu. A first-principles predictive model of the pedestal height and width: development, testing and ITER optimization with the EPED model. *Nucl. Fusion*, 51(10):103016, 2011.

[236] P.B. Snyder, H.R. Wilson, J.R. Ferron, L.L. Lao, A.W. Leonard, T.H. Osborne, A.D. Turnbull, D. Mossessian, M. Murakami, and X.Q. Xu. Edge localized modes and the pedestal: A model based on coupled peeling–ballooning modes. *Phys. Plasmas*, 9(5):2037–2043, 2002.

[237] P.B. Snyder, H.R. Wilson, T.H. Osborne, and A.W. Leonard. Characterization of peeling–ballooning stability limits on the pedestal. *Plasma Phys. Controll. fusion*, 46(5A):A131, 2004.

[238] E.R. Solano, S. Jachmich, F. Villone, N. Hawkes, Y. Corre, R.A. Pitts, A. Loarte, B. Alper, K. Guenther, and A. et al. Koroktov. ELMs and strike point jumps. *Journal of nuclear materials*, 337:747–750, 2005.

[239] P. Sonato, G. Chitarin, P. Zaccaria, F. Gnesotto, S. Ortolani, A. Buffa, M. Bagatin, W.R. Baker, S. Dal Bello, and P. et al. Fiorentin. Machine modification for active MHD control in RFX. *Fusion engineering and design*, 66:161–168, 2003.

[240] M. Spolaore, P. Agostinetti, C. Killer, M. Moresco, M. Brombin, R. Cavazzana, R. Ghirardelli, G. Grenfell, O. Grulke, and S.A. et al. Lazerson. High resolution probe for filament transport and current density study at the edge region of W7-X. *Journal of Instrumentation*, 14(09):C09035, 2019.

[241] M. Spolaore, V. Antoni, R. Cavazzana, G. Regnoli, G. Serianni, E. Spada, N. Vianello, H. Bergsåker, and J.R. Drake. Effects of E× B velocity shear on electrostatic structures. *Phys. Plasmas*, 9(10):4110–4113, 2002.

[242] M. Spolaore, V. Antoni, E. Spada, H. Bergsåker, R. Cavazzana, J.R. Drake, E. Martines, G. Regnoli, G. Serianni, and N. Vianello. Vortex-induced diffusivity in reversed field pinch plasmas. *Phys. Rev. Lett.*, 93(21):215003, 2004.

[243] M. Spolaore, R. Cavazzana, L. Marrelli, L. Carraro, P. Franz, S. Spagnolo, B. Zaniol, M. Zuin, L. Cordaro, S. Dal Bello, G. De Masi, A. Ferro, C. Finotti, L. Grando, G. Grenfell, P. Innocente, O. Kudlacek, G. Marchiori, E. Martines, B. Momo, R. Paccagnella, P. Piovesan, C. Piron, M.E. Puiatti, M. Recchia, P. Scarin, C. Taliercio, N. Vianello, and L. Zanotto. H-mode achievement and edge features in RFX-mod tokamak operation. *Nucl. Fusion*, 57(11):116039, 2017.

[244] M. Spolaore, K. Kovařík, J. Stöckel, J. Adamek, R. Dejarnac, I. Ďuran, M. Komm, T. Markovic, E. Martines, and R. et al. Panek. Electromagnetic ELM and inter-ELM filaments detected in the COMPASS Scrape-Off Layer. *Nuclear Materials and Energy*, 12:844–851, 2017.

[245] M. Spolaore, N. Vianello, M. Agostini, R. Cavazzana, E. Martines, P. Scarin, G. Serianni, E. Spada, M. Zuin, and V. Antoni. Direct measurement of current filament structures in a magnetic-confinement fusion device. *Phys. Rev. Lett.*, 102(16):165001, 2009.

[246] M. Spolaore, N. Vianello, M. Agostini, R. Cavazzana, E. Martines, G. Serianni, P. Scarin, E. Spada, M. Zuin, and V. Antoni. Magnetic and electrostatic structures measured in the edge region of the RFX-mod experiment. *Journal of Nuclear Materials*, 390:448–451, 2009.

[247] M. Spolaore, N. Vianello, I. Furno, D. Carralero, M. Agostini, J. A. Alonso, F. Avino, R. Cavazzana, G. De Masi, A. Fasoli, C. Hidalgo, E. Martines, B. Momo, A. Scaggion, P. Scarin, S. Spagnolo, G. Spizzo, C. Theiler, and M. Zuin. Electromagnetic turbulent structures: A ubiquitous feature of the edge region of toroidal plasma configurations. *Phys. Plasmas*, 22(1):012310, 2015.

[248] M. Spolaore, N. Vianello, I. Furno, D. Carralero, M. Agostini, J.A. Alonso, F. Avino, R. Cavazzana, G. De Masi, and A. et al. Fasoli. Electromagnetic turbulent structures: A ubiquitous feature of the edge region of toroidal plasma configurations. *Phys. Plasmas*, 22(1):012310, 2015.

[249] P.C. Stangeby. *The plasma boundary of magnetic fusion devices*. CRC Press, 2000.

[250] P.C. Stangeby. A tutorial on some basic aspects of divertor physics. *Plasma Phys. Control. Fusion*, 42(12B):B271–B291, dec 2000.

[251] A. Stegmeir, A. Ross, T. Body, M. Francisquez, W. Zholobenko, D. Coster, O. Maj, P. Manz, F. Jenko, and B.N. et al. Rogers. Global turbulence simulations of the tokamak edge region with GRILLIX. *Phys. Plasmas*, 26(5):052517, 2019.

[252] U. Stroth. A comparative study of transport in stellarators and tokamaks. *Plasma Phys. Control. Fusion*, 40(1):9, 1998.

[253] H.J. Sun, P.H. Diamond, Z.B. Shi, C.Y. Chen, L.H. Yao, X.T. Ding, B.B. Feng, X.L. Huang, Y. Zhou, and J. et al. Zhou. Experimental evidence of the non-local response of transport to peripheral perturbations. *Nucl. Fusion*, 51(11):113010, 2011.

[254] M.A. Sutton, J.J. Orteu, and H. Schreier. *Image correlation for shape, motion and deformation measurements: basic concepts, theory and applications*. Springer Science & Business Media, 2009.

[255] R.D. Sydora, V.K. Decyk, and J.M. Dawson. Fluctuation-induced heat transport results from a large global 3d toroidal particle simulation model. *Plasma Phys. Control. Fusion*, 38(12A):A281, 1996.

[256] D. Tafalla and F.L. Tabarés. First boronization of the TJ-II stellarator. *Vacuum*, 67(3-4):393–397, 2002.

[257] P. Tamain, H. Bufferand, G. Ciraolo, C. Colin, Ph. Ghendrih, F. Schwander, and E. Serre. 3D Properties of Edge Turbulent Transport in Full-Torus Simulations and their Impact on Poloidal Asymmetries. *Contributions to Plasma Physics*, 54(4-6):555–559, 2014.

[258] R. J. Taylor, M. L. Brown, B. D. Fried, H. Grote, J. R. Liberati, G. J. Morales, P. Pribyl, D. Darrow, and M. Ono. H-mode behavior induced by cross-field currents in a tokamak. *Phys. Rev. Lett.*, 63(21):2365–2368, 1989.

[259] P.W. Terry. Suppression of turbulence and transport by sheared flow. *Reviews of Modern Physics*, 72(1):109, 2000.

[260] C. Theiler, I. Furno, A. Kuenlin, Ph. Marmillod, and A. Fasoli. Practical solutions for reliable triple probe measurements in magnetized plasmas. *Rev. Sci. Instrum.*, 82(1):013504, 2011.

[261] C. Theiler, I. Furno, P. Ricci, A. Fasoli, B. Labit, S.H. Müller, and G. Plyushchev. Cross-field motion of plasma blobs in an open magnetic field line configuration. *Phys. Rev. Lett.*, 103(6):065001, 2009.

[262] C. Theiler, J.L. Terry, E. Edlund, I. Cziegler, R.M. Churchill, J.W. Hughes, B. LaBombard, T. Golfinopoulos, and Alcator C-Mod Team et al. Radial localization of edge modes in Alcator C-Mod pedestals using optical diagnostics. *Plasma Phys. Controll. Fusion*, 59(2):025016, 2017.

[263] L.N. Trefethen and D. Bau III. *Numerical linear algebra*, volume 50. Siam, 1997.

[264] C. Tsallis. *Introduction to nonextensive statistical mechanics: approaching a complex world*. Springer Science & Business Media, 2009.

[265] C.K. Tsui, J.A. Boedo, J.R. Myra, B. Duval, B. Labit, C. Theiler, N. Vianello, W.A.J. Vijvers, H. Reimerdes, and S. et al. Coda. Filamentary velocity scaling validation in the TCV tokamak. *Phys. Plasmas*, 25(7):072506, 2018.

[266] H.Y.W. Tsui, R.D. Bengtson, G.X. Li, H. Lin, M. Meier, Ch.P. Ritz, and A.J. Wootton. A new scheme for Langmuir probe measurement of transport and electron temperature fluctuations. *Rev. Sci. Instrum.*, 63(10):4608–4610, 1992.

[267] M.V. Umansky, S.I. Krasheninnikov, B. LaBombard, and J.L. Terry. Comments on particle and energy balance in the edge plasma of Alcator C-Mod. *Phys. Plasmas*, 5(9):3373–3376, 1998.

[268] J.A. Van Allen. Inference of magnetospheric currents from multipoint magnetic field measurements. *American journal of physics*, 74(9):809–814, 2006.

[269] B. Van Milligen, B. Carreras, L. García, and J. Nicolau. The Radial Propagation of Heat in Strongly Driven Non-Equilibrium Fusion Plasmas. *Entropy*, 21(2):148, 2019.

[270] B.Ph. Van Milligen, G. Birkenmeier, M. Ramisch, T. Estrada, C. Hidalgo, and A. Alonso. Causality detection and turbulence in fusion plasmas. *Nucl. Fusion*, 54(2):023011, 2014.

[271] B.Ph. van Milligen, B.A. Carreras, L. García, A. Martín de Aguilera, C. Hidalgo, J.H. Nicolau, and TJ-II Team. The causal relation between turbulent particle flux and density gradient. *Phys. Plasmas*, 23(7):072307, 2016.

[272] B.Ph. Van Milligen, E. Sánchez, A. Alonso, M.A. Pedrosa, C. Hidalgo, A.M. De Aguilera, and A. L. Fraguas. The use of the biorthogonal decomposition for the identification of zonal flows at TJ-II. *Plasma Phys. Controll. Fusion*, 57(2):025005, 2014.

[273] G. Van Oost, J. Adamek, V. Antoni, P. Balan, J.A. Boedo, P. Devynck, I. Ďuran, L. Eliseev, J.P. Gunn, and M. et al. Hron. Turbulent transport reduction by e× b velocity shear during edge plasma biasing: recent experimental results. *Plasma Phys. Control. Fusion*, 45(5):621, 2003.

[274] J. Velasco and F. Castejón. Study of the neoclassical radial electric field of the TJ-II flexible heliac. *Plasma Phys. Controll. Fusion*, 54(1):015005, 2011.

[275] J.L. Velasco, J.A. Alonso, I. Calvo, and J. Arévalo. Vanishing neoclassical viscosity and physics of the shear layer in stellarators. *Phys. Rev. Lett.*, 109(13):135003, 2012.

[276] N. Vianello, D. Carralero, C.K.-W. Tsui, V. Naulin, M. Agostini, I. Cziegler, B. Labit, C. Theiler, E. Wolfrum, and D. et al. Aguiam. Scrape off layer (SOL) transport and filamentary characteristics in high density tokamak regimes. *Nucl. Fusion*, 2019.

[277] N. Vianello, V. Naulin, R. Schrittwieser, H.W. Müller, M. Zuin, C. Ionita, J.J. Rasmussen, F. Mehlmann, and V. et al. Rohde. Direct observation of current in type-I edge-localized-mode filaments on the ASDEX upgrade tokamak. *Phys. Rev. Lett.*, 106(12):125002, 2011.

[278] N. Vianello, M. Spolaore, M. Agostini, R. Cavazzana, G. De Masi, E. Martines, B. Momo, P. Scarin, S. Spagnolo, and M. Zuin. On the statistics and features of turbulent structures in RFX-mod. *Plasma Phys. Control. Fusion*, 58(4):044009, 2016.

[279] F. Wagner. A quarter-century of H-mode studies. *Plasma Phys. Controll. Fusion*, 49(12B):B1, 2007.

[280] F. Wagner, G. Becker, K. Behringer, D. Campbell, A. Eberhagen, W. Engelhardt, G. Fussmann, O. Gehre, J. Gernhardt, and G.v. et al. Gierke. Regime of improved confinement and high beta in neutral-beam-heated divertor discharges of the ASDEX tokamak. *Phys. Rev. Lett.*, 49(19):1408, 1982.

[281] N.R. Walkden, L. Easy, F. Militello, and J.T. Omotani. Dynamics of 3D isolated thermal filaments. *Plasma Phys. Control. Fusion*, 58(11):115010, 2016.

[282] R.E. Waltz and J. Candy. Heuristic theory of nonlocally broken gyro-Bohm scaling. *Phys. Plasmas*, 12(7):072303, 2005.

[283] R.E. Waltz, G.D. Kerbel, J. Milovich, and G.W. Hammett. Advances in the simulation of toroidal gyro-Landau fluid model turbulence. *Phys. Plasmas*, 2(6):2408–2416, 1995.

[284] H.Q. Wang, G.S. Xu, B.N. Wan, S.Y. Ding, H.Y. Guo, L.M. Shao, S.C. Liu, X.Q. Xu, E. Wang, and N. et al. Yan. New edge coherent mode providing continuous transport in long-pulse H-mode plasmas. *Phys. Rev. Lett.*, 112(18):185004, 2014.

[285] W.X. Wang, T.S. Hahm, W.W. Lee, G. Rewoldt, J. Manickam, and W.M. Tang. Nonlocal properties of gyrokinetic turbulence and the role of E× B flow shear. *Phys. Plasmas*, 14(7):072306, 2007.

[286] V. Weinzettl, R. Panek, M. Hron, J. Stockel, F. Zacek, J. Havlicek, P. Bilkova, D.I. Naydenkova, P. Hacek, and J. et al. Zajac. Overview of the COMPASS diagnostics. *Fusion Engineering and Design*, 86(6-8):1227–1231, 2011.

[287] J. Wesson and D.J. Campbell. *Tokamaks*, volume 149. Oxford university press, 2011.

[288] R.R. Weynants, G. Van Oost, G. Bertschinger, J. Boedo, P. Brys, T. Delvigne, K.H. Dippel, F. Durodie, H. Euringer, and K.H. et al. Finken. Confinement and profile changes induced by the presence of positive or negative radial electric fields in the edge of the TEXTOR tokamak. *Nucl. Fusion*, 32(5):837, 1992.

[289] G.S. Xu, V. Naulin, W. Fundamenski, C. Hidalgo, J.A. Alonso, C. Silva, B. Goncalves, A.H. Nielsen, J.J. Rasmussen, and S.I. et al. Krasheninnikov. Blob/hole formation and zonal-flow generation in the edge plasma of the JET tokamak. *Nucl. Fusion*, 49(9):092002, 2009.

[290] X. Xu, M. Umansky, B. Dudson, and P. Snyder. Boundary plasma turbulence simulations for tokamaks. *Communications in Computational Physics, vol. 4, no. 5, July 1, 2008, pp. 949-979*, 4(LLNL-JRNL-404082), 2008.

[291] X.Q. Xu. Simulations of tokamak boundary plasma turbulent transport. Technical report, Lawrence Livermore National Lab.(LLNL), Livermore, CA (United States), 2018.

[292] X.Q. Xu, N. Li, Z. Li, B. Chen, T.Y. Xia, T.F. Tang, B. Zhu, and V. Chan. Simulations of tokamak boundary plasma turbulence transport in setting the divertor heat flux width. *Nucl. Fusion*, 2019.

[293] X.Q. Xu, T.Y. Xia, N. Yan, Z.X. Liu, D.F. Kong, A. Diallo, R.J. Groebner, A.E. Hubbard, and J.W. Hughes. Toward integrated multi-scale pedestal simulations including edge-localized-mode dynamics, evolution of edge-localized-mode cycles, and continuous fluctuations. *Phys. Plasmas*, 23(5):055901, 2016.

[294] S. Yi, J.M. Kwon, P.H. Diamond, and T.S. Hahm. Effects of q-profile structure on turbulence spreading: A fluctuation intensity transport analysis. *Phys. Plasmas*, 21(9):092509, 2014.

[295] S. Yi, J.M. Kwon, P.H. Diamond, and T.S. Hahm. Turbulence spreading as a non-local mechanism of global confinement degradation and ion temperature profile stiffness. *Nucl. Fusion*, 55(9):092002, 2015.

[296] G.Q. Yu and S.I. Krasheninnikov. Dynamics of blobs in scrape-off-layer/shadow regions of tokamaks and linear devices. *Phys. Plasmas*, 10(11):4413–4418, 2003.

[297] G.S. Yun, W. Lee, M.J. Choi, J. Lee, H.K. Park, B. Tobias, C.W. Domier, N.C. Luhmann Jr, A.J.H. Donné, and J.H. et al. Lee. Two-dimensional visualization of growth and burst of the edge-localized filaments in KSTAR H-mode plasmas. *Phy. Rev. Lett.*, 107(4):045004, 2011.

[298] J. Zajac, R. Panek, F. Zacek, J. Vlcek, M. Hron, A. Krivska, R. Hauptmann, M. Danek, J. Simek, and J. Prosek. Power supply system for the COMPASS tokamak re-installed at the IPP, prague. *Fusion Engineering and Design*, 84(7-11):2020–2024, 2009.

[299] P. Zanca, L. Marrelli, G. Manduchi, and G. Marchiori. Beyond the intelligent shell concept: the clean-mode-control. *Nucl. Fusion*, 47(11):1425, 2007.

[300] D. Zhang, R. König, Y. Feng, R. Burhenn, S. Brezinsek, M. Jakubowski, B. Buttenschön, H. Niemann, A. Pavone, and M. et al. Krychowiak. First Observation of a Stable Highly Dissipative Divertor Plasma Regime on the Wendelstein 7-X Stellarator. *Phys. Rev. Lett.*, 123(2):025002, 2019.

[301] H. Zohm. Edge localized modes (ELMs). *Plasma Phys. Control. Fusion*, 38(2):105, 1996.

[302] H. Zohm. *Magnetohydrodynamic stability of tokamaks*. John Wiley & Sons, 2014.

[303] M. Zuin, N. Vianello, M. Spolaore, V. Antoni, T. Bolzonella, R. Cavazzana, E. Martines, G. Serianni, and D. Terranova. Current sheets during spontaneous reconnection in a current-carrying fusion plasma. *Plasma Phys. Control. Fusion*, 51(3):035012, 2009.

[304] S.J. Zweben. Search for coherent structure within tokamak plasma turbulence. *The Physics of fluids*, 28(3):974–982, 1985.

[305] S.J. Zweben, J.A. Boedo, O. Grulke, C. Hidalgo, B. LaBombard, R.J. Maqueda, P. Scarin, and J.L. Terry. Edge turbulence measurements in toroidal fusion devices. *Plasma Phys. Controll. Fusion*, 49(7):S1, 2007.

[306] S.J. Zweben, J.R. Myra, W.M. Davis, D.A. DIppolito, T.K. Gray, S.M. Kaye, B.P. LeBlanc, R.J. Maqueda, D.A. Russell, and D.P. et al. Stotler. Blob structure and motion in the edge and sol of NSTX. *Plasma Phys. Control. Fusion*, 58(4):044007, 2016.